Advanced Design, Test and Fabrication of Silica Based Micro Optics

Matthew Oren Currie

Submitted for the degree of Doctor of Engineering

Heriot-Watt University

School of Engineering and Physical Sciences

May 2016

ABSTRACT

This thesis presents important advances in the laser processing of fused silica in order to create micro-optical structures using the techniques originally developed by the Lasers and Photonics Applications (LPA) group at Heriot-Watt University and subsequently by PowerPhotonic Ltd., the company created to commercialise the technology. This technology uses a CO_2 laser operating in two separate modes at a wavelength of 10.6µm in order to first create a desired surface profile and subsequently to polish the surface, creating arbitrary freeform surface topologies with high quality optical surfaces.

The first fabrication mode undertaken during processing, referred to as laser cutting, was investigated to determine whether the upper limit of achievable cut depth could be increased, which was approximately 60µm at the start of the EngD project. This resulted in the establishment of new methods that increase the sag of optics that can be manufactured using this laser machining process, with cut depths over 400µm. This in turn enabled the design and fabrication of fast-axis collimator arrays (FACAs), for which a patent was granted in 2014.

During fabrication of these deep optics it was found that the silica dust produced during the laser cutting process can have a detrimental effect on final surface quality as it may be re-melted and fuse with the optical surface, changing the expected shape. Mechanisms that remove the dust as it is being produced were investigated and refined and subsequently used to create a system and methodology that is suitable for use in a production environment. This extraction system can now be used to create high quality optics even where volume removal, and thus dust generated, is large.

The experience gained when designing, fabricating and testing a wide range of optical surfaces over the course of this EngD period enabled the design, development and implementation of a web-based rapid fabrication service for prototype freeform optics called LightForge. This original work now offers the unique ability in the micro-optics market for a customer to upload a fully defined optical design through a web portal and have it manufactured within 2 weeks. This revolutionary service has, and continues to, considerably expand the visibility and reach of PowerPhotonic within the micro-optics market. A patent has been applied to cover this process and is currently being examined.

DEDICATION

This work is dedicated to all of the friends, family, colleagues and university staff that have helped to make it a reality, whether through coaching, encouragement, understanding or indeed exasperation. This list is short, but the number of people who I am grateful to have in my life is long and I wouldn't have it any other way.

A huge thank you to Andy, Jozef and Roy at PowerPhotonic for teaching me the skills and knowledge that underpin essentially everything contained within this work, as well as putting up with me for so long on a day-to-day basis. Julian deserves a special mention for helping me to find the time to complete writing and for your (possibly masochistic) willingness to take a roguish engineer in to your team. This thesis literally would not have been possible without the continued guidance and support from you all.

Howard, your help and support have proven invaluable. Our discussions about the past, present and future of PowerPhotonic's capabilities have not only helped form the ideas present here but given me a better understanding of the state of the art. Linda, Alison, Alex and Derryck from Heriot-Watt University, you have gone out of your way to help me a number of times over the years. I hope that one day I can pay you back!

Emma and Neil, taking me to Portugal was one of the best things that could have happened to this thesis. It wasn't quite Roald Dahl's writing hut but it certainly did the trick. Who knew that sitting on a sunny balcony with a cold beer, sea breeze ruffling the nearby flowers, would allow for a writing output several orders of magnitude higher than doing the same thing in the back garden at home? I look forward to many more good times in the future.

To my parents, your care and words of encouragement over the years ensured I got over all of these various educational hurdles that I seem to like setting for myself. Perhaps I wouldn't even be writing this now if we didn't have "fun" maths challenges when I was off ill from school. The lessons that you taught me (both academic and moral) are what makes me the person I am, so in many ways this thesis is yours as well.

And finally to Lorraine, your love and dedication over the years can never be repaid. Thinking back to when I undertook this EngD, I had no clue how difficult it would be to get to where I am now. I suspect that you are the only reason I managed to finish at all thanks to your unending support and desire to help wherever possible. Your ability to appear interested when I drone on about glass properties and laser materials processing is legendary. I can't wait to get old and wrinkly with you.

DECLARATION STATEMENT

ACADEMIC REGISTRY
Research Thesis Submission

Name*:*	Matthew Currie		
School/PGI:	School of Engineering and Physical Sciences		
Version: *(i.e. First, Resubmission, Final)*	Final	Degree Sought (Award **and** Subject area)	Doctor of Engineering

Declaration

In accordance with the appropriate regulations I hereby submit my thesis and I declare that:

1) the thesis embodies the results of my own work and has been composed by myself
2) where appropriate, I have made acknowledgement of the work of others and have made reference to work carried out in collaboration with other persons
3) the thesis is the correct version of the thesis for submission and is the same version as any electronic versions submitted*.
4) my thesis for the award referred to, deposited in the Heriot-Watt University Library, should be made available for loan or photocopying and be available via the Institutional Repository, subject to such conditions as the Librarian may require
5) I understand that as a student of the University I am required to abide by the Regulations of the University and to conform to its discipline.

* *Please note that it is the responsibility of the candidate to ensure that the correct version of the thesis is submitted.*

Signature of Candidate*:*		Date:	

Submission

Submitted By *(name in capitals):*	
Signature of Individual Submitting:	
Date Submitted:	

For Completion in the Student Service Centre (SSC)

Received in the SSC by *(name in capitals):*			
Method of Submission *(Handed in to SSC; posted through internal/external mail):*			
E-thesis Submitted (mandatory for final theses)			
Signature:		Date:	

PUBLICATION LIST

PowerPhotonic White Papers

1. M. O. Currie, *‘Laser beamshaping for industrial applications’*, PowerPhotonic white paper (2014)

Conference Publications and Presentations

1. R. M. McBride, N. Trela, M. O. Currie, J. J. Wendland, H. J. Baker, *‘Monolithic fast-axis collimation of diode laser stacks’*, Proceedings of the SPIE vol. 8605, Photonics West Conference, San Francisco, USA (2013)
2. R. M. McBride, D. Walker, M. O. Currie, H. J. Baker, *‘Refractive beamshaping for high-power laser applications’*, AILU Conference, Cambridge, UK (2013)
3. M. O. Currie, R. M. McBride, *‘Rapid Manufacture of freeform micro-optics for high power applications’*, Proceedings of the SPIE vol. 8970, Photonics West Conference, San Francisco, USA (2014)
4. R. M. McBride, N. Trela, M. O. Currie, D. Walker, H. J. Baker, *‘Beamshaping for high-power lasers using freeform refractive optics’*, Proceedings of the SPIE vol. 8963, Photonics West Conference, San Francisco, USA (2014)
5. M. O. Currie, *‘Beamshaping for high-power lasers using freeform refractive micro-optics’*, Lahat Technologies 6th Optic Seminar, Tel Aviv, Israel (2014)
6. M. O. Currie, *‘Laser beamshaping using freeform optics for industrial materials processing’*, EPIC Workshop on Freeform Optics, Copenhagen, Denmark (2015)

Patent Applications

1. R. McBride, M. O. Currie and J. J. Wendland, “Fast-Axis Collimator Array”. United States of America Patent US8570657 (2014)
2. R. McBride, M. O. Currie and J. J. Wendland, “Fast-Axis Collimator Array”. United Kingdom Patent GB2485464 (2014)

3. R. McBride, M. O. Currie and J. J. Wendland, “Fast-Axis Collimator Array”. European Union Patent EP2450737 (2014)
4. M. O. Currie, C. Y. Younger and R. M. McBride, “Design and Manufacture of Custom Optical Elements”. United Kingdom Patent GB2510420 (2014).
5. M. O. Currie, C. Y. Younger and R. M. McBride, “Process for the Manufacture of Custom Optical Elements”. United States of America Patent US2014222182 (2014)

TABLE OF CONTENTS

Chapter 1 – Introduction and background

This thesis describes advances in the fields of micro-optical design and particularly the fabrication of micro-optical structures. The research presented was carried out entirely at PowerPhotonic Ltd., a company formed in 2004 to commercialise the results of extensive research carried out in the Lasers and Photonics Applications (LPA) group at Heriot-Watt University. The fabrication method uses a CO_2 laser in two different modes of operation to create micro-optical structures out of fused silica substrates that have very low surface roughness. This process is implemented in such a way that arbitrary freeform surfaces with no axes of symmetry may be manufactured.

Within this work a number of aspects of the manufacturing process are investigated with the purposes of enhancing the existing process or creating new processes that expand the commercial product catalogue offered by PowerPhotonic.

1.1 – Background

The first publication by the LPA group about the CO_2 laser machining of micro-optical structures in to fused silica in 2002 [1], which described the removal of volumes of material when illuminated by the laser under various conditions. This work established a process window in terms of beam size, temporal pulse width and pulse energy that provided the optimum balance of volume removal rate and surface quality.

It was found that, when using a laser beam with focussed spot diameter of 54μm, short pulse widths on the order of μs that would normally be used in a laser material removal application created filamentary melt ejection (see Figure 1) that reduced the usefulness of the surface created. Experimentation with different pulse widths showed that values in the range of 30-50μs produced significantly smoother machined surfaces. In this regime the primary volume removal mechanism is relatively slow thermal evaporation due to absorption rather than other types of micromachining processes that rely on fast thermal processes or disassociation by multiphoton absorption.

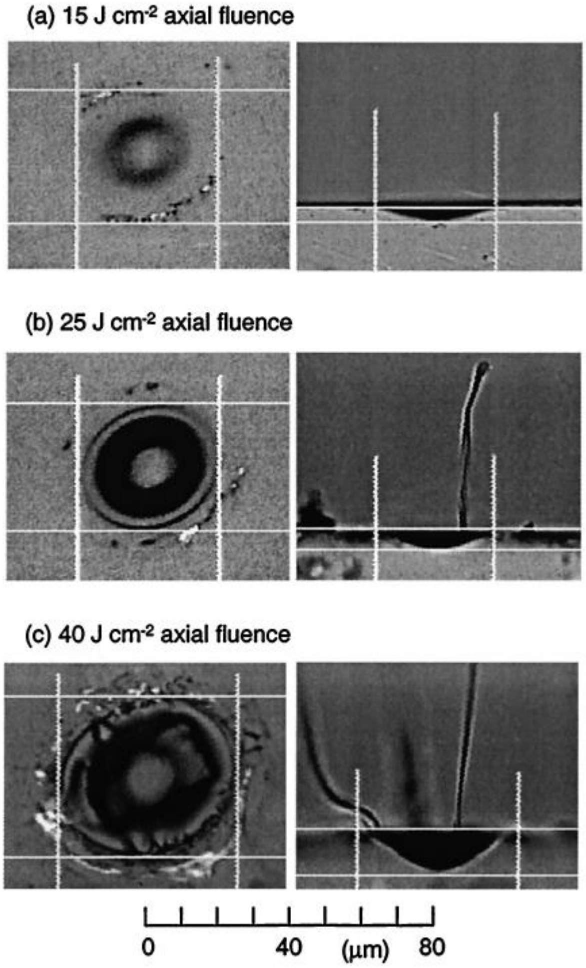

Figure 1: Micrographs of the view from the side and top of laser machined craters in fused silica with varying axial fluence. Note the filamentous melt ejection features protruding from the surface in (b) and (c). Taken from [1]

The Markillie paper also introduced the concept of overlapping these individual craters in order to machine structures in to the surface that are larger than the spot size:

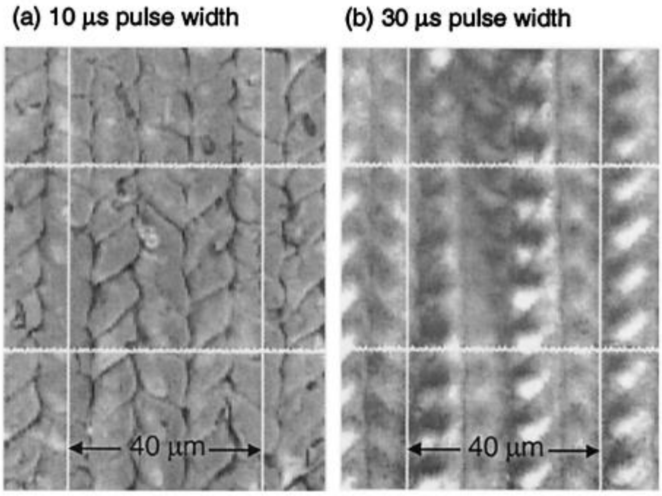

Figure 2: Planar surfaces machined using a laser beam with 27µm radius and 25Jcm^{-2} axial fluence, raster scanned with a 10x10µm grid and comparing the difference in surface texture produced when using 10µs and 30µs pulse widths. Taken from [1].

Although this work was fundamental in defining a suitable process window for material removal, it alone did not produce surfaces that were sufficiently smooth to be used as laser optics. In 2003 Nowak [2] from the LPA group presented a paper that built upon previous machining work of creating a micro-lens shape by varying the pulse energy of the each individual pulse as the laser beam was scanned over the surface of the fused silica, thereby fabricating a 3-dimensional structure as seen in Figure 3.

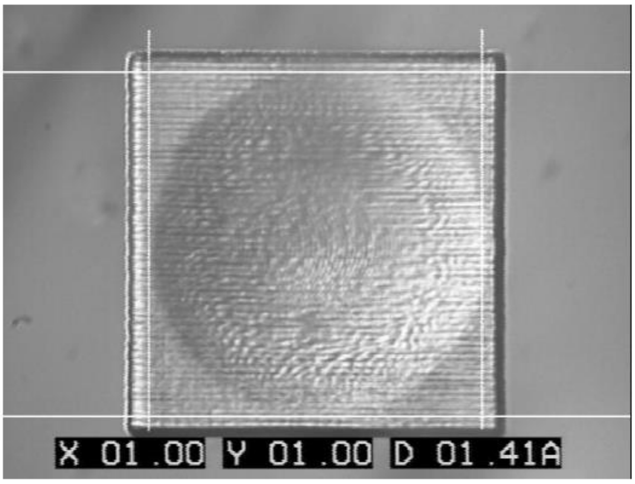

Figure 3: A microlens with 1mm aperture size and radius of curvature of approximately 12mm, showing after the material removal step. Units shown are in millimetres. Taken from [2].

After the shape of the lens was created, a laser melting process was applied to the surface to smooth without deforming the lens shape. This involved scanning a focussed laser beam over the machined surface in a fixed raster pattern, which melts a thin layer of the substrate. This melt pool then flows outwards due to the thermal tension gradient established by the laser beam intensity distribution and resolidifies, leaving a smooth surface.

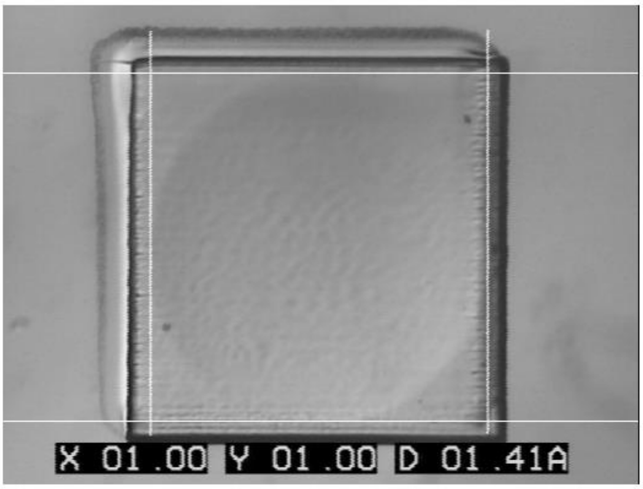

Figure 4: The microlens shown in Figure 3 after undergoing the laser melting process. Units shown are in millimetres. Taken from [2].

Laser polishing had been used for some time, with a team from Lawrence-Livermore National Labs [3] using it in 1982 to increase laser damage resistance of fused silica optics. However this was the first time a CO_2 laser polishing step had been applied to optics that were themselves manufactured with a CO_2 laser. It was shown in a further paper from Nowak [4] that the laser polishing step acted as a low-pass filter on the spatial frequency content of the machined fused silica surface. This paper also showed that the cut-off frequency of the low-pass filtering mechanism could be adjusted by changing certain laser processing conditions such as laser power, laser beam spot size, velocity of the laser beam spot travelling over the surface and overlap of the raster lines. When investigating these process conditions it was found that a certain range of process parameters resulted in a favourable regime where the mass loss due to evaporation of the melt pool was minimised, which would preserve the shape that had been created during the machining process.

As the laser machining step was operated with a fixed grid, a significant proportion of the spatial frequency content would be consistent even between different optical surface designs. For example, an optical surface that was machined with a raster grid of 10x10µm would have a significant spatial frequency peak at 100 lines/mm when examined in frequency space using a suitable Fourier transform. Knowing this, the parameters of the laser polishing process were optimised such that mass loss due to evaporation was minimised yet the characteristic spatial frequency content of the machining process was highly attenuated.

By this time PowerPhotonic had been established to commercialise the machining and polishing processes by using them to produce saleable optical surfaces, and the laser micromachining systems used for the machining (which was subsequently patented [5] [6], [7] in 2012) and polishing the substrates had been productionised. These first machines were capable of producing smooth freeform optical surfaces in fused silica with maximum sags up to approximately 40µm. This sag range and the freeform capability allowed for the design and manufacture of optical surfaces to correct for the phase errors inherent in high power diode laser (HPDL) arrays, developed first by the LPA group [8] and further improved at PowerPhotonic [9], as well as optical surfaces that can transform the intensity distribution of single-mode laser beams [10] known as field mappers [11].

1.1.1 – Phase errors in HPDL arrays

The first product offered by PowerPhotonic was used to correct for the phase and pointing errors found when HPDL emitters are organised in to arrays, whether a single bar of diode emitters that creates a 1-dimensional array or a stack of bars that creates a 2-dimensional array. The output of laser diode emitters is commonly described using two orthogonal axes known as the fast-axis (x-axis on Figure 5) and slow-axis (y-axis on Figure 5), due to the fact that laser beam diverges much faster in the fast axis. The slow- and fast-axes are typically lensed with separate cylindrical optics, known as fast-axis collimators (FAC) and slow-axis collimators (SAC) in order to produce a nominally circular collimated beam.

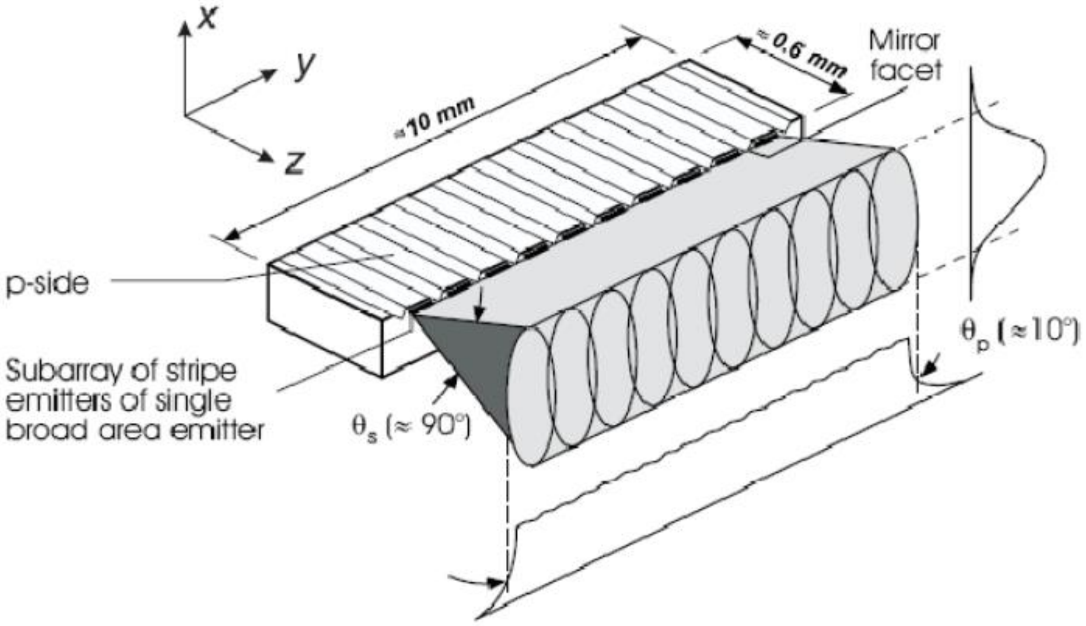

Figure 5: A diagram showing the layout and output of a single unlensed laser diode bar with 10 emitters. Taken from [12].

HPDL arrays are used in a variety of different applications, most commonly as pump sources for solid state and fibre lasers where high power outputs are required. HPDL arrays are highly efficient, compact and robust. However manufacturing errors result in poor overall beam quality due to the geometry of the array after fabrication and lensing with the FAC and SAC is completed. Although highly efficient at converting electrical energy to radiation, cooling is often still required in order to maintain a useful lifetime of diode operation. This necessitates soldering of the substrate of diode emitters to a heat sink, which in turn induces stress and causes the substrate to warp. This warping creates spatial offsets between the diodes in the fast-axis, which is translated to angular offsets after the emitter radiation passes through the FAC. This angular offset is commonly referred to as “smile” due to the fact that it can sometimes be parabolic in shape, and it decreases the overall brightness of the HPDL array.

These additional lensing errors can also occur:

1. Some of the emitters can be out located away from the focal plane of the FAC lens due to rotation of the FAC about the fast-axis, reducing the level of collimation achieved and thus brightness.
2. Form error of the FAC lenses, such as features left after grinding, that create wavefront errors in the transmitted beam and reduce brightness.

These errors are highly undesirable due to their effect on brightness, so the ability to mitigate or eliminate them can significantly improve the performance of an HPDL array.

1.1.2 – Measuring and correcting HPDL arrays

In order to design and manufacture the corrective optical surface, the wavefront HPDL array must be measured during full power operation so that the thermal conditions are the same as the ultimate use case. This potentially involved the measurement of multi-kW HPDL arrays during their operation and there was no solution available. Thus a wavefront sensing method was first developed by the LPA group [8] and subsequently developed and patented by PowerPhotonic [13] [14] [15], that allowed for high resolution scanning of the wavefront of an entire HPDL array while in operation. The wavefront sensor is raster scanned in front of the HPDL array and samples a small portion of the array output while directing the remainder on to beam dumps and records the wavefront pointing at that point (as shown in Figure 6). In this way a high-resolution wavefront map of the entire array can be constructed.

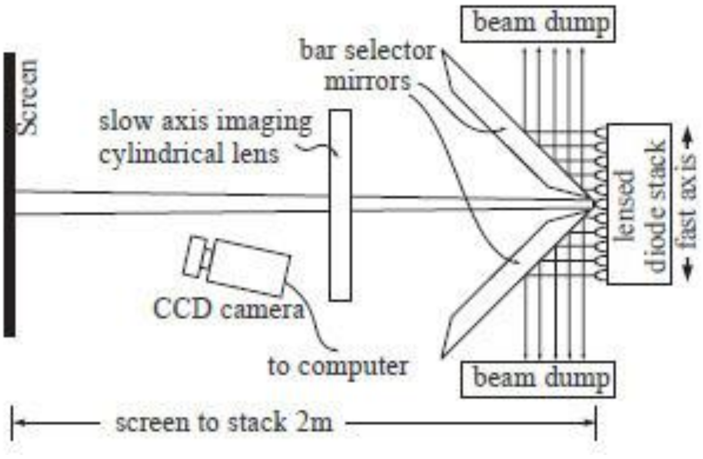

Figure 6: A top view of the wavefront sensor measuring an HPDL laser diode array, taken from [8].

The wavefront pointing data can then be used to design an optical surface (as shown in Figure 7) that will remove phase and pointing discrepancies between individual emitters, increasing total brightness of the HPDL array back to nearly diffraction-limited levels, as shown by the individual diode bar images in Figure 8.

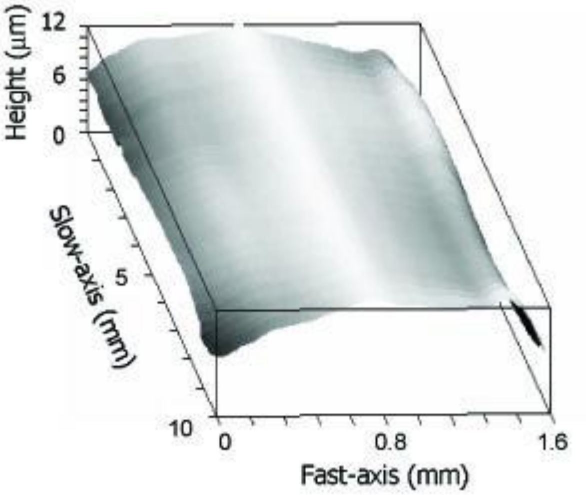

Figure 7: The surface profile of a corrective phase plate for a laser diode bar. Taken from [8].

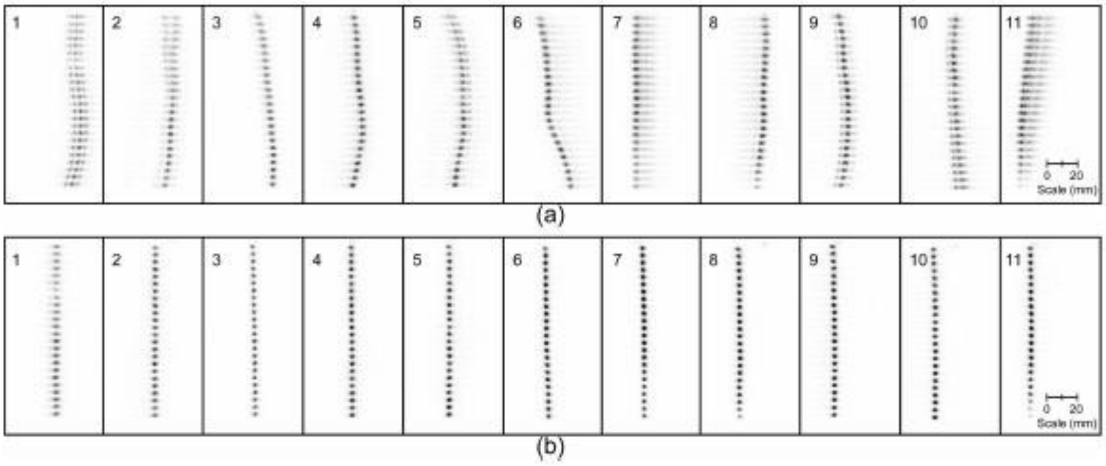

Figure 8: Far-field images of the individual bars within the HPDL array measured in [8]; row (a) are the images of the bars before correction, row (b) are the images after correction. Taken from [8].

This type of product has proven to be highly desirable in the marketplace and PowerPhotonic are uniquely placed to supply it due to the highly complex and freeform nature of the surfaces that PowerPhotonic can manufacture, requirement for fused silica due to the very high power and fast turnaround time from array measurement to phaseplate manufacture. PowerPhotonic recently announced that these HPDL correction optics have been integrated in to the High Repetition-Rate Advanced Petawatt Laser System (HAPLS), the highest peak power diode laser array currently operating in the world [16].

1.2 – Motivation

As an EngD thesis, there is a strong element of commercial motivation for undertaking the projects contained herein. The two-stage manufacturing process developed by the LPA group and now used at PowerPhotonic is highly flexible and capable of fabricating a very wide range of optical surfaces. This flexibility also enables engineers at PowerPhotonic to speculate about and test optical surfaces that might be disregarded as too expensive or difficult to manufacture by engineers not familiar with the manufacturing process. The motivation for the research carried out in this thesis is to create new processes that allow for the expansion of the product catalogue offered by PowerPhotonic, as well as create a mechanism to offer the PowerPhotonic fabrication process to optical engineers in a low-risk package.

1.3 – Objectives

The objective of this thesis are as follows:

1. Investigation of the impact on the expected surface form when using different raster patterns during the laser machining process and determining the optimum raster pattern for an arbitrary surface shape.
2. Increase the material removal depth that can be achieved by the laser machining process, while still maximising form accuracy.
3. Investigate the removal of the dust produced during the laser machining process, in order to increase the form accuracy of all optical structures and particularly structures of high depth.
4. Design and implement a system that allows optical engineers to send optical surface design files to PowerPhotonic that can be manufactured with minimal engineering effort.

1.4 – Thesis Structure

This thesis is divided in to 6 chapters:

1. This chapter focuses on the motivation behind the work presented herein as well as the specific objectives behind the work conducted during the EngD period.
2. Chapter 2 discusses the background information required to understand the investigations described in the later chapters of the thesis. It then details a method of monitoring the smoothing conditions developed as a project during this EngD.

It also describes the methodology of surface specification and how the product development process occurs internally at PowerPhotonic.

3. Chapter 3 presents two separate studies that are both aiming to enhance the capability of the laser machining process. The first investigates the effect of different raster patterns and proposes a test structure along with analysis methodology that can be used to periodically check process conditions. The second presents a method to manufacture very deep structures while reducing machining depth errors when machining occurs far away from the laser focus. This chapter culminates in the design, manufacture and test of an optical surface that was patented during the course of this EngD: a fast-axis collimator array (FACA).
4. Chapter 4 is an investigation into the dust produced during the laser machining process and how this dust might be removed as it is being produced using an assembly that creates a targeted airflow near the laser/substrate interaction site while ensuring that the laser machining process conditions are not affected. As this work was conducted on a working laser micromachining system that was expected to generate revenue for the company, it was particularly important for the assembly to be easily installed, removed and maintained when required.
5. Chapter 5 is in many ways the culmination of all of the knowledge gained over the EngD period, and almost all work was undertaken exclusively by the author. This chapter describes the design, development and implementation of an innovative new rapid fabrication service that allows optical engineers to upload their own optical designs to a website in a custom format that explicitly describes the surface for manufacture by PowerPhotonic. The website processes the surface file in order to ensure it is manufacturable, presents a representation of the final product to the engineer and accepts payment via credit card. The processing ensures that the surface design files have already been checked for compatibility with the process so can be loaded on to the laser micromachining system and manufactured without the input of an engineer within PowerPhotonic. This has the two-fold benefits of drastically reducing lead time and cost of the optical components, enabling quick and inexpensive trialling of novel optical designs.
6. Chapter 6 provides a conclusion to the work presented in this thesis and discusses future work that may be undertaken in order to build upon this work.

Chapter 2 – The PowerPhotonic fabrication process

The fundamental product offered by PowerPhotonic is a freeform micro-optical structure fabricated out of fused silica. As described in Chapter 1, these surfaces are created using a single mode CO_2 laser functioning in two different operational modes, although within PowerPhotonic and externally to customers these two modes are referred as laser cutting (instead of laser machining) and laser smoothing (instead of laser polishing).

The latest design of the micromachining system that is in use by PowerPhotonic is a combined system that allows an optic to be cut and smoothed fully without intermediate external intervention. Previously a single system could undertake both the cut and smooth operations but there was significant time delays as the laser was driven with different radio frequency pump power for cutting and smoothing, and changing this pump power caused instability in the cavity due to thermal changes that took a number of hours to relax. In the latest system, the laser is operated in a pulsed mode, and the total pulse energy is determined by a signal applied to an acousto-optic modulator (AOM). Due to the requirement for significantly different beam diameters for cutting and smoothing, there are two automated flip mirrors (FM1 and FM2 in Figure 9) in the optical path down which the laser beam travels. In this way the laser system can quickly and automatically switch between the cutting and smoothing modes, allowing for the large majority of optics to be manufactured without human intervention.

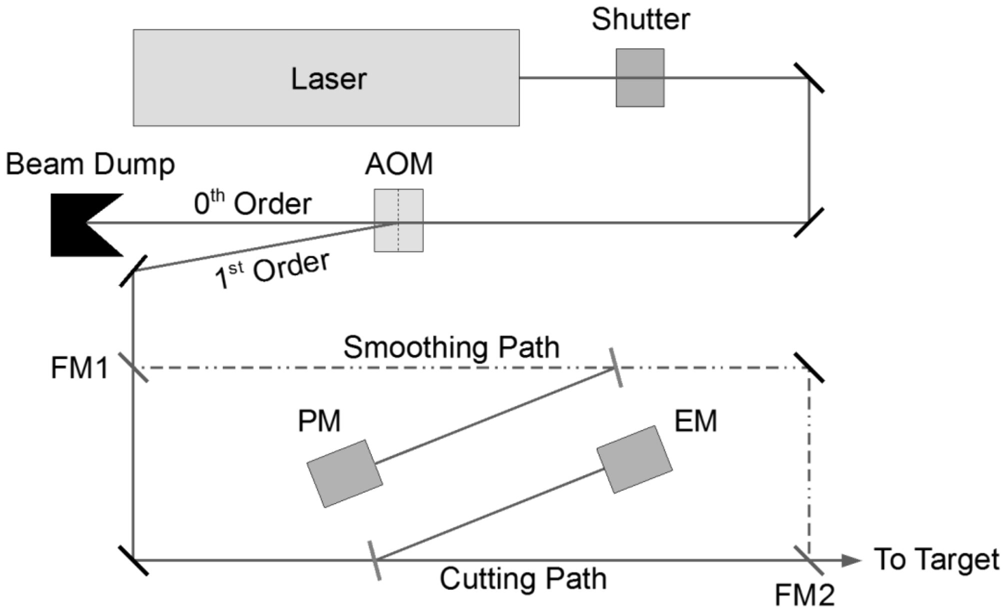

Figure 9: A schematic of the PowerPhotonic laser machining system showing the paths of the cutting and smoothing beams and main components. Flip Mirrors 1 and 2 (FM1 and FM2) are used to automatically switch between the cutting and smoothing modes. Power Monitor PM is used to measure and control smoothing beam power whilst Energy Monitor EM is used to measure and control cutting beam pulse energy.

The delivery end of the system is illustrated in Figure 10. The cutting and smoothing beams are folded through 90 degrees by a mirror assembly that acts as a phase retardation component which rotates the s- and p- polarisations by $\frac{\lambda}{4}$ with respect to each other. This was installed in the system in order to produce circularly polarised light incident on the surface, which ensures that the laser performance is isotropic in all directions of motion.

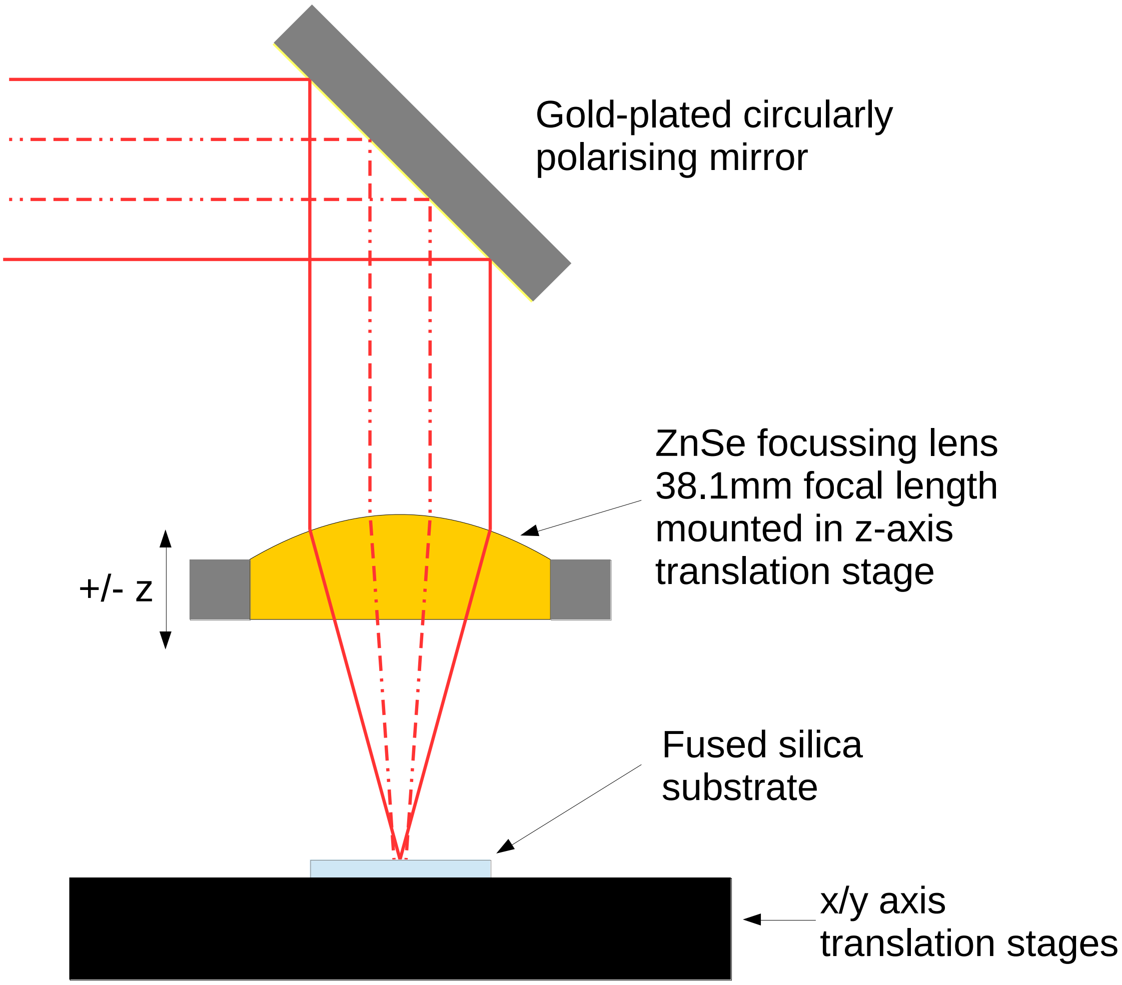

Figure 10: A representation of the delivery optics, showing the fused silica substrate location and the x/y axis translation stages. The solid line indicates the cutting beam and the dotted line indicates the smoothing beam. Drawing not to scale.

The circularly polarised laser beam ensures that the amount of light reflected from the surface of the fused silica substrate is independent from the orientation of the surface being illuminated. There are three different properties that vary the amount of reflection that occurs when light travels from one medium to another: the refractive indices of the two media, the angle at which the light intersects the new medium and the polarisation of the light. The equations that describe this interaction are the Fresnel equations, and are split into reflection of s-polarised light and p-polarised light:

$$R_s = \left| \frac{n_1 \cos\theta - n_2\sqrt{1 - \left(\frac{n_1}{n_2} sin\theta\right)^2}}{n_1 \cos\theta + n_2\sqrt{1 - \left(\frac{n_1}{n_2} sin\theta\right)^2}} \right|^2 \qquad (1)$$

$$R_p = \left| \frac{n_1\sqrt{1 - \left(\frac{n_1}{n_2} sin\theta\right)^2} - n_2 cos\theta}{n_1\sqrt{1 - \left(\frac{n_1}{n_2} sin\theta\right)^2} + n_2 cos\theta} \right|^2 \qquad (2)$$

$$R_{mean} = \frac{R_s + R_p}{2} \qquad (3)$$

Where n_1 and n_2 are the refractive indices of the first and second medium respectively, θ is the angle at which the light is incident upon the second medium and R_s and R_p denote the reflection of s-polarised and p-polarised light respectively. To illustrate, when $R_s(\theta)$ and $R_p(\theta)$ are plotted using n_1 = 1 and n_2 = 1.45, it is clear that the reflection behaviour of the s- and p-polarised start to diverge after around 10^o, and are significantly different at around 30^o and greater as shown in Figure 11. A circularly polarised beam has the reflection characteristics of the mean of the s- and p-polarisations, ensuring that the machining conditions will not alter due to the effects of linear polarisation incident upon varying slope.

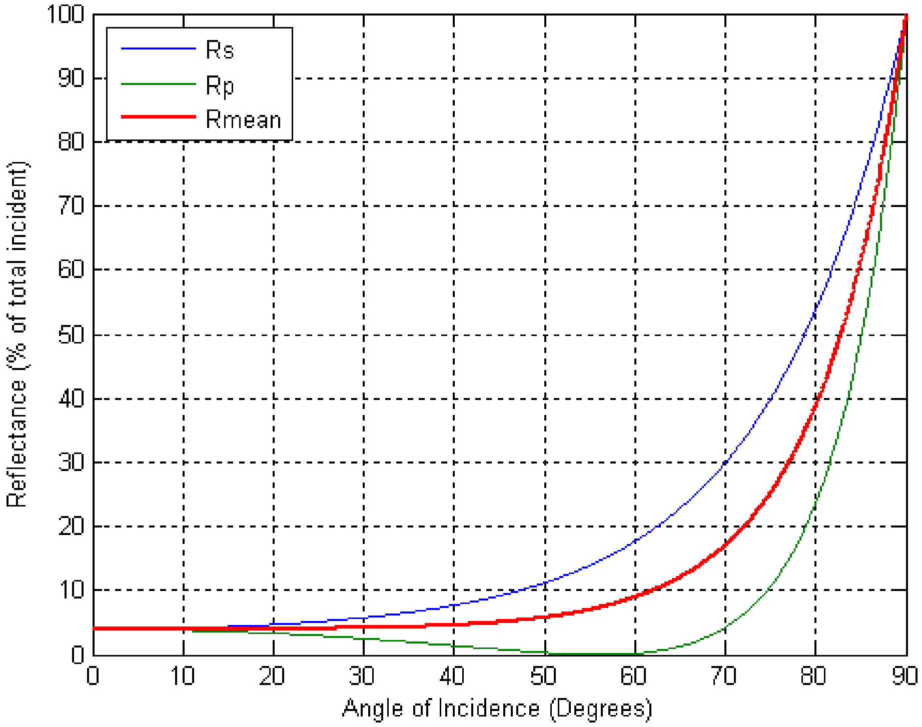

Figure 11: A plot of the Fresnel equations showing the behaviour of s- and p-polarised light as a function of incident angle; along with the mean of the two curves which describes the reflection behaviour of circularly polarised light.

To calculate the reflectivity of the surface during cutting, both the real part (n) and the imaginary part (k) of the complex refractive index must be used, the reflectivity at normal incidence is calculated using the equation from [17]:

$$R = \frac{(n-1)^2 + k^2}{(n+1)^2 + k^2} \tag{4}$$

Inserting the values of n = 2.224 and k = 0.102 for fused silica illuminated with a wavelength of 10.53µm, taken from [18], the reflectivity is calculated to be 14.5%.

2.1 – The cutting process

The cutting process is the first step of the optical fabrication process in which a blank fused silica substrate is ablated by a series of pulses from a CO_2 laser and forms the gross shape of the required structure. A silica substrate is moved under a focussed CO_2 laser beam by translation stages such that the laser focal point translates across the surface in a raster pattern and the laser beam removes material via a laser ablation process. Each point of the raster pattern is associated with a single laser pulse; multiple pulses are not used on a single raster point. The laser pulse width is on the order of 10s of microseconds, with a repetition rate of only a few hundred hertz in order to avoid thermal carryover from the pulses gradually heating the substrate and thus changing the absorption characteristics [19].

The laser beam spot diameter is between 2.5 and 10 times larger than the pitch for each laser pulse, so there is a significant degree of spatial overlap that allows for the fabrication of features that are similar to the spot diameter. This overlap also allows structures to be fabricated that are significantly deeper than the depth achieved using a single laser pulse; a single laser pulse removes a volume with depth of up to 8um whereas structures up to 60um can be fabricated using laser pulses that are spatially overlapping. However, the overlapping pulsed ablation method does leave behind a rough microstructure (Figure 12 and Figure 13) that must be eliminated for the surface to be used in an optical system.

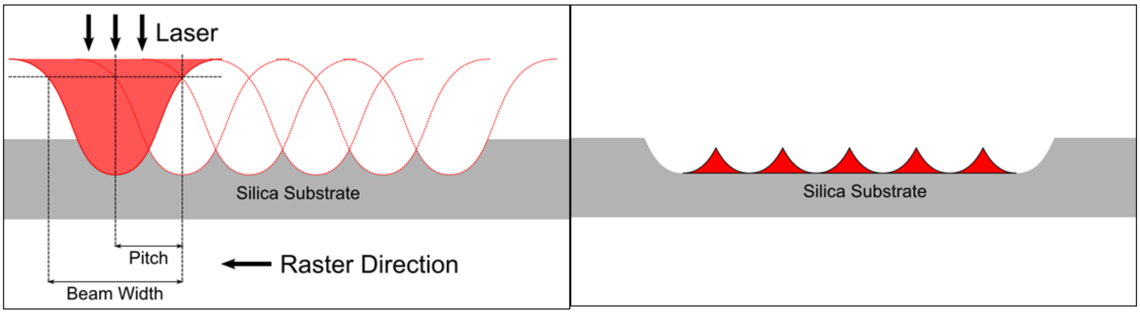

Figure 12: Left, a diagram showing silica volume removal along a raster cut line. Right, a diagram highlighting the rough microstructure left over after cutting (diagrams not to scale)

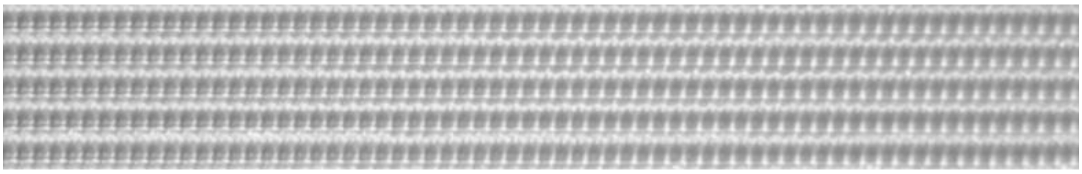

Figure 13: A micrograph of a surface after cutting a region of constant depth, showing the uniform structure left after the ablation process. The point spacing is 10um and the line spacing is 20um.

2.1.1 – Surface evolution during cutting

The overlapping ablation points mean that every point within the grid of a defined surface, apart from the very first, will be incident upon a surface that is non-planar. So rather than a simplistic point-wise machining process, the evolution of the surface occurs over a number of individual ablation points as illustrated in Figure 14.

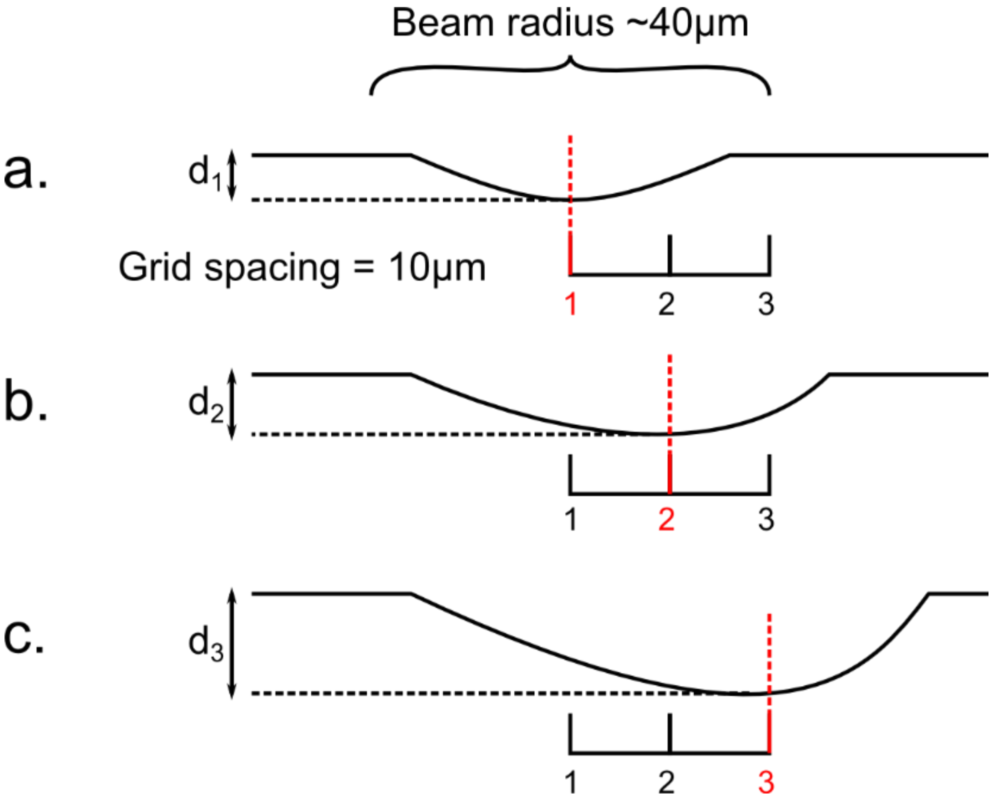

Figure 14: An illustration showing the surface evolution over 3 shots of the cutting laser. a. Shows the surface after a single shot. b. and c. show subsequent change in surface depth and profile after further illumination with the cutting laser (not to scale).

This evolving surface means that the surface topology at each ablation point is unique in slope and form as it depends on any previously machined surrounding ablation sites as well as the desired optical shape. Consider the machining of a small flat-bottomed pit, where the evolution to steady state depth occurs by the second ablation point along a cut row (Figure 15):

1. The first ablation point will be incident upon a flat surface (black circle)
2. The subsequent points will be incident upon a sloped surface that is only affected by previous ablation points in the x dimension (blue circles)
3. The first point on every line after line 1 will also be affected by previous ablation points in one dimension, but in the y dimension (red circles)
4. The remaining points will be incident upon a sloped surface that has been affected by previous points in both the x and y dimensions (yellow circles). These could be considered the points at which the cutting process has reached a steady state as the topology of the surface at each ablation point is very similar.

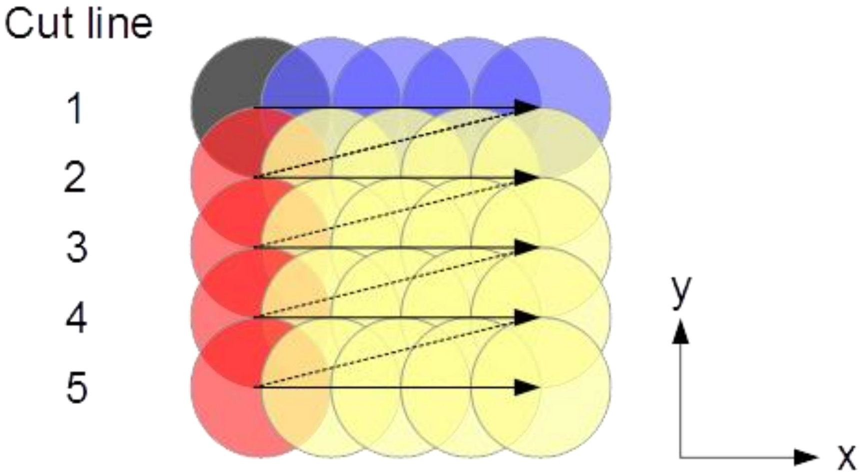

Figure 15: A simplified diagram showing similar groups of ablation sites for a small flat-bottomed pit. Machining starts at the black spot and progresses right along the blue line then returns to the left and ablates another row offset from the first. Different colours denote ablation sites where the laser is incident on a surface with the same slope and form.

Modelling this in 3 dimensions shows that the surface topology can be complex and evolves over significantly more than a single ablation site. To illustrate this surface topology, we can approximate a surface during the cutting process by subtracting truncated Gaussian volumes from a surface in a raster pattern. The radial profile of the truncated Gaussian volume removed was determined with a simple model taking in to account measured laser and material properties. The threshold laser fluence required to just start evaporating material has been previously found in the work of Markillie et al [1] to be 10 Jcm^{-2}.

The maximum axial fluence of a laser pulse with Gaussian intensity distribution can be determined by evaluating the radial integral of a Gaussian profile:

$$P(r) = \int_0^r I_0 e^{-\frac{2r^2}{w_0^2}} * 2\pi r\, dr \tag{5}$$

thus: $$P(r) = \frac{\pi w_0^2}{2} I_0 \left[1 - e^{-\frac{2r^2}{w_0^2}}\right] \tag{6}$$

where *P(r)* is the power enclosed within a circle of radius *r*, I_0 is the axial irradiance, and w_0 is the 1/e^2 radius of the distribution. In order to calculate the total enclosed power of the beam, the limit where *R* tends to infinity is determined:

$$P_{total} = \frac{\pi w_0^2}{2} I_0 \tag{7}$$

rearranging: $$I_0 = 2 * \frac{P_{total}}{\pi w_0^2} \tag{8}$$

and given: $$\phi_{max} = I_0 * t_{pulse} \tag{9}$$

$$\phi_{max} = \frac{2 * P_{total} * t_{pulse}}{\pi w_0^2} \tag{10}$$

where t_{pulse} is the laser pulse time and ϕ_{max} is the maximum pulse fluence. As an example, a laser pulse with P_{total} = 7W, t_{pulse} = 50μs and w_0 = 25μm, corresponds to ϕ_{max} = 35.65 Jcm^{-2}. An illustrative fluence profile of a TEM$_{00}$ laser beam can then be calculated:

$$\phi = \phi_{max} * e^{\frac{-2(x^2+y^2)}{r^2}} \tag{11}$$

Which gives the Gaussian fluence profile shown in Figure 16:

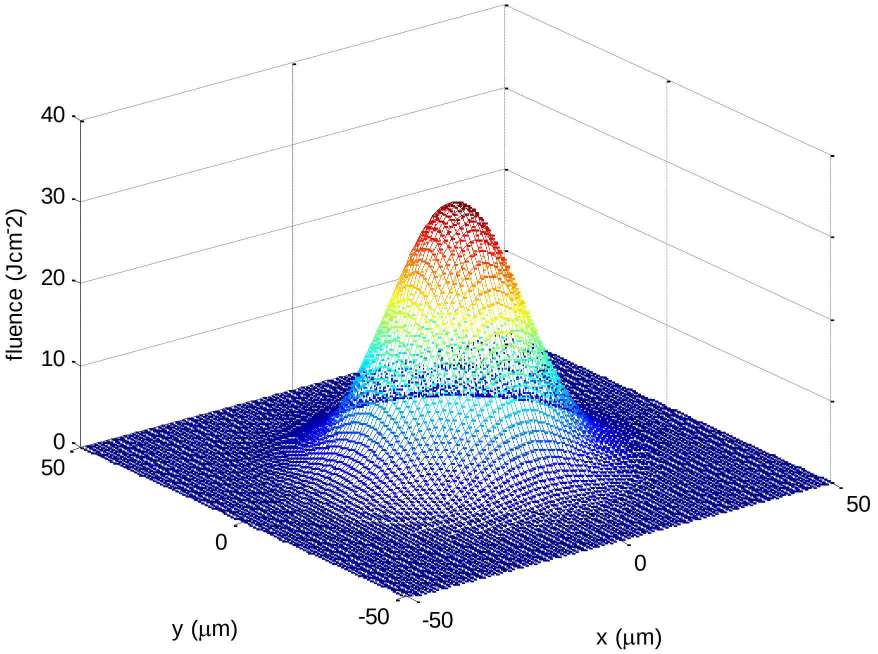

Figure 16: Fluence profile of the focussed laser beam at the beam waist

Subtracting the threshold fluence ϕ_{th} of 10 Jcm^{-2}, which incorporates loss from surface reflection R, which has been found above to be 14.5%, the truncated fluence profile can be found:

$$\phi_{truncated} = \phi - \phi_{th} \tag{12}$$

In order to convert the truncated fluence profile to an ablated surface volume, the energy density required to remove a unit volume of silica must be known. For the purposes of continuing this illustration, a value of 5x10^{-8} Jμm^{-3} has been used. The depth profile of the ablated volume can then be estimated using the following:

$$V_{ablated} = \frac{\phi_{truncated}}{\psi} \tag{13}$$

Where ψ is the energy density required to remove a unit volume of silica. This then gives the profile of the volume removed from a planar surface:

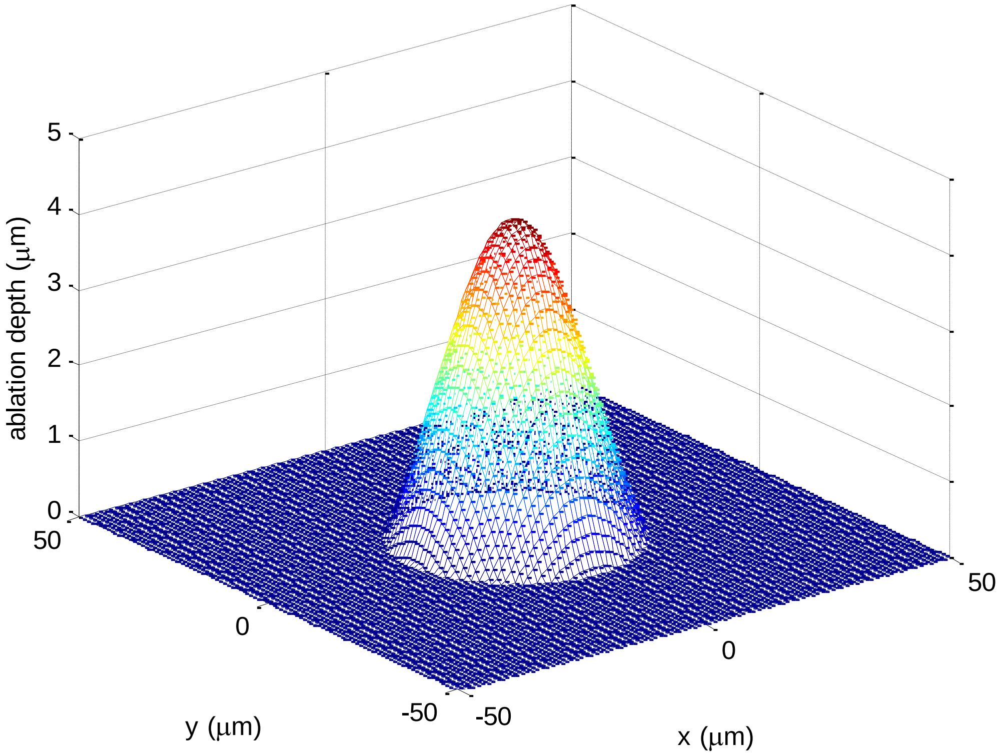

Figure 17: Truncated Gaussian profile of the glass volume removed during ablation

Shown in Figure 18 below is a square region created by progressively subtracting the truncated Gaussian volumes from a surface using a grid of 10x10μm and subtracting in the order that a simple raster pattern would follow. The first ablation point is located at (0,0) and progresses along a cut line in the positive y direction and steps to the next cut line in the positive x direction.

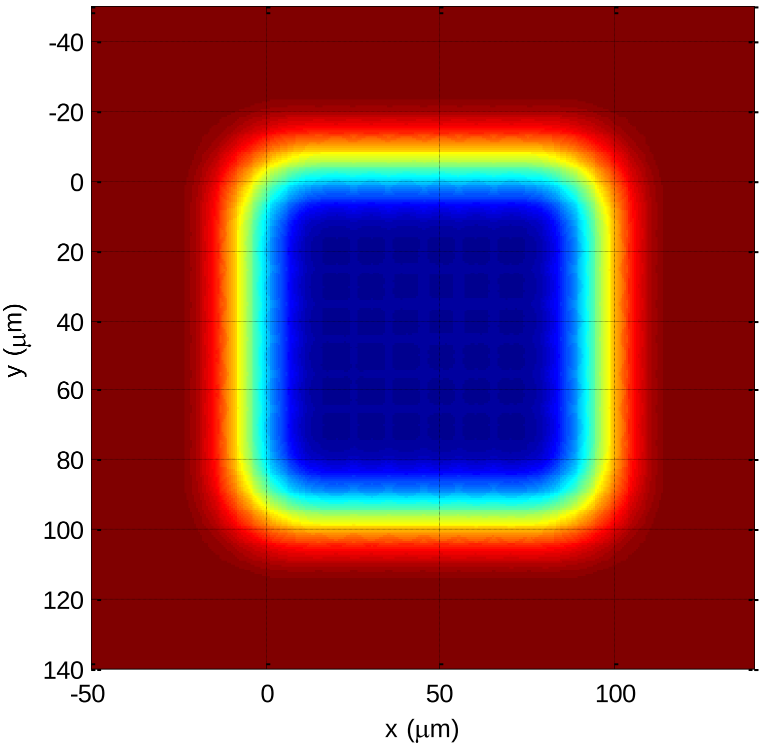

Figure 18: A surface created by subtracting identical truncated 10x10 Gaussian profiles from a plane with an ablation point grid = 10x10um

Looking at the ablation point of the second laser shot in the grid shows that the laser is not incident upon a simple surface:

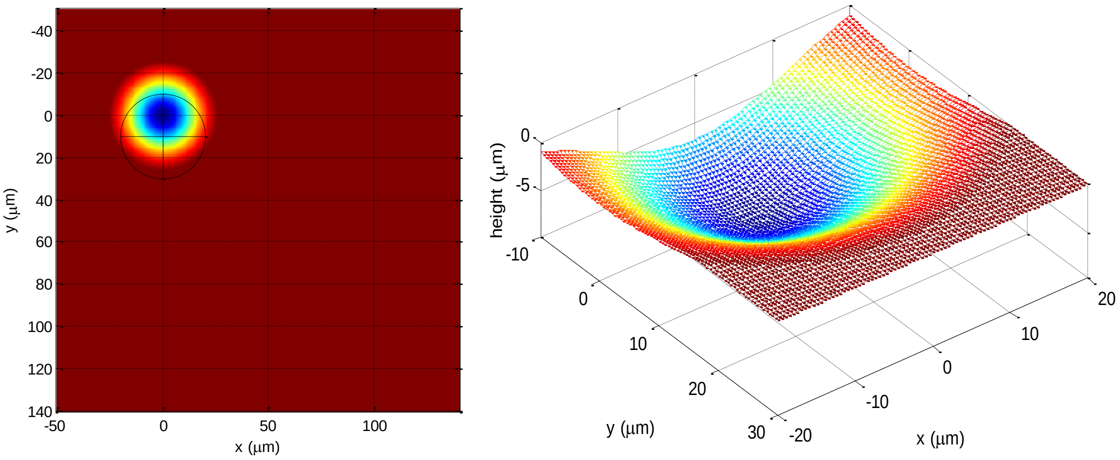

Figure 19: Left, a full view of the surface after subtracting the first ablation volume. The black cross indicates the location of the next laser pulse to occur. Right, a 3-dimensional surface plot of the region indicated on the left.

The first laser pulse (Figure 19) has removed a symmetrical volume of fused silica with a truncated Gaussian shape thus where the first pulse was incident upon a flat surface, the second pulse will be incident upon a constantly changing sloping surface. Subtracting the second pulse (Figure 20) and observing the site of the third ablation point shows that the surface has evolved from the effect of the first two pulses:

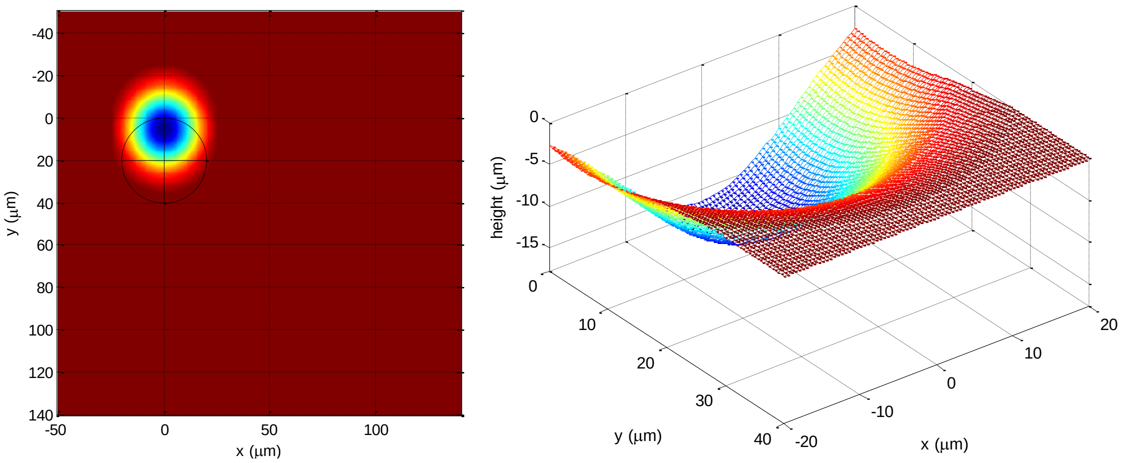

Figure 20: Left, a full view of the surface after subtracting two ablation volumes. The black cross indicates the location of the next laser pulse to occur. Right, a 3-dimensional surface plot of the region indicated on the left.

Although the shape is similar, the magnitude of the slope has increased. This will have an effect on the absorption efficiency due to slight changes in the reflection as demonstrated in Figure 11. Observing the surface at two different points (Figure 21) on the second line after the first 10 laser pulses complete on the first line shows that the surface evolves rapidly and changes between surface topology are significant after only a few pulses:

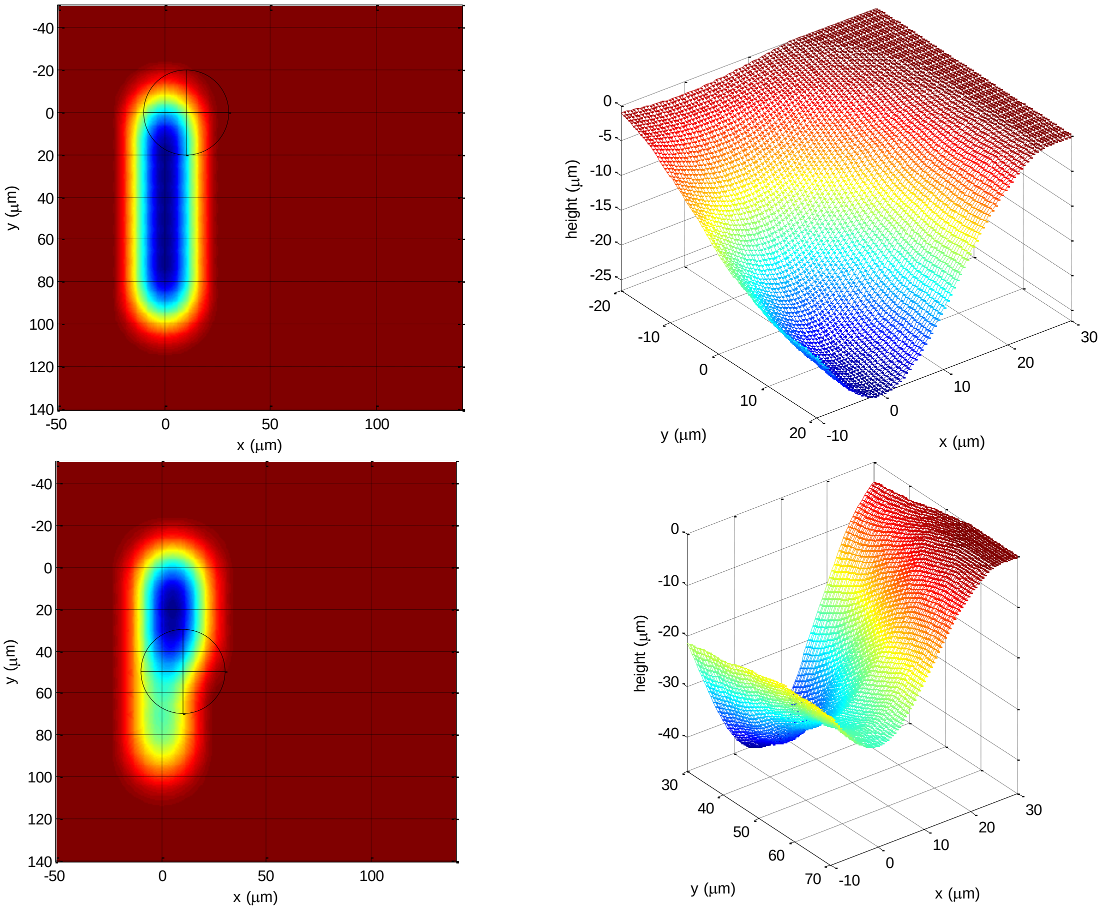

Figure 21: Left column, full views of the surface after subtracting 10 and 15 volumes from the surface. The black crosses indicate the location of the next laser pulse to occur. Right column, 3-dimensional surface plots of the regions indicated on the left.

The top row shows the surface shape at the beginning of the next line, the shape being similar to that illuminated by the first line but with a mean surface normal component in both the x- and y-axes due to the x-offset applied by the raster pattern. After the first pulse on the second line, it can be seen the second pulse will be incident on a surface that is more complex; and by the fifth pulse on the second row the surface has almost completely altered. However, the surfaces illuminated by the pulses eventually reach a steady state at the centre of the structure (Figure 22) where the mean surface normal is constant. Calculating the illuminated surface of the fifth pulse on the fifth line shows the expected steady state shape as seen in Figure 22

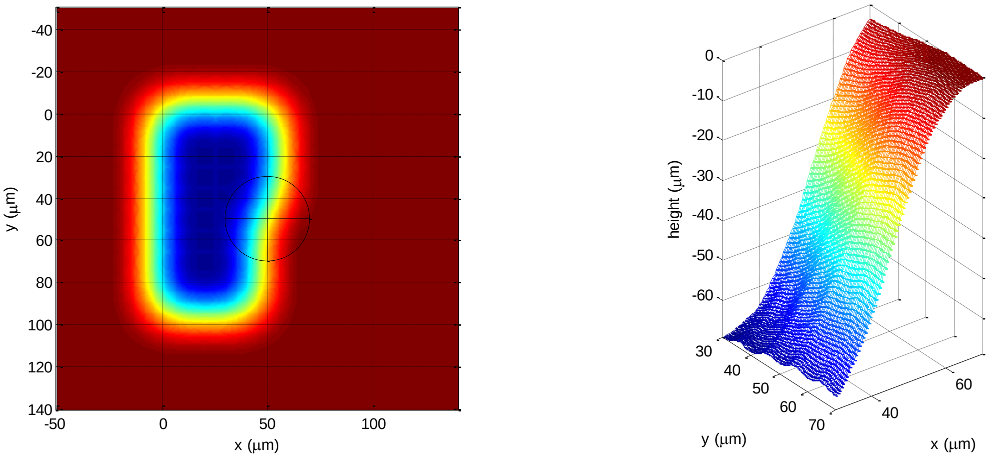

Figure 22: Left, a full view of the surface after subtracting 5 ablation volumes on the fifth line. The black cross indicates the location of the next laser pulse to occur. Right, a 3-dimensional surface plot of the region indicated on the left.

2.1.2 – Calibration of the cutting process

The material volume removal, and thus the depth removed when the laser intensity distribution and spot diameter are fixed, is controlled by varying the energy of the laser pulse. The laser pulse energy is a product of the laser power, which is freely adjustable using the AOM, and the temporal pulse length, the optimal value of which has been determined previously [1]. The temporal pulse length is controlled and allowed to vary by a few percent to account for small variations in laser power due to environmental effects such as short-term changes in laser cavity temperature. Thus both laser power and temporal pulse length are used to control the pulse energy delivered to the substrate.

The ultimate objective of the cutting process is to provide the finest control possible over the depth of the removed volume, yet longer term environmental changes such as the seasonal air temperature can have effects on the precise pulse energy delivered to the work piece. Thus the exact relationship between laser pulse energy and surface depth achieved is determined empirically at regular intervals by cutting test structures with specified laser pulse energy values. This allows for a direct correlation between the energy values being used by the system and the ablation depth achieved by these values. As the laser is operating in CW mode at a constant power and the pulses are being generated by the AOM, which has a non-linear response between control voltage and transmission in to the first diffracted order that is used, there is an intermediate control system which accounts for this and both normalises and linearises the energy values that can be obtained. Thus the energy values presented here have values between 0 and 1 and do not correspond to the pulse energies actually incident upon the substrate during cutting.

The test structures are designed as sloping surfaces which are produced by changing the laser pulse energy linearly over a specified distance. There are also single shot lines on either side of the test structure to allow for post-measurement alignment, allowing for accurate spatial registration of the energy values. These energy values are supplied directly to the laser micromachining system and the test structures are cut and then smoothed. The structures are then measured using a STIL CHR350 non-contact optical profilometer to obtain the structure's depth profile as shown in Figure 23.

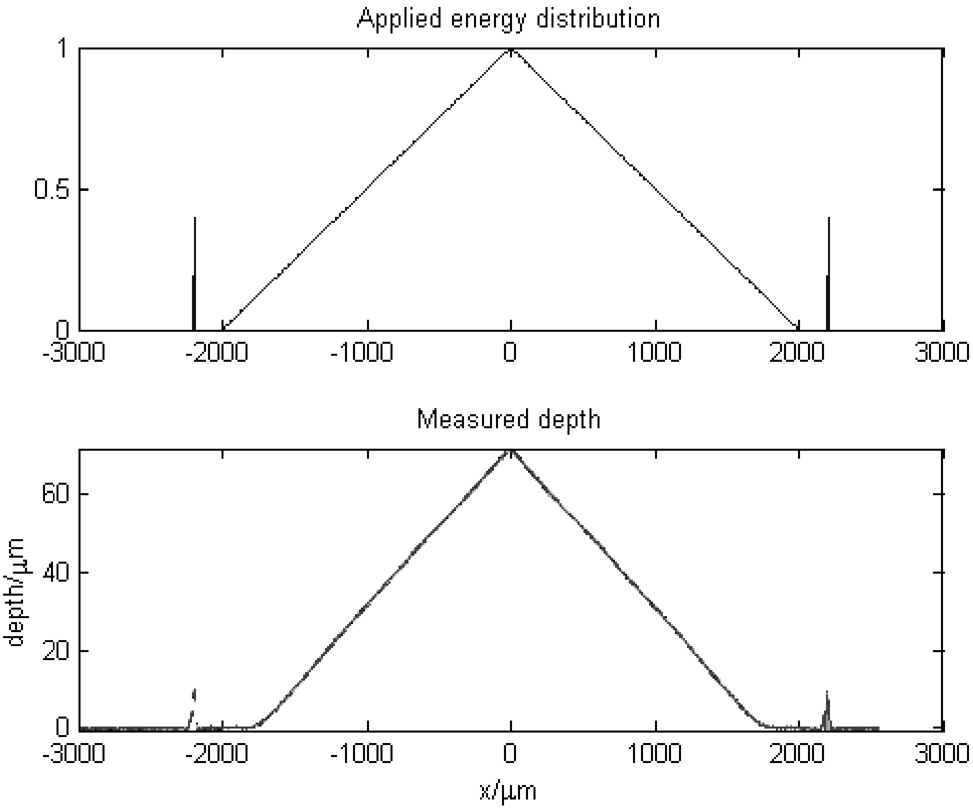

Figure 23: Top, the normalised energy distribution of the test structure used to determine the relationship between laser pulse energy and resulting surface depth. Bottom, the measured profile of the test structure produced using the energy values in the top graph. Note the as-cut test structure is narrower than the design due to the energy values at the edge being below the ablation threshold.

By correlating the pulse energy requested with the cut depth measured, a set of values known as the energy-depth (ED) curve can be found. These ED values are subsequently used to quickly convert any desired 2-dimensional depth map, from an optical design program for example, to an energy map usable by the cutting laser system. The ED curve also illustrates a desirable process windows where the depth achieved is linear with respect to input energy. For this reason all surfaces have a minimum cut depth of at least 5µm in to the surface so that the cutting process operates in the linear regime of the ED curve and away from the rounded threshold region. This ED curve also shows the maximum achievable depth of a given cut strategy, in this case the maximum achievable depth is just over 60µm as can be seen in Figure 24.

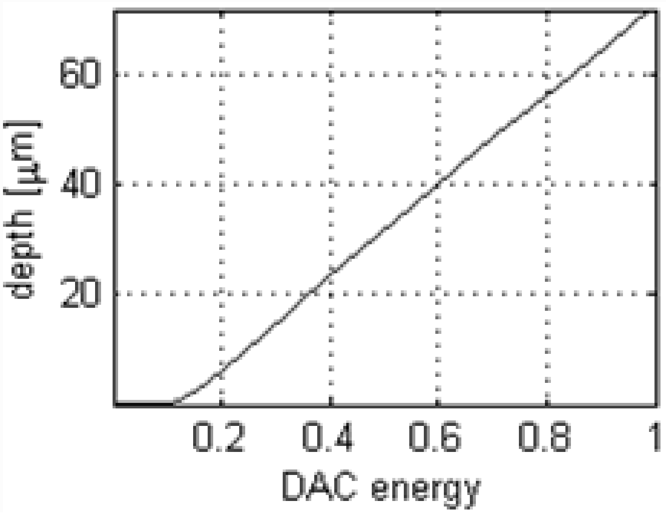

Figure 24: An example ED curve showing the relation between normalised pulse energy and depth of the test structure. Note the non-linear behaviour at around 0.1 energy and the highly linear behaviour from 0.2 energy onwards. DAC stands for Digital Analogue Converter, which controls the AOM voltage.

Using this cutting process the gross optical shape of a micro-optical structure can be fabricated in fused silica but, as described previously, after cutting the surface contains a rough microstructure that must be removed in order for the surface to be optically useful. This microstructure has a low amplitude but a high spatial frequency and is uniformly distributed across the surface, so will both strongly scatter transmitted light and act as a diffraction grating with a period equal to that of the raster point grid. In order to make the structure fit for purpose the high spatial frequency rough microstructure must be highly attenuated while minimally affecting the low spatial frequency gross structure shape. This is carried out in the second stage of fabrication, smoothing.

2.2 – The smoothing process

The smoothing process is a thermal polishing process that uses a focussed continuous wave CO_2 laser with beam size on the order of 100s of micrometres to melt a surface layer of fused silica with melt depth on the order of a few micrometres [20]. This melt pool has viscosity low enough to allow material flow, the direction and speed of which is governed by surface tension forces. The surface tension force is directly related to the temperature distribution of the melt pool, for a laser spot with a Gaussian intensity distribution this means that the material flows outwards from the centre of the melt pool. After the laser spot has passed over a region on the structure, the melt pool solidifies leaving a highly polished surface which was measured by the LPA group to have roughness <10nm [20]. Measurement of surfaces after subsequent improvements to the smoothing system by PowerPhotonic have shown that surface roughness is now around 1nm.

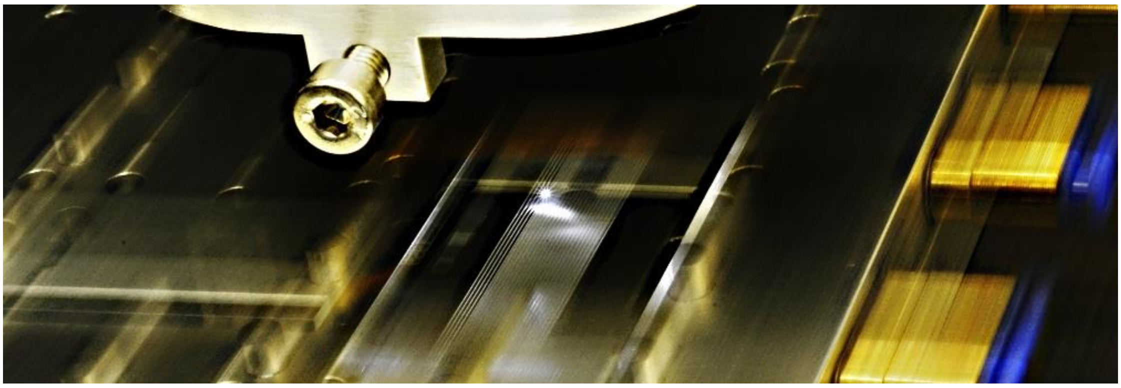

Figure 25: A picture of an optic being laser smoothed. The stage motion along a raster line is from top to bottom, the stage motion from line to line is from left to right. Note the clearly different surface texture on the left side of the optic that has been laser smoothed.

Like the cutting process method, the substrate is positioned on xy translation stages and moved under the smoothing laser beam in a raster pattern as shown in Figure 25. The smoothing process is significantly more sensitive to laser power change than the cutting process, so a major challenge in smoothing has been to reduce this sensitivity and improve the resolution and speed of the power stabilising feedback mechanism. Like cutting, the main factor in process variability occurs due to thermal changes in the environment; a small change in laser cavity temperature changes the cavity length and therefore the wavelength(s) emitted, which may change the lasing efficiency and thus the output power.

The LPA group conducted extensive research of the smoothing of a number of different glasses [21]. However the PowerPhotonic process has been developed and optimised to use only fused silica as the substrate material. Specifically, the laser smoothing process induces a residual stress of approximately 60MPa in the substrate surface during thermal expansion and contraction [22] [23]. Fused silica, with a particularly low coefficient of thermal expansion (CTE) of 0.5 ppm/K, is one of the few glasses that can be smoothed at room temperature without the occurrence of catastrophic cracking that renders an optic useless [24].

The processing window for optimum smoothing to occur is also thermal; the laser must heat a thin layer of silica enough to reduce the viscosity to enable reflow, but not enough so that significant mass loss arises when the silica vapour pressure approaches atmospheric pressure. This processing window has previously been found [22] to fall within a temperature range of around 1950-2700 °C, with the lower limit being defined by the maximum melt pool viscosity required for volumetric flow to occur and the upper limit being defined by a vapour pressure of 1 bar above the surface of the melt pool, which would correspond to undesirable volumetric loss to evaporation as shown in Figure 26.

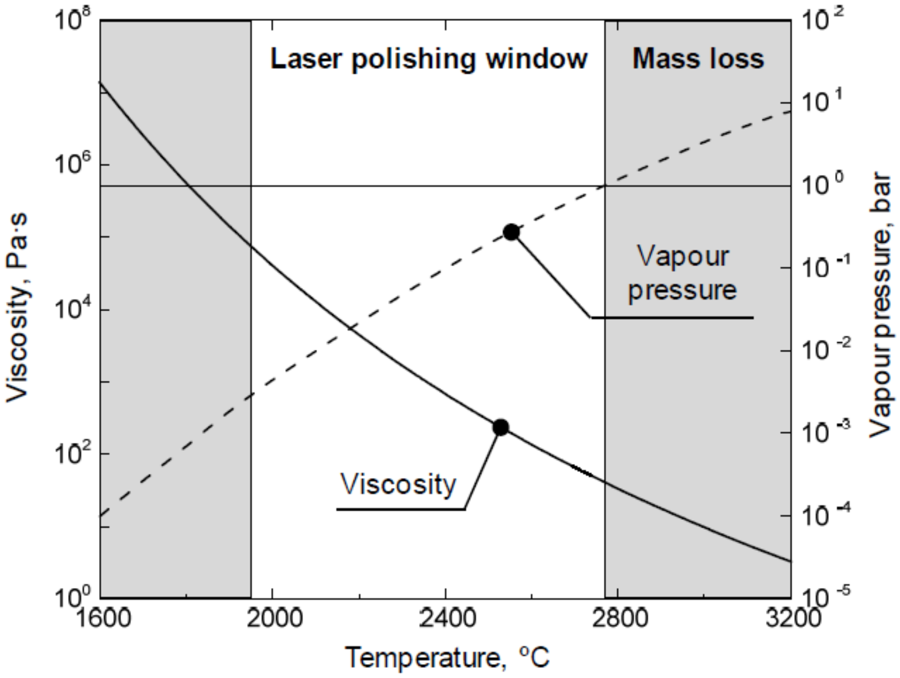

Figure 26: The upper and lower limits of the laser smoothing processing window are defined by the process temperature, which determines both the viscosity of the melt pool and the vapour pressure above the surface. Taken from [21].

The challenge of operating within this regime is compounded by the Gaussian intensity distribution of the laser beam. Due to the nature of the intensity distribution, only the middle region of the beam will contribute to smoothing when operating within the laser smoothing process window. Small changes in beam radius or laser power can cause variations in the smoothing process which can have detrimental effects on the final surface finish (see Figure 27). As such the high-resolution control of the laser parameters is critical to effective smoothing.

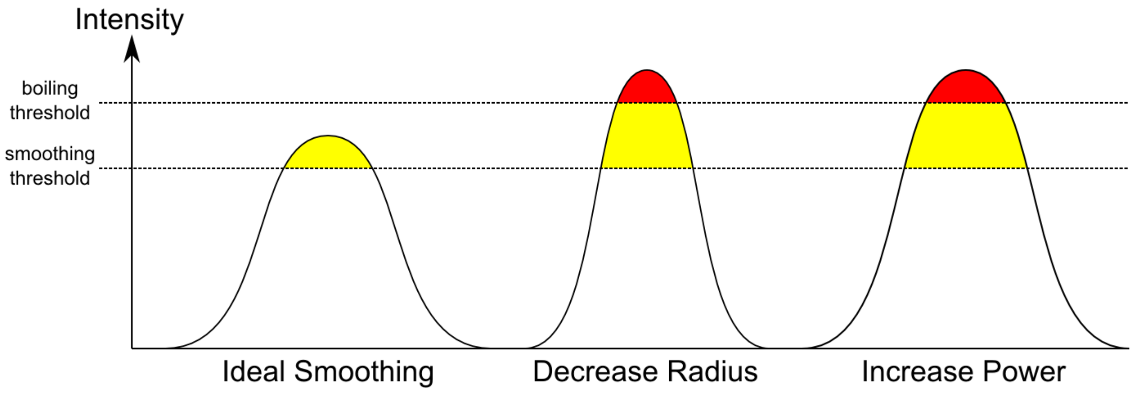

Figure 27: A diagram showing the effects of decreasing the spot size or increasing laser power on the smoothing process.

2.2.1 – Smoothing as a spatial frequency filter

As described previously in detail [23] [4] [25] [26] [27], the smoothing process acts as a low-pass spatial frequency filter by strongly attenuating the high spatial frequency rough microstructure produced by the cutting process but leaving the optically important low spatial frequency surface shape unaffected. Previously this spatial frequency filtering was characterised by smoothing pseudo-random surfaces manufacturing using the cutting process [23] as well as smoothing vertical edges manufactured using a lithography process [25]. Due to the sensitivity of the smoothing process to small changes, it was imperative that PowerPhotonic had the ability to quickly and effectively measure the current state of the smoothing process.

As the lithographically produced structures required an external source of test structures and the pseudo-random structures required expertise to evaluate, a new test structure was designed that could be produced in-house and analysed without necessarily requiring an engineer. This test structure had a sinusoidal profile with chirped spatial frequencies ranging between 2 and 200 lines/mm. Both a linearly chirped structure (shown in Figure 28) and a logarithmically chirped structure were designed using the equations:

linear:
$$f(x) = \sin\left[2\pi\left(f_0 x + \frac{k}{2}x^2 + \phi_0\right)\right] \qquad (14)$$

logarithmic:
$$f(x) = \sin\left[\frac{2\pi f_0(k^x - 1)}{\ln(k)} + \phi_0\right] \qquad (15)$$

where *f0* is the initial frequency, *k* is the chirp rate and ϕ_0 is the initial phase.

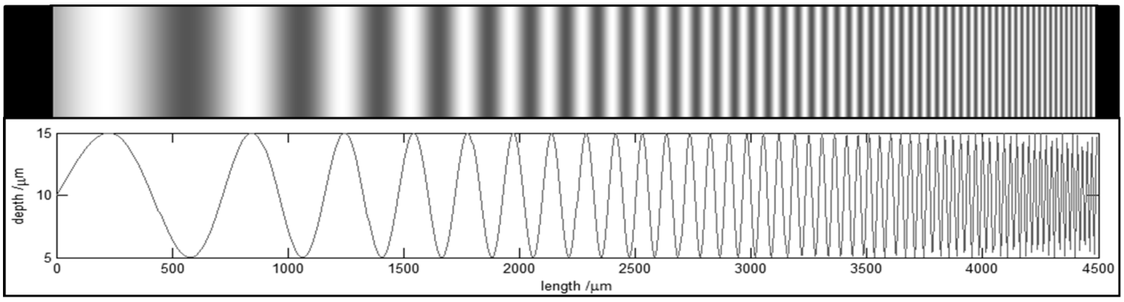

Figure 28: The linearly chirped test structure. Top: the surface design. Bottom: the chirp profile.

These test structures were fabricated using the cutting system, smoothed under various conditions and profiled with the STIL CHR-350 profilometer to produce profiles showing how the smoothing process attenuated the different spatial frequencies in the test structure. Figure 29 shows an example of the test structure after spatial frequency filtering with the smoothing process.

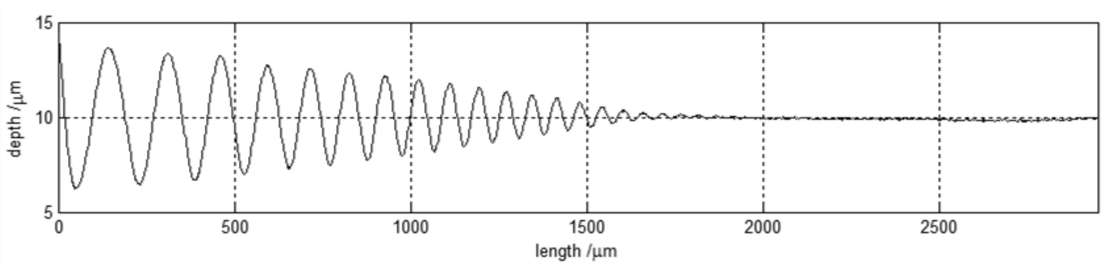

Figure 29: The measured profile of a smoothed linearly chirped test structure.

This was then processed to find the envelope of the signal by determining the analytic signal representation:

$$\boldsymbol{u}(t) = u^{(r)}(t) + iu^{(i)}(t) = A^{(r)}(t)e^{i\phi(t)} \qquad (16)$$

where $u^{(r)}(t)$ is the real component of a signal $\boldsymbol{u}(t)$, $u^{(i)}(t)$ is the imaginary component of a signal $\boldsymbol{u}(t)$, $A^{(r)}(t)$ is the envelope of the signal and $\phi(t)$ is the initial phase.

This is carried out in the frequency domain by multiplying the Fourier transformed real component of the signal by the Heaviside step function to find $\boldsymbol{u}(t)$:

$$\boldsymbol{\mathcal{F}}\{\boldsymbol{u}(t)\} = 2h(v) * \mathcal{F}\{u^{(r)}(t)\} \qquad (17)$$

where *h(v)* is the Heaviside step function.

The envelope of the signal is then found by taking the inverse Fourier transform of the previous result:

$$A^{(r)}(t) = \mathcal{F}^{-1}\{\boldsymbol{u}(t)\} \qquad (18)$$

Applying this methodology to the measured chirped test structures then recovers the envelope of the signal, shown by the red curve in Figure 30.

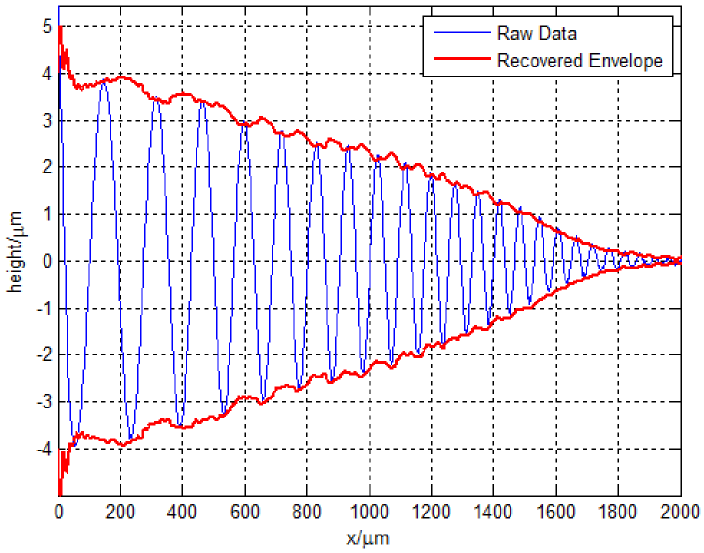

Figure 30: A measured chirped test structure showing the calculated envelope.

The difference between the calculated envelope from the smoothed structure and the envelope of the design part (which has constant amplitude) is used to calculate gain vs. spatial frequency for a given smoothing condition. The difference between linearly chirped and logarithmically chirped test structures were compared (Figure 31).

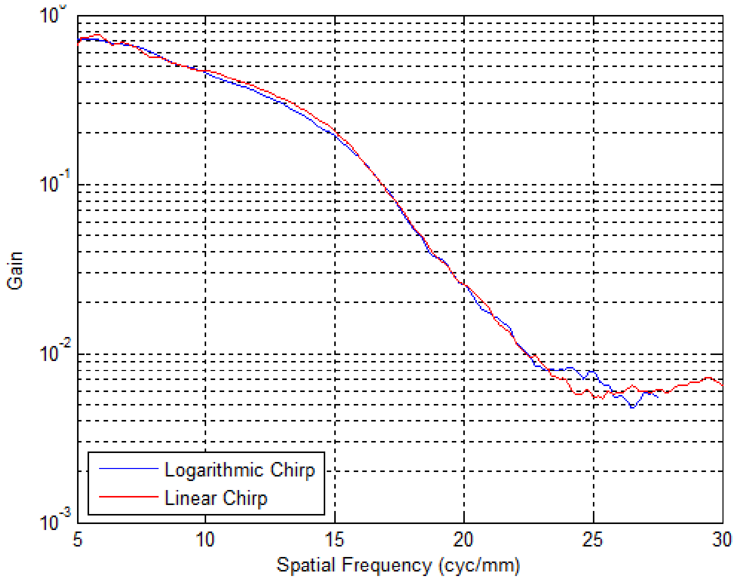

Figure 31: Gain vs. spatial frequency response of the linearly and logarithmically chirped test structures after smoothing under the same conditions.

The differences between the two chirped test structures were small enough to be regarded as measurement noise and small process drifts during smoothing. As only a single test structure was required, the linearly chirped structure was therefore used exclusively for further analysis. Three chirped test structures were then smoothed and the laser power was varied by ±1.2% from its nominal value used for production to determine the effect of small variations in laser power as shown in Figure 32.

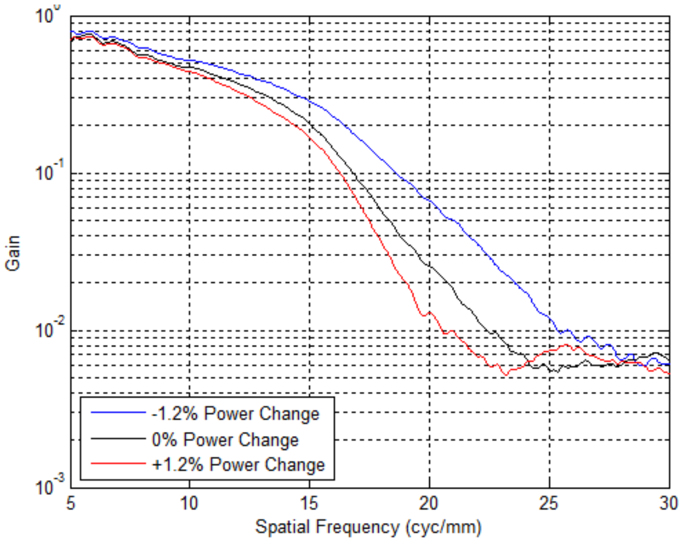

Figure 32: Gain vs. spatial frequency of the linearly chirped test structure when smoothed with various laser powers.

The change in spatial frequency filtering is as expected: a higher smoothing laser power attenuates spatial frequencies more than the nominal laser power, shifting the curve to the left of the nominal curve; while the lower smoothing laser power attenuates spatial frequencies less than the nominal laser power and shifts the curve to the right of the nominal curve. In order to determine the effect of laser beam radius, three chirped test structures were then smoothed by the laser with small decreases in spot radius as shown in Figure 33.

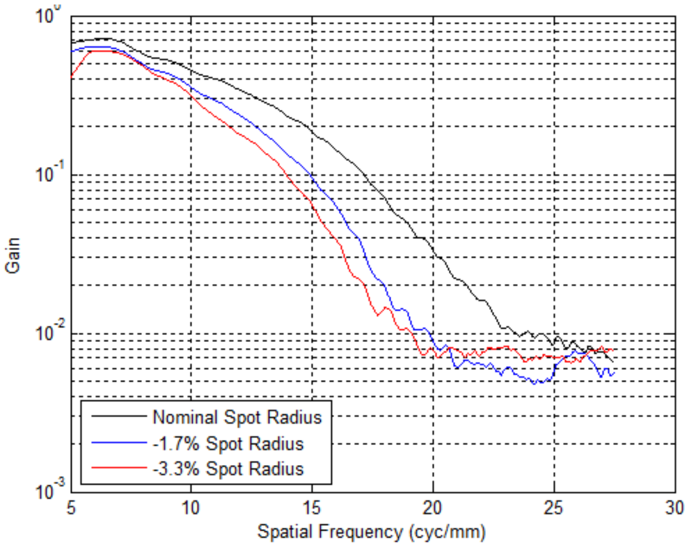

Figure 33: Gain vs. spatial frequency of the linearly chirped test structure when smoothed with various laser spot radii.

As before, the change in spatial frequency filtering responds as expected to the beam radius change. The smaller spot radii equate to higher fluence during smoothing, which has caused a noticeable increase in spatial frequency attenuation. These results show that the chirped test structure is very effective in acting as a standard test structure to test or calibrate the smoothing conditions on the laser system.

2.3 – Specifying freeform surfaces

While [28] describes how to measure the errors associated with spherical and aspherical surfaces such as lens arrays, the deviation from an ideal freeform optical surface does not yet have a universally accepted definition. PowerPhotonic uses an internally developed method when comparing an ideal design with the resulting manufactured optical surface for freeform surfaces. This method calculates two different surfaces parameters of a fabricated optical surface: scaling error and form error.

Scaling error is a term used to describe the linear depth error between the design and measured surfaces. This is analogous to the radius of curvature (RoC) error that describes traditional rotationally symmetric lenses, which is calculated by scaling the design surface with a vector normal to the lens surface. By converting this RoC error to focal length error the optically significant error value is obtained. Because a truly freeform structure like those produced by the PowerPhotonic process cannot be expected to have any axes of symmetry or focal length, it is not appropriate to describe these surfaces using the same methodology as applied to rotationally symmetric lenses. Instead, freeform surface scaling occurs along vectors parallel to the z or height axis. This allows a scaling error value to be obtained that relates to the surface itself rather than the direct optical impact of this scaling error, illustrated in Figure 34.

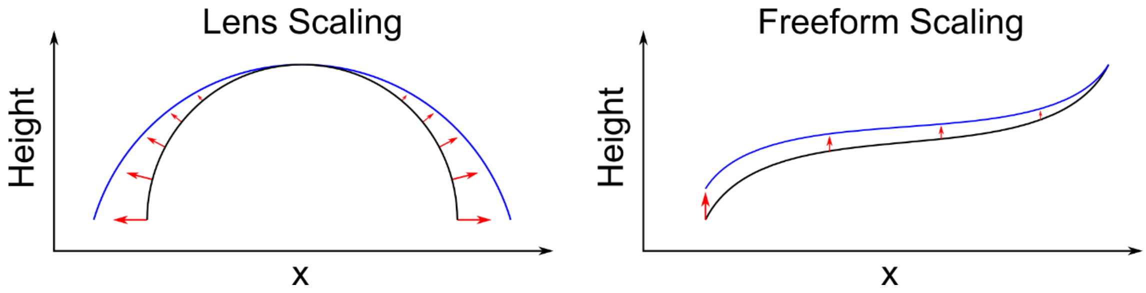

Figure 34: Lens scaling compared to freeform scaling: the blue curve denotes the measured surface, the black curve denotes the design surface, and the red arrows show the direction in which scaling error is calculated.

To illustrate the process of calculating the scaling and form error of a freeform surface, a non-rotationally symmetric surface has been designed and random noise and a scaling factor have been added in order to simulate the features seen in a real fabricated surface. The scaling error and form error have then been calculated.

Consider a surface that is a map of height *z* over the *x*,*y* plane such as Figure 35.

$$z_d = z(x, y) \tag{19}$$

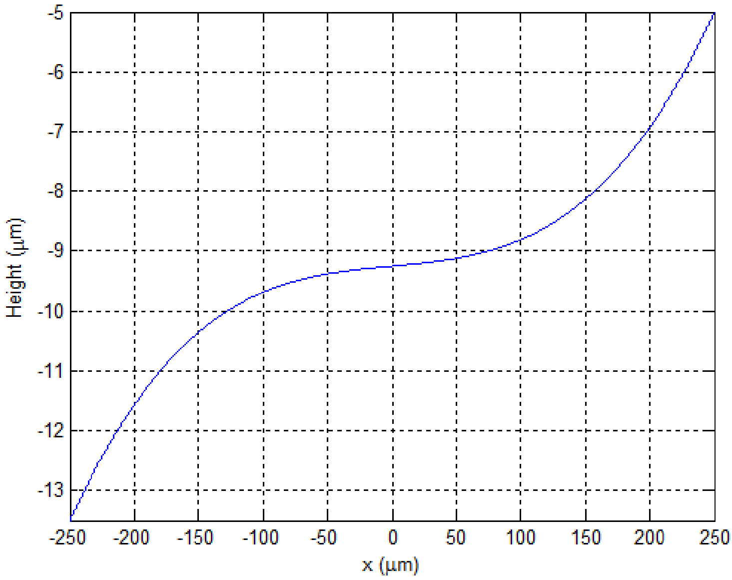

Figure 35: A 1-dimensional freeform surface profile used as the initial design surface.

The design profile z_d was summed with smoothed random noise N(x,y) and then multiplied by a scaling factor M, for which a value of 1.03 was used, in order to simulate a measured freeform optical surface (z_m) after fabrication as shown in Figure 36.

$$z_{m(x,y)} = M * (z_d(x, y) + N(x, y)) \tag{20}$$

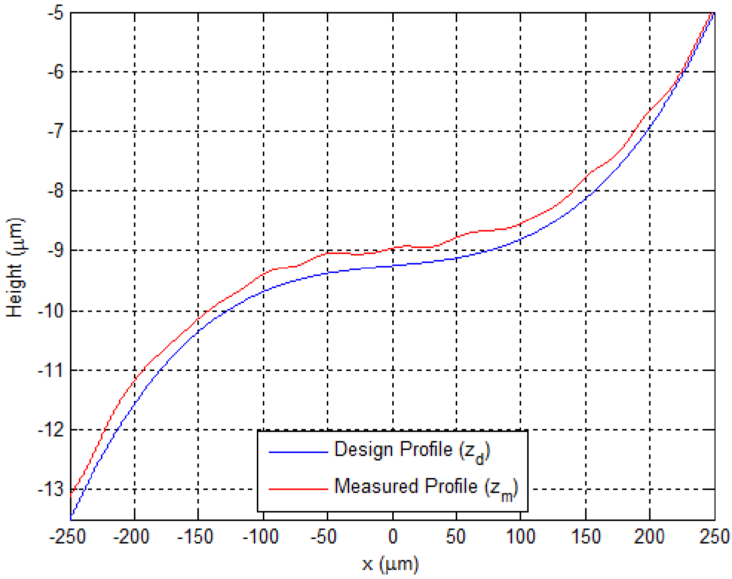

Figure 36: A 1-dimensional freeform surface (blue) and a simulated surface with added form and scaling error (red)

The measurement residual z_{rd} is then found by subtracting the design profile z_d from the measured profile z_m (residual shown in Figure 37):

$$z_{rd}(x,y) = z_m(x,y) - z_d(x,y) \tag{21}$$

For comparative purposes, the peak-valley and RMS form error values for the initial measurement are calculated from the measurement residual z_{rd}:

$$error_{P-V} = \max\big(z_{rd}(x,y)\big) - \min\big(z_{rd}(x,y)\big) \tag{22}$$

$$error_{RMS} = \sqrt{\frac{1}{N}\sum_{x,y}\big(z_{rd}(x,y)\big)^2} \tag{23}$$

where N is the total number of elements in $z_{rd}(x,y)$ when x and y describe uniformly sampled points over the clear aperture. Applying equations (22) and (23) to the z_{rd} data gives the peak-to-valley and RMS form errors of the residual, shown in Table 1.

Error Type	**Calculated Value**
$\boldsymbol{error_{P-V}}$	0.315µm
$\boldsymbol{error_{RMS}}$	0.28µm

Table 1: The calculated values for P-V and RMS error from the absolute measurement residual z_{rd} .

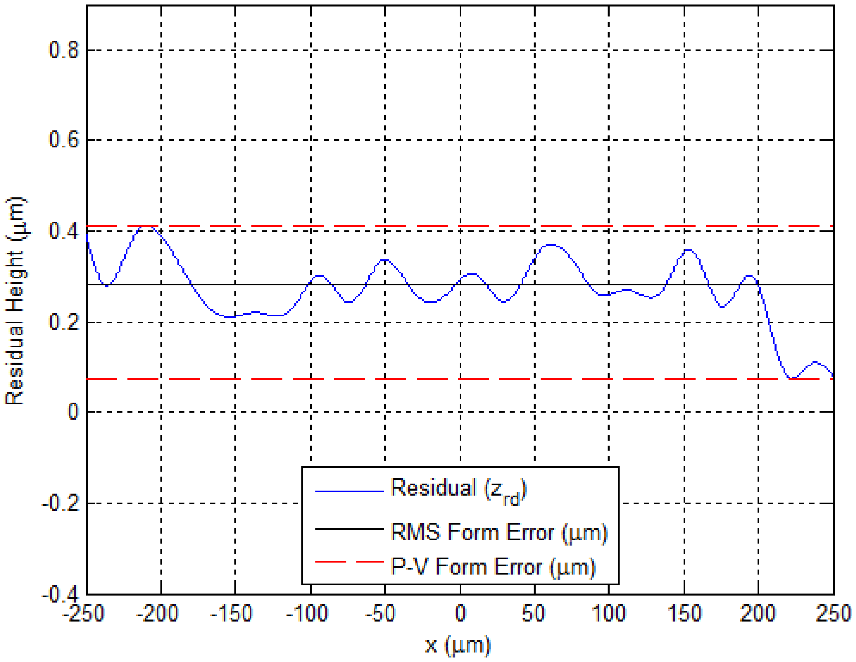

Figure 37: The measurement residual z_{rd} (blue), with lines indicating the peak-valley form error (red hatched) and calculated RMS form error (black)

A scaling error C can then be accurately determined by plotting the design profile height z_d against the measured profile height z_m and finding the gradient of a linear fit (m) to these data points as shown in Figure 38. C is then found using equation (24).

$$C = m - 1 \tag{24}$$

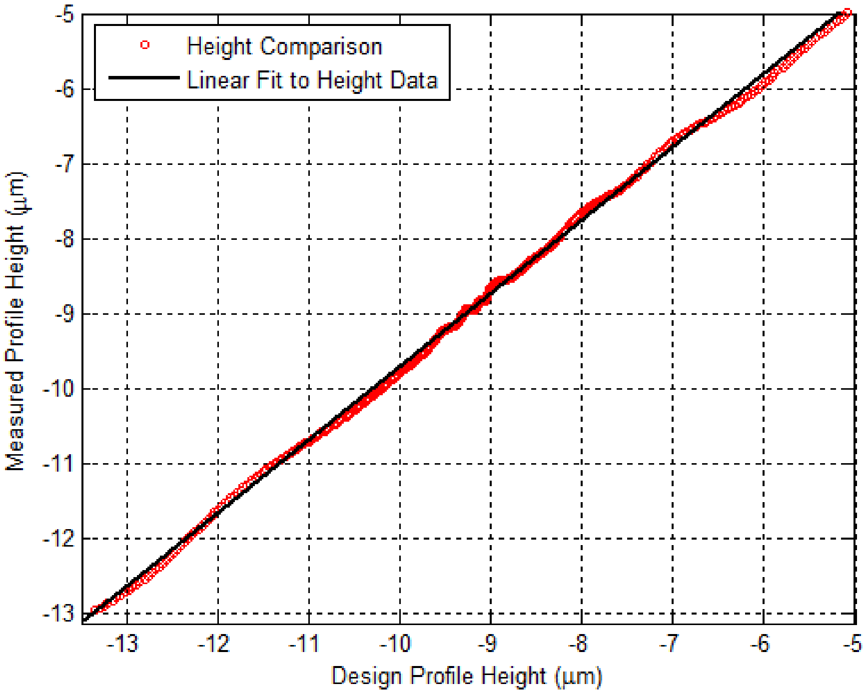

Figure 38: Finding the scaling error by plotting the height of each point in the design profile against the height of each point in the measured profile.

The scaled design surface z_a is then obtained by multiplying the design surface z_d by m (Figure 39).

$$z_a(x, y) = m * z_d(x, y) \tag{25}$$

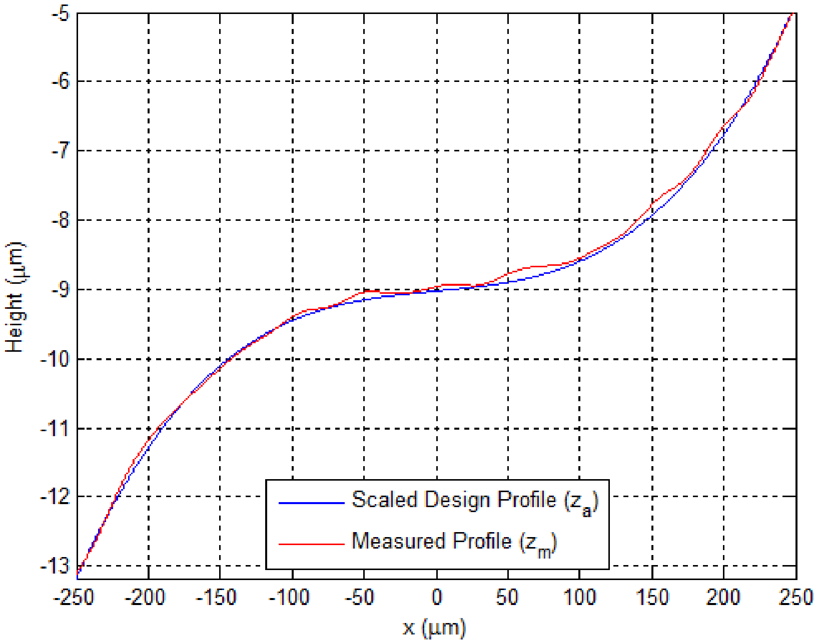

Figure 39: The scaled design profile z_a plotted with the measured profile z_m.

The residual to the scaled surface z_{ra} is then found by subtracting the scaled design surface z_a from the measured surface z_m as shown in Figure 40

$$z_{ra}(x,y) = z_m(x,y) - z_a(x,y) \tag{26}$$

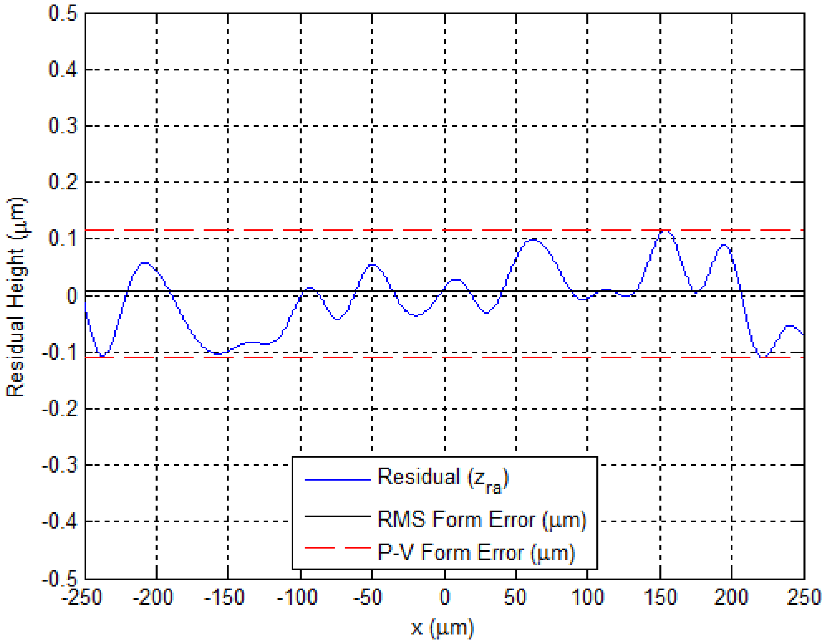

Figure 40: The measurement residual z_{ra}, with indicator lines for RMS and P-V form error.

The peak-valley and RMS form error values are then calculated for the residual of the scaled surface from the measurement residual z_{ra}:

$$error_{P-V} = \max\left(z_{ra}(x,y)\right) - \min\left(z_{ra}(x,y)\right) \tag{27}$$

$$error_{RMS} = \sqrt{\frac{1}{N}\sum_{x,y}\left(z_{ra}(x,y)\right)^2} \tag{28}$$

Comparing these scaling-adjusted error values to the absolute results calculated from the measurement without removing the scaling error first shows a much different result:

Absolute Errors z_{rd}	
Scaling error C	N/A
$error_{P-V}$	0.315µm
$error_{RMS}$	0.28µm
Scaled Errors z_{ra}	
Scaling error C	3%
$error_{P-V}$	0.22µm
$error_{RMS}$	0.01µm

Table 2: The calculated values for P-V and RMS error from the scaled measurement residual z_{ra}.

Separating the scaling error from the form error is particularly useful for freeform optical surfaces as they can be used to determine the separate optical effect that they might have on a system. For example, minimising scaling error is likely to be more critical than form error for an intra-cavity phaseplate that corrects the thermal lensing of a wavefront from a gain medium. Scaling error will affect the amount of phase correction that is applied across the wavefront, acting to directly scale the phase error:

$$\phi_m = \frac{2\pi * \left((C * z_{md}) - z_{md}\right) * (n-1)}{\lambda} \tag{29}$$

where ϕ_m is the maximum error of the phase of a beam after transmission through an optical surface, C is the scaling error, z_{md} is the maximum depth of the design surface and n is the refractive index of the optic at wavelength λ. To illustrate, consider a laser with λ = 1064nm that is transmitted through a phaseplate with maximum depth of z_{md} = 20µm that has a scaling error of C = 3%; the maximum error between the output wavefront and the wavefront expected according to the design is 0.8 waves.

For other applications, form error can be more critical than scaling error. Optical surfaces that are to be used as reflective components instead of transmissive ones are particularly susceptible to form error as the phase error is not only multiplied by 2 after reflection but it does not benefit from reduction due to the $(n-1)$ term. The RMS form error can be used to calculate a good approximation of the Strehl ratio of an optical surface [29], which is used to describe the quality of image formation by an optical system and has values between 0 and 1. This approximation is achieved by first calculating the RMS phase error after interacting with a surface:

Reflective:

$$\phi_{RMS} = \frac{4\pi * error_{RMS}}{\lambda} \tag{30}$$

Transmissive:

$$\phi_{RMS} = \frac{2\pi * error_{RMS} * (n-1)}{\lambda} \tag{31}$$

and then finding the approximate Strehl ratio S:

$$S \approx e^{-\phi_{RMS}^2} \tag{32}$$

Taking the previous example of a laser with λ = 1064nm that is incident upon a surface with $error_{RMS}$ = 100nm; the estimated Strehl ratio for the surface in reflection is S = 0.248 while in transmission S = 0.932. This can have a significant impact on single-mode applications such as coupling light into a single-mode fibre. The Strehl ratio due to form error can be used to estimate the coupling loss of such a system, which is commonly used in the telecommunications industry where maximising efficiency in single mode fibre coupling applications is critical:

$$L \approx 10\log(1 - S) \tag{33}$$

where L is the total insertion loss measured in dB (not including Fresnel reflection at refractive index interfaces) when an optical component is inserted in to a single mode fibre coupling system and is often required to impart a loss of less than -0.5dB. Using the previously calculated Strehl ratio values for a reflective and transmissive optic and calculating the total insertion loss, $L \approx$ -6.06dB for the reflective surface and $L \approx$ -0.31dB for the transmissive surface.

Clearly both scaling and form error are important specifications to determine individually as the impact of each type of error can vary between the ultimate application.

2.4 – The product development process

The flexibility of the PowerPhotonic fabrication process allows for a very wide variety of optical surfaces to be manufactured, not only functionally distinct but customised for a particular system or application. A consequence of this flexibility is that almost all of the surfaces designed to meet a customer requirement have not been manufactured previously. The nature of the fabrication process is such that a number of different parameters might be altered in order to more accurately reproduce the design as an optical surface, but it is not necessarily known what parameter alterations are required before manufacturing the surface for the first time.

In order to increase surface form accuracy or meet a required specification, PowerPhotonic can apply an iterative product development process that allows for convergence on an optimum parameter set when manufacturing a new optical surface. This involves a number of different stages.

1. Fabricate the new optical surface design, either as a representative fraction of the ultimate optical surface in order to minimise fabrication time, or as the full surface.

2. Measure the surface using appropriately chosen tools and measurement methodologies. For example a cylindrical lens array with low sag and surface slope can be characterised accurately within minutes using a non-contact optical profilometer such as the STIL CHR-350, by taking a small number of profiles across the array in a direction orthogonal to the lens length. However an optic with high surface slope or one that has complex 3 dimensional topology is more efficiently measured using a white light interferometer (WLI) such as the Taylor-Hobson CCI. In both cases, the surface must be

measured so that meaningful initial results can be inferred for the design as a whole.

3. Analyse the resulting measured data in order to determine the scaling and form errors as described in Section 2.3. The surface form residuals are used in the product development process as well as the P-V or RMS form error values.
4. Compare the derived scaling and form error numbers found during the analysis stage with the customer specification. If values for both scaling and form error are found to be within the required specification, the remaining optical surfaces required to fulfil the order are manufactured. If not, the design surface is modified.
5. Modify the design surface to correct for scaling or form errors.
   a. Scaling error mainly arises from slow changes in the energy-depth relationship over time, which can be a result of a number of things including laser aging and the thermal environment of the laser micromachining system, and may change in between periodic calibrations. This error is often simple to correct as it involves multiplying the height of the entire surface by a value that would reduce the scaling error, for example a surface with a scaling error of 1.03 would have each individual z value multiplied by $\frac{1}{1.03}$.
   b. Form error results from the laser interaction with the substrate itself when cutting and smoothing the required surfaces. Correcting for form error is less deterministic than scaling error correction, as the form of a given regions of the surface has an effect on the form of surrounding regions during manufacture. In ideal circumstances, the form error residual z_{ra} could be subtracted from the design surface so that when the cutting and smoothing operations take place this form error is reduced or removed. This works particularly well on surfaces of very low slope, as small changes to the surface form have little impact on surrounding regions. However, higher slope structures and especially uniform repeating structures need a more customised approach to applying form error correction. A simple example of this is in the fabrication of a cylindrical lens array where the “cusp” regions in between lenses will have the highest

form error because of the lack of sharp transition zone due to the smoothing process. Trying to correct for this will negatively affect the lens surface due to the effect of the altered surface in the cusp regions. Therefore the form error correction that is applied is truncated so that the majority of the lens surface is corrected and the form error in the cusp regions is left uncorrected (see Figure 41 below).

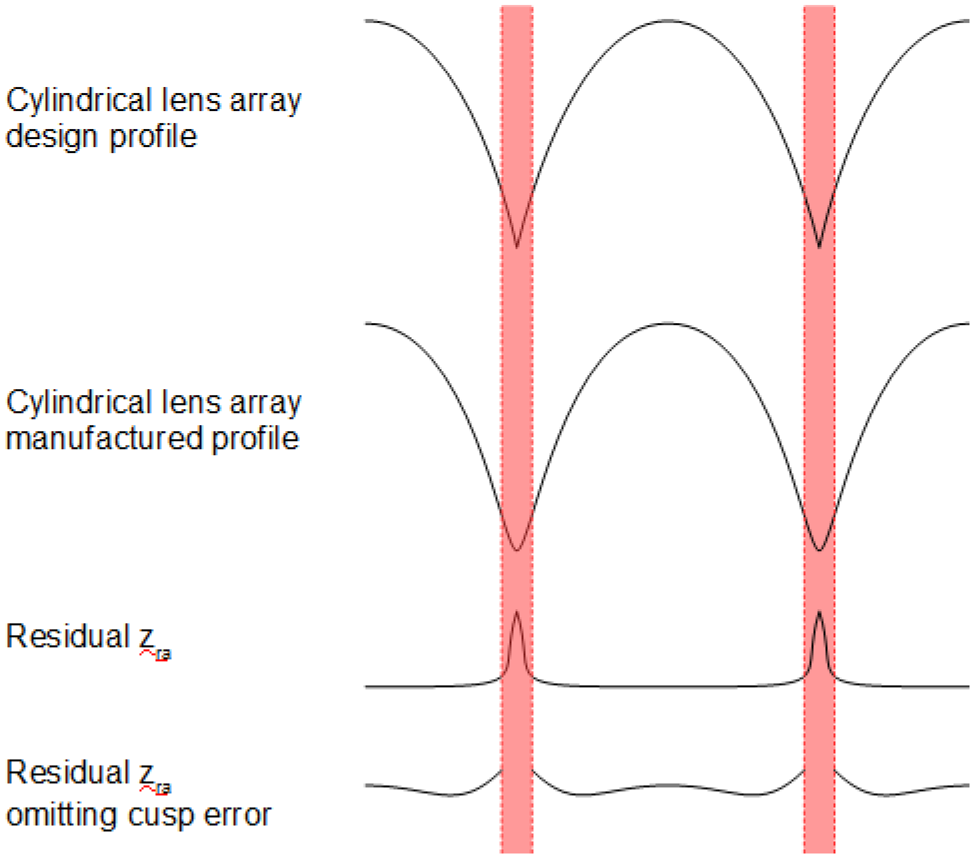

Figure 41: The impact of the cusp error when analysing form error on a cylindrical lens array. The red bar denotes the area of the surface that will not be corrected in order to optimally correct the majority of the lenses. Images are not to scale and for illustration only.

6. The modified surface is then re-fabricated with the scaling and/or form correction applied and the measurement and analysis is repeated in the same way as previously in order to determine the impact of the corrections applied.

Often both scaling and form errors are reduced sufficiently to meet or exceed the customer target specification after the first iteration. Occasionally the target specification for form error is not met after 1 product development iteration so the process is repeated on the iterated surface in order to refine the form error correction. Rarely, a surface cannot be produced that meets the target specification even after multiple iterations. This can happen when the smoothing process starts to affect the form of a surface with high slope or with high spatial frequency content. As form error starts to become dominated by smoothing, simply modifying the input surface for cutting to optimise the surface shape produces little reduction of surface form error. However, current work on the product development process is focussing on the deconvolution of the smoothing filter function from the surface in order to create a “pre-emphasised” surface design that takes in to account the impact of smoothing. This has been successfully demonstrated on 2-dimensional gratings and work is on-going to apply it to 3-dimensional surfaces.

2.5 – Summary and conclusions

Presented in this chapter is an overview of the current state of the laser cutting and smoothing processes originally developed at the LPA group at Heriot-Watt and now under continuous development at PowerPhotonic.

Also presented is work conducted as part of this EngD project to define a suitable test structure to monitor and calibrate the smoothing process. This test structure and the methodology presented here are now an integral part of the PowerPhotonic production process, used not only as a regular monitor to check the smoothing system, but as a calibration process when implementing a system change or building a new system.

An overview of the way that freeform surfaces are specified internally and externally by PowerPhotonic has been presented in conjunction with a worked example to clarify the process. It is intended as a simple alternative to the proposed complicated methods of specifying these surfaces such as with NURBS [30].

The methodology behind the product development process was then explained, highlighting the ability for a skilled engineer to apply intelligent changes to an input surface in order to better recreate the shape of a desired design. Work in to pre-emphasis of an input design in order to account for anticipated changes caused by smoothing is currently on-going.

Chapter 3 – Enhancing cutting capability

At the beginning of this EngD project a single well-proven parameter set was used to manufacture all optical surfaces. This parameter set, referred to as a cut strategy, consisted of a number of different system parameters the most relevant to this chapter being stage motion direction, ablation point grid spacing in x and y and laser pulse repetition frequency. Although this cut strategy accurately reproduced many different optical structures it had two major limitations: cut time per unit area could not easily be decreased and the maximum depth of an optical structure was limited to approximately 60µm.

3.1 – Raster pattern optimisation

The stage motion pattern used during cutting was a basic raster pattern: lines were cut sequentially and always with the same direction along a scan line. As can be seen from Figure 14, the method of removing material by overlapping a number of Gaussian spots can produce an undesired asymmetric surface profile related to the direction of the raster scan. It was expected that reversing the scan direction on each alternate line (see Figure 42) would reduce this asymmetry by averaging out the opposing asymmetry over each line.

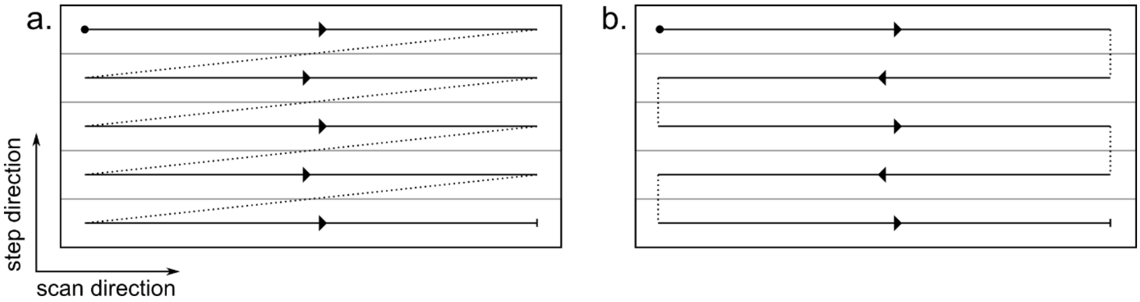

Figure 42: The basic raster pattern (a) and the proposed pattern to improve symmetry of the final surface (b). Dotted lines indicate stage motion with no laser illumination (flyback).

These two raster patterns are referred to UNISCAN and BISCAN patterns, with their descriptions detailed in Table 3.

Pattern Name	Long form pattern name	Description
UNISCAN	Unidirectional in the scan direction	Laser cutting scan lines travel in the same direction for all scan lines
BISCAN	Bidirectional in the scan direction	Laser cutting scan lines alternate direction in the scan direction after each scan line

Table 3: A table summarising the terminology used to describe the two raster patterns investigated.

3.1.1 – Process time reduction

Using the BISCAN raster pattern also decreases the time required by a modest amount for a given surface to be cut by decreasing the necessary stage motion distance per line according to:

$$D_a - D_b = \sqrt{D_x^2 + D_y^2} - D_y \tag{34}$$

where $D_a - D_b$ is the difference between flyback distances of raster patterns a. and b. in Figure 42; D_x is the distance travelled along the line in the scan axis; and D_y is the distance travelled along the line in the step axis. These distances correspond to a time depending on the linear acceleration a of the translation stages as well as the maximum stage velocity v if the linear acceleration and deceleration regions of stage motion are shorter than the total required stage distance. Examination of the motion of the system provides the following equations:

Acceleration distance: $$d_{acceleration} = \frac{v^2}{2a} \tag{35}$$

If $d_{acceleration} < \frac{D_x}{2}$: $$t_{flyback} = \frac{v}{a} + \frac{D_x}{v} \tag{36}$$

If $d_{acceleration} > \frac{D_x}{2}$: $$t_{flyback} = 2\sqrt{\frac{D_x}{a}} \tag{37}$$

To illustrate the time difference, the typical values for a 10x10mm optical area are inserted in to the above equations:

- Line length $D_x = 10\text{mm}$
- Step distance between lines $D_y = 10\mu\text{m}$
- Unidirectional flyback distance $D_u = \sqrt{D_x^2 + D_y^2} \approx 10\text{mm}$
- Target stage velocity during motion $v = 100\text{mms}^{-1}$
- Linear stage acceleration $a = 100\text{mms}^{-2}$

$$d_{acceleration} > \frac{D}{2} \qquad t_{diff} = 2\left(\sqrt{\frac{D_x}{a}}\right) - 2\left(\sqrt{\frac{D_y}{a}}\right) \tag{38}$$

Calculating t_{diff} shows that there is a time difference due to flyback distance of 0.61 seconds, which equates to approximately 10 minutes reduced time over the full 10x10mm area. Additionally, it is necessary from a production standpoint to cut multiple individual optics on a single substrate, separated by some kerf width for post-production dicing purposes as shown in Figure 43. In this case, using a bidirectional cutting pattern to reduce flyback distance reduces the time even further.

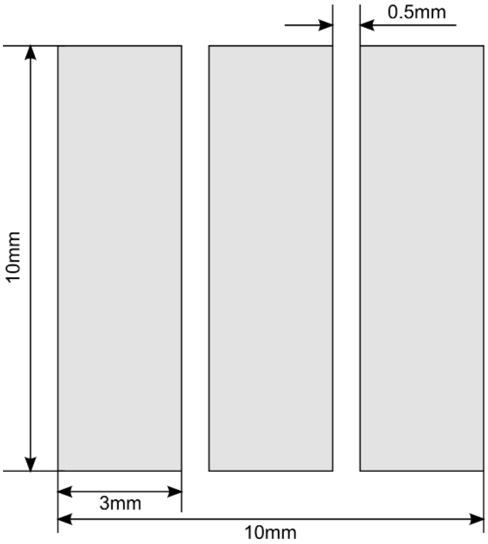

Figure 43: A representative optical requirement: 3 optics of size 3mmx10mm with inter-optic 0.5mm wide kerf zone

The time saved per optic when using a bidirectional cutting pattern is about 5.5 minutes, giving a total time reduction of about 16.5 minutes. Despite the cut area being the same, this is a 60% improvement in time reduction over the previously calculated 10mm square surface cut, showing that using a bidirectional cutting pattern is increasingly preferable for use when cutting optics with a short scan line length.

3.1.2 – Test structure definition

It was thought that the BISCAN strategy may reduce or eliminate any absolute spatial registration errors created when cutting a surface relative to a reference feature that is derived from the evolution of the surface during cutting. Like the symmetry of a structure this spatial lag may be averaged out using BISCAN cutting to provide better spatial registration to a reference feature, but may also broaden out the structure. A suitable test structure was designed in order to evaluate the symmetry differences and spatial lag when cutting using the two different raster patterns, shown in Figure 44.

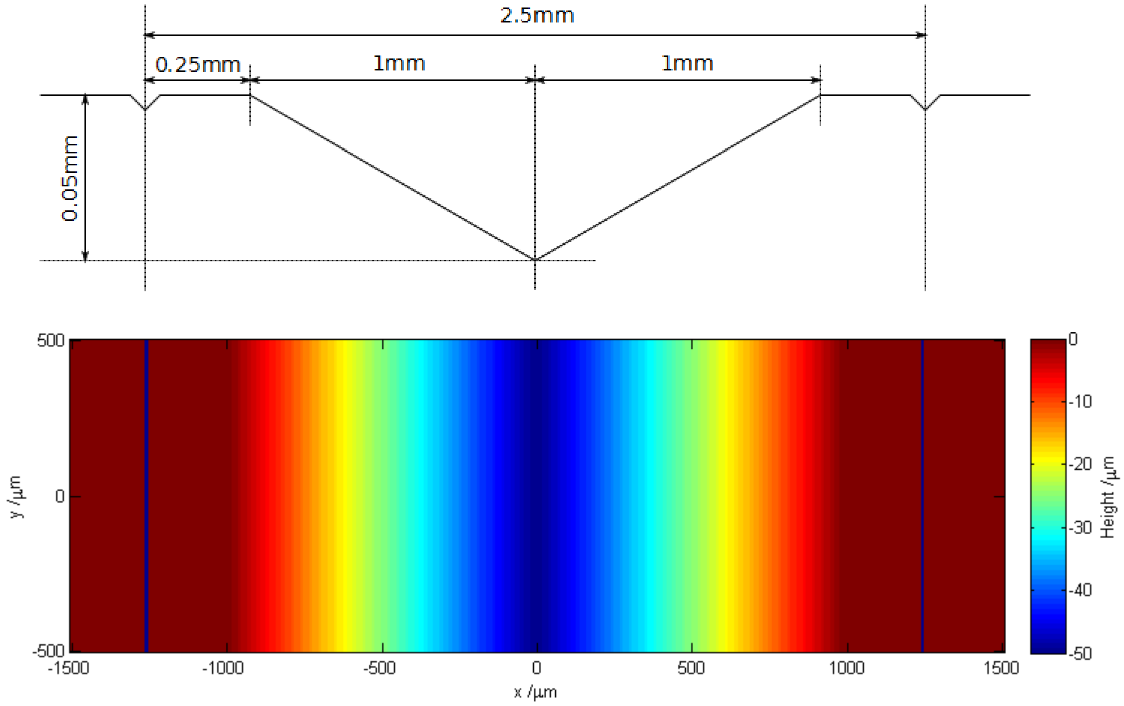

Figure 44: Top: A cross-sectional view of a test structure used to evaluate the difference in form of an optic when using unidirectional and bidirectional cutting patterns Bottom: A plan view of the proposed test structure surface.

This structure consisted of two sloped surfaces that meet at a point, flanked by two reference lines that are comprised of a single laser shot per raster line. The surfaces have a slope direction with is aligned to the scan direction of the cut raster pattern. The two lines consisting of single shots are used as a reference features for analysis: because these lines do not contain multiple shots they should experience no change in position due to raster scan direction, and can be used to examine the change in form and position of the test structure.

This structure was cut using 3 different cutting strategies to analyse the effect of direction on form error:

1. unidirectionally from right to left (UNISCAN L-R)
2. unidirectionally from left to right (UNISCAN R-L)
3. bidirectionally (BISCAN)

It was expected that 1. and 2. above will produce a test structure that is skewed in the direction of the raster direction, with the deepest point of the test structure moving by some value δx (see Figure 45). In all cases, the width between reference lines (W_p) and the height of the test structure (H) should remain equal.

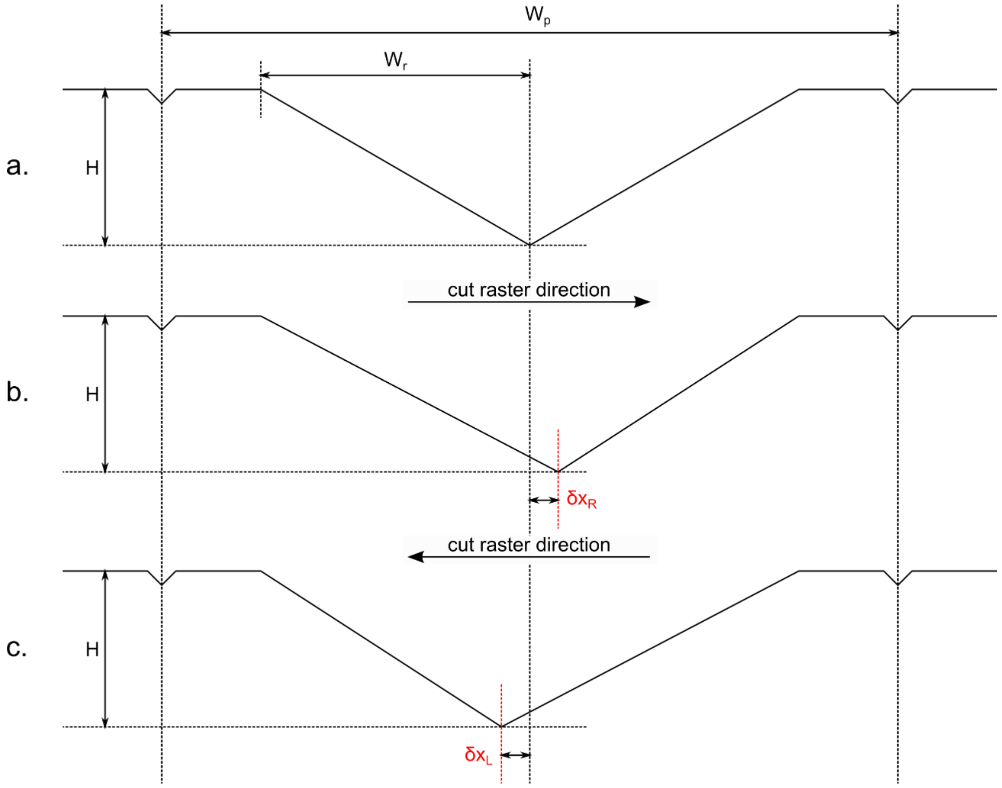

Figure 45: a. the profile of the test structure design, b. the expected outcome when cutting this structure unidirectionally from left to right, c. the expected outcome when cutting this structure unidirectionally from right to left

Under ideal conditions the offsets δx_R and δx_L would be equal, although machine setup (e.g. the laser beam is not orthogonal to the substrate surface) and process variability (e.g. short timescale temperature changes affecting process conditions to give slightly different results between test structures) may produce structures where these offsets are not the same. If a difference is observed where $\delta x_R > \delta x_L$ or vice versa this may indicate an issue with the setup that needs to be corrected, making this test structure potentially useful for calibration and process diagnosis.

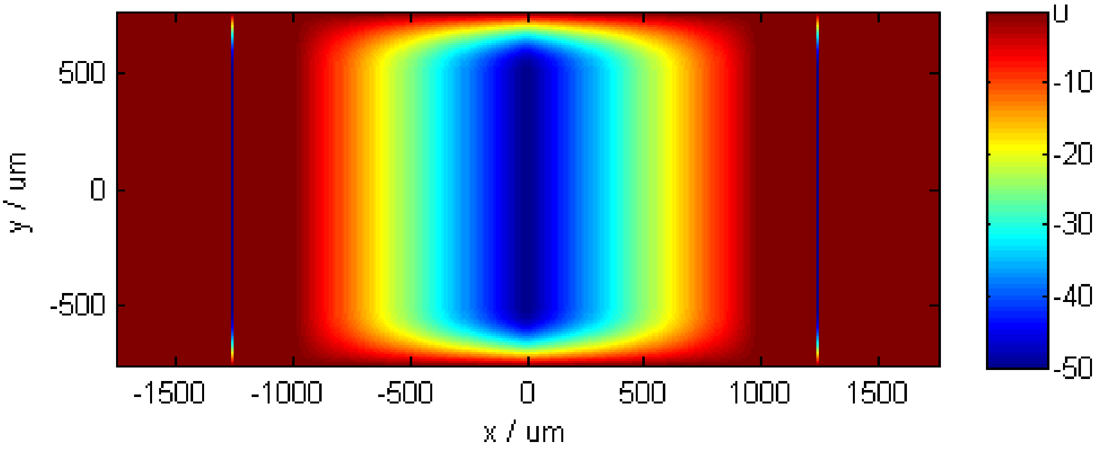

Figure 46: A plan view of the final surface design for the directionality test structure

In order to avoid issues with creating high slope features at the top and bottom of the test structure, a 250µm border was added that smoothly transitioned the surface from the points at the edge back up to zero, following a parabolic shape as seen in the outer 500um regions of the structure in Figure 47. This ensured that the form of the test structure is not affected by cutting or smoothing errors due to regions of high slope.

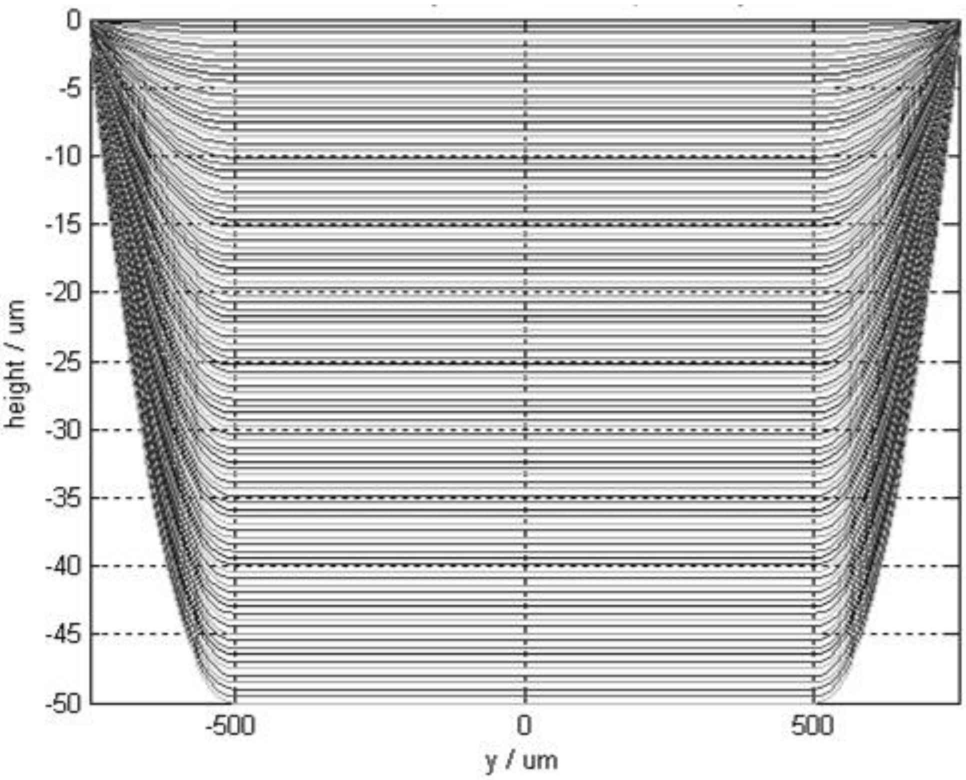

Figure 47: The cross-sectional profile of the directionality test structure in the y-axis, showing the added parabolic border outside the region between -500um to 500um

As the shape of the test structure returns to 0 in the x-axis no border is applied in this axis.

3.1.3 – Test structure fabrication and measurement

Three test structures were cut on the same substrate, each one with a different raster pattern described above but with otherwise identical parameters. They were smoothed using identical smoothing conditions and profiled using the STIL CHR-350 confocal chromatic probe with a measurement resolution of 5µm in the scan direction and 20µm in the step direction. The data was processed to remove any residual spatial rotation that arises when the optical surface is not perfectly normal to the axis of the chromatic probe, as well as rotated to remove any axial rotation of the surface, with the resulting surface image shown in Figure 48.

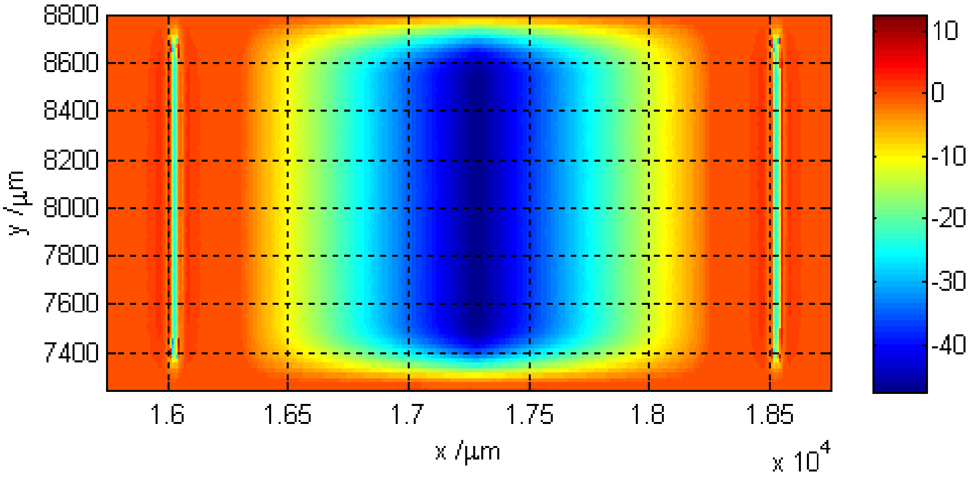

Figure 48: The measured surface of the bidirectionally fabricated directionality test structure

The x-axis position of the left reference line was found by integrating the reference line surface profile, normalising and finding the x-position of the 50% value. The x-origin was then offset to be coincident with the reference line. The central region of interest was selected to remove the parabolic border and a mean profile was found by calculating the average of all profiles along the x-axis (shown in Figure 49).

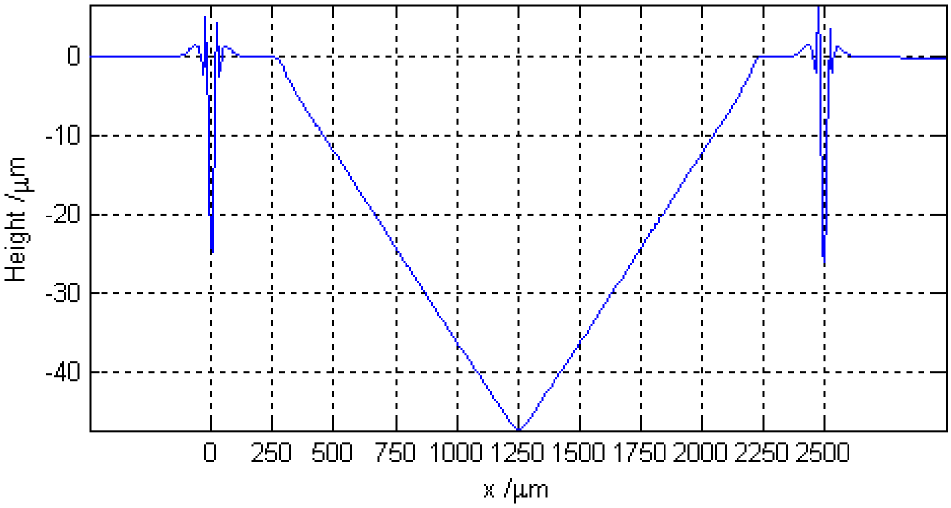

Figure 49: The mean measured profile of the bidirectionally fabricated directionality test structure

The design profile is similarly offset in x so that the x axes of the design and measured profiles match. The residual can then be found by subtracting the measured profile from the design profile for each cut strategy (as described in Section 2.3). The residuals obtained from the test structures cut using the different cutting strategies are shown in Figure 50, Figure 51 and Figure 52.

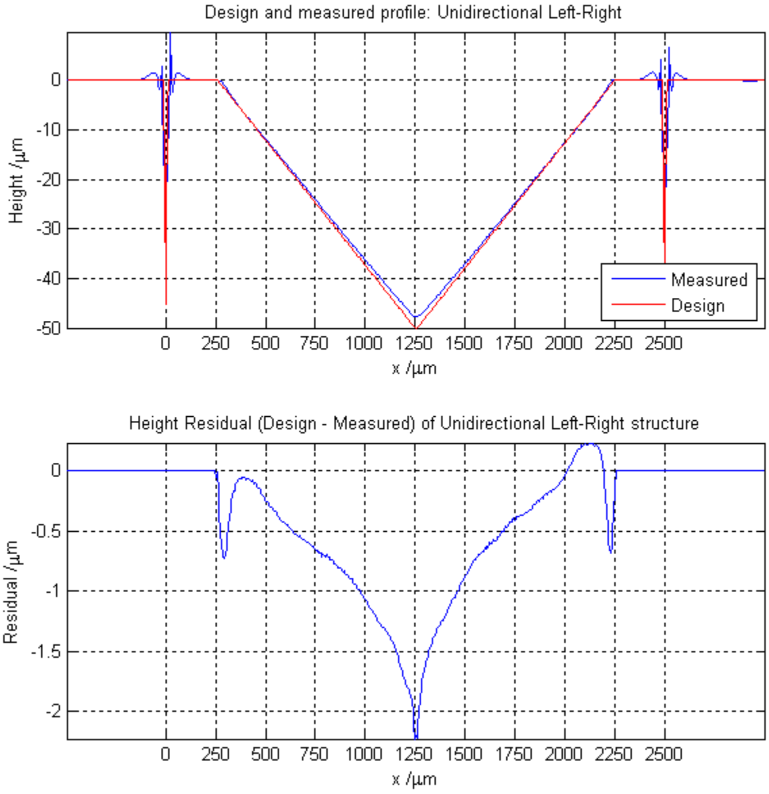

Figure 50: Top: the design and the measured mean profile of the unidirectional L-R fabricated directionality test structure. Bottom: the surface residual when the measured profile is subtracted from the design profile.

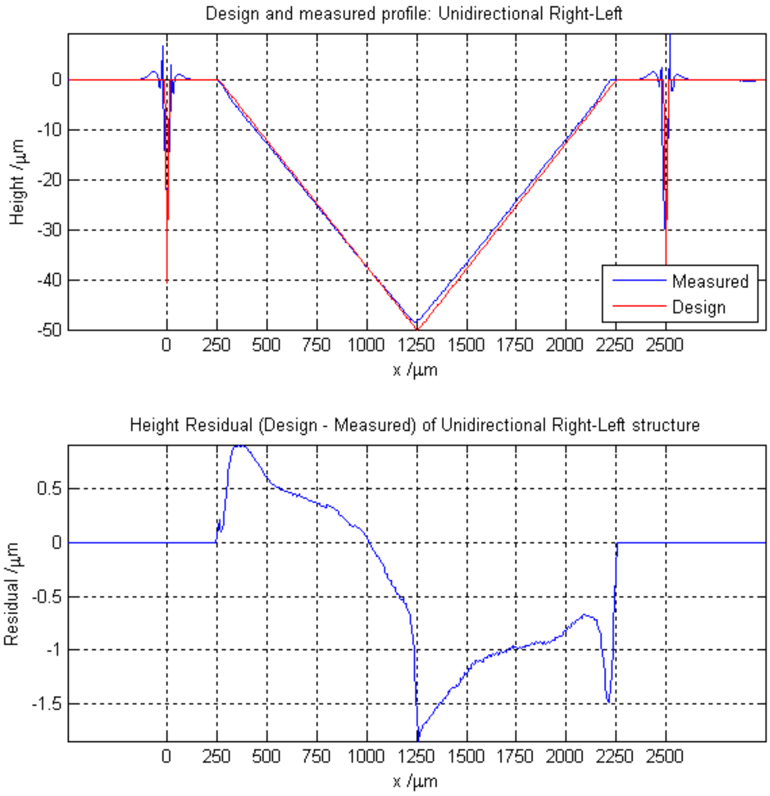

Figure 51: Top: the design and the measured mean profile of the unidirectional R-L fabricated directionality test structure. Bottom: the surface residual when the measured profile is subtracted from the design profile.

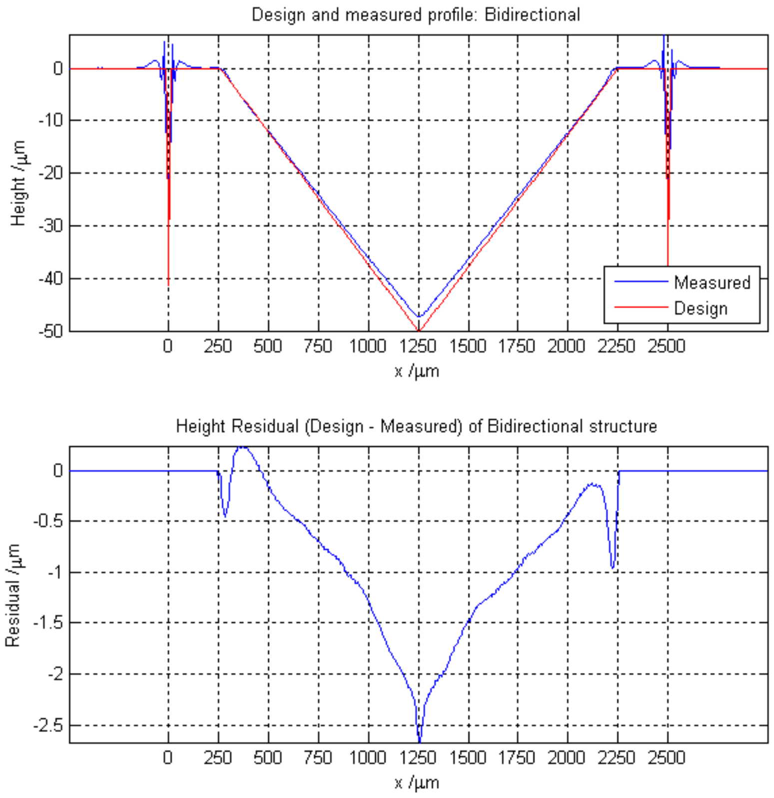

Figure 52: Top: the design and the measured mean profile of the bidirectional fabricated directionality test structure. Bottom: the surface residual when the measured profile is subtracted from the design profile.

The residuals obtained show that there is a clear surface scaling error of approximately 3-4% for each test structure, along with some form error that means the linear slopes have some curvature. The shape of the surface residual error at the centre and edges of the test structure was as expected due to the higher spatial frequency and the low-pass filtering mechanism of the smoothing process.

In order to obtain more meaningful results from these profile data, a linear fit to the sloped surface was found using the central 800µm portions of each sloping surface to avoid the areas of higher spatial frequency skewing the fit. Using these two linear fits, the absolute slope of the two sloped surfaces can be obtained to determine the ratio of slopes, and thus an indication of how symmetrical the test structure surfaces can be when using the different raster patterns. The linear fits can also be used to find the distances to the edges and centre of the test structure relative to the reference line in order to determine the surface specific and average spatial lag that each raster pattern creates. The two linear fits to the test structure were found using a least-squares fit to determine the slope and y-intercept of each line. The x-positions of the two edge points, dx_1 and dx_3, were then calculated by finding their intercept point with the $y = 0$ value, while the x-position of the centre of the test structure, dx_2, was calculated by finding the point of interception between the lines:

$$x_{centre} = \frac{c_1 - c_2}{m_2 - m_1} \tag{39}$$

A schematic of the surface with the positions indicated is shown in Figure 53 while the fitted positions are shown on the surfaces in Figure 54.

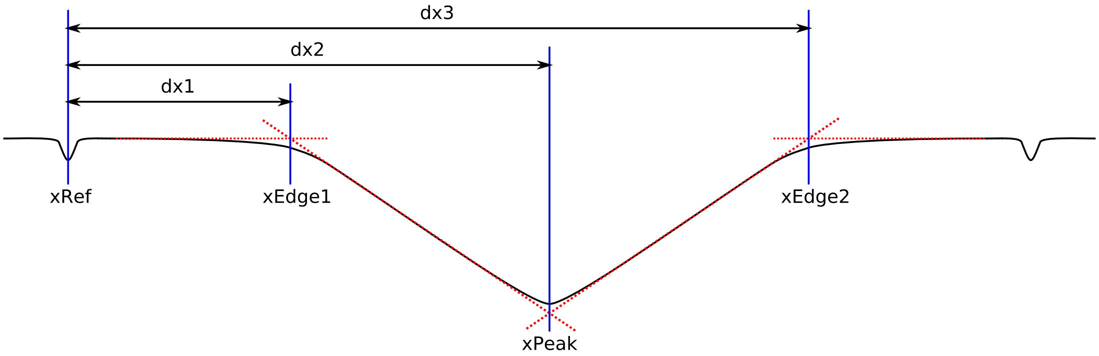

Figure 53: The three distances necessary to calculate angular and spatial parameters of the directionality test structures.

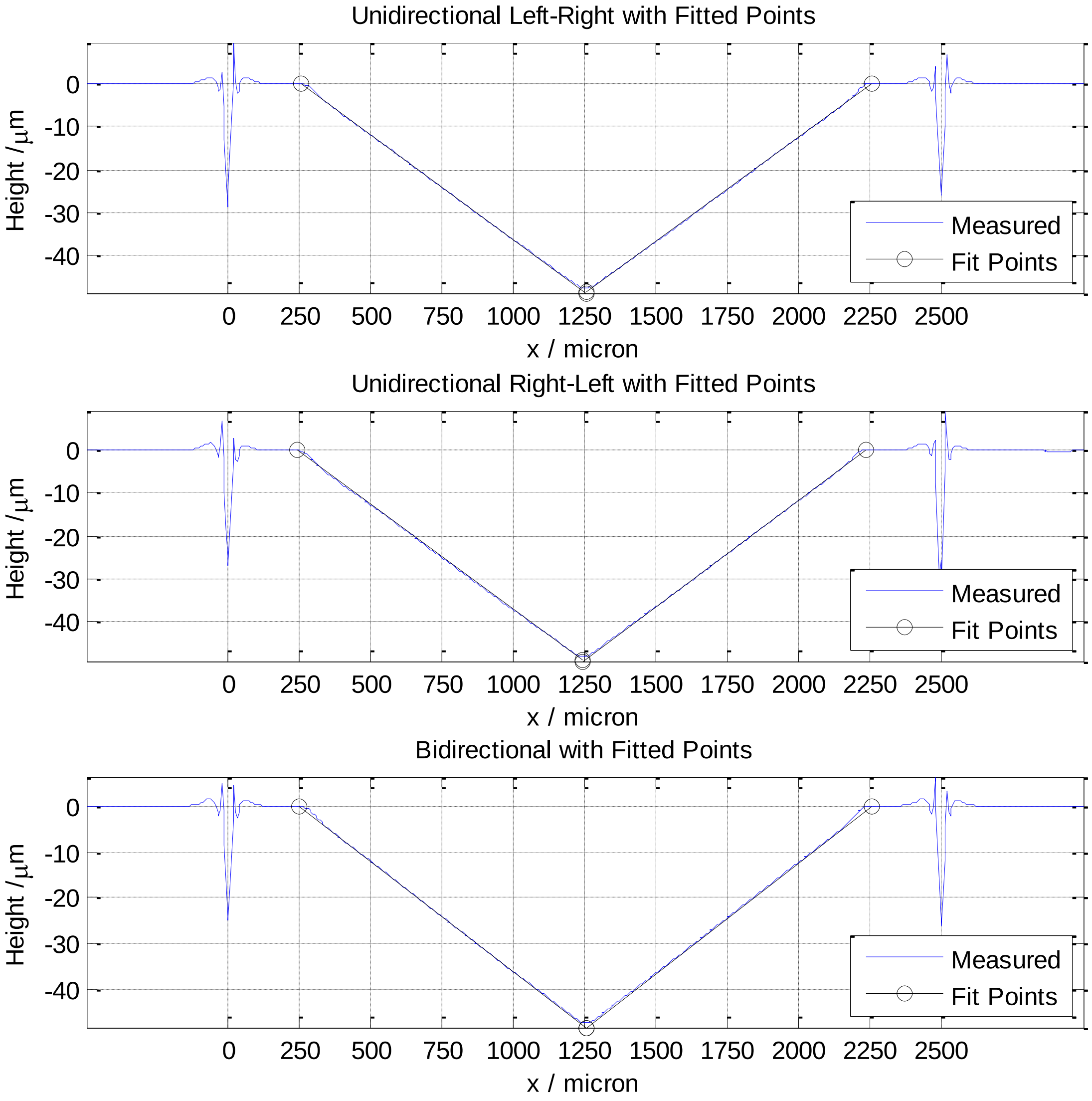

Figure 54: The three directionality test structures manufactured with different raster patterns shown with their linear fits and calculated intercept points.

Using data derived from the intercept point positions and linear fits, shown in Table 4, allows for the differences in cut strategy to be analysed.

	Unidirectional Left-Right	**Unidirectional Right-Left**	**Bidirectional**
Angular			
Absolute Slope S_1: x = 250-1250μm (mrad)	48.795	49.097	47.991
Absolute Slope S_2: x = 1250-2500μm (mrad)	48.653	49.600	48.214
Slope Ratio: (S_1/S_2)	1.0029	0.9899	0.9954
Slope Ratio Difference: (Slope Ratio - 1)	+0.0029	-0.0101	-0.0046
Spatial			
Spatial Lag of Fitted Points: (μm)	x1 = 250: 6.905 x2 = 1250: 6.630 x3 = 2250: 9.245	x1 = 250: -10.435 x2 = 1250: -5.983 x3 = 2250: -12.159	x1 = 250: -0.493 x2 = 1250: 3.758 x3 = 2250: 3.336
Mean Spatial Lag of Fitted Points: (μm)	7.593	-9.526	2.208
Width Error of Test Structure (μm)	+2.340	-1.724	+3.829
Second Reference Line Location Error (μm)	+1.080	-3.843	+0.428

Table 4: Angular and spatial data of the directionality test structures calculated from the linear fits.

3.1.4 – Angular analysis of test structures

The data calculated that is of interest is summarised in Table 4 and shows some unexpected results between the different cut raster patterns. It was anticipated that the Slope Ratio Difference, S1/S2-1, between the two angled surfaces S1 and S2 would be close to zero for the bidirectional raster pattern with the ratios of Unidirectional L-R and Unidirectional R-L roughly the same but with opposite sign. Table 4 shows instead that the Unidirectional L-R has the lowest absolute value which implies that this structure is the most symmetrical. This can potentially be explained by a difference between the substrate normal and the laser beam axis in the scan direction which would create a difference in beam diameter between the two angled surfaces.

To test whether this was the case, the angle of the laser beam axis was estimated by using paper that darkens when exposed to infrared radiation. With the focussing lens in the position for cutting, a laser pulse was generated which marked the paper. The focussing lens was then moved along the z-axis by 1mm while keeping the paper stationary and another pulse were generated to mark the paper. The centres of the two marks was then found to be approximately 35µm apart in the scan direction of stage motion, which corresponds to a laser angle of 2.00 degrees. The surface angle of the directionality test structures was 2.86 degrees, which will change the laser beam area in the scan direction during cutting by:

$$\delta A_{surface} = \frac{1}{\cos(\theta)} = \frac{1}{\cos(2.86)} = 1.0013 \tag{40}$$

The angle between the laser beam axis and the surface normal is either 4.86° or 0.86° depending upon which side of the directionality test structure the laser beam is incident upon. Calculating the laser beam area change gives:

$$\delta A_{surface+beamangle} = \frac{1}{\cos(2.86 + 2.00)} = 1.0036 \tag{41}$$

$$\delta A_{surface-beamangle} = \frac{1}{\cos(2.86 - 2.00)} = 1.0001 \tag{42}$$

Thus, due to the angle of the laser beam on the substrate surface, the laser beam area changes by 0.35% between cutting one side of the directionality test structure and the other. It is not expected that this would create the marked asymmetry in surface slopes observed, however Chapter 2 illustrates that the local surface slope during the cutting process is demonstrably different from that of the overall surface. The $\frac{1}{cos}$ dependence of beam area has a greater impact when the local surface slope is high, and it is expected that the local slope of the region on which the laser beam is incident during cutting will be significantly higher than the final test structure slope.

The reference lines that were put of the test structure, for example the feature located at xref in Figure 53, consist of single laser shots in the scan direction. They can therefore be used to examine the shape of the cut surface on which the laser is incident during the cutting process (reference line shown in Figure 55). This cut surface shape can then be used to provide an estimate for the value of local surface slope as the cutting process progresses, and this value can be used to determine whether the laser beam angle has a greater impact during the cutting process than might be expected when considering the gross slopes of the test structure.

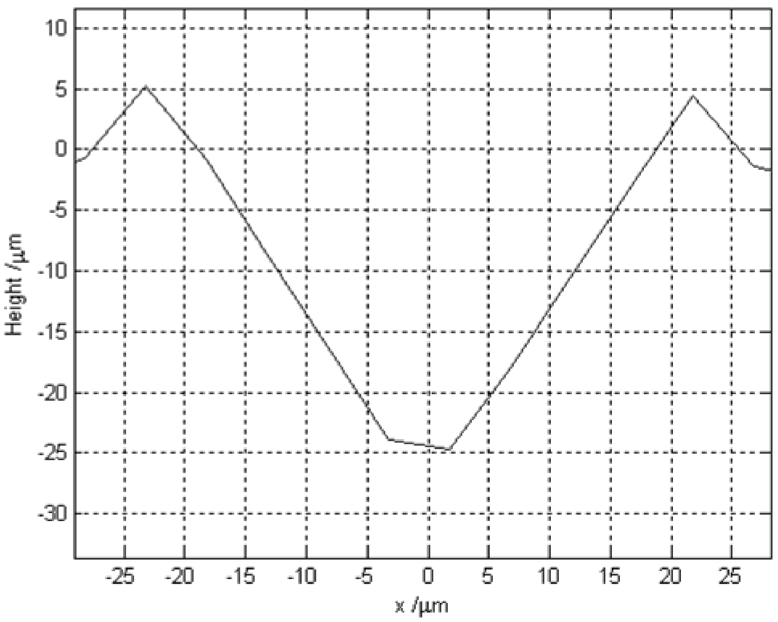

Figure 55: The average height profile of the origin reference line.

Finding the slope over 4 points on the positive x side of the feature:

$$\theta_{local\_surface} = \tan^{-1}\left(\frac{-3.003-(-24.64)}{16.75-1.745}\right) = 55.26^{o} \qquad (43)$$

Then using this value to calculate change in beam area:

$$\delta A_{local\_surface+beamangle} = \frac{1}{\cos(55.26+2.00)} = 1.8490 \qquad (44)$$

$$\delta A_{local\_surface-beamangle} = \frac{1}{\cos(55.26-2.00)} = 1.6717 \qquad (45)$$

This shows that when calculating the contribution of beam angle to surface slope asymmetry using estimated local surface slope the difference in beam area from one side of the test structure to the other is 17.73%. This is a more significant change in beam area and is expected to cause a difference in cutting process conditions.

3.1.5 – Spatial analysis of test structures

The spatial data calculated using the test structures is consistent with the angular data with the width of test structure components changing in line with the measured slope changes. The spatial data corresponded well with expectations in the following key parameters:

1. Spatial lag directionality and magnitude: The UNISCAN L-R test structure has a point-by-point and mean positive lag (shifted to the right relative to the reference line in Figure 54), matching the direction of surface evolution during cutting. The UNISCAN R-L test structure has a point-by-point and mean negative lag (shifted

to the left relative to the reference line in Figure 54), matching the direction of surface evolution during cutting. The BISCAN test structure has a mean positive lag (shifted to the right relative to the reference line in Figure 54), with the point x1 having a negative lag. The expected symmetry is negative at point x1, zero lag at point x2 and positive lag at point x3 with a zero mean lag. The BISCAN test structure does show the lowest magnitude for mean spatial lag for the three test structures, although it does not lie at the midpoint between the values for the two UNISCAN test structures.

2. Test structure width: As the BISCAN test structure was expected to average the effects of UNISCAN L-R and UNISCAN R-L, the BISCAN test structure was expected to be the widest of the test structures due to the spatial lag being applied in both directions. This has been shown to be the case, although the width errors of the two UNISCAN test structures were not close to zero as expected.

3. Second reference line location: The location of the second reference line (located at x = 2500µm in Figure 54) was examined. As this line is produced using a single laser shot, there should be no positional error related to the directionality of stage motion during cutting. However, larger than expected distance errors between reference lines can be seen that are not similar between cutting directions.

Most of the above differences from expectations can be explained by the incident beam angle on the substrate as described in Section 3.1.3. However the location error of the second reference line is not associated with an angled beam or direction of stage motion. It is likely that the positional error measured is a combination of factors, both real and from analysis: these test structures were fabricated serially and as such occupy different locations on a fused silica wafer. This means that the region of the stage motion used during fabrication was from a different part of the range for each structure. It is likely that the motion accuracy of the stages is variable across its range, creating positional errors whose magnitude and sign are dependent on the stage area used during fabrication. However, given that these are high-precision motion stages factory calibrated with an interferometer, it is highly likely that the stage motion accuracy is sub-micron and its variation over small regions is not measurable using these test structure scans. Of higher likelihood for a real offset is residual substrate warping from the smoothing process that has caused some lateral shift in features relative to each other.

3.2 – Multi-pass cutting

It is advantageous to be able to fabricate very high sag surfaces in order to increase the addressable market for PowerPhotonic's products. Specifically, the ability to cut surfaces that exceeded the cut depth limit of approximately 60μm would be of marked benefit, thus during the investigation the ability to increase cut depth was reviewed in addition to alternative raster patterns.

It might be expected that the maximum depth available during the cutting process is limited only by the laser's maximum output power and the maximum transmission of the AOM. Increasing the maximum delivered power of the system is possible, however using maximum delivered power for fabricating deeper structures is ultimately not a viable option; as pulse energy increases so does the energy of the ablation reaction. At irradiance levels above 1.2 MWcm^{-2}, the material removal interaction changes from being a largely evaporative process that removes smooth and uniform craters of material, to a highly vigorous interaction that produces craters with edge effects while ejecting solid material onto the surrounding area [1]. This produces highly undesirable residual surface shapes that are ultimately not suitable as optical surfaces. Additionally, increasing individual crater cut depth also increases the slope of the local surface illuminated by the cutting pulses. As shown in Figure 11 surface reflectivity increases rapidly at high surface slopes, which eventually results in laser absorption being lower than the ablation threshold and the cutting reaction is arrested.

In order to enable the fabrication of deeper surface profiles and overcome this individual pulse energy limitation, the solution investigated was to pass the cutting laser multiple times over the same surface. This not only keeps the pulse energy below the melt ejection threshold, but also ensures that the local surface slopes during cutting remain low enough for good absorption. The principle behind the multi-pass cutting strategy is simple: design a surface to be fabricated using n number of passes, divide the surface depth by n to receive the individual pass design and then cut this individual pass design n times in the same location. Figure 56 illustrates this concept for a surface that is cut using 2 passes.

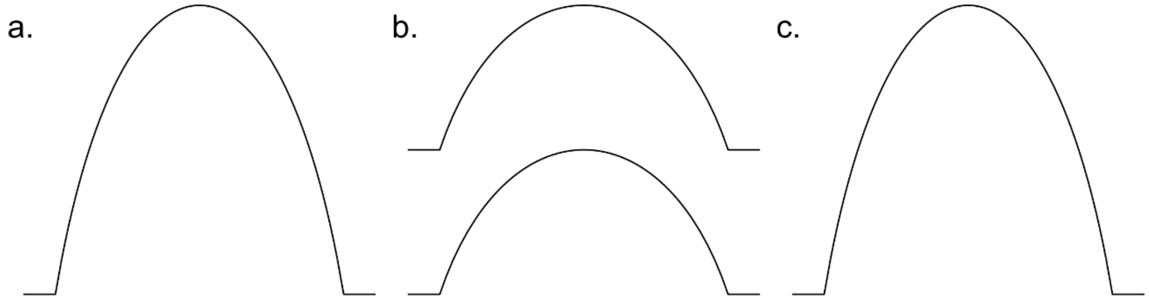

Figure 56: A figure showing the basic principle behind designing a structure for 2-pass cutting. a. shows the desired surface, b. shows the 2 half-depth surfaces used for the cutting process and c. shows the final cut surface

There are a number of geometries that can be used when cutting a surface using more than one pass of the laser, referred to as UNISTEP and BISTEP. The nomenclature used to refer to these different cutting geometries is given in Table 5. BISTEP cutting is only applicable for an optic that is manufactured with an even number of cut passes, so that a similar number of cutting passes occur from top-to-bottom as bottom-to-top in the step axis.

Pattern Name	**Long form pattern name**	**Description**
UNISTEP	Unidirectional in the step axis	Motion in the step direction between laser cutting scan lines remains the same after each cutting pass
BISTEP	Bidirectional in the step axis	Motion in the step direction between laser cutting scan lines alternates direction after each cutting pass

Table 5: A table summarising the terminology used to describe the cutting geometries investigated

Both the UNISTEP and BISTEP geometries could also be interlaced such that the raster pattern on a second cutting pass could be offset by half the raster pitch in the step direction. It was thought that doing this may increase achievable cut depth while keeping the overall processing time the same as a single pass. Figure 57 illustrates the stage motion geometries investigated.

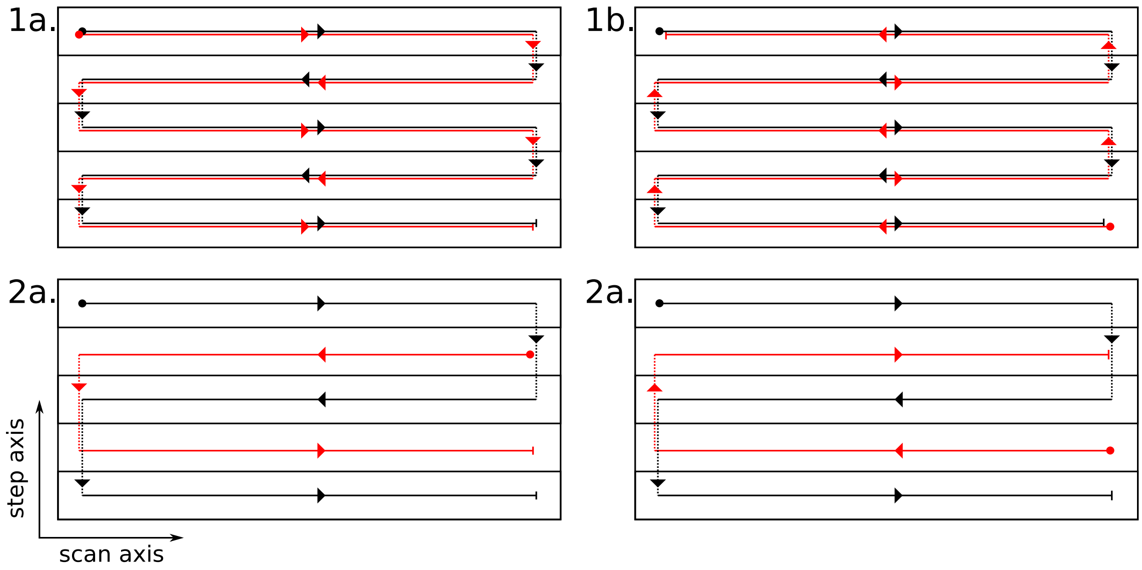

Figure 57: A diagram of the four main geometries tested during trials of multi-pass cutting. 1a: UNISTEP. 1b: BISTEP. 2a: interlaced-UNISTEP. 2b: interlaced-BISTEP. The black line is the first cutting pass, the red line is the second cutting pass. The circle indicates cut start position and the line indicates cut end position. The offset between red and black lines is only for clarity, during cutting they are expected to overlap. All scan directions were as the BISCAN geometry.

Although some cutting trials were completed using the test structure defined in Subsection 3.1.2, time constraints did not allow for complete analysis of the effects of using the different cut strategies. It was clearly observed that the interlaced patterns were not useful, creating very roughly textured surfaces that would not correspond to suitable optical components. It was found that there was very little difference between the test structures fabricated using UNISTEP and BISTEP, although as with the trials done with UNISCAN and BISCAN it is anticipated that BISTEP may provide superior form reproduction due to better symmetry during surface formation. More work is required to determine the detailed effects when using the UNISTEP and BISTEP cut strategies, which could follow the format of the UNISCAN/BISCAN investigation detailed in Section 3.1.

Despite this lack of detailed analysis, using a multi-pass cutting strategy proved to be very successful at creating structures significantly deeper than 60µm. Test structures consisting of flat-bottomed square wells with edge length of 3mm were cut with 8 passes deeper than 400µm. To determine the precise depth limitation, further work is required.

3.3– Defocus compensation

An important attribute of the laser beam used for the cutting process must be considered when fabricating high sag surfaces, the depth of focus (DOF) of an acceptable process window. The Rayleigh range, z_R, of a beam is the most commonly used parameter in industrial settings to define the axial range over which the beam parameters are relatively consistent. It is defined as the distance from the beam waist to the plane in which the area of the cross-section of the beam is double that of the beam waist and is given by the equation:

$$z_R = \frac{\pi \omega_o^2}{\lambda} \tag{46}$$

where ω_o is the beam waist radius and λ is the laser wavelength. The beam waist ω_o at the focus of the cutting laser with $\lambda = 10.6$μm has previously been measured to be 20μm, and using these values in (*46*) gives a Rayleigh range of 118.55μm. As the beam is symmetrical about the beam waist, the usable DOF would then be two times the calculated Rayleigh range, or 237.1μm. However, this is a poor criterion to use to determine the DOF for the PowerPhotonic fabrication process. It was shown in Section 3.1 that an area change of just 17% had an effect on cut surface accuracy, so an increase in area of 100% at the edge of the Rayleigh range would represent a drastic change to the material removal conditions. Using the Gaussian beam radius equation described in [31], the beam diameter some axial distance from the beam waist can be calculated:

$$\omega(x)^2 = \omega_o^2 \left[1 + \left(\frac{\lambda x}{\pi \omega_o^2}\right)^2\right] \tag{47}$$

where $\omega(x)$ is the radius of the beam at position x. Rearranging for x gives:

$$let\ R = \frac{\omega(x)}{\omega_o}: \qquad x = \frac{\pi \omega_o^2}{\lambda}\left(\sqrt{R^2 - 1}\right) = z_R\sqrt{R^2 - 1} \tag{48}$$

The variable R allows for direct examination of the percentage increase in laser beam radius with respect to x. The changes in surface accuracy due to beam radius variation observed in Section 3.1 had a measurable effect on structure symmetry due to anisotropy of the system. However, given a beam orthogonal to the substrate surface, cutting away from the beam waist will isotropically increase beam radius which will have the effect of altering the energy-depth curve of the process at that point. Given the small change in shape observed, using an R value to give a similar order of magnitude beam area increase is appropriate and for a 15% beam area increase, $R = \sqrt{1.15}$. Using the previously supplied values of ω_o and λ, the axial range on one side of the beam waist is 45.9μm and the DOF is 91.8μm. If the focal plane is appropriately positioned, any surfaces requiring cutting that have a sag greater than the DOF will be subject to form errors. These form errors will increase with distance outside the DOF due to the defocussed beam producing an altered relationship between pulse energy and cut depth.

In order to maximise the cut volume that occurs within the DOF, the focal plane of the laser must be located DOF/2 below the surface of the substrate and this plane must be shifted before each subsequent pass by half of the maximum cut depth of the upcoming pass as shown in Figure 58. This ensures the focal plane of the laser lies at the centre of the depth map for the pass that is about to occur and therefore optics with a sag of up to 91µm still remain within the DOF.

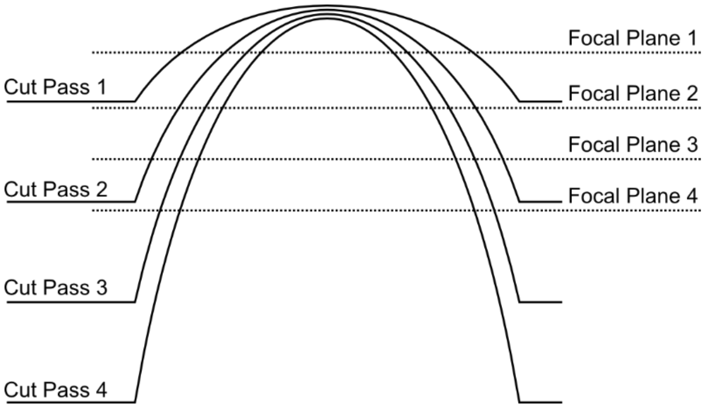

Figure 58: A figure showing the evolution of a profile over 4 identical passes along with the position of the laser's focal plane for each pass.

When cutting a surface that has a sag of greater than 91µm, the form error due to defocus can no longer be mitigated by shifting the focal plane. The defocussed spot changes the energy density of the beam on the surface, which in turn causes the cut depth to be less than expected. Figure 59 also illustrates an important point that the DOF is a useful figure to consider when fabricating structures with sags of hundreds of µm, but the form error related to this value is not binary. Form error due to defocus is also present within the DOF and increases as the limits of the DOF are approached.

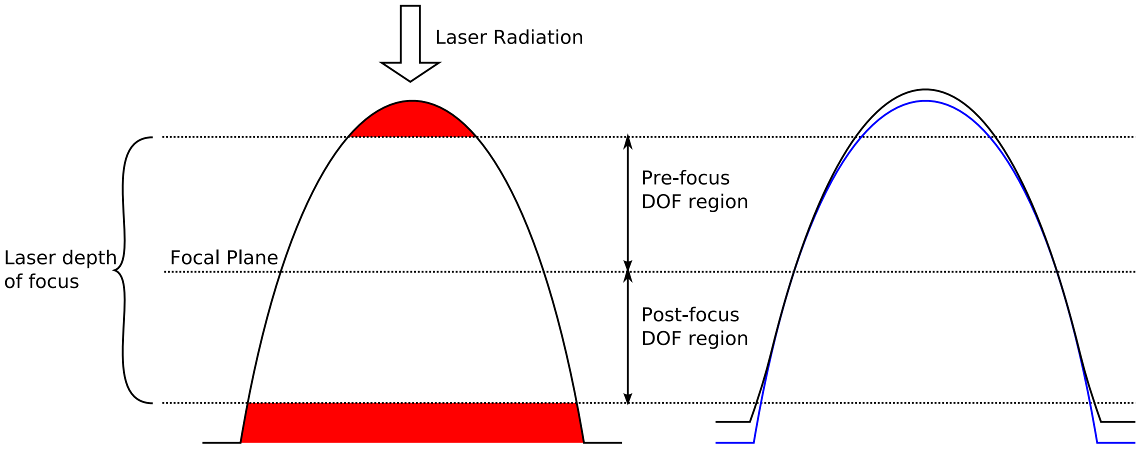

Figure 59: Cutting a surface with a sag greater than the laser DOF. Left shows the expected cut profile with regions outside the DOF denoted in red. The right diagram shows the resulting cut profile in black, with the reference profile in blue.

In principle the simplest way to eliminate DOF restrictions would be to move the focal plane of the laser in the z-axis as cutting occurs, tracking the topography of the surface. This was implemented and it was found that, at normal cutting speed, vibrations induced by the required motion of the z-stage on which the focussing lens was mounted caused serious cutting issues. These could be mitigated by considerably reducing the speed of the cutting process, which allows for smoother velocity transitions of the z-stage and lower system vibration. However this had the effect of directly reducing the capacity of the laser micromachining system, which was not acceptable from a business perspective. In order to cut high sag structures, there remained the requirement to reduce the effect of cutting outside the laser DOF without fast modulation of the focal plane z-position.

3.3.1 – Measuring the effect of defocus

This defocus effectively alters the laser energy to cutting depth relationship due to local energy density reduction. It follows then, that the way to compensate for this local energy density reduction is to increase the beam pulse energy based on the anticipated amount of defocus expected at a given point. Figure 60 shows a test structure that was created that was very similar to those in Section 3.1, but with the axial values defining energy instead of depth. A number of these test structures were fabricated and the focal plane location was altered to measure the effect of cutting depth with defocus.

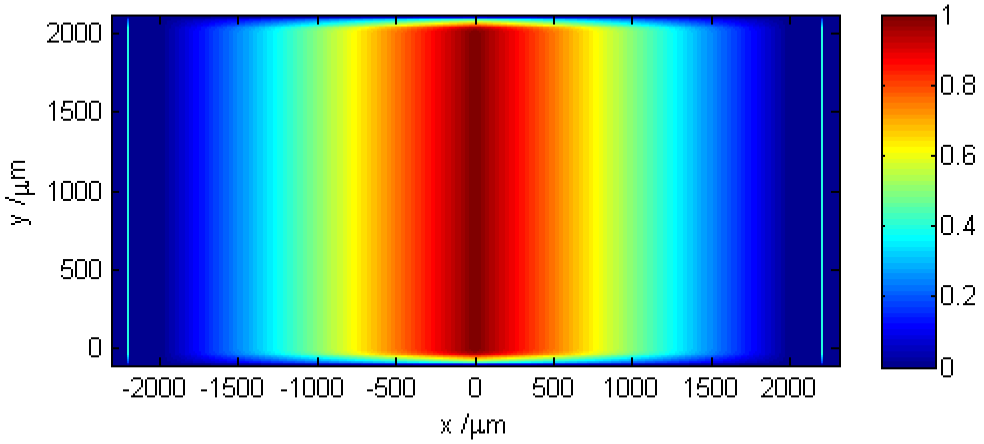

Figure 60: A test structure used to examine the impact of defocus on the energy-depth process relation.

These test structures were cut with increasing amounts of defocus in steps of 80µm, chosen to examine the effect of defocus well past the 45.9µm post-focus limit defined earlier. The first test structure had the focus on the surface of the substrate, with the lens moved away from the substrate by 80µm per test structure so that the defocus is consistently post-focus. The position of the focal plane relative to the substrate surface was found experimentally by using a number of rows consisting of 30 laser shots with increasing energy, arranged 2-dimensionally so that the z-position of the focussing lens changes by a small amount for each row, as shown in Figure 61 and Figure 62.

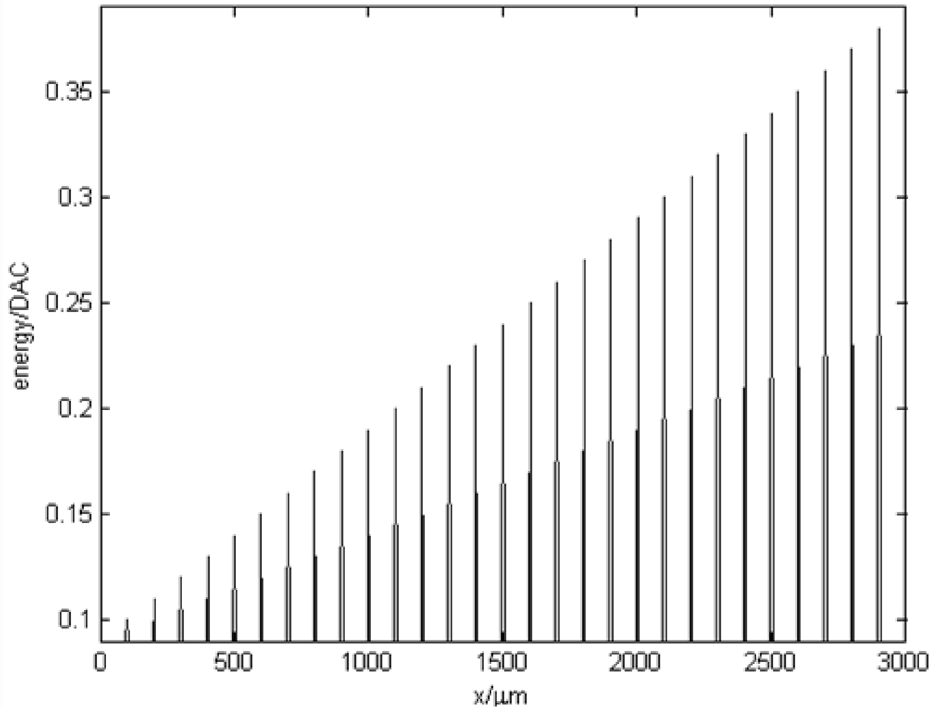

Figure 61: The 1-dimensional energy map of the focal plane test structure showing linearly increasing pulse energy values along x

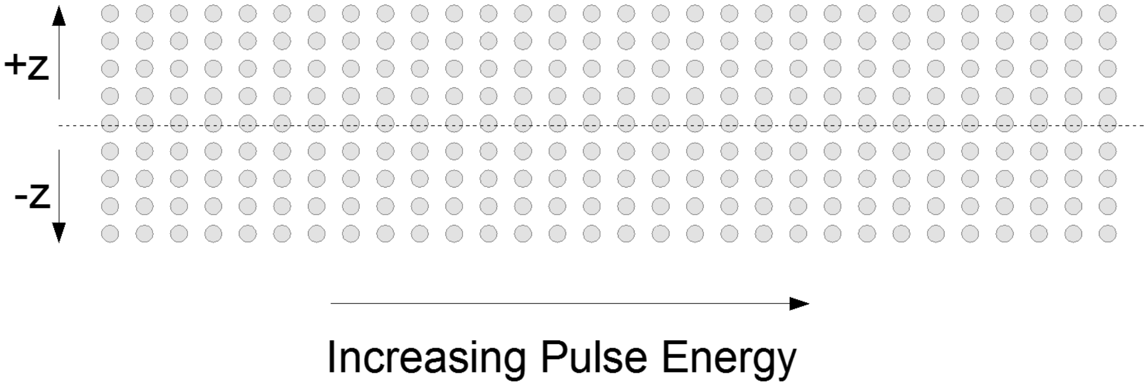

Figure 62: Layout of the 2-dimensional focal plane test structure. Nominal expected focal plane is indicated by the dotted line. The positive and negative z-values indicate the focussing lens motion direction.

By cutting the same design several times and changing the z-axis value of the lens translation stage, the lens translation stage value that corresponds to the focal plane location at the surface of the substrate can then be found. The line in which the spots produced by the laser beam extend furthest to the left indicates the best focal plane position as the threshold energy of the interaction is minimised with the minimum spot size and can be clearly seen in Figure 63.

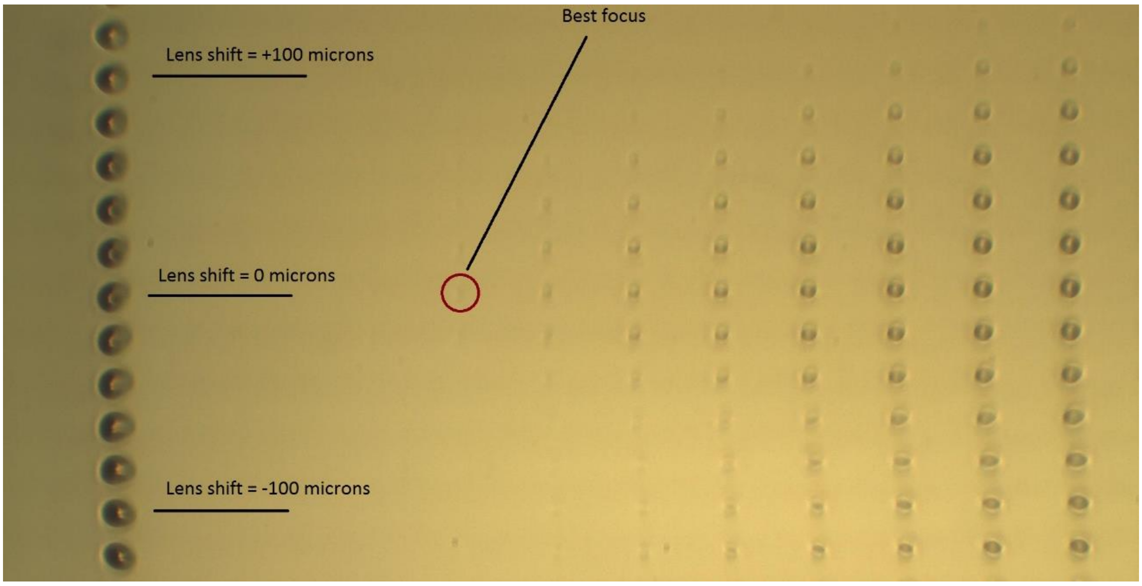

Figure 63: A micrograph of the focal plane test structure with a 20µm step adjustment of the focussing lens position.

Once the focal plane location was identified and set to be at the surface of the substrate, the 6 tapered test structures were fabricated and then profiled using a STIL CHR-350 confocal chromatic probe. They were then correlated with their designed energy values to give a number of energy *vs.* depth curves that show how defocus effects the fabrication process of the test structures.

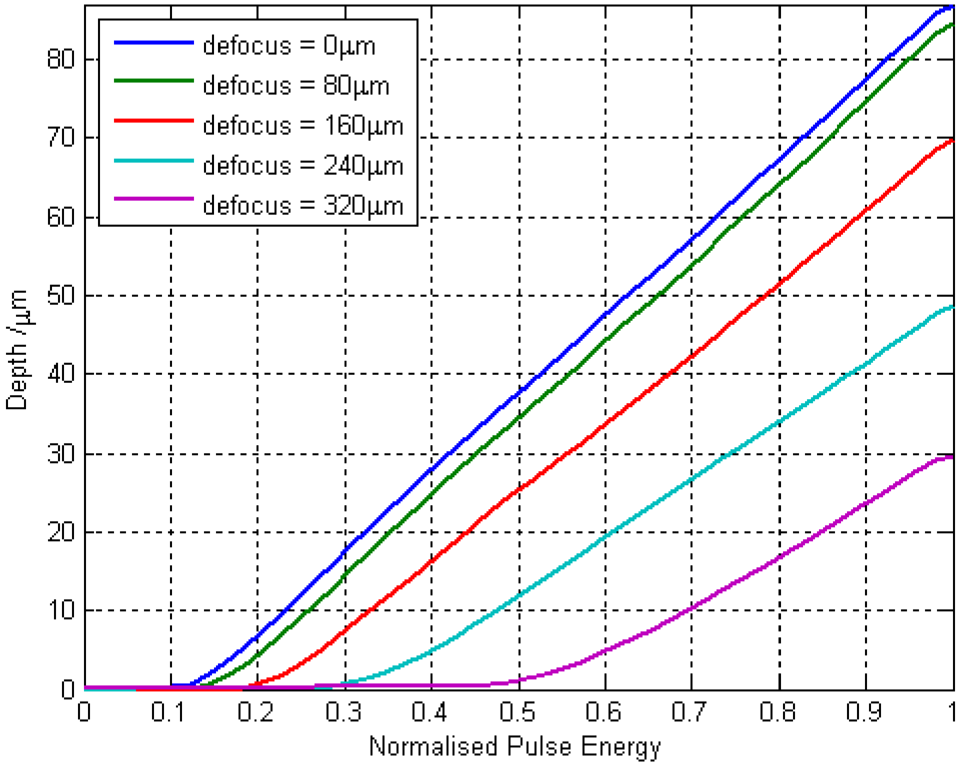

Figure 64: The energy-depth curves generated from the test structures at increasing levels of defocus.

As can be seen from Figure 64 the threshold value for removal increases and the slope of the linear region decreases as defocus increases, which is the expected result. This shows that not only will there be a form error associated with defocus, but that laser pulses with lower energy than the defocussed threshold will have no effect on the surface at higher levels of defocus. It should be noted that, due to the focal plane being located on the substrate surface when cutting the defocus = 0µm structure, the beam was outside the DOF according to the definition above for around half of the structure depth. However, the linearity of the curve above threshold shows that the energy-depth relationship also remains linear at distances of up to 88µm away from the beam waist, corresponding to a beam radius of 24.9µm, or an area increase of 55% over that at the beam waist. This suggests that using a beam area increase of 15% to define the DOF threshold is too conservative and further testing is needed to determine a more appropriate threshold.

3.3.2 – Development of the defocus compensation method

Using these data, along with the focal plane shift distance to be used, the energy of each pulse can be adjusted based on the calculated level of defocus at that point. This compensates for the larger spot size and gives the correct cutting depth. This must be done for each pass because as the surface evolves over multiple passes every point will have a different level of defocus. Thus each pass must be completed with its own unique surface design, and these unique designs must be cut in a specific order.

To calculate the pulse energy increase required to account for the defocus of the laser at any given point, the intercept and slope of each energy-depth curve were given by the coefficients of a 1st order polynomial fit to the linear region of curves (above 10µm cut depth) using a least squares method, these lines corresponding to these fits are shown on Figure 65 . The x-axis intercept gives the threshold energy for laser cutting at a given defocus value, and the slope is the cut depth per unit pulse energy above the threshold energy. These values are shown in Table 6.

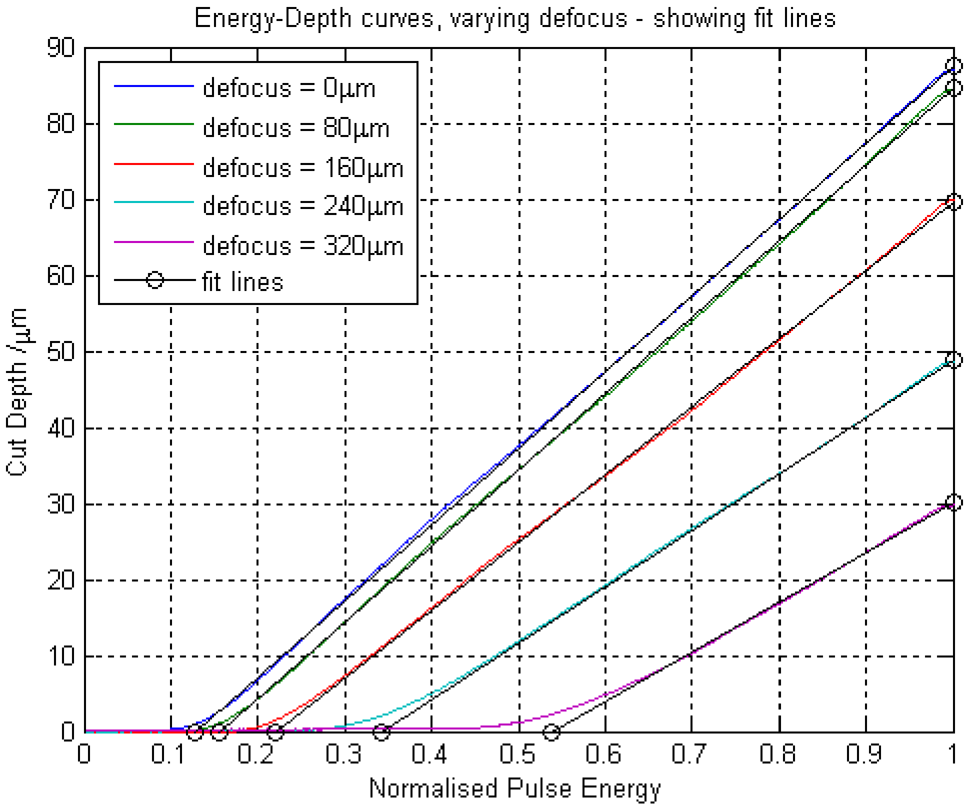

Figure 65: The defocus test structure energy-depth curves, shown with 1st order polynomial fits in black.

Defocus (µm)	x-axis Intercept (Normalised Pulse Energy)	Slope (µm/Normalised Pulse Energy)
0	0.127	100.362
80	0.155	100.000
160	0.220	89.339
240	0.341	74.263
320	0.537	65.075

Table 6: The values found using a 1st order polynomial fit to the linear regions of the energy-depth curves from the defocus test structures.

Plotting the fitted values of slope and x-intercept in Figure 66 and Figure 67 implies that there is a suitable fit model, but with the limited number of defocus values used it is not possible to determine which model should be used. For example, the points calculated for the slope from 80-320µm in Figure 66 appear to be linearly decreasing but finer sampling of this is required to draw any conclusions.

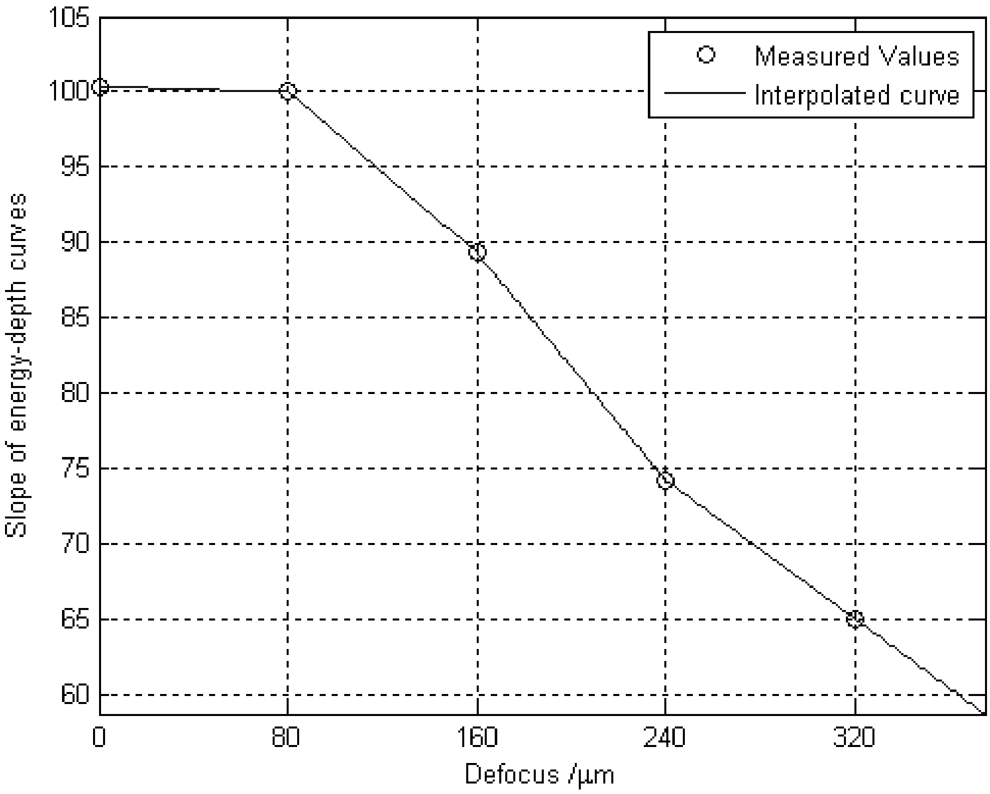

Figure 66: The slope of each energy-depth fit line plotted against defocus. The blue line is a linear interpolation and has been extrapolated past 320µm.

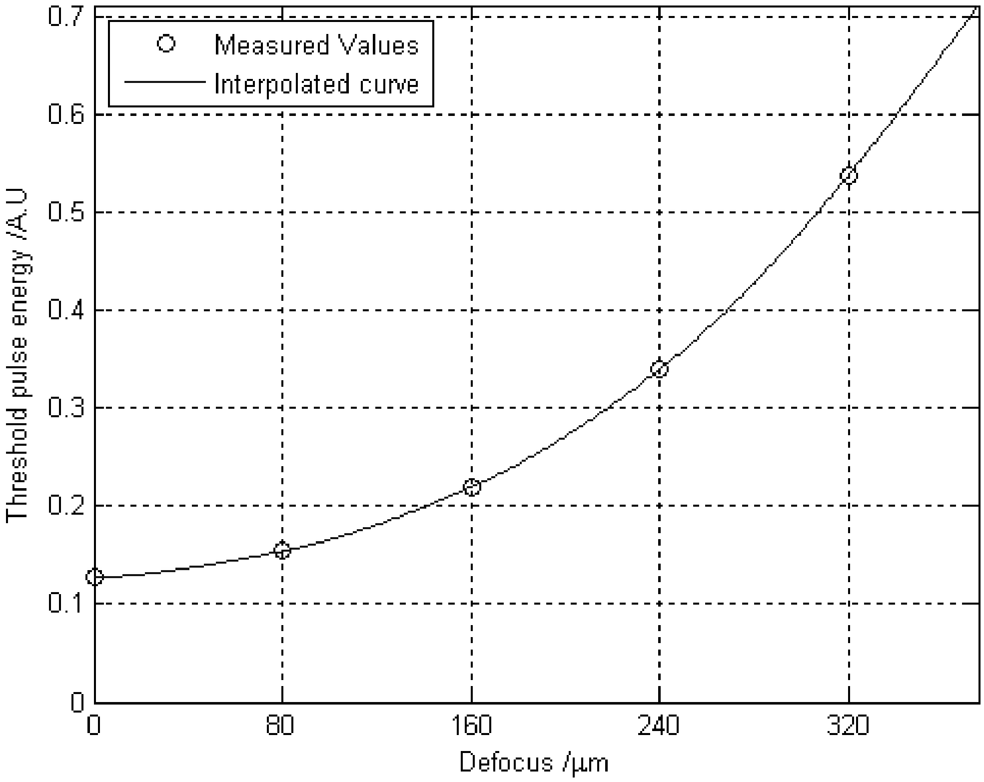

Figure 67: The threshold pulse energy (x-intercept) of each energy-depth fit line plotted against defocus. The blue line is a cubic interpolation and has been extrapolated past 320µm.

These values were interpolated in order to allow for fine pointwise adjustment of pulse energy. When the surface shape, the number of cutting passes required to fabricate the surface, the starting focal plane position and the lens shift per cutting pass are all known, the amount of defocus at each point for each pass can be calculated as shown diagrammatically in Figure 68.

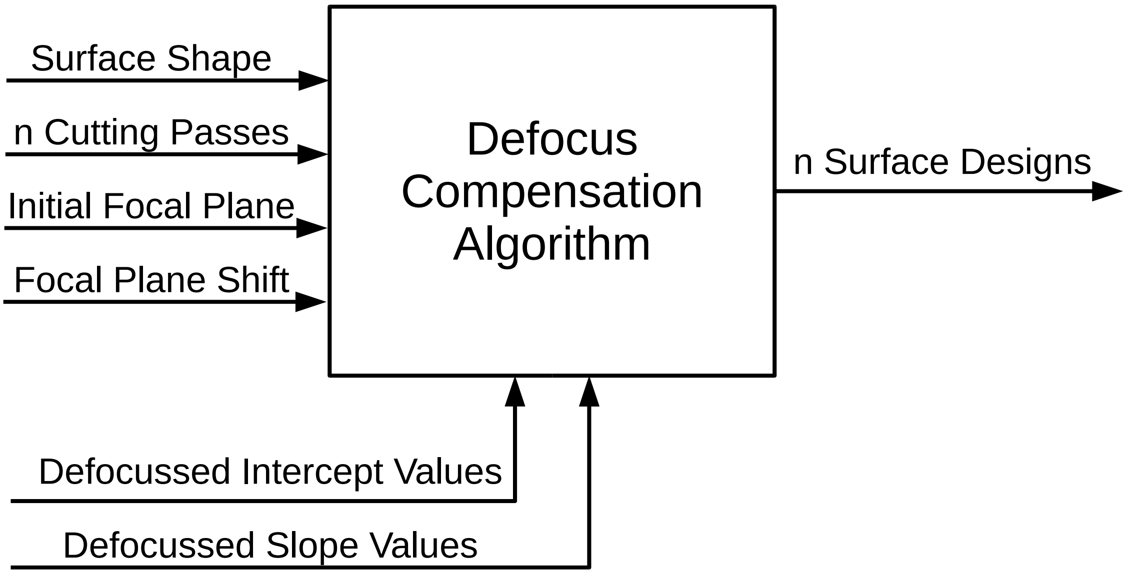

Figure 68: A simple diagram showing the information flow in to and out of the defocus compensation algorithm.

An algorithm was written in Matlab that calculates the level of defocus, based on calculated focal plane location and surface form during a given cut pass at every individual point within each cutting pass and calculates the slope and intercept values required to give the correct surface depth. The pulse energy necessary to create a point with the expected depth is then calculated and each pass is saved as an individual surface design.

3.3.3 – Application of defocus compensation

In order to illustrate the defocus compensation method, a test structure was designed that would be expected to have an optically significant change in form error due to defocus during manufacture. It was found that a 3-dimensional pointwise implementation of the algorithm was extremely slow, taking more than 12 hours to generate the three surface designs for a 3-pass structure consisting of 1000x1000 points, therefore a cylindrical lens shape was used that could have defocus compensation applied in 2 dimensions. The test profile, shown in Figure 69, was created to have higher sag than the defocus obtained using the defocus test structures, so that the effect of extrapolating the intercept and slope values might be evaluated.

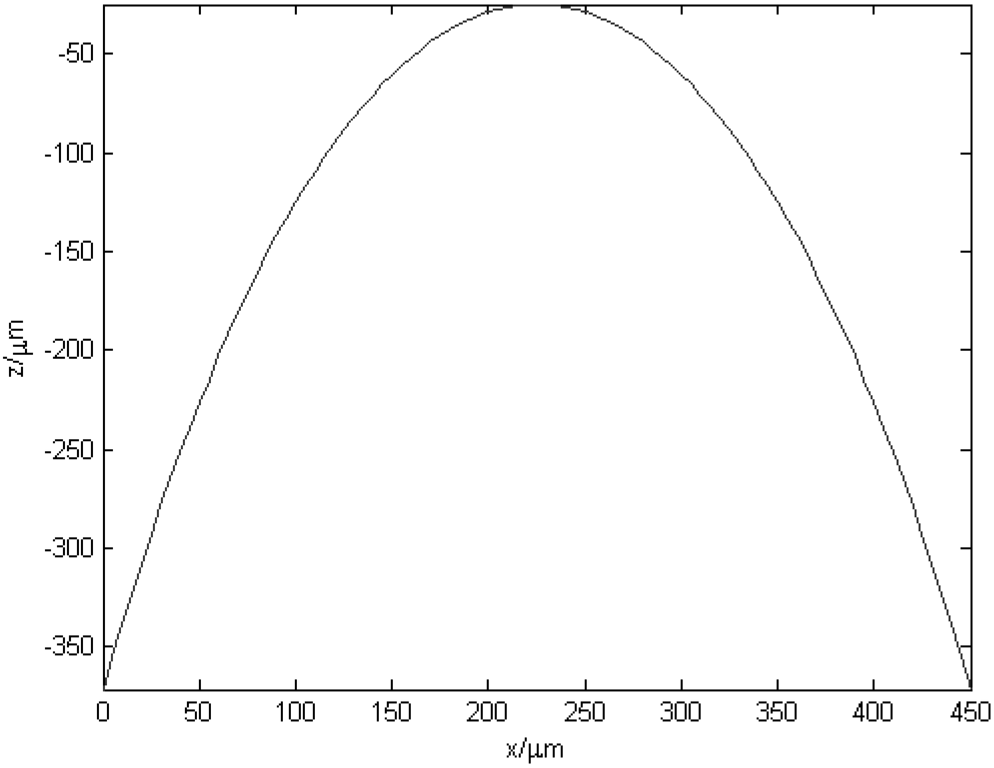

Figure 69: The shape of the test profile used to evaluate the defocus compensation algorithm.

For this test cylindrical lens profile to be fabricated on the laser micromachining system, 5 cutting passes would be required, with each pass having a maximum height of 5µm and a minimum height of 74µm giving a total sag of 345µm.

The energy maps that incorporate defocus compensation were generated using two variations: the first being a half-depth focal plane position shift, the energy maps of which are shown in Figure 70, that will minimise the change in defocus over the whole surface (as described in Figure 58), and the second being a full-depth focal plane position shift, the energy maps of which are shown in Figure 71, that should minimise the maximum pulse energy required in the deepest regions of the surface. As long as the number of passes chosen is appropriate for the surface sag, the full-depth focal plane position shift will also prevent the algorithm from requiring pulse energies that exceed 1 which are not achievable by the system. If the pulse energies required do exceed 1, either the focal plane position shift needs to be adjusted or the number of cut passes needs to be increased.

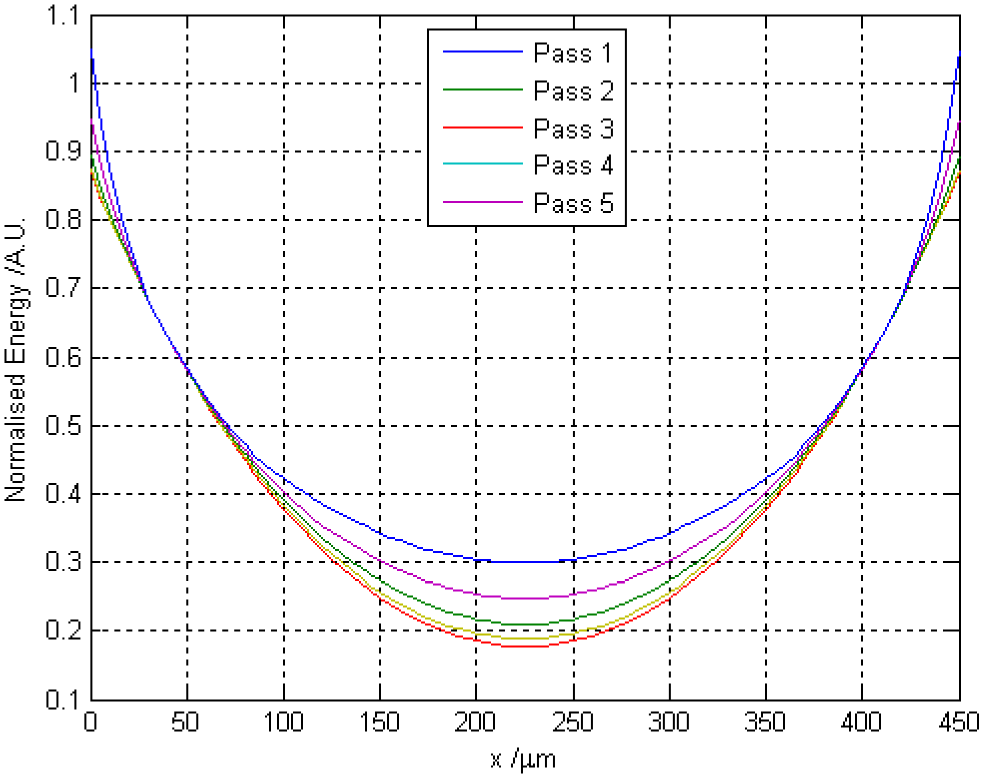

Figure 70: The energy map profiles of the 5 different passes generated using the defocus compensation algorithm when the focal plane position is kept at the median height between minimum and maximum height of the current cutting pass.

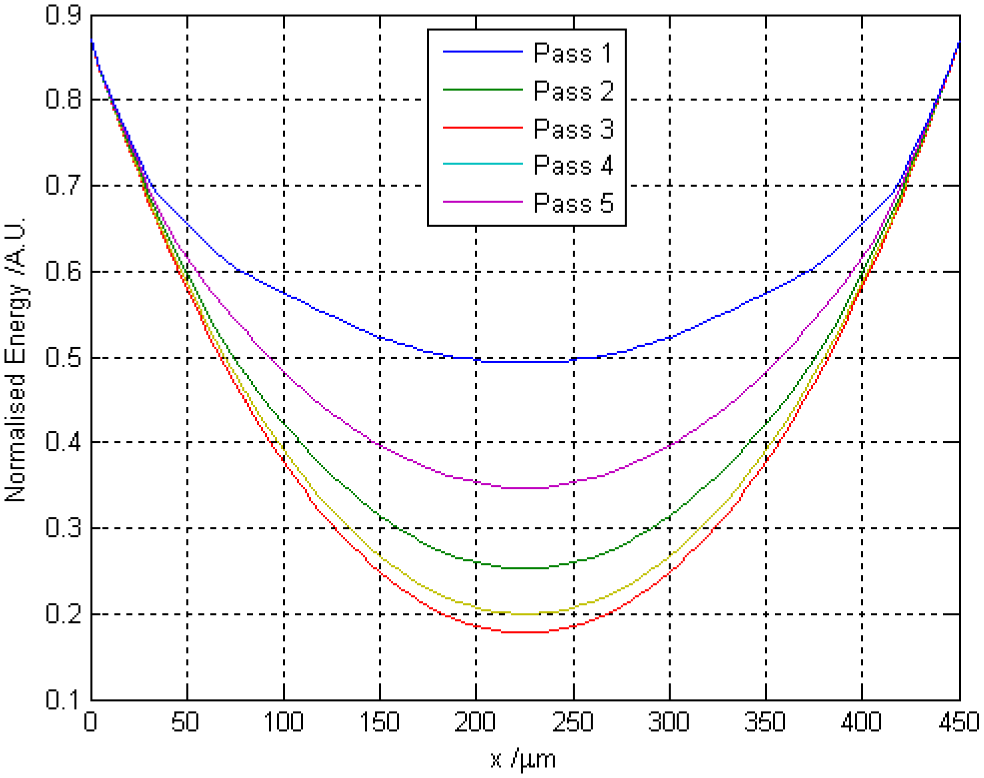

Figure 71: The energy map profiles of the 5 different passes generated using the defocus compensation algorithm when the focal plane position is kept at the minimum height of the current cutting pass.

The algorithm produces expected results, with the energy values per pass increasing as the pass number increases. The energy values of the half-depth focal shift profile have slightly exceeded 1 at the very edges of the final pass, which would slightly truncate the surface during the final pass. The energy values of the full-depth focal shift profile do not exceed 1, although the amount of defocus compensation required in the centre portion of the profile is more significant.

When using optics with laser sources that have a Gaussian intensity distribution the central portion of a lens element interacts with the highest intensity region of the laser beam. Although the correct cut depth may be achieved using defocus compensation, the spot radius may be significantly different thereby changing the surface quality after manufacture. Thus, using the algorithm with full-depth focal plane position shift may not produce the best optical result, as the high amount of compensation in the central portion of the lens will have the most significant impact on optical performance. An effective way of determining the optical effect of the defocus compensation is to analyse its effects on a laser beam by creating a real optic using the defocus compensation method.

3.4– Fast-Axis Collimator Array (FACA) development

The use of multi-pass cutting combined with the development of defocus compensation enabled work on optical structures that required higher sags than were previously obtainable. Due to the size and shape of a laser diode output facet, diffraction effects cause the output light to be much more divergent in one axis compared to the other because the aperture sizes are not the same. This highly divergent axis is known as the fast axis (FA) and, correspondingly, the less divergent axis is known as the slow axis (SA), see Figure 72 for an illustration of this explanation. One of the key optics used in many single laser diode and laser diode array systems is the Fast-Axis Collimator (FAC), which is a cylindrical lens that collimates the highly divergent output of a laser diode in its fast-axis.

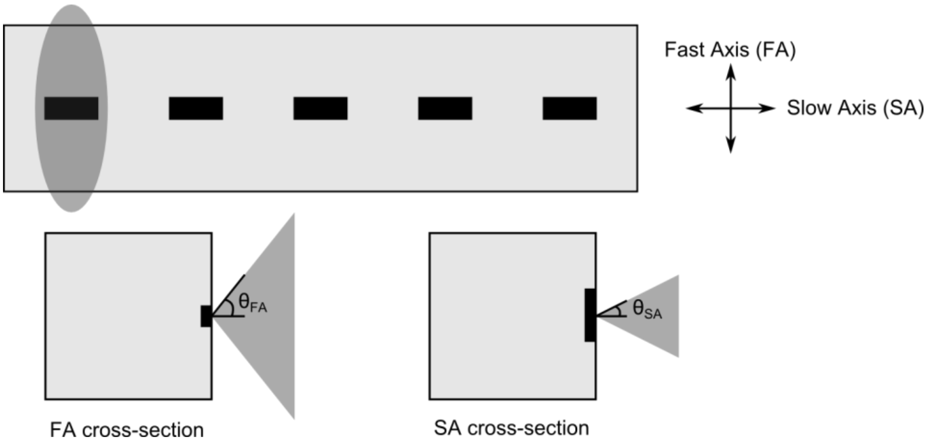

Figure 72: A diagram of an unlensed 5 emitter bar showing the output of a single emitter, with cross-sections in fast and slow axes (diagram not to scale).

Due to this difference in divergence between axes collimation of the light usually requires two separate cylindrical optics of different focal power, with axis of curvature oriented orthogonally to one another, to produce a nominally circular collimated beam (see Figure 73). Fittingly, these two optics are known as the fast axis collimator (FAC) and slow axis collimator (SAC). Because the FAC must collimate highly divergent light, not only must it be placed close to the facet of the emitter, but it must also have a short focal length to produce a collimated output.

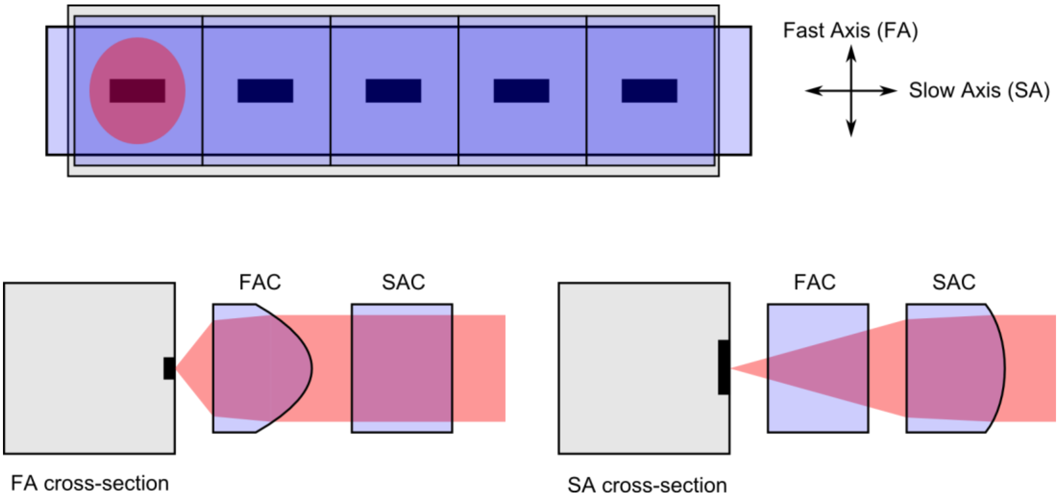

Figure 73: A diagram of a lensed 5 emitter laser diode bar showing the collimation of a nominally circular beam.

The sag of a plano-convex/concave spherical or cylindrical lens can be calculated using the formula:

$$S = R - \sqrt{R^2 - \frac{w^2}{4}} \tag{49}$$

where S is the lens sag, R is the radius of curvature and w is the required lens width. Extending this formula to incorporate focal length is a simple matter for a plano-convex/concave lens as $R = f(n-1)$:

Therefore: $$S = f(n-1) - \sqrt{f^2(n-1)^2 - \frac{w^2}{4}} \tag{50}$$

where f is the effective focal length and n is the refractive index of the lens at a given wavelength. The magnitude of the surface slope also determines not only the difficulty of manufacturing a surface but also whether the surface is measurable. The maximum surface slope of a spherical or cylindrical lens also needs to be determined:

$$\theta_{surface} = \frac{\pi}{2} - \cos^{-1}\left(\frac{w}{2f(n-1)}\right) \tag{51}$$

where $\theta_{surface}$ is the maximum slope of the surface relative to the unmachined surface in radians. Using equations (50) and (51), it can be seen that the sag and maximum surface slope required for a fused silica FAC (with refractive index of approximately 1.45) of focal length 1000µm and a width of 900µm, collimating a laser diode with a wavelength of 0.808µm, are about 400µm and 1.45rad respectively. Compare this to the sag and maximum surface slope required for a fused silica SAC of focal length 2mm and width of 500µm at the same wavelength which are about 35µm and 0.28rad, and it is clear that the major challenge in producing collimation optics using the PowerPhotonic fabrication process lies with the FAC.

The principal way FAC optics are produced by the optics industry without requiring very high sags or surface slopes is to use glasses with high indices of refraction. Glasses such as S-TIH53 have indices of refraction ≥1.8 at 0.808µm, which would take the sag required in the FAC mentioned above from 400µm to around 138µm. As discussed in Chapter 2, fused silica is the only material suitable for use with the PowerPhotonic fabrication technology at room temperature, so other solutions for FAC fabrication must be found that do not involve high refractive index materials. Fortunately, fused silica has preferable optical properties such as low dispersion and very low birefringence, as well as desirable physical characteristics, such as very high laser damage threshold, robustness and environmental stability, which makes it an excellent candidate for operation in high power laser diode systems.

FAC optics have always, until the work conducted during this thesis, been supplied as individual optical elements that are aligned to, and used with, single laser diodes or laser diode bars. However, alignment of individual FAC lenses can be a painstaking process in the production of laser diode bar arrays, also known as laser diode stacks. These laser diode stacks consist of laser bars, usually between 5 and 20, stacked on top of each other in the fast-axis direction to provide a compact diode source of high power. The alignment of individual FAC lenses on these bars presents a significant resource cost, as each FAC must be aligned to a bar and fixed in place, in addition there is a reduction in system robustness as each FAC is fixed with adhesive and individual glass tabs on the side of the laser diode stack. As the FAC and their accompanying fixtures have a minimum height, this also limits the minimum pitch of the laser diode bars within a stack.

During the course of this work a monolithic array of FAC lenses (FAC array or FACA) was envisioned that could be accurately fabricated and customised for an entire laser diode stack to minimise FAC alignment time, increase system robustness and minimise laser diode bar pitch as illustrated in Figure 74.

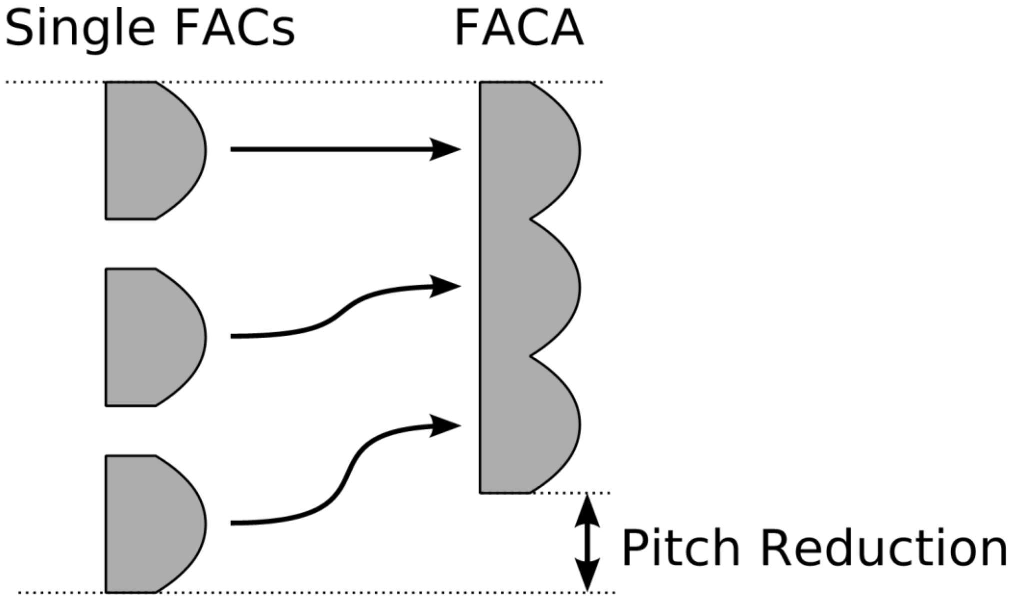

Figure 74: How using a FACA with a laser diode stack might provide a laser diode bar pitch reduction within the stack when compared to using single FAC elements.

This concept was proven using the multipass cutting approach and the effect of defocus compensation was evaluated optically and was subsequently patented and supplied to a customer in significant volumes.

3.4.1 – FACA design

The numerical aperture (NA) of an optic can give a good indication of the magnitude of spherical aberration present within the beam after passing through a spherical (or cylindrical) lens. As the NA increases the impact of spherical aberration increases which can affect transmission efficiency as well as image resolution; spherical lenses that have NA > 0.2 show noticeable spherical aberration. NA can be calculated precisely using the following equation:

$$NA = \sin\left(tan^{-1}\left(\frac{w}{2f}\right)\right) \qquad (52)$$

Using Equation (52) it can be seen that the FAC is a high NA optic. For example the previous case of f = 1mm and w = 0.9mm has NA = 0.41. Spherical aberration can be largely reduced in a lens by modifying the lens surface so that it is no longer spherical in shape. This is commonly done by describing the lens surface including a conic constant, which changes the lens shape to be parabolic or hyperbolic depending on the magnitude of the conic term. Zemax, a common optical design package that was used in the design of the FACA lenses, describes a conic modified spherical surface with the following equation:

$$z = \frac{cy^2}{1 + \sqrt{1 - (1 + k)c^2y^2}} \tag{53}$$

where z is the z-coordinate of the lens surface at y, c is the lens curvature, y is the y-coordinate of the lens surface relative to the lens centre, and k is the conic term. Using this equation a spherical, parabolic or hyperbolic lens shape can be defined using the different ranges of conic constant values shown in Table 7.

Conic constant value	**Lens shape**
k = 0	Spherical
-1 < k < 0	Parabolic
k ≤ -1	Hyperbolic

Table 7: The range of conic constant values and the lens shapes produced when using them.

For many moderate NA lens surfaces used to collimate divergent light or focus collimated light a conic constant of -0.5 provides a sufficient reduction in spherical aberration. However, lens shape can be further refined by adding higher order polynomial terms that modify the lens shape in more complex ways. Typically, these polynomial terms are used to refine the lens shape near the edge of the lens in order to nearly eliminate spherical aberration, and their coefficients are calculated by least-squares optimisation in Zemax based on an appropriately defined merit function. Zemax defines the equation for an asphere with even higher order polynomial terms (referred to within Zemax as an Even Asphere surface) as:

$$z = \frac{cy^2}{1 + \sqrt{1 - (1 + k)c^2y^2}} + \alpha_1 y^2 + \alpha_2 y^4 + \alpha_3 y^6 + \alpha_4 y^8 + \cdots \tag{54}$$

where the α_n terms are the polynomial coefficients.

As the PowerPhotonic fabrication process is a freeform one, complex refractive surfaces such as the Even Asphere can be as straightforward to manufacture as a simple spherical surface. Thus an optimised surface design from Zemax can be fabricated that includes not only conic terms but higher order polynomial terms. This means that despite the high sag requirement for a fused silica FAC lens, a lens can be designed such that the fabricated part still has good performance near the edge of the lens aperture. In fact, for large numerical aperture (NA) optics like FAC lenses, the use of a conic constant in order to minimise spherical aberration can actually reduce both the maximum sag and slope of the optics.

In order to illustrate the impact of spherical aberration when collimating a source with high NA, a simple Zemax system was constructed which could switch between using a spherical (referred to in Zemax as Standard) lens surface and Even Asphere surface. The source NA for this illustration was 0.625 with all distances and lens thicknesses fixed. The Standard surface was optimised in Zemax Sequential Mode using a least squares fit to minimise the RMS angle of incidence of the collimated rays at the image plane, with the only variable being radius of curvature of the lens, the resulting lens shape collimated transmitted rays poorly as shown in Figure 75.

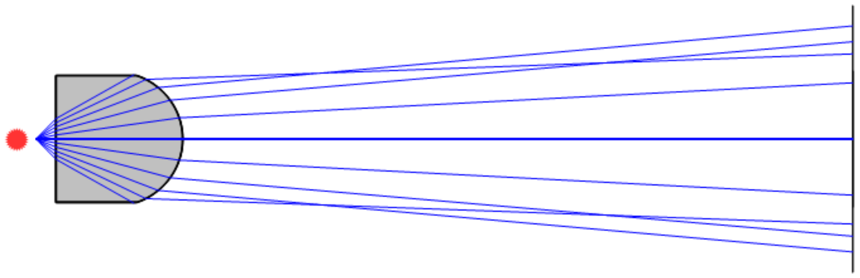

Figure 75: The effect of the Standard lens on the source after radius of curvature optimisation. The red dot indicates the diode source location while the blue lines show the rays that are traced through the system.

An Even Asphere surface was then used to collimate the beam, starting with the same radius of curvature found after optimisation of the Standard surface. The conic constant and polynomial coefficients $\alpha_3 - \alpha_6$ were set as variables and the least squares optimisation was conducted with the same merit function parameters as with the Standard surface, producing obviously superior collimation performance in Figure 76.

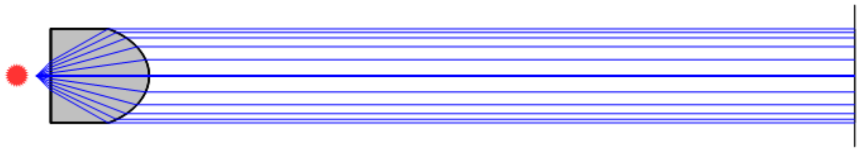

Figure 76: The effect of the Even Asphere lens on the source after optimisation of variables.

Using the Even Asphere surface and the same optimisation methodology detailed above, a FAC lens was designed according to a customer requirement shown in Table 8.

Wavelength (λ)	780nm
Refractive index (n) at λ	1.454
Focal length (f)	0.8mm
Lens width (w)	1mm
Desired angular aperture with maximised efficiency	4^{o} full angle

Table 8: A summary of the relevant customer parameters used to design a FAC lens.

Optimising the Even Asphere surface using these input parameters produced a surface design that had the attributes shown in Table 9.

Sag (S)	437.6μm
Approximate maximum slope ($\theta_{surface}$)	64°

Table 9: Surface values derived from the optimised FAC design.

This single element design was used to create a FACA surface in Matlab with a laser diode bar pitch of 1.2mm. The initial test piece consisted of two FAC elements with a half element at either end to determine the ability of the machining process to recreate the individual elements within an array, shown in Figure 77 and Figure 78.

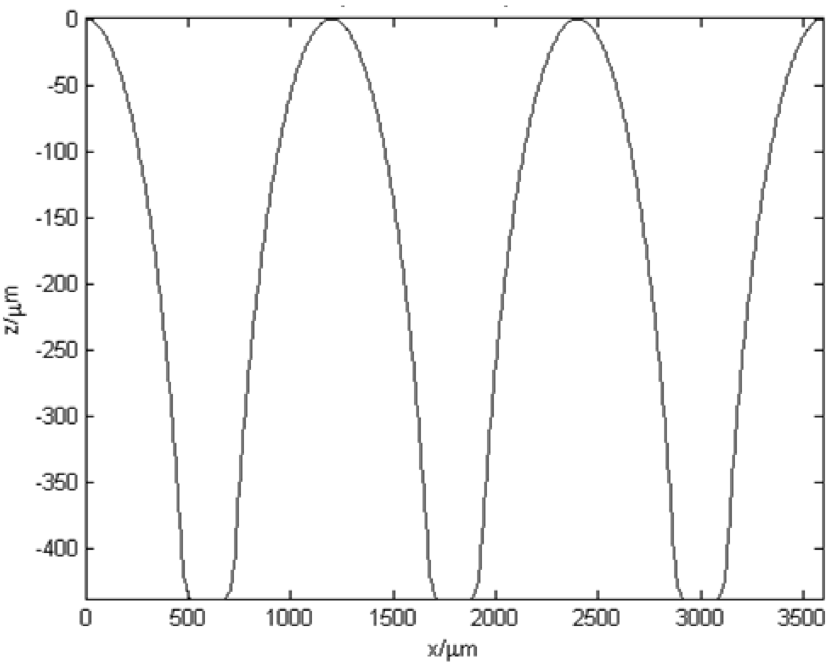

Figure 77: The profile in x of the FACA test structure.

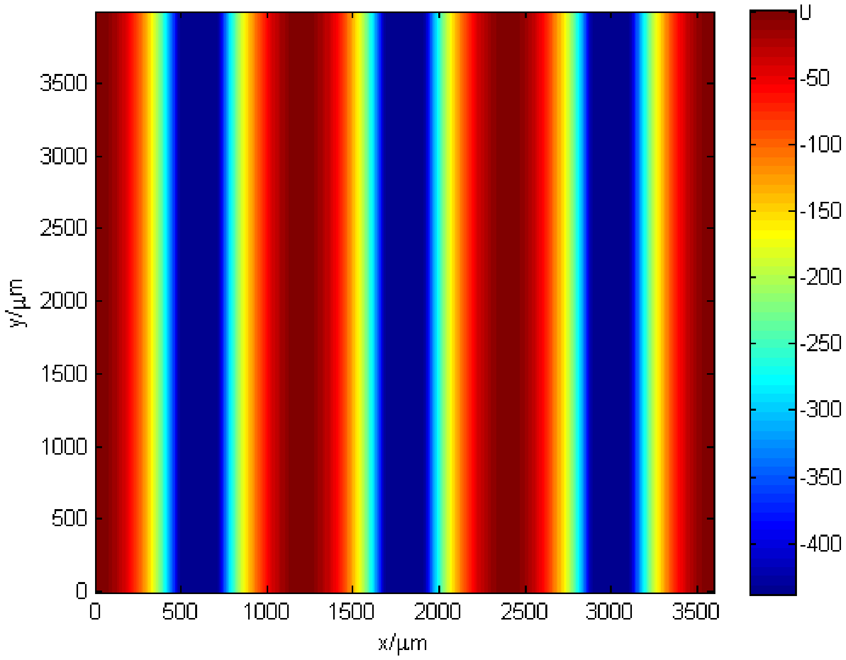

Figure 78: The surface map in height of the FACA test structure.

3.4.2 – FACA manufacture

The maximum cutting depth needed to also include the minimum cut depth per pass. The FAC was designed with a centre thickness of 0.945mm, thus the maximum depth of the fabricated structure was (1-0.945) + 0.4376 = 0.4926mm when starting with a 1mm thick substrate. Using the cut strategy that was previously used to determine the defocus compensation results, which has a maximum cut depth of 88µm, it can be seen that a minimum of 6 cut passes were required with a maximum per pass cut depth of 82.1µm or a normalised energy value of 0.933, the depth profile of each pass is sown in Figure 79.

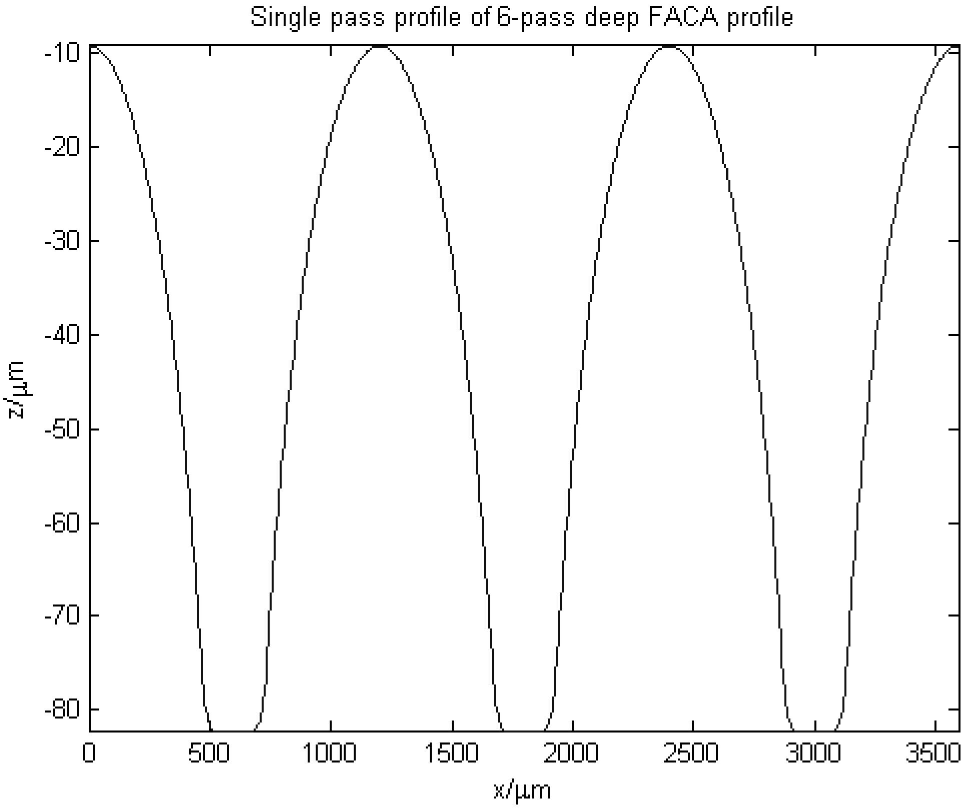

Figure 79: The height profile of each of the 6 passes required.

Due to the very high sag requirement, using the defocus compensation algorithm with a half-depth focal plane shift produced energy values that were well above energy values of 1 at the maximum depth regions of the lenses as shown in Figure 80. In order to use the half-depth focal plane shift while remaining manufacturable, the number of passes could be increased but this increases cutting time by about 17% per additional pass which was not acceptable when developing a product for volume manufacturing. Instead, the defocus compensation algorithm used a focal plane shift per pass that was equal to the maximum depth per pass: 82.1µm (the energy map profiles can be seen in Figure 81). This ensured that the maximum normalised pulse energy required on any pass would be limited to 0.933 and all passes would remain manufacturable.

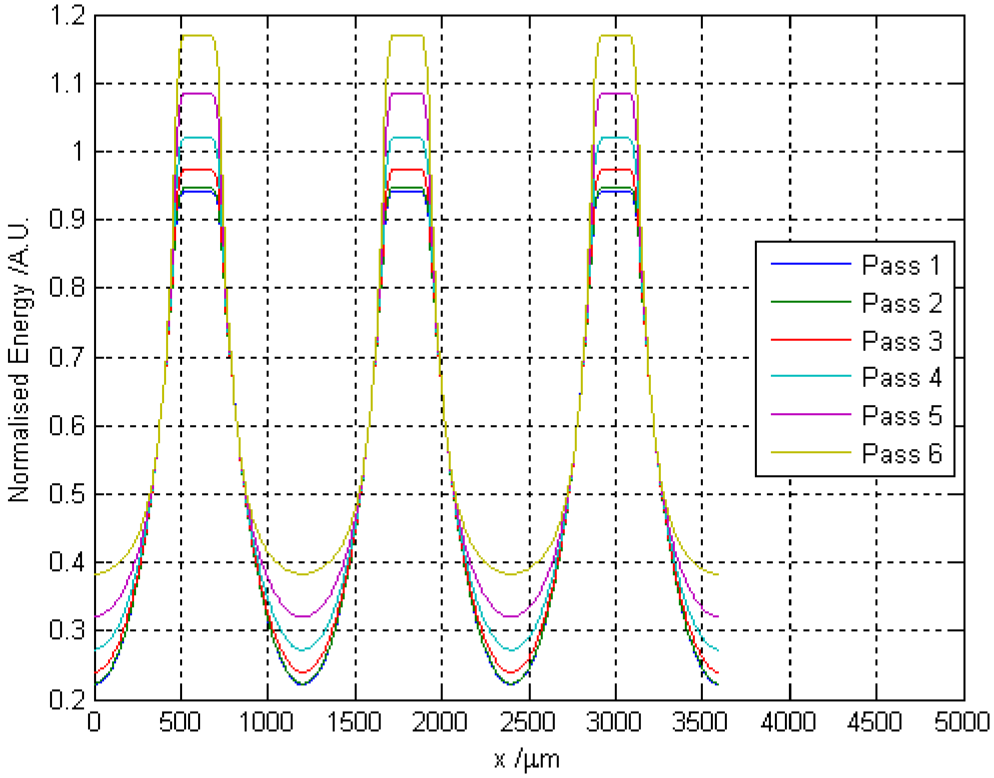

Figure 80: The energy profiles of each pass after application of the defocus compensation algorithm when the focal plane is shifted by half the maximum depth per pass.

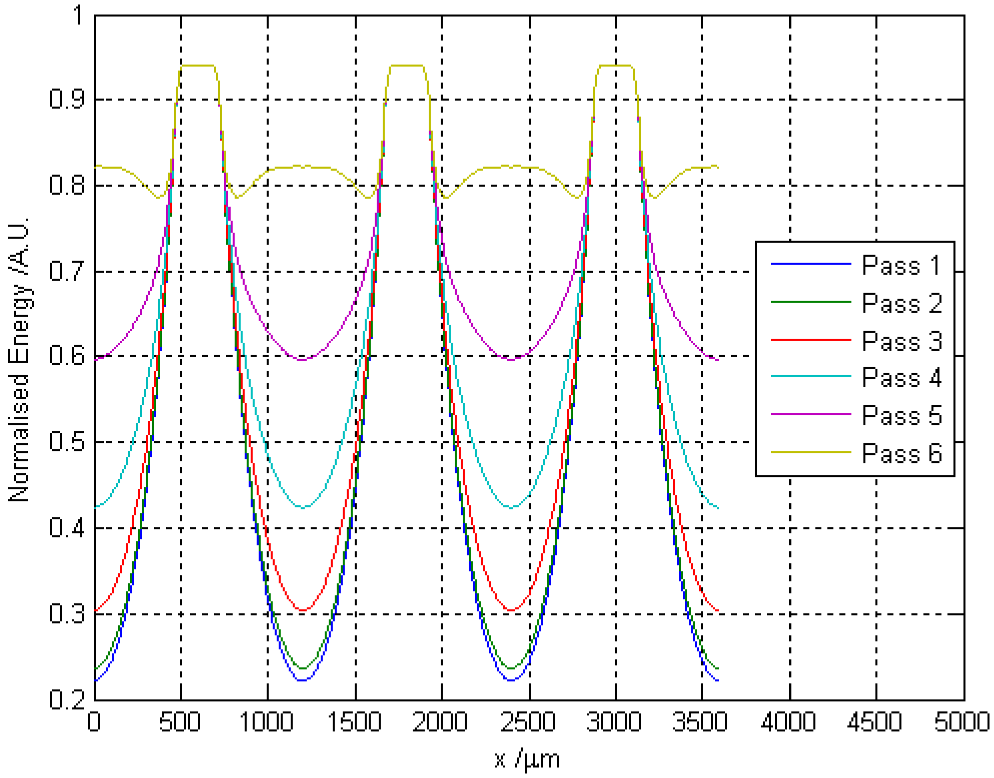

Figure 81: The energy profiles of each pass after application of the defocus compensation algorithm when the focal plane is shifted by the maximum depth per pass.

The 6-pass FACA design with defocus compensation using full depth focal plane shift was manufactured. It was quickly noted that there were two main issues with manufacturing these very deep and steep structures that needed to be dealt with:

1. During the cutting process it was known that small amounts of glass dust were produced when using single-pass cutting strategies. Due to the much larger volumes of glass being removed in this high sag optic, the amount of dust present on the surface of the optic after manufacture was significant. The dust was concentrated particularly in the deep regions in between lenses. It was unknown what effect this dust would have in a multi-pass cutting strategy, especially on the later passes where dust build-up is considerable. Due to the uncertainty of the effect of this dust on the lens form the test structure was washed in an ultrasonic bath for 10 minutes at the end of every cutting pass to remove any loose dust. The substrate was then carefully realigned to 4 fiducial alignment marks using a machine vision system; it was expected that the realignment error in each pass was less than 5μm in x and y. This procedure is described in further detail in Chapter 4.

2. The smoothing process was highly variable over the surface of the FACA. The thermal conditions at the top and bottom of the lenses when illuminated by the smoothing laser were significantly different, with the lens apices requiring much lower energy density in order to achieve approximately the same smoothing as the cusp region in between the lenses. Smoothing with a uniform laser beam power over the whole surface resulted in an unacceptably high amount of material removal from the lens apex region and almost no smoothing in the cusp region. This was solved by precisely aligning the spot location to the FACA structure and varying both the laser beam power and spot radius on the surface depending on the part of the FACA on which the beam was incident. Although this work was fundamental to the production of FACAs, a detailed description of it is outwith the scope of this thesis.

3.4.3 – Surface metrology and optical test

In order to evaluate the effect of the defocus compensation two FACA test structures were cut, one with full-depth focal plane shift defocus compensation applied and one without. However, measurement of the FACA surfaces to determine their accuracy after manufacture proved to be extremely challenging. The STIL CHR-350 chromatic confocal probe can reliably measure surface angles up to 22°, but above this surface angle the accuracy of any measurements taken is not specified and often returned either an erroneous or null data value. As the lens apices and cusp regions were expected to be below this angle, the probe was used to measure the surface to obtain an indication of the total sag achieved during manufacture. The total measurement range of this probe was 350µm but it had previously been found that near the edge of this range the data was less accurate. Therefore the central 250µm region of the probe range was used to scan the top region of the FACA test structure without defocus compensation, the scan data with any null or erroneous data removed is shown in Figure 82.

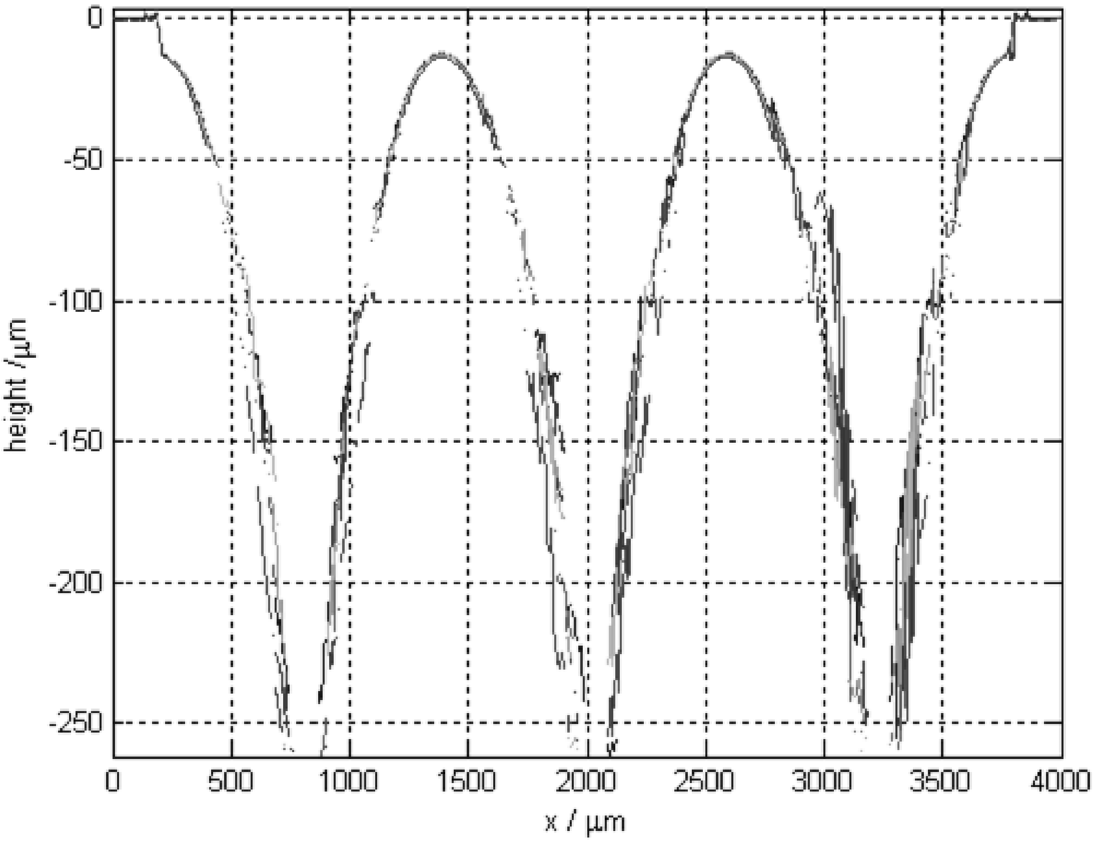

Figure 82: A number of profile scans taken of the top region of the FACA test structure.

The probe was then moved 250µm closer to the substrate and the same region was scanned again in order to obtain data from the bottom of the lenses in the “cusp” region, shown in Figure 83.

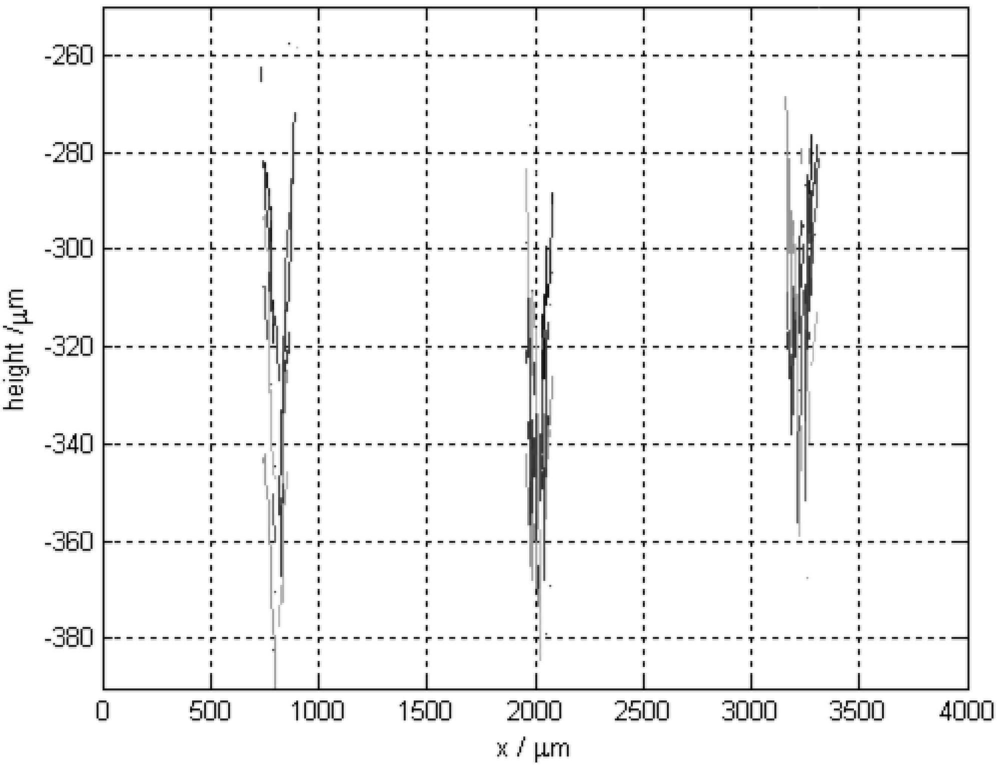

Figure 83: A number of profile scans taken from the bottom region of the FACA test structure.

Given the known 250µm offset between profile scans and the fact that the two scans were laterally aligned, the two scans were stitched together to find a total profile shown in Figure 84.

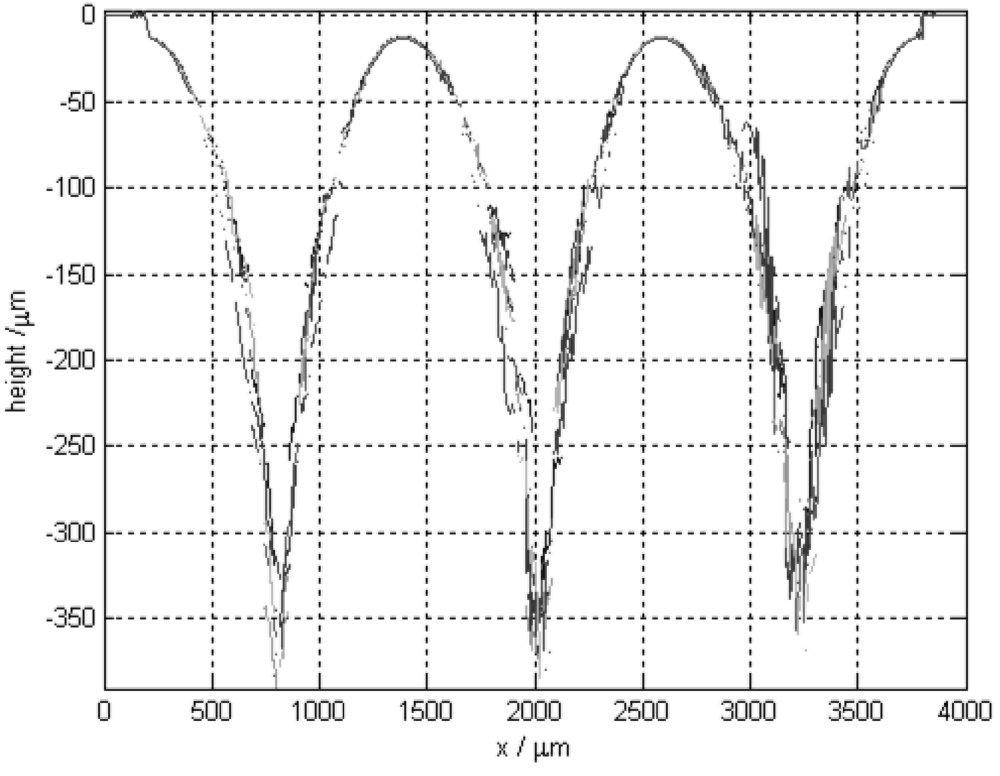

Figure 84: The stitched profile scans found by adding the profiles of the top region scan, shown in Figure 82, and the bottom region scan, shown in Figure 83.

In an attempt to reduce the noise of the measurements to estimate the surface shape of the FACA, the individual profile scans were averaged, shown in Figure 85.

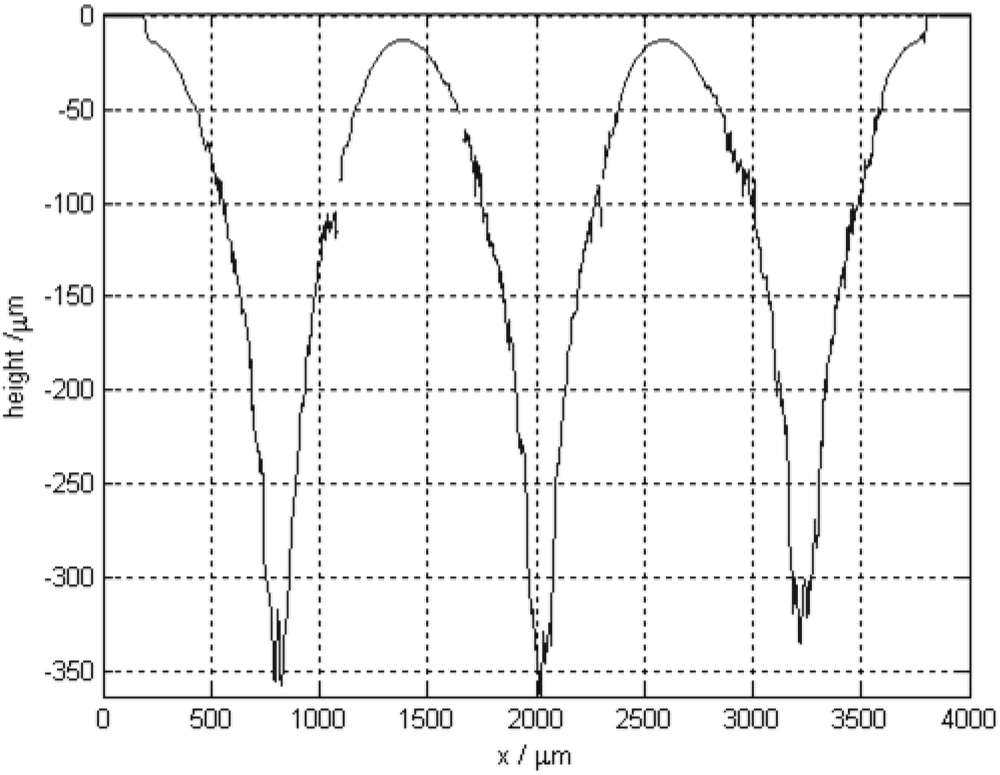

Figure 85: The profile of the FACA, found by taking the mean of each scanned profile after stitching.

The low slope of the lens apices should give accurate results relative to the uncut surface located at 0µm. It can be seen in Figure 85 that they were located at around 20µm from the uncut surface instead of the 55µm expected, indicating that the lack of defocus compensation may have had a significant impact on the lens profile. It was expected that the sag of the optic would be within a few 10s of micrometres of the design, however the probe data shows that the total depth is around 150µm less than designed which called in to question the reliability of the probe data in the FACA cusp regions.

In order to observe the lens profile more reliably, a diamond tipped cleaving tool was used to slice the FACA test structure orthogonal to the direction of the cylinder axis, and positioned end on in a microscope to view the profile. This allowed for direct imaging of the FACA shape and approximate measurements of its sag, as shown in Figure 86.

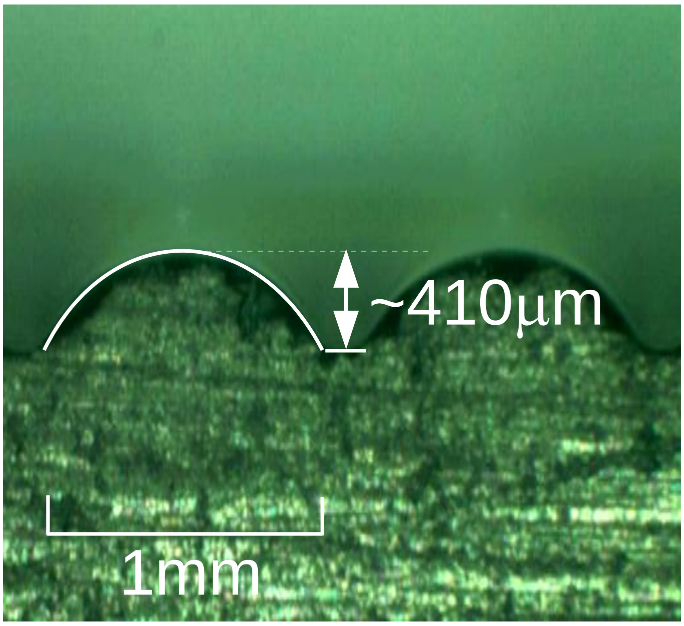

Figure 86: A micrograph of a FACA test structure showing the profile of a cleaved piece. The white lines highlight the lens shape as well as the position of the lens cusp.

This showed that the lens sag was approximately 410µm, with an expected error on this measurement of ±10µm. It also suggests that the data recorded using the CHR-350 was unreliable in the cusp regions, this may be because the cusp regions were poorly smoothed and/or the cone of light used by the chromatic confocal probe was incident upon the sidewalls of the FAC lenses when scanning the cusps which gave an erroneous depth result. In order to further evaluate the difference between the FACA test structures, the cusp regions were compared (in Figure 87 and Figure 88) as these were the only regions that could be effectively examined manually using the microscope.

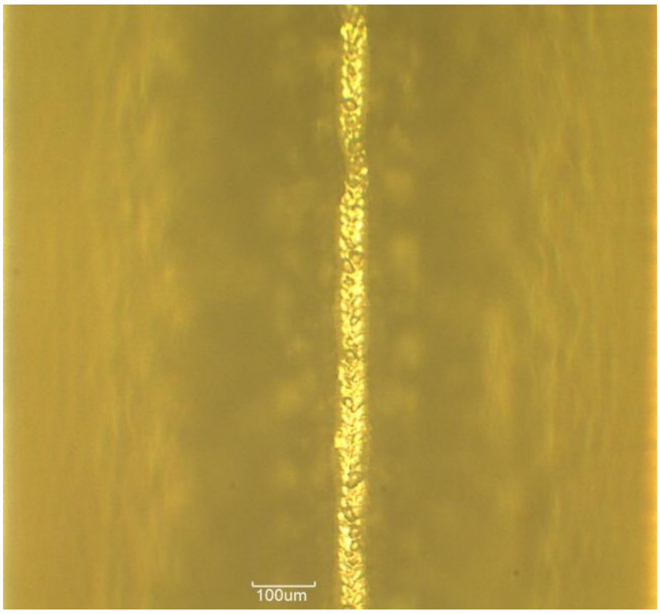

Figure 87: A micrograph of the cusp region of the FACA without defocus compensation.

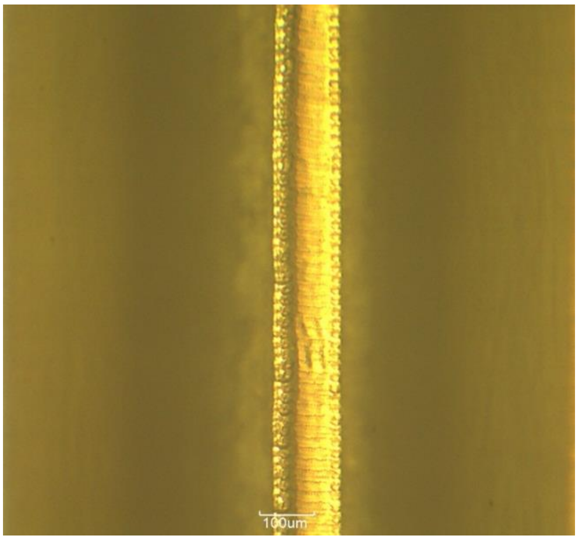

Figure 88: A micrograph of the cusp region of the FACA that used full-depth focal plane shift defocus compensation.

As expected, the cusp region of the FACA with full-depth focal plane shift defocus compensation shows a much more uniform result than the cusp region of the FACA without defocus compensation. The cusp region of the defocus compensated FACA (Figure 88) is also much closer to the design width of 200µm. In contrast the FACA without defocus compensation (Figure 87) shows variable surface quality along the cusp as well as some unsmoothed surface features just outside of the cusp region on the lens surface.

In order to determine and compare the optical performance of the FACA lenses with and without defocus compensation, they were used to collimate a single laser diode and the output was imaged using a 1m focal length field lens Spiricon SP503U camera. With this setup, illustrated in Figure 89, image distances in millimetres are equivalent to angular far-field image distances in milliradians, which were subsequently converted to degrees to display results.

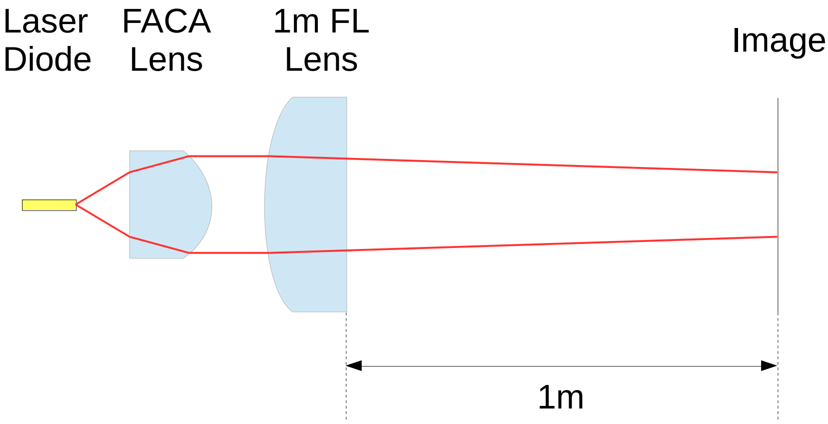

Figure 89: Optical test setup to evaluate far-field produced by the FACA lenses.

The FACA lenses were positioned in front of the laser diode using an assembly of Thorlabs PT3/M 3-axis translation stage and Elliot Scientific MDE185 pitch and yaw stages that could both translate in the x, y and z axes as well as allow for rotation about the y and z axes. Given that the lens length along the beam slow-axis was much longer than the size of the beam in this axis, alignment along this axis was not critical.

The FACA lens was aligned in the y-axis such that the beam centroid was in the same image location as the centroid of the unlensed diode. The alignment in z was determined by finding the z-position of the FACA lens that maximised the total power delivered in to a 4^o full angle aperture. Rotational orientations were made by observation of the image as lens rotation about the x-axis produces noticeable asymmetry in the fast-axis of the beam and presents as a skewed profile. Rotation about the y-axis produces a beam that varies in width along its length in the slow axis, although as the beam is small in the slow axis at the FACA plane this alignment is not critical. Rotation about the z-axis produces an asymmetry along the slow axis of the beam which is obvious in the image and simple to eliminate. Once a single FACA lens from each test structure was aligned to the laser diode, the Spiricon camera was used to record an image of the far-field. These images are found in Figure 90 and Figure 91.

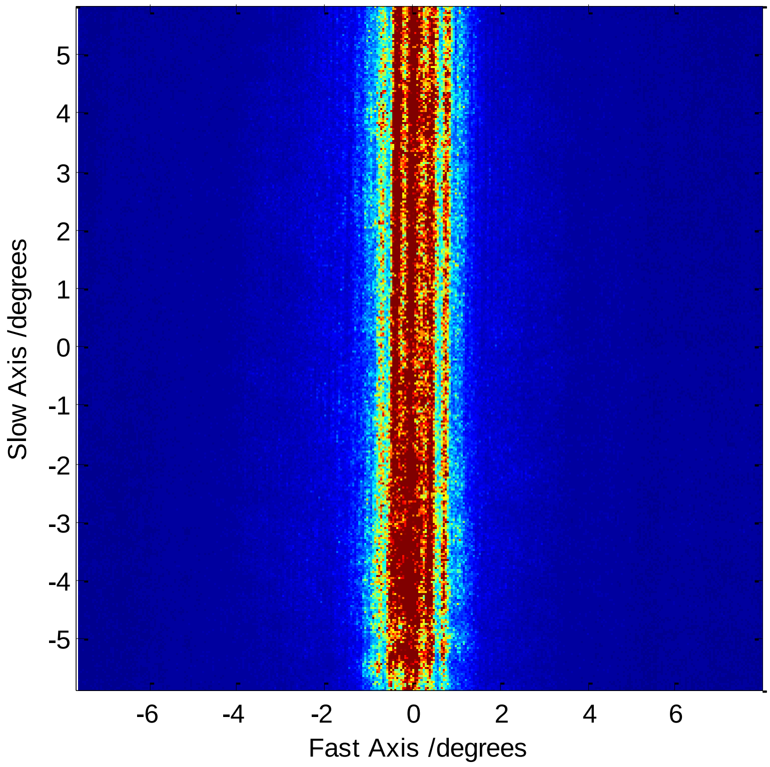

Figure 90: A far-field image of the laser diode beam after collimation with the FACA fabricated without defocus compensation.

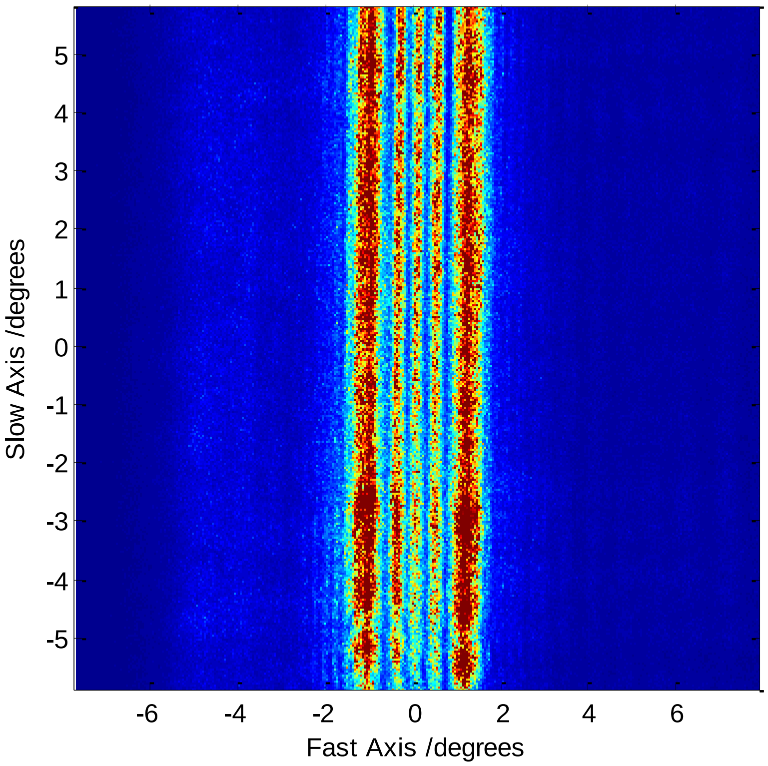

Figure 91: A far-field image of the laser diode beam after collimation with the FACA fabricated with defocus compensation.

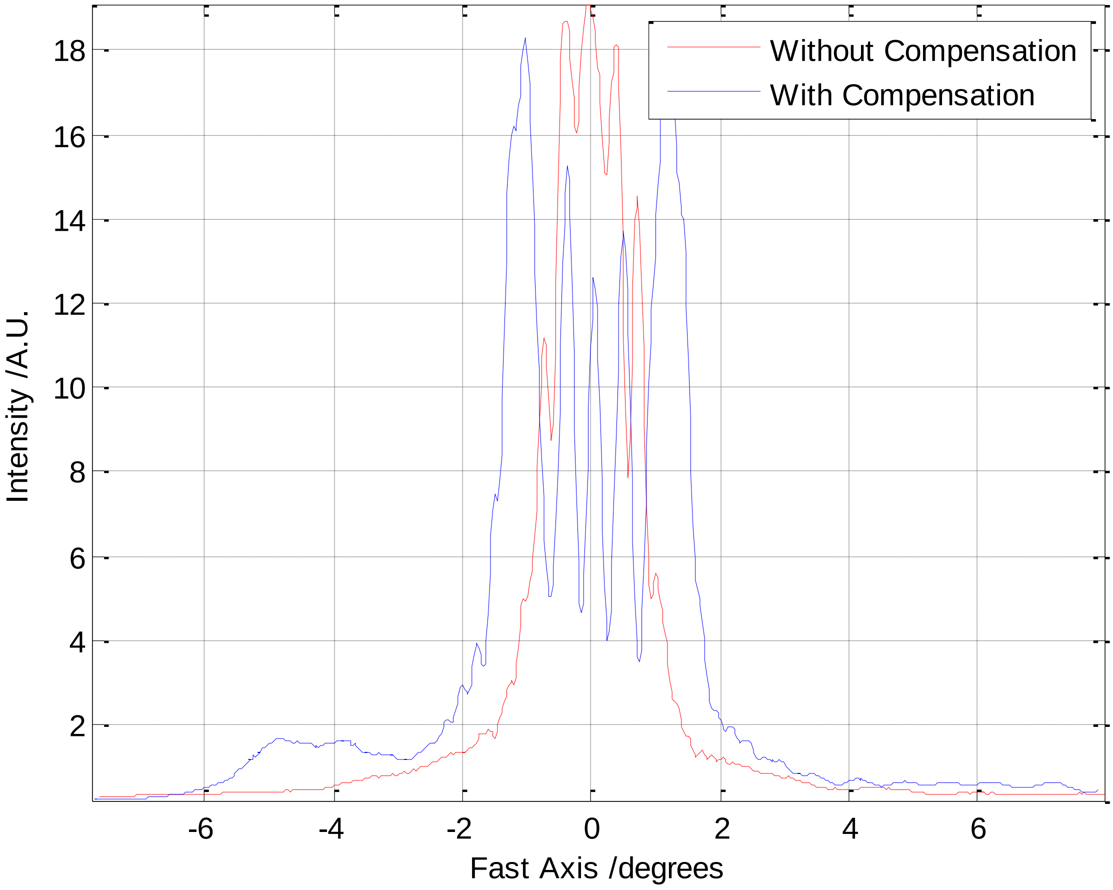

Figure 92: A comparison of the mean profiles of the intensity distributions from the laser when lensed with the two different FACA lenses.

The expected shape of the fast-axis intensity distribution after collimation using standard FAC lenses is very close to Gaussian. As can be seen in Figure 92, the mean profile shape of the FACA lens without defocus compensation is closer to the expected shape as it has a symmetrical single high intensity peak. The FACA lens with defocus compensation not only has two main peaks along with smaller central peaks but has an asymmetry in the higher angle regions of the beam, noticeably a peak at around -4^{o} to -5^{o}. However, calculation of the cumulative integrated power curves, as evidenced in Figure 93, shows the FACA lens with defocus compensation generates higher total delivered efficiency.

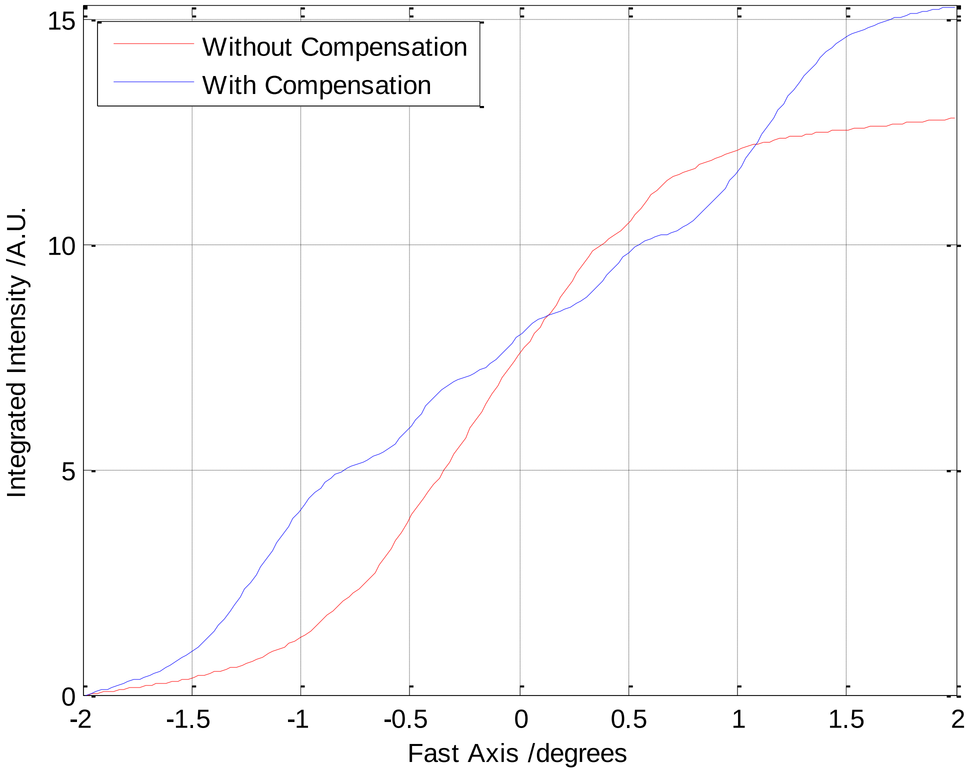

Figure 93: A comparison of the integrated power curves calculated from the mean profiles of the intensity distributions from the laser when lensed with the two different FACA lenses.

Examination of the total power delivered in to the 4^{o} degree full angle aperture shows that the FACA lens with defocus compensation transmits about 20% higher power into this angle than the FACA lens without defocus compensation. So although the shape of the intensity distribution is significantly different from the ideal Gaussian shape when using a diffraction limited FAC lens, the FACA lens manufactured using defocus compensation was more efficient than the FACA lens manufactured without defocus compensation. Due to the lack of large peaks in the higher angle part of the beam when lensed with the FACA lens without defocus compensation, it is likely that this efficiency difference is due to insufficient smoothing of portions of the lens surface which has resulted in a fraction beam power being scattered at higher angles than those measured.

The peaks in the defocus compensated far-field can be used to calculate the spatial frequency that is required to generate them, potentially giving insight into the surface profile using the equation relating diffraction angle to spatial period of a grating:

$$\Lambda = \frac{m\lambda}{\sin(\theta)} \tag{55}$$

where Λ is the grating spatial period, m is the diffraction order and θ is the diffraction angle in the far-field. In this case m is expected to be 1. The largest peaks are located at θ = 19.2mrad which corresponds to a spatial period of 40.6μm using the above equation. This period does not correspond to any aspect of the cutting or smoothing strategies such as line-line distance in the step direction during cutting or smoothing, and is an order of magnitude larger than any expected mechanical errors such as stage motion errors or misalignment errors after replacement following the cleaning step in between cutting passes. It is likely that the larger spot radius incident upon the apex of the lens during cutting with full-depth focal plane shift defocus compensation introduce different spatial frequencies than those that are expected; however more work is required to analyse this in detail.

Comparing the performance of both of these FAC lenses to a standard high refractive index lens, for example the Ingeneric FAC-08-900, shows that the far-field divergence is significantly higher. According to the Ingeneric FAC datasheet [32], the standard version of this lens achieves 75% enclosed power within a full angle of 1.6mrad, or 0.09°.

3.5 – Summary and conclusions

This chapter presents a number of seemingly disparate analyses, however they all stem from the same requirement of increasing the efficiency of the cutting process and enabling the development of new products. Examination of the potential raster patterns available for use in cutting, highlighted the unexpected effect of asymmetry in fabricated structures when the laser beam is not orthogonal to the surface of the substrate. The test structure and analysis methodology defined in this chapter continues to be used at PowerPhotonic in order to periodically confirm laser beam orthogonality with a good level of accuracy.

Using defocus compensation did produce a more efficient FACA lens than a FACA produced without defocus compensation, although it also introduced new process conditions that require further investigation in order to be fully utilised. It is likely that full-depth focal plane shift is not ideal even though it may minimise the number of passes as the level of defocus, and thus the variation from standard processing, is maximised at the lens apex and this is generally where the highest intensity portion of a transmitted laser beam is located.

The work on FACA design and manufacture was carried out on an almost exclusively individual basis within the scope of this project and culminated in the granting of a patent in the US, UK and EU [33] [34] [35], along with sales of custom FACAs in quantities that were materially significant to PowerPhotonic. Based heavily on the work presented here, development of FACAs continued, resulting in the design and fabrication of bi-convex FACAs which reduced the sag requirement of either surface compared to a plano-convex FACA and eliminated the need for defocus compensation [36]. Bi-convex FACAs now form a core part of PowerPhotonic sales and are offered as a standard product.

Chapter 4 – Extraction of silica dust during cutting

4.1 – Introduction

The high sag multi-pass cutting approach described in the FACA manufacture subsection of Chapter 3 highlighted a potentially important mechanism that had not been well characterised previously when using this particular fabrication method, namely the production and potential redeposition of silica dust during the cutting process. Examination of a structure after a single pass clearly shows a white dust covering anisotropically both the surface of the structure and an area of the unmachined substrate outside the cut structure. The ability of the multi-pass cutting process to remove a greater volume than that achievable by the single pass process likely increases the amount of dust produced per unit area machined. It is unclear what the effect of this dust would be on a subsequent cutting laser pass if left *in situ*, particularly given the anisotropic distribution over the surface. Absorption of a fraction of the laser pulse energy by the dust would reduce the accuracy of the machined surface by reducing the conformity of the process to the empirical calibration used to control pulse energy. An isotropically distributed layer of dust would thus manifest as a simple depth scaling error of the entire surface whereas an anisotropic distribution would be observed as a more complex surface form error.

The likely increase in dust volume also introduces health and safety concerns for the personnel in regular contact with the laser machining system. It is well known that crystalline silica dust, produced when processing various natural and synthetic materials such as sandstone and concrete, can produce debilitating lung diseases such as silicosis and lung cancer [37]. The silica exists in a crystalline form within the substrate before being liberated as a dust by certain processes such as sanding or grinding. The fused silica used by PowerPhotonic, Corning 7980, is entirely amorphous [38] so there is no possibility of liberating crystalline silica during processing. Studies that analysed silica dust produced using flame hydrolysis, which is similar to the production of silica dust using laser ablation, showed that the resulting silica dust consists of small spheres that are almost totally amorphous [39]. Medical trials conducted on rats showed that, while there was significant and long term impact on rat health when exposed to crystalline silica dust, amorphous silica exposure produced little impact and was reversible [40]. However, there have been reported cases of silicosis in humans exposed to amorphous silica that was ostensibly not contaminated with crystalline silica [41]. In order to mitigate the health and safety risk associated with inhalation of silica dust particles, it is highly desirable to have an extraction system that removes and collects as much of the dust as possible.

This project aims to produce a system that allows for both in-process dust extraction to minimise potential surface form errors due to unintended laser pulse absorption, and to eliminate the potential health and safety risk associated with the production of silica dust particles.

4.1 – Dust composition

The loose white dust produced during laser cutting is highly likely to be composed exclusively from silica (SiO_2) particulate, instead of the two other binary silicon oxides that have been documented: silicon monoxide (SiO) and silicon sesquioxide (Si_2O_3). SiO and Si_2O_3 are both metastable compounds, meaning they may spontaneously disproportionate to Si + SiO_2, and are rather challenging to reliably produce in anything other than thin films [42]. SiO differs visibly from the dust seen during laser machining as it is black in colour, and its metastable state means that it readily oxidises at room temperature to give SiO_2. Si_2O_3 is normally synthesised via various routes chemically [43] but has also been produced as smoke-sized particulates by evaporating solid SiO under high vacuum [44]. However, Si_2O_3 is the least stable of the binary silicon oxides and also readily oxidises to SiO_2 at room temperature.

The particles may be composed of a different sizes and shapes depending on their mechanism of generation.

- Condensation of airborne gasses. SiO gas produced during ablation which oxidises in air to produce SiO_2, or SiO_2 gas evaporated from the substrate during ablation, precipitate out as nanoparticles during cooling. Depending on their temperature and density in air, these nanoparticles may immediately settle on the substrate surface or agglomerate to form larger particles before settling.

- Ejection of solid material. SiO_2 particles are ejected from the substrate by the reaction of the ablation process. Given sufficient pulse energy material can be ejected while it is still molten, producing fibre-shaped particles with lengths of up to 1mm [1]. This fibre-creation regime is avoided as it not only produces undesirably large dust particles, but ablation craters with a greater amount of edge structure than normal ablation craters which manifest as higher surface noise in the final surface.

The size distribution of particles, and their shape, should give some indication as to the dominant particle generation method. Spherical or globular particles are likely to be produced by condensation of airborne gases (with size determining whether the particles were in a hot, dense region of the ablation cloud) whereas elongated blobs and strings are likely to be produced by the force of the ablation reaction.

4.2 – Dust removal investigation

For single cutting pass structures, the dust produced during the cutting process is removed before undergoing the smoothing process by washing the machined substrate in warm water and detergent in an ultrasonic bath. This was attempted for multi-pass structures by pausing at the end of each pass and washing the substrate. This method had several major drawbacks that ultimately made it nonviable, especially for volume production of multi-pass structures:

- Pausing the cut job and removing the substrate from the rig for washing is a manual process that must be done for each substrate, meaning a long cut job cannot be left unsupervised and production time is wasted.
- Alignment of the substrate to its previous position after washing proved to be a delicate manual task, using further production time and requiring an engineer rather than a production technician.
- It was observed that multiple washings in the ultrasonic bath occasionally produced cracks and fractures in the substrate, causing the substrate to be scrapped.

After some experimentation into alternative dust removal techniques, it was found that brushing the structure with a stiff bristled brush removed a large proportion of the dust (although not as thoroughly as ultrasonic cleaning). A brush was used to manually scrub the surface of a substrate in between passes, allowing the substrate to be left in place, but it was found that not only did this contaminate surrounding substrates but misalignment remained an issue due to the vigorous scrubbing required.

In an attempt to remove the manual brushing step so that the laser machining could take place without regular intervention, the brush was fixed in position near the substrate stages. A length of 6mm copper pipe was connected to the inlet side of a rotary vane pump that had a rated displacement of 60Lmin^{-1}, creating a flow of air into the tube that could carry with it some or all of the dust being released by scrubbing, and software was written which ordered the stages to move the current substrate under the brush and scrub the surface after each cutting pass. While this did remove the manual brushing step as well as the contamination of surrounding substrates, was not particularly effective at dislodging the dust which was probably due to the limited downwards force exerted on the substrate by the brush using this method.

4.2.1 – Initial gas extraction method

The rotary vane pump was used to test for extraction of the dust as the cutting was taking place and dust was being generated, by placing a 4mm diameter copper pipe attached to the inlet side of the rotary vane pump close to the cutting. Three different inlet designs were tried to determine whether there was an optimal geometry: round, rectangular with dimensions 3mm x 2mm, and rectangular with dimensions 5mm x 1mm. However, none of these geometries in this approach appeared to have any effect on the volume or spatial distribution of dust generated, likely because the copper pipe could not be placed very close to the ablation zone without partially aperturing the laser beam which converges at a $\frac{1}{e^2}$ half angle of about 19^o.

This gas extraction method was improved by fabricating an extraction head designed to allow for extraction of particulates and gases uniformly around the cutting region without aperturing the laser beam. Test pieces were made, illustrated in Figure 94, by soldering brass sheet into three-dimensional structures in order to evaluate whether this was a viable method for investigation.

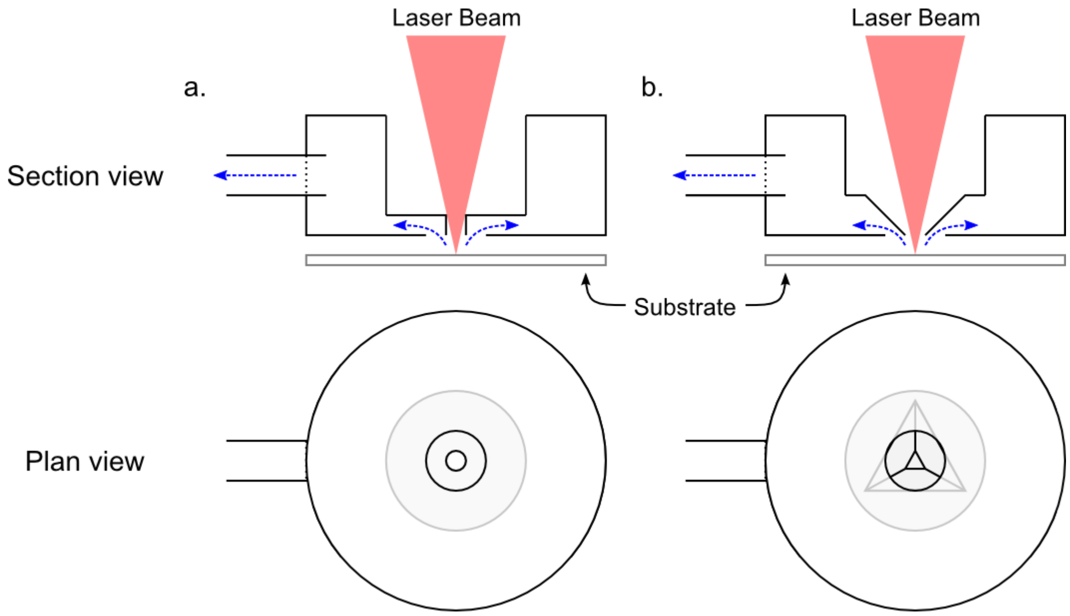

Figure 94: Section and plan views of the proof of concept design for a gas extraction head. a. shows the first design b. shows an updated version of this design. The dotted blue arrows indicate expected airflow when suction is applied.

The first test piece (Figure 94a) was made using a number of cylinders, with the top of the small cylinder slightly larger than the calculated beam diameter at this z position. The intention was to create a void within the extraction head that, when connected to the rotary vane pump, generates an annulus of air physically separated from the laser beam by the upper housing, and allows the extraction head to act as a removable free-standing piece when required. The pressure in the void is lower than atmospheric which causes air to flow in, carrying with it silica dust produced during the cutting process.

The extraction head was suspended with its flat underside 3mm above a substrate, aligned so that the cutting laser beam passed through its centre, and connected to the inlet side of the rotary vane pump via several meters of 8mm diameter tubing. The rotary vane pump came equipped with cotton filters on both the inlet and outlet side of the pump chamber, rated for a minimum particulate size of 20µm. A flow rate indicator, Key Instruments MR3A18BVBN, with a measurement range of 10-100 Lmin^{-1}was positioned between the extraction head and rotary vane pump and showed a maximum attainable flow rate near the extraction head of approximately 50 Lmin^{-1}. The flow meter included a manually adjustable control valve to adjust the flow rate through the system. The diagrammatical representation of this system is shown in Figure 95.

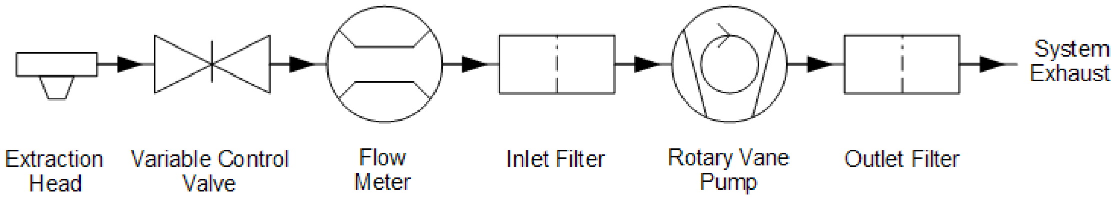

Figure 95: A system diagram showing the serial order of the gas extraction system. The arrows indicate the direction of airflow when the rotary vane pump is in operation.

With the extraction head *in situ*, a flat bottomed square test structure was cut which had previously been shown to produce visible silica dust when observed both by eye and under a microscope. After cutting the structure, the optic was examined to subjectively determine the effect of the suction device on the silica dust re-deposition.

The initial design proved challenging not only to align successfully to the laser and prevent aperturing of the beam during the cutting process, but to maintain alignment during cutting as the mount was not rigid enough to maintain alignment when small external knocks or bumps occurred (Figure 96). This caused the alignment to vary during the cutting of test pattern, intermittently aperturing the beam.

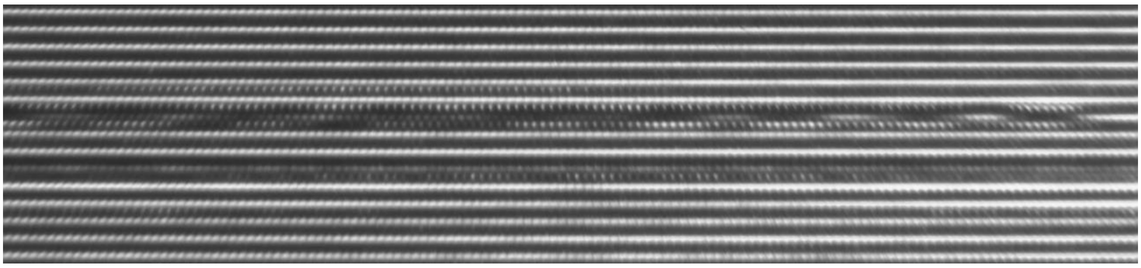

Figure 96: A micrograph of a cut pattern showing how a sharp but low amplitude impulse caused the extraction head to vibrate and aperture the laser beam.

This test piece was modified to replace the small cylinder with a trigonal pyramid which would allow for a greater range of freedom of the beam within the aperture without the beam being clipped (Figure 94b). The trigonal pyramidal shape was used due to the difficulty in accurately hand-making a small truncated cone out of brass sheet and there is no significance to its shape otherwise. The mounting mechanism was also modified in order to increase rigidity and reduce the chance of aperturing the beam if the extraction head was displaced. After rerunning the trial with the modified extraction system, if was observed that there was significant movement of dust from the cut surface to outside the cut area (Figure 97).

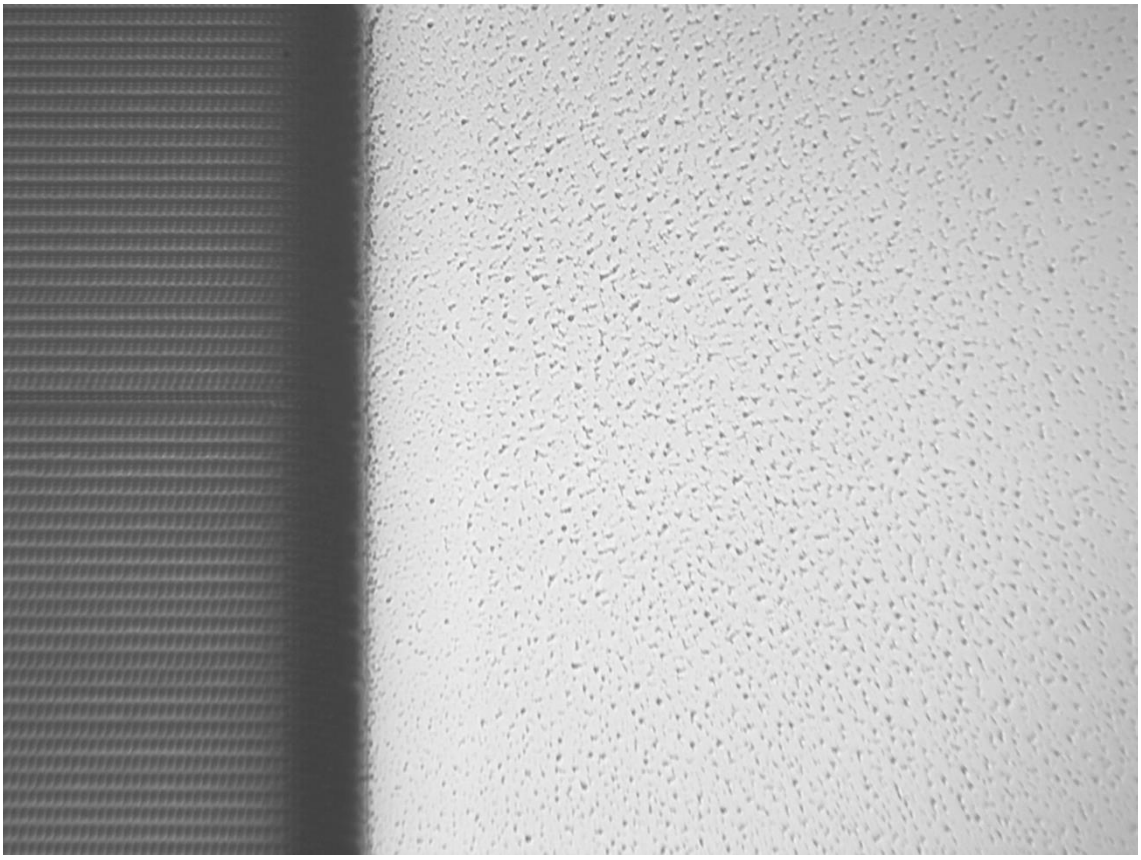

Figure 97: A micrograph showing the presence of visible dust on the substrate outside the laser machined area.

One of the main unknown factors in this experiment is to what extent, if any, fast airflow close to the cutting location will affect the cutting condition. Cutting has previously always taken place in normal ambient room conditions and a directed flow of air is a markedly different environment. Specific concerns were:

- The fast airflow near the cutting spot will alter the thermal conditions during an individual pulse by increasing the convective cooling of region being illuminated, which may subsequently alter the depth achieved per pulse.
- The airflow may be turbulent, which could change refractive index of the air that the beam passes through, thereby changing the position of the spot on the substrate.

Although it was difficult to determine if any dust had actually been removed or prevented from re-depositing on the surface, the presence of dust outside the cut area, particularly enough dust so that it is easily visible with a microscope in light-field mode, is not seen when cutting structures without the extraction head in place. This indicates that this extraction method is able to affect either the generation of dust, the distribution of dust or a combination of the two.

A number of further test structures were cut with the suction device at different heights above the surface, which appeared to show a reduction in the amount of silica dust present on the optic surface as the height decreases. The updated rigid mounting solution was not able to entirely eliminate aperturing of the beam related to instability in extraction head positioning during cutting. This also means that no conclusions can yet be drawn on whether the airflow affects spot positioning or depth as the unstable aperturing of the beam is the primary source of error. However, for the purposes of this investigation, i.e. if dust can be reduced on the cut area during cutting of multi-pass structures, the initial test has been successful.

4.2.3 – Improving the gas extraction method and design

Initial extraction tests showed promise in reducing dust on the cut area, but proved impractical for volume production use due to the handmade nature of the extractor, in particular alignment remained difficult, removal and installation were non-trivial and the positioning of the aperture relative to the laser was unstable. An improved extraction head was designed that would allow for volume production use as well as flexibility in testing so that the optimum extraction conditions could be found. This new design included repeatable, moderately precise alignment features, improvements in stability as well as being easy to install and remove as production requirements dictated. A major new change to this design was that the final focussing lens of the laser was an integral part of the assembly, acting to seal the housing and enabling the gas extraction column to be open instead of annular as shown in Figure 98.

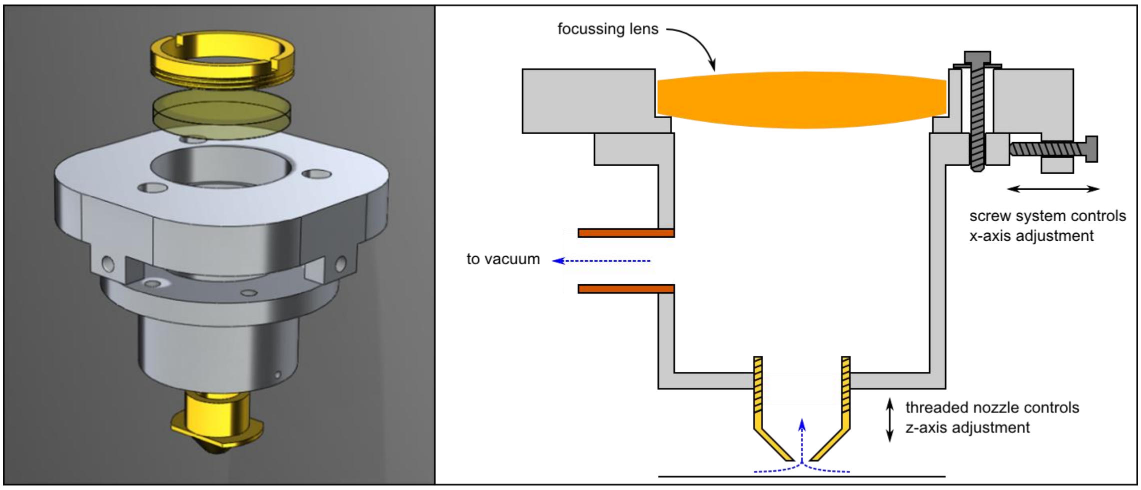

Figure 98: The updated "open" design, an exploded view of the CAD model shown on the left; a cross-section showing x and z adjustment mechanisms shown on the right

This design enables x,y and z position adjustment between the nozzle aperture and the focussing lens without interfering with focussing lens position. Two screws control x and y motion, as well as allowing for repeatable alignment when reinstalling the extraction head, while the nozzle itself was externally threaded and can be screwed in or out in order to adjust its position relative to the substrate. The open design was also expected to give better performance than an annular design due to the lack of any potential "dead zone" created by the central non-extracting area of the annulus.

Having a removable nozzle allows for investigation in to the effect on dust removal when varying the nozzle aperture radius and accordingly 5 nozzles were designed and manufactured with different nozzle radii ranging from 1-5mm. The simple open design permits for simulation of expected air velocity over the substrate near the nozzle by assuming the nozzle height h and nozzle diameter D generates a cylindrical surface area through which the air velocity is uniform, specifically:

$$v = \frac{Q}{\pi D h} \tag{56}$$

where Q is the measured inline air flow rate, D is the diameter of the aperture and h is the height of the suction device above the surface of the substrate (as shown in Figure 99).

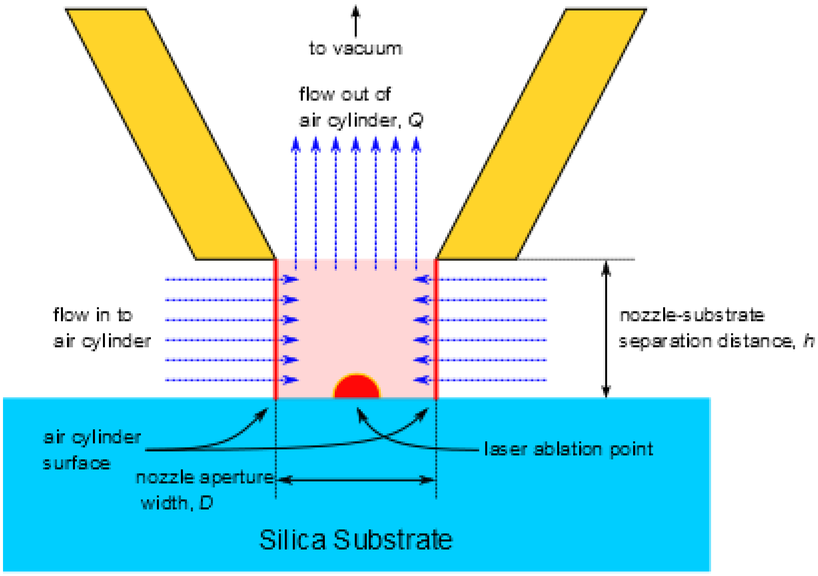

Figure 99: A cross-sectional diagram of the nozzle aperture illustrating the air cylinder and the relevant parameters for calculating air velocity through the cylinder surface.

As observed in the initial tests, the greatest apparent dust removal occurred when the extraction head was positioned as close as possible to the substrate surface during cutting. The threaded nozzle is able to adjust the nozzle to substrate separation quite precisely, to about 100µm accuracy, so the first trial was conducted with the nozzle approximately 100µm from the substrate surface before cutting a 2mmx2mm square flat bottomed test structure 50µm deep with the rotary vane pump connected. This was quickly seen to be an incompatible setup for quality cutting as significant material build-up on the nozzle tip which subsequently fell back on to the substrate created unacceptable errors in cutting. As the nozzle-substrate separation was increased, it was observed that the rate at which the material build-up occurred decreased. This change in material deposition rate with separation distance was likely due to two factors:

- As the rising hot vaporised SiO_2 gas touches the room temperature brass part, it immediately condenses and adheres to the brass.
- As the particulate moves through the air after being produced by the laser pulse, it decelerates. At some point above the substrate the particles have decelerated to the extent that their velocity is similar to the air velocity produced by the extraction head, allowing for their capture rather than deposition on the extraction head itself.

It was found that the minimum nozzle-substrate separation distance in which no material build-up occurred on the nozzle tip after cutting a single 2mmx2mmx50µm structure was 1mm. This was then taken as the minimum distance for all subsequent testing.

It was observed that the 1mm diameter nozzle caused the highest density of dust found outside the optic after cutting a test structure, with the test structure itself objectively appearing the most dust-free when analysing under a microscope. A graph of Equation (56) using a flow rate of 50Lmin^{-1} for the available aperture diameters of 1-5mm with variable separation distance between the nozzle and substrate, shown in Figure 100, shows that the 1mm aperture nozzle generates a simulated air velocity over the surface of the substrate of 265ms^{-1}. This suggests that the optimum dust extraction conditions are that which generate the highest air velocity over the surface near the extraction nozzle.

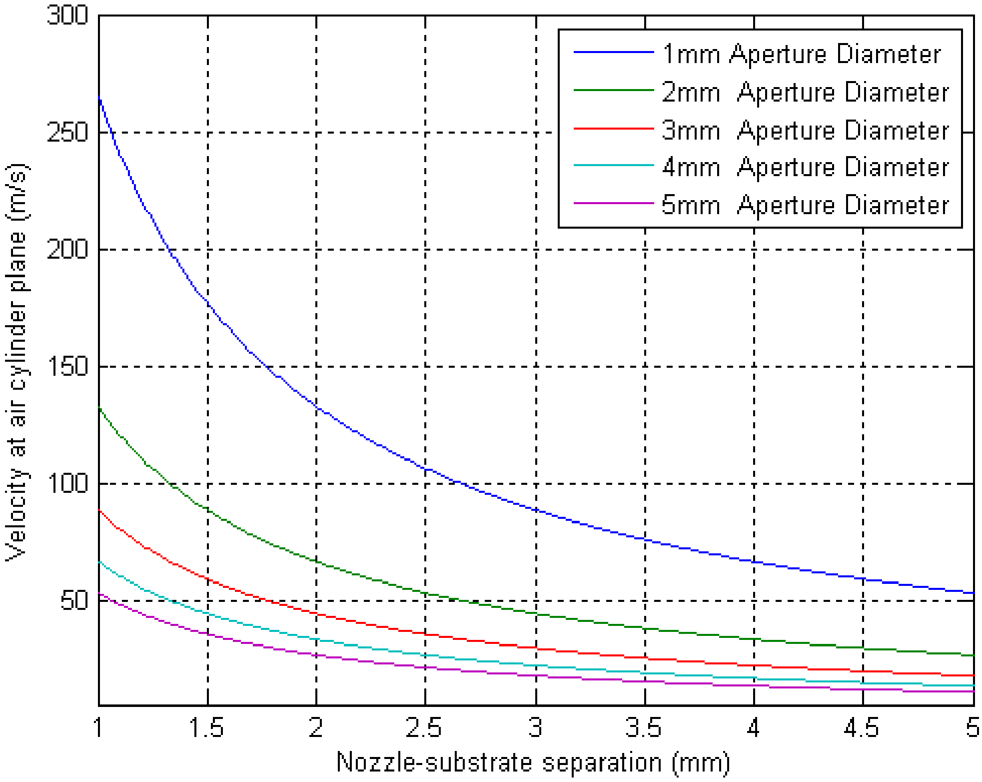

Figure 100: A graph showing the simulated air velocity over the substrate surface for various aperture diameters and nozzle-substrate separation distances for flow rates of 50L/min

The laser system on which the extraction head was tested was also operating to produce commercial product for PowerPhotonic. After installing, testing and removing the extraction head it was observed that there was a discrepancy between expected cut depths and actual cut depths on normal production substrates which increased each time the extraction head was tested. Examination of the final focussing lens showed that use of the extraction head was creating a build-up of dust on the under surface of the lens (Figure 101), which was subsequently reducing the amount of laser energy transmitted to the substrate. After cleaning the lens, the expected-actual cut depth discrepancy disappeared entirely. This level of process-altering dust being deposited on the focussing lens had only been generated after cutting 5 of the 2x2mm test structures, or a total cut volume of

0.2 mm^3. Considering that a typical overnight production run could remove a volume of up to 200 mm^3, this extraction head was clearly not suitable for production use.

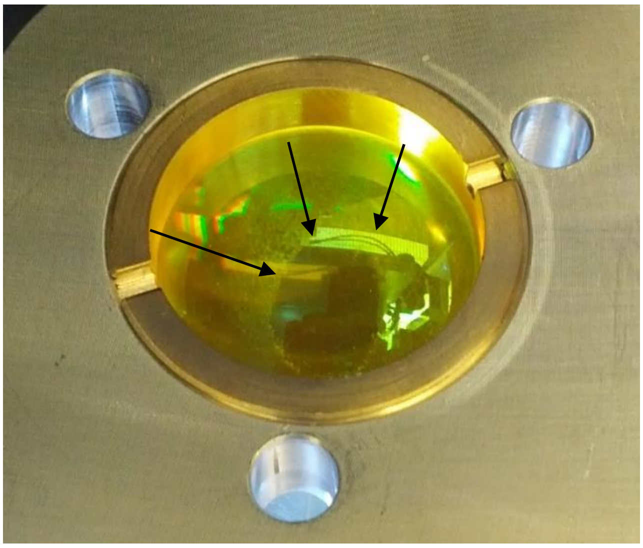

Figure 101: A picture showing the dust build-up on the underside of the focussing lens, here with part of the dust removed for contrast. Black arrows indicate the edge of the region with the dust removed.

In an attempt to modify the existing hardware to minimise this issue, an experiment was carried out to investigate the effect of a small gap introduced between the lens holder piece and the extraction assembly. The supposition was that this could create a protective flow of clean air within the extraction assembly near the lens that would travel in the opposite direction to the dust being removed during cutting and reducing contact between dust and the lens surface. The modifications are illustrated in Figure 102.

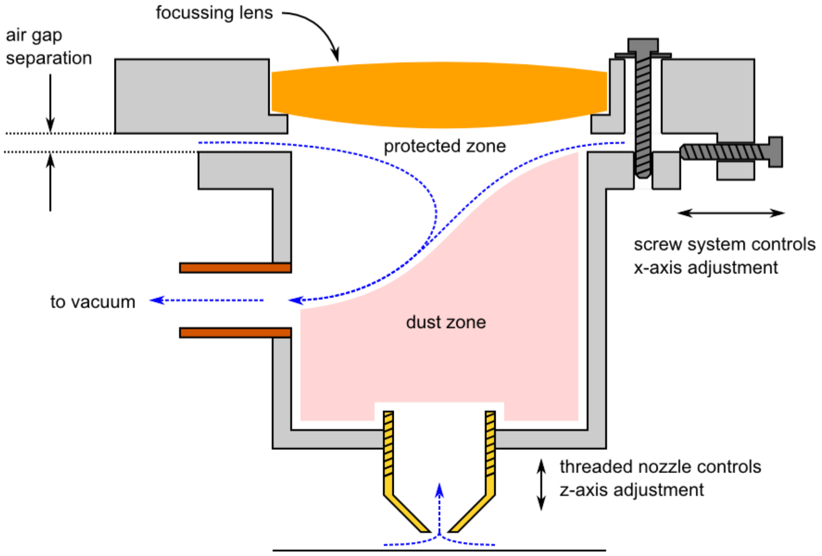

Figure 102: A diagram of a cross-section of the extraction head assembly showing the anticipated air flow after the introduction of an air gap to protect the focussing lens.

Because the extraction head had previously been shown to interrupt standard production mechanisms by causing undesirable dust deposition on the focussing lens, this experiment was required to be conducted without using production equipment. A Perspex plate was used in place of the lens and its mount, which created a good seal when fixed in place. Spacers of varying thicknesses were placed at intervals around the extraction head cylinder before attaching the Perspex plate, allowing for a good indication of the relationship between deposition on the lens and air gap separation required. A controlled amount of smoke was created by fully burning a piece of paper of size 1cm x 3cm x 100μm in a transparent container, with air supplied by a thin straw. A second straw was then attached to the extraction assembly with the 5mm nozzle attached and suction applied with a flow rate of 65Lmin^{-1} to remove the smoke from the container (Figure 103)

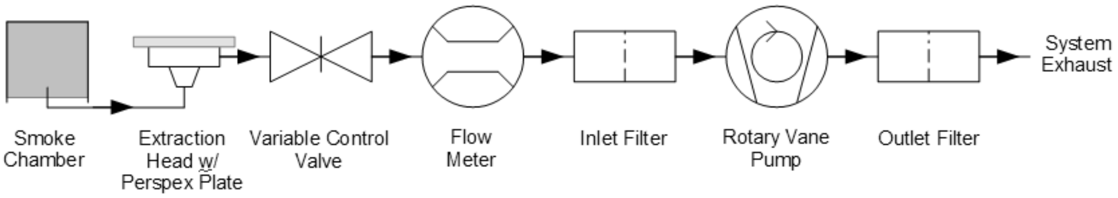

Figure 103: A system diagram showing the serial order of the gas extraction system when tested for smoke contamination

After the smoke was fully extracted, the Perspex plate was removed and examined for evidence of deposition and then cleaned with isopropyl alcohol between tests with different spacer thicknesses, photograph results shown in Figure 104.

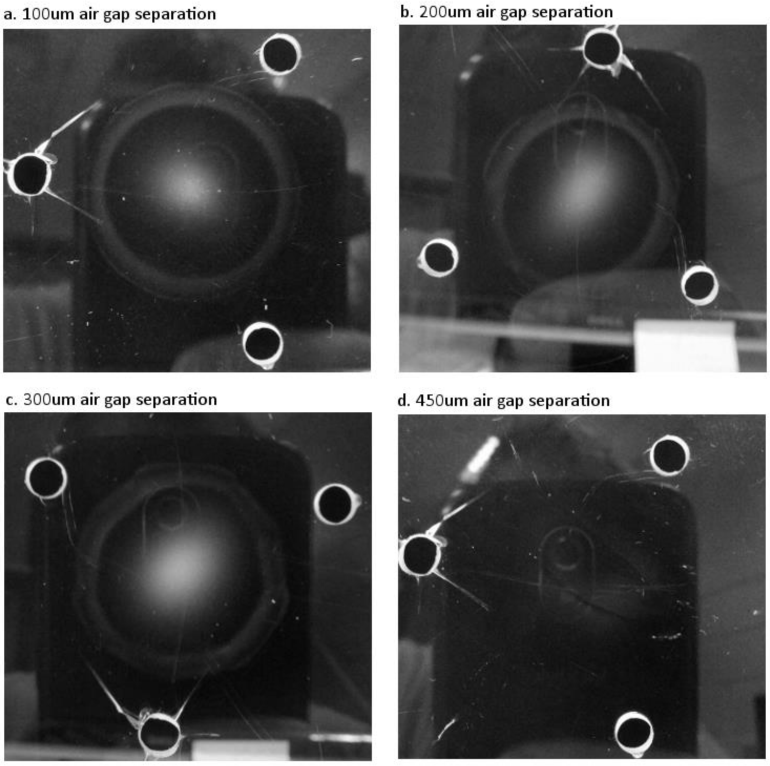

Figure 104: Pictures showing the appearance of the Perspex plate after removing a volume of smoke from a container, with varying air gap separation distances. The cloudy ring is where the smoke has been deposited on the Perspex instead of being removed from the housing via suction.

As can be seen in Figure 104, there was no significant change in smoke deposition on the Perspex plate until an air gap separation of 450µm was introduced between the Perspex plate and the extraction assembly (although deposition still occurred, it is difficult to see in the above photograph). However, it is not likely this indicates the presence of a current of air having a protective effect, but rather that the flow through the nozzle was so low that a significant portion of the smoke was able to dissipate in to the environment before being removed via the extraction head. When comparing surface areas this is unsurprising: the 5mm diameter nozzle hole has a surface area of 19.6mm^2 while the cylindrical side surface area of the air gap at 450µm was 42.4mm^2; meaning that much more of the air flowing to the rotary vane pump is originating from the air gap than the smoke container.

These tests show that the open extraction assembly is unsuitable for use as a low-maintenance permanent part on the laser cutting system and that to mitigate lens fouling using spacers, the flow through the nozzle must be diminished to the extent that is ineffective during cutting operation. However experimentation with this assembly did establish a minimum separation distance requirement of 1mm between the nozzle and substrate; as well as show that even a small amount of dust that finds its way on to the final focussing lens can drastically affect process stability.

4.2.4 – Annular gas extraction and extraction head surface quality

The lens fouling issue seen with an open design suggested that a physical separation between the focussing lens and the generated dust would be required with an extraction system in place. As the initial annular part had acted as a good proof of principle, it was decided to revisit this design using the knowledge gained when working with the previous designs, specifically:

- Good alignment and mount rigidity is critical when passing the laser through small apertures to avoid aperturing the laser beam and changing the conditions of cutting.
- Minimising aperture size through which the beam passes brings the annular airflow stream as close as possible to the dust generation region during cutting.
- Minimising nozzle area maximises the air flow velocity which in turn provides a better extraction condition.

- An extraction head that is completely decoupled from the focussing lens and can be installed or removed without having to come in to contact with the focussing lens mount.

This knowledge was used to design an annular extraction head similar in principle to the initial handmade piece but of much higher quality. The part was fabricated out of two interlocking pieces of brass to form a central cone for the laser beam to pass through, and creating an annular void in a similar fashion to the initial design. The extraction requirements are:

- No dust deposition on the focussing lens.
- No dust deposition on the nozzle such that the deposits could dislodge and fall back on to the surface of the substrate and potentially foul the surface being cut.
- Silica dust removal without affecting the beam position or other cutting condition.

As before the design was carried out in SolidWorks and consisted of three main components: a mounting plate, the upper extraction head piece and the lower extraction head piece, shown in cross section in Figure 105 and Figure 106. The mounting plate enabled the assembled extraction head to be fixed to the lens mount while also providing adjustment in the z-axis in order to optimise the position of the extraction head above the cutting zone. Adjustments in the x and y axes were done somewhat roughly by sliding the bolts suspending the extraction head around in their oversized holes while loosened.

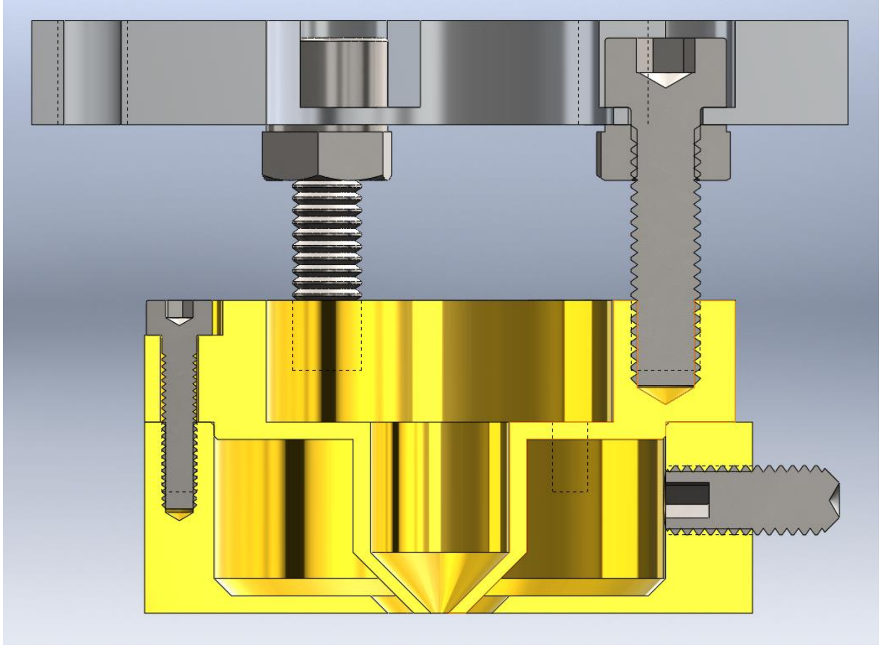

Figure 105: A cut-away of the extraction head solid model showing the three main components of the updated design

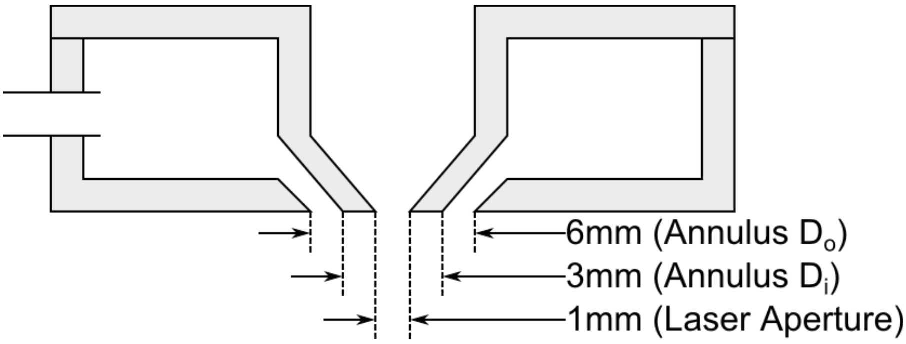

Figure 106: A cross-sectional representation of the annular design showing the annulus dimensions

The annular design was expected to be less effective at silica dust removal due to the significantly larger area of the annulus compared to the open design: the area of the annulus with dimensions shown in Figure 106 is 21.2 mm^2 as opposed to the 1mm diameter nozzle in the open design which has an area of 0.8 mm^2.

It was found that attaching the extraction head to the lens mount was not practical as it required realignment at the start of every experiment and dismantling at the end. The extraction head was therefore suspended underneath the lens mount via a steel rod connected to a Thorlabs DT12XYZ/M manual translation stage assembly which allows for adjustment in all three axes while taking up minimal space. This stage assembly was mounted on a Thorlabs KB75/M magnetic kinematic base which allowed for easy removal while enabling repeatable positioning when re-installing. This, in conjunction with the lock feature of the stages once alignment was achieved, eliminated the need for realignment between uses. Using this setup, a very precise alignment could be found with the laser beam passing directly through the aperture centre. Thermally sensitive paper was attached to the underside of the extraction head using suction, and the paper was held firmly. The external pressure on the paper created markings corresponding to the edges of features on the underside of the extraction head, and a few pulses of the laser induced a dark spot where the laser illuminated the paper. Turning off the suction and removing the paper showed how centred the laser spot was with respect to the laser beam aperture on the extraction head. The extraction assembly x, y translation stages were then used to bring the spot to the centre of the aperture.

The aligned extraction head was placed 1mm above the surface of the substrate as previously determined before cutting a 2mm square test structure. The mounting and alignment solution used proved to be appropriate as no errors due to aperturing were seen in the cut structure and removing, then replacing the assembly showed alignment was maintained (see Figure 107).

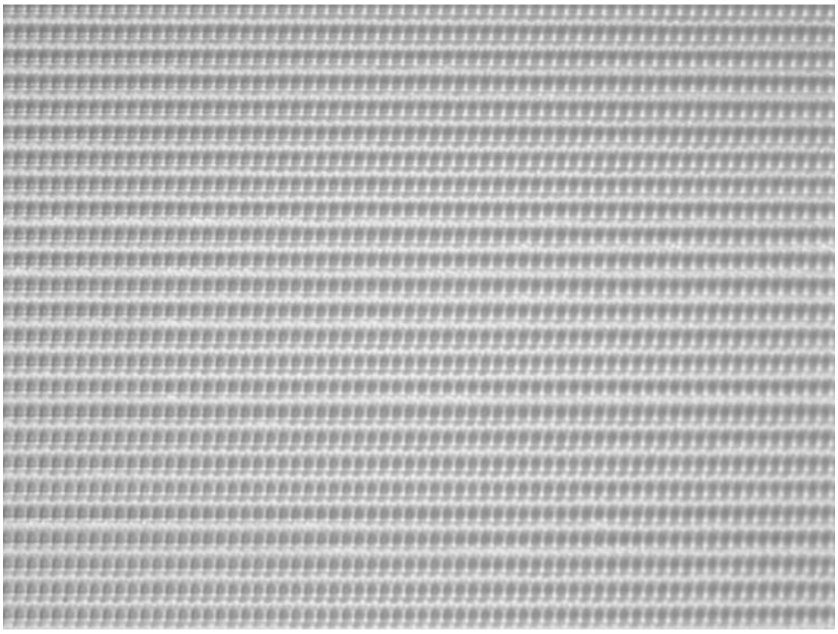

Figure 107: A micrograph of the test structure after cutting with extraction head in place, showing no beam aperturing errors and a very uniform cut grid.

It quickly became obvious that the reduced air velocity due to the larger area of the extraction head nozzle meant that deposition of dust on the nozzle housing occurred. Additionally, the part design stipulated that the nozzle wall thickness be 1mm, which created a comparatively large flat surface directly adjacent to the laser beam aperture allowing for significant dust deposition. To minimise this area, the nozzle reworked to pare down the exterior side of the cone and create a sharp edge close to the extraction zone as shown in Figure 108.

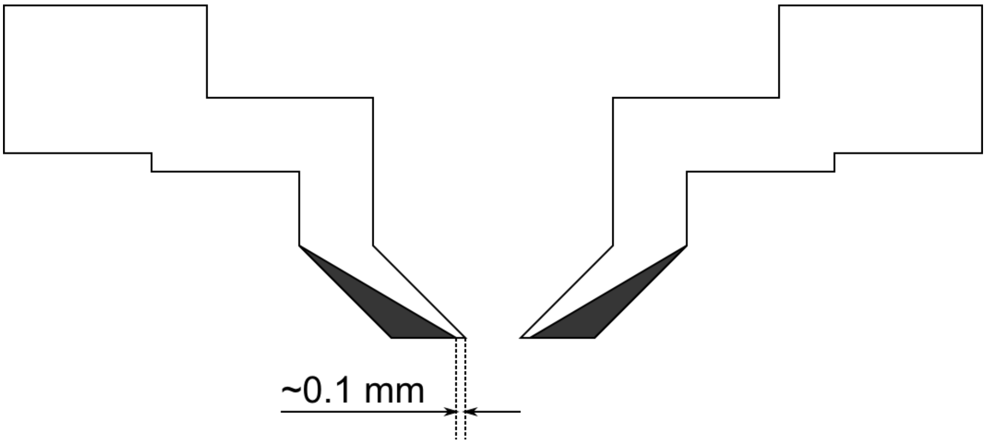

Figure 108: A cross-sectional diagram of the extraction assembly's upper part containing the interior half of the nozzle. The shaded sections indicate the removed material in order to produce a part whose cone tapers to a relatively sharp edge.

After rework the extraction head was tested under the same conditions and showed no sign of dust deposition on the nozzle tip or within the housing of the assembly itself. This showed that the extraction head fulfilled the previously stated conditions over the relatively short cutting runs of small test structures. A significantly larger test structure was designed with dimensions 20mm x 20mm x 50µm deep cut using 3 passes to produce a 150 µm deep total structure with a volume of 60 mm^3, to investigate the effects of having the extraction head in place for a production run of significant duration. Two of these test structures were queued for cutting overnight which would give a total cut volume during the test of 120 mm^3.

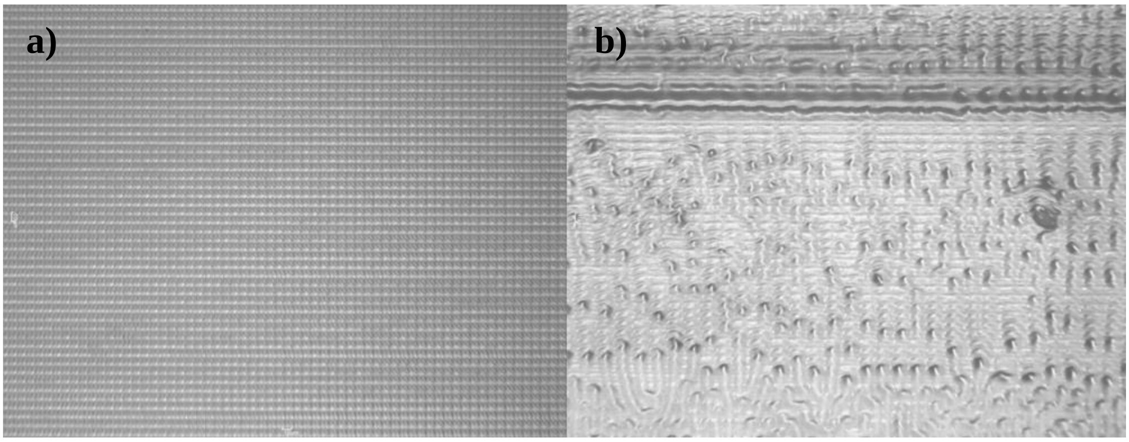

Figure 109: A micrograph showing the difference between cut pattern when the extraction head is present with rotary vane pump in operation (a), compared to the extraction head present but with rotary vane pump not in operation (b).

In this test the first substrate was cut as intended (see Figure 109a), with the cut pattern showing no beam aperturing or other positioning errors and with little dust present on the cut surface. However an incorrectly set timer switched the rotary vane pump off during the cutting of the second substrate, which created an interesting example of why the extraction head cannot be in place without suction. The surface was catastrophically damaged as seen in Figure 109b. This occurs because the dust continually accumulates on the nozzle and falls back on to the surface of the substrate. When the cutting laser passes over these deposits during any subsequent passes, it removes a volume of the deposit along with the substrate and also appears to melt part of the deposit material which solidifies back into the substrate bulk. Additionally, it was observed that the laser beam aperture was partially blocked by these deposits (see Figure 110) which would create further errors in the cut structure during cutting.

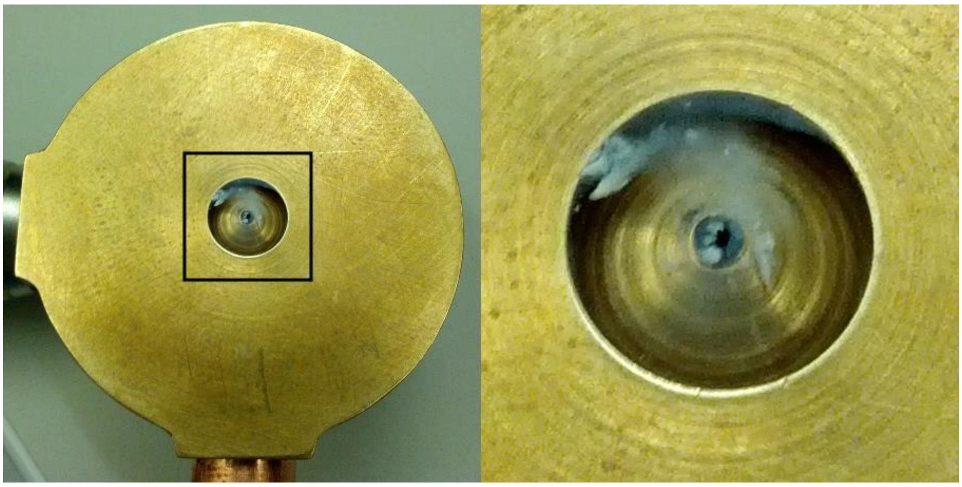

Figure 110: A photograph of the extraction head after the long cutting trial (left). The picture on the right is a zoomed view of the area within the black square, showing deposition within the laser beam aperture and annular extraction aperture.

Disassembling the extraction head allowed for closer examination of the dust, shown in Figure 111, that had accumulated on the nozzle and with the assembly itself. A number of observations were made:

1. The laser beam aperture was mostly covered by deposits and only approximately 30% of the aperture area was free from deposit in the centre of the aperture.
2. There were two distinct types of deposit
    a. The nozzle was coated in a pliable deposit, referred to as veneer-type deposit, which came away as one large piece but was particularly concentrated in the machining grooves of the nozzle left after reworking.
    b. The interior of the assembly was filled with a fine fluffy material similar to very loose cotton wool (referred to as cotton-type deposit). This material was also covering the veneer-like deposit as seen in Figure 110.
3. There was a directional component to the deposition on the nozzle, with significantly more material on one half, which was on the opposite side of the extraction head from the tube leading to the rotary vane pump.
4. There was no deposition on the underside of the assembly outside of the annulus, showing that the annulus is large enough to encompass the gas and particulates ejected during cutting.
5. There was no accumulation of dust on the focussing lens, and subsequent cutting of test structures with the extraction head removed showed that cutting conditions remained as normal.

Figure 111: Photographs of the interior of the extraction head after the long cutting trial. The top piece of the assembly is on the left and the lower piece of the assembly is on the right. The black arrow indicates where some of the veneer-type deposit was removed.

The long cutting trial was repeated with a properly setup timer on the rotary vane pump and was successfully completed. While the first substrate did not have any obvious signs of debris that had accumulated and fallen on the substrate, the second substrate did have debris covering portions of the structure as seen in Figure 112. The debris did not appear to be remelted by subsequent passes, indicating that its production occurred during the final laser pass. After closely inspecting the second substrate under the microscope, it was seen that the cut pattern was not flawed as when the laser passes over this debris. This again indicates that the debris production occurred only during the last laser pass, meaning that the approximate time before maintenance is required is around 13 hours.

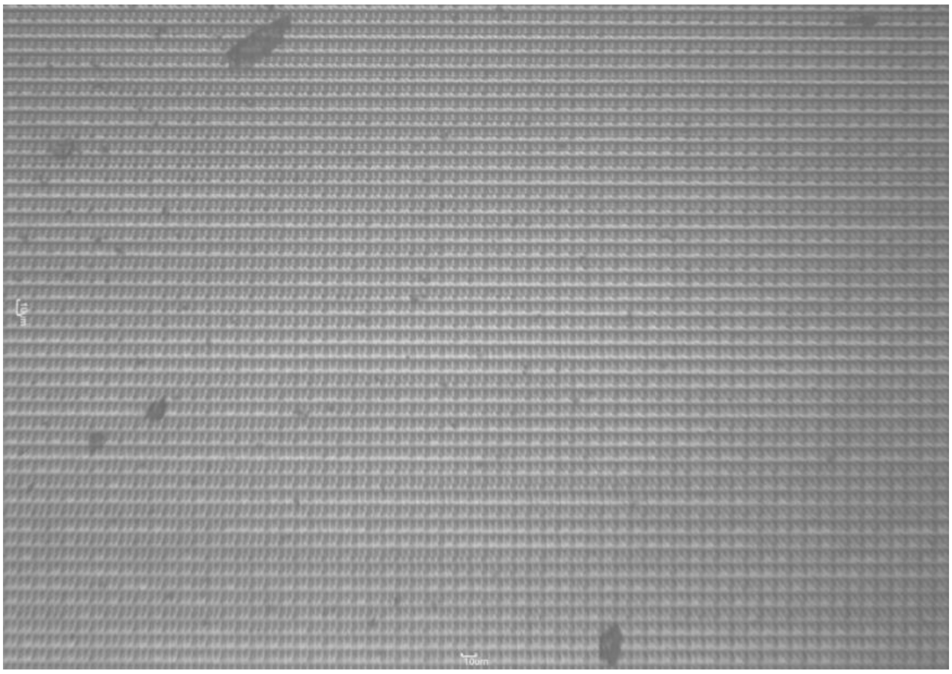

Figure 112: A micrograph showing loose dust debris on the surface of a cut structure.

Examination of the extraction head shows that having the rotary vane pump in operation gives a markedly different result to the initial trial where the rotary vane pump was off for a portion of the cutting time. Specific points are as follows.

- The laser beam aperture was almost entirely free of deposit, with only a small number of very fine deposits developing at the periphery of the aperture (Figure 113).
- There was much less of the veneer-type deposit present, and what was present was found exclusively in the machining grooves near the nozzle tip.
- There was significantly more of the cotton-type deposit within the extraction head assembly and covering the nozzle (see Figure 113).
- The dust deposition asymmetry observed previously, was now much more obvious than the first trial, particularly on the upper part of the assembly. Again, the side which had significantly more deposits was on the opposite side of the nozzle from the copper pipe which led to the rotary vane pump (Figure 114).
- As in the first trial, there was no accumulation of dust on the focussing lens.

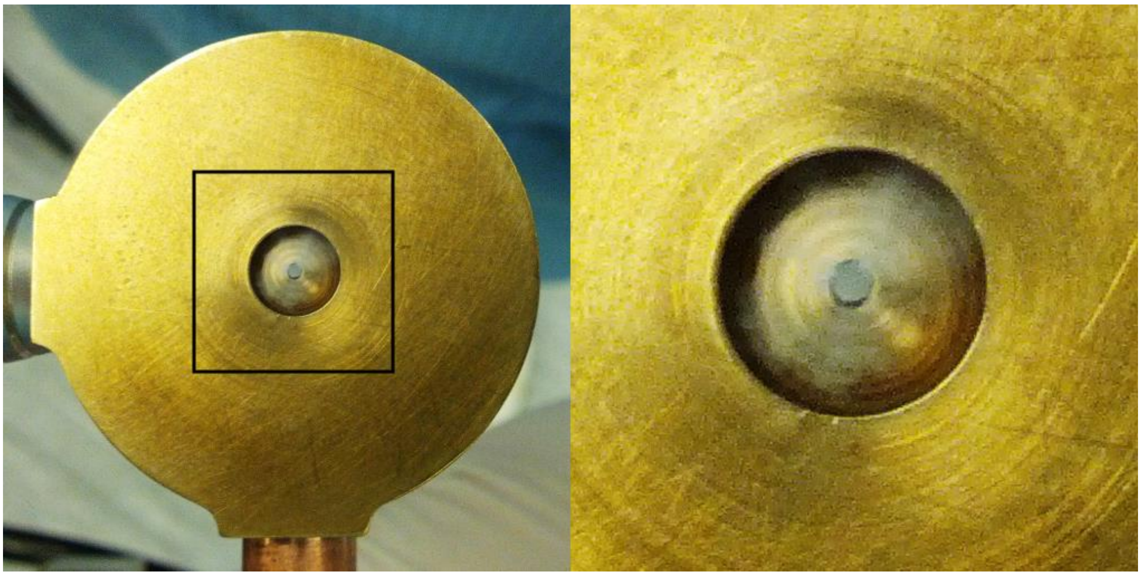

Figure 113: A photograph of the extraction head after the second long cutting trial (left). The picture on the right is a zoomed view of the area within the black square, showing deposition within the annular extraction aperture and around the laser beam aperture.

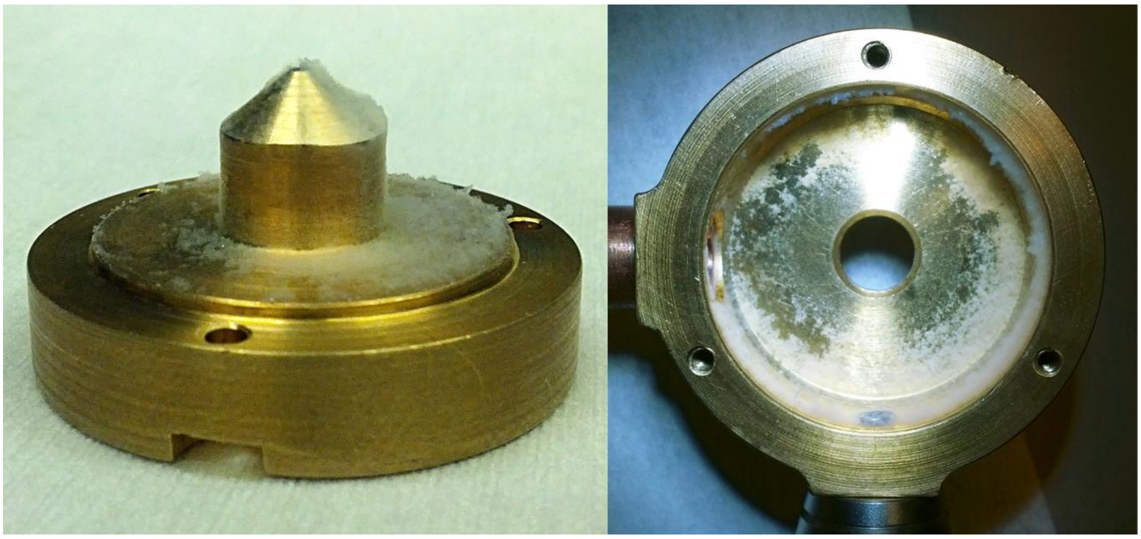

Figure 114: Photographs of the interior of the extraction head after the second long cutting trial. The top piece of the assembly (left) shows a clear asymmetry in dust distribution. The lower piece of the assembly is on the right.

As the veneer-type deposit has only been found on the nozzle, and covered in the cotton-type deposit, it is likely that it is formed from multiple compacted layers of the cotton-type deposit. If the dust is not adequately removed between individual laser pulses, this may cause compaction of the dust as the higher energy particulates impact the dust layer**.** Additionally, on the second run in which the rotary vane pump was in continuous operation, the veneer-type deposit was found exclusively in the grooves formed when the brass nozzle was reworked. This suggests that the machining grooves slowed the air passing over the nozzle (see illustration in Figure 115), which in turn locally captured a greater volume of dust that was not adequately removed by the suction before the next laser pulse occurred. Moreover, the surface shape increases the surface area over which dust can accumulate and the asperity of the machined surface increases the skin friction experienced by the air travelling over the surface.

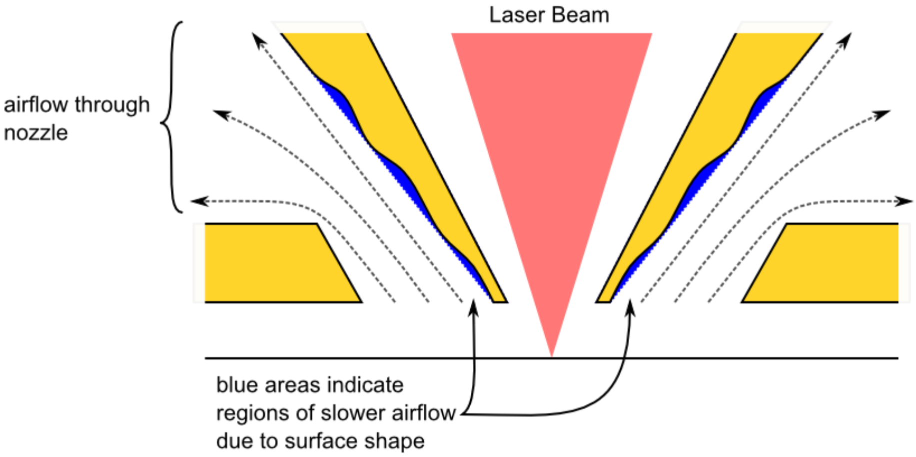

Figure 115: A representation of the extraction head nozzle tip showing expected airflow and the machining grooves of the nozzle (drawing not to scale).

In order to make the extraction head more aerodynamically efficient, the internal surfaces were finely lapped and polished using diamond lapping paper in conjunction with a mechanical polishing tool and jewellers rouge, giving a mirror finish as shown in Figure 116.

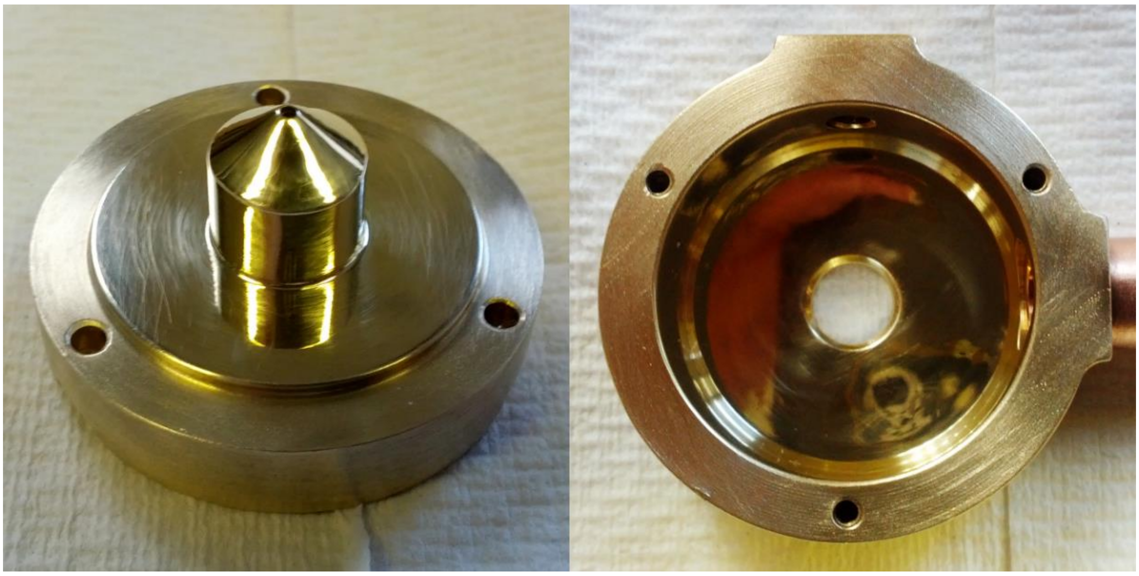

Figure 116: A picture of the upper (left) and lower (right) halves of the extraction head assembly after polishing.

After polishing, the long cutting trial was repeated for a third time to observe the effects, if any, that polishing has on the dust accumulation within the assembly, and particularly of veneer-type deposits on the nozzle. Like the previous test, the first substrate was cut successfully with no debris present, while the second substrate did have debris on the surface. Unlike the previous test however, the debris did not consist of many small particles but of a single large particle that appeared to be an agglomeration of dust particles. This large particle was situated approximately 3mm away from the end of the test structure and as the underlying cut pattern looked normal it is highly likely that this particle fell out of the extraction head during the final cutting pass. This means that, providing the particle was observed to be situated where it originally landed, the failure occurred around 15 hours and 44 minutes into the cutting run, or 16 minutes before completion.

Examination of the extraction head after the cutting run showed an improvement in both the extraction performance and in the amount of dust deposited within the assembly, specifically:

- Dust deposits on the nozzle are reduced and the laser beam aperture is free from any accumulation (Figure 117).

- There were no veneer-type deposits present within the extraction head.
- The amount of dust deposited within the polished assembly was observed to be less than when unpolished. However polishing served to make the dust much more visible due to the nature of the mirror effect on the brass (Figure 118), so the reduction in dust deposition may be greater than observed.

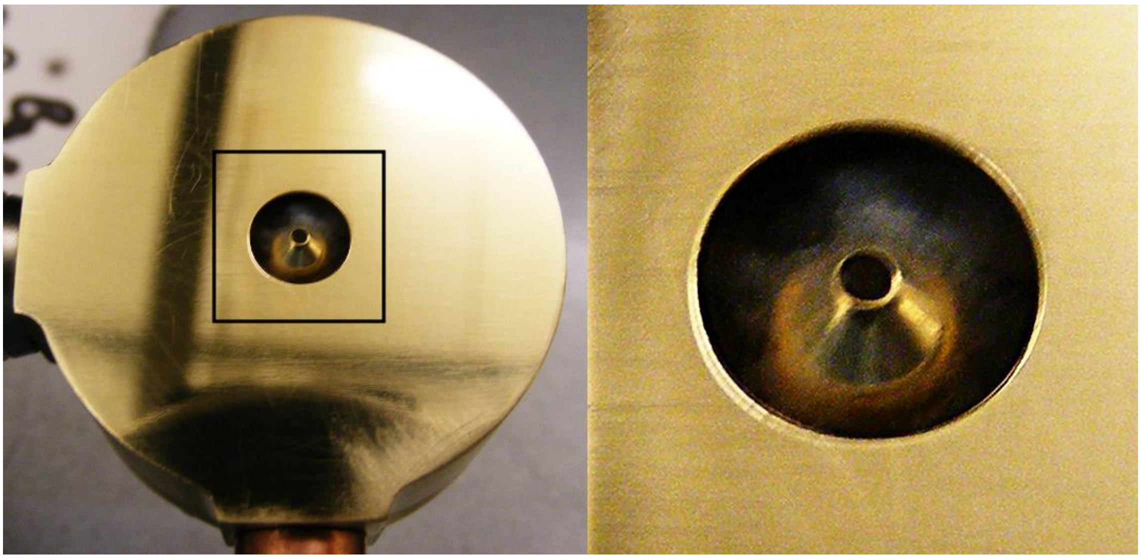

Figure 117: A photograph of the polished extraction head after the third long cutting trial (left). The picture on the right is a zoomed view of the area within the black square, showing deposition within the annular extraction aperture.

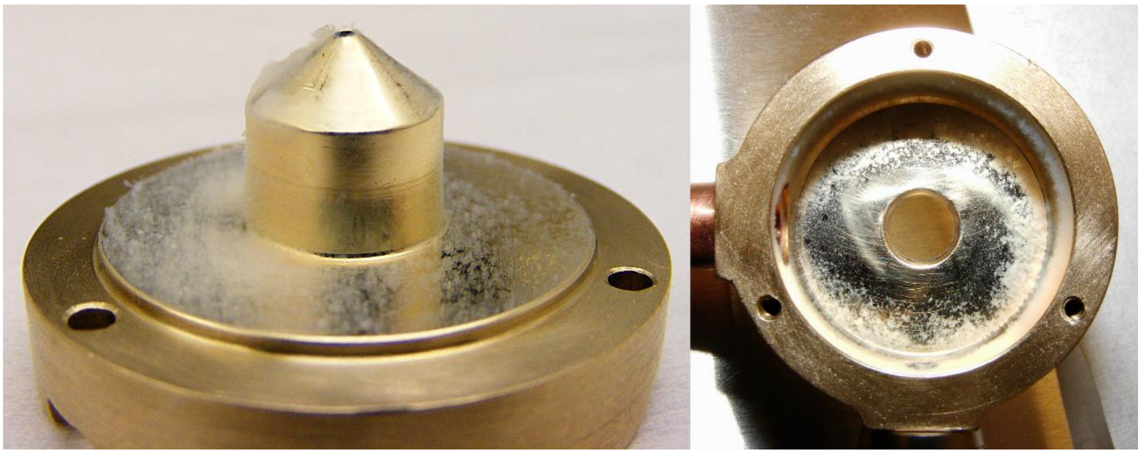

Figure 118: Photographs of the interior of the polished extraction head after the third long cutting trial. The top piece is on the left, lower piece on the right.

An unexpected benefit of polishing the interior of the extraction head is that the distribution pattern of the dust after a trial was much more obvious than in trials conducted with the unpolished parts. This distribution not only showed the asymmetrical distribution of the dust, but two particularly dense regions within the zone in which the dust was accumulating more rapidly. These dense regions were rotated approximately 90° from one another around the nozzle and 45° from the step direction of translation stage motion when the extraction head was in place during the cutting trial as seen in Figure 119.

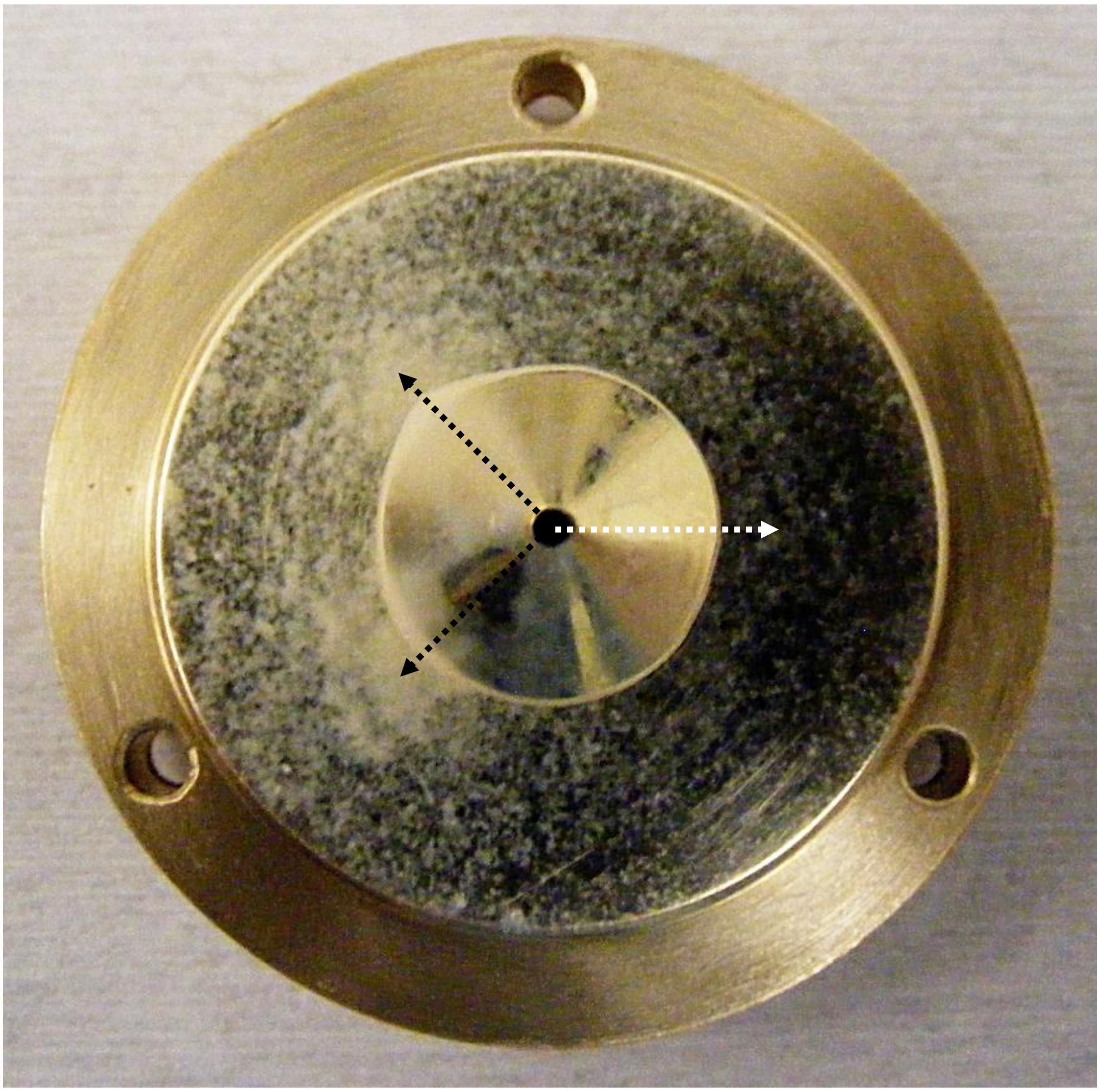

Figure 119: A photograph of the upper piece of the extraction head, showing the dense regions of dust accumulation after the third long cutting trial. The dotted black lines indicate the expected plume directions during cutting, the dotted white arrow indicates the position of the connection to the rotary vane pump.

These two dense regions correspond to the expected directions of the gas/dust plume produced during cutting when using a cut pattern that is unidirectional in the step direction and bidirectional in the scan direction. As the raster pattern progresses on every cut line after the first, the laser pulse is incident upon a surface that is sloped in the xy plane (where x is the direction of raster scan and y is the direction of raster step). The plume of material produced by the laser pulse is directed roughly normal to this surface, and because the direction of the raster scan line alternates between scan lines, the plume direction also alternates as illustrated in Figure 120. This gives rise to the higher density regions seen on the interior of the extraction head after cutting. The extraction head was positioned in such a way that the pipe connecting the extraction head to the rotary vane pump was on the opposite side of the assembly to the plume locations during cutting and by either rotating the extraction head by 180° or reversing the step direction of cutting may decrease the amount of dust deposited within the assembly.

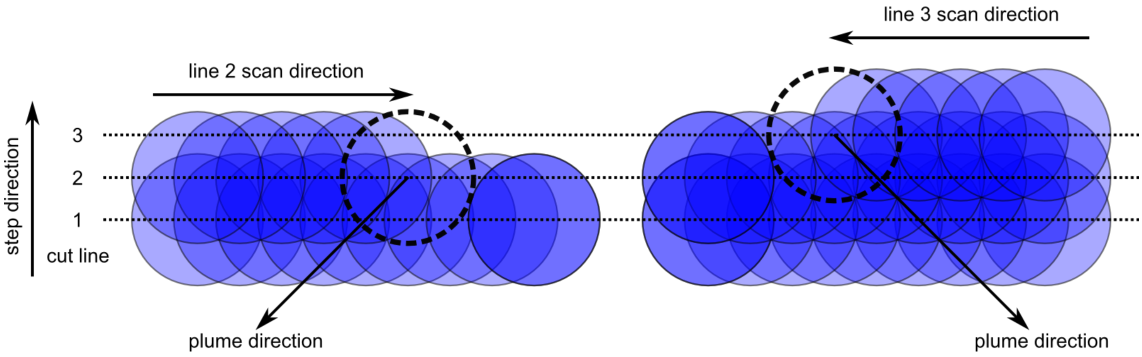

Figure 120: A simple representation of the overlapping laser pulses when cutting in a raster pattern that switches direction between each line. The dotted black circle indicates the position of the next laser pulse in the pattern and the arrow indicates the direction of the plume originating from this pulse.

Commercially available laser machining nozzles (such as those available from Centricut) are almost always coated with a hard material, usually chrome, in order to increase resistance to wear and corrosion. These nozzles are generally intended for use in industrial machining laser systems that cut materials such as metals, ceramics, wood and plastics and therefore subject to significantly more environmental stress than the nozzle used at PowerPhotonic. However, a chrome coating offers the additional property of reducing the coefficient of friction between the chrome plated part and many other materials, this is referred to as intrinsic lubricity. During consultation with coating suppliers, a number of coatings were identified as potential candidates for this experiment and shown in Table 10.

Coating	**Lubricity**	**Wear Resistance**	**Cost**
Gold	Poor	Good	Expensive
Electroless nickel-phosphorus	Good	Very good	Inexpensive
Electroless nickel-boron	Excellent	Very good	Very expensive
Hard chrome	Very Good	Excellent	Expensive
Nickel-PTFE	Excellent	Poor	Very expensive

Table 10: A table comparing the key features used to evaluate coatings for decreasing the build-up of dust deposits within the extraction head during cutting

For the purposes of this trial, it was decided that the electroless nickel-phosphorus coating was the most appropriate as the low cost, along with very good wear resistance for cleaning and production use meant that this coating was more suitable despite not having the best lubricity characteristic. The electroless nickel-phosphorus coating consists of approximately 5% phosphorus and 95% nickel and is applied uniformly to the surface of the brass with a thickness of about 25µm. The thin, uniform deposition means that no machining will be required post-coat: threaded holes and apertures will still be the same shape and nominally the same size.

The long trial was run once more as before, with two substrates cut for 16 hours, however for this trial the step direction was reversed so that the pipe leading to the rotary vane pump was on the same side of the nozzle as the plumes produced during cutting. After completion it was noted that both substrates were pristine with no evidence of debris on either one using visual and microscope inspection.

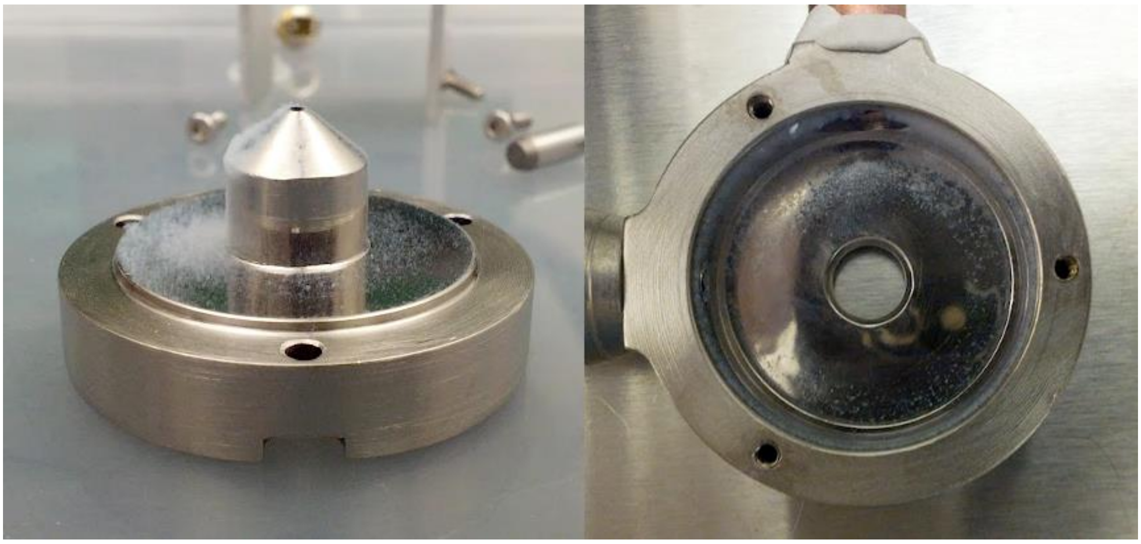

Figure 121: Photographs of the interior of the nickel plated extraction head after the fourth long cutting trial. The top piece is on the left, lower piece on the right.

Examination of the extraction head interior (Figure 121) shows a drastic reduction in the amount of dust accumulated on both the upper and lower pieces of the assembly. Of particular note being the disappearance of the higher density dust regions associated with the plumes produced during cutting, the resulting dust deposit was instead distributed fairly evenly over the quadrant bounded by the plumes (Figure 122).

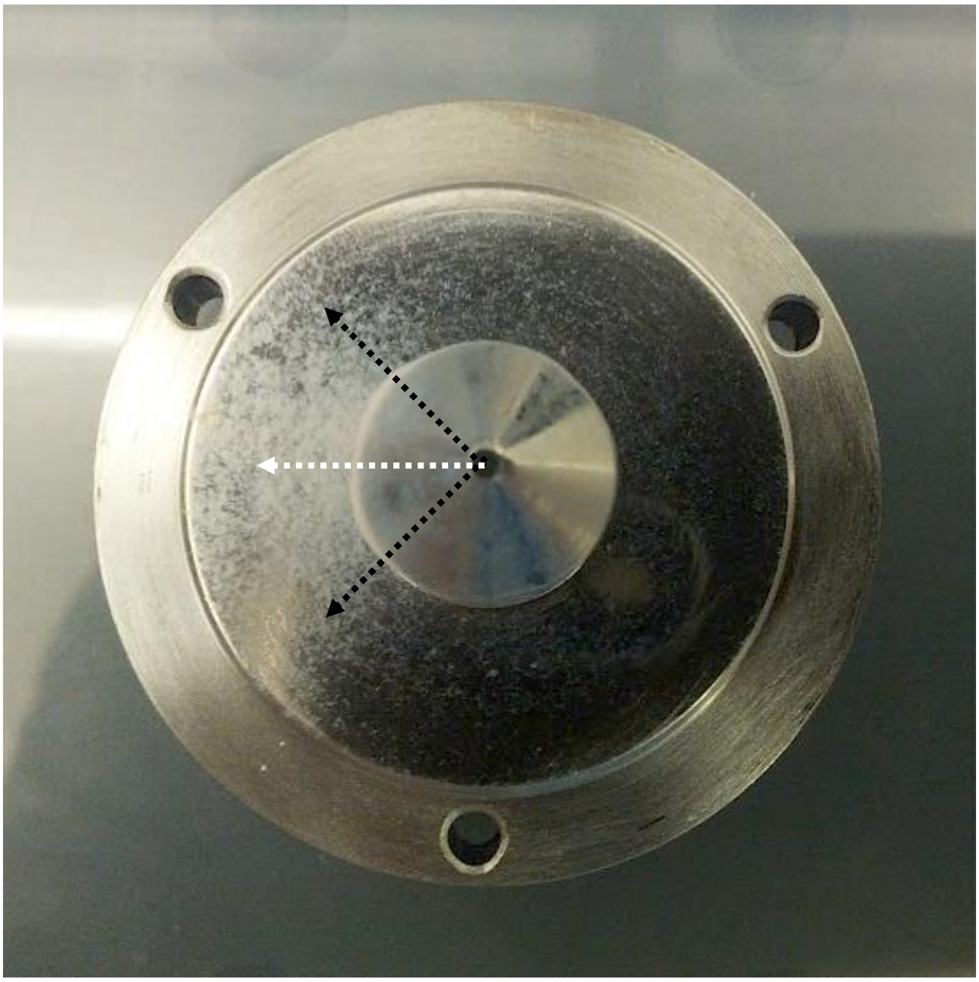

Figure 122: A photograph of the upper piece of the nickel plated extraction head, showing the dense regions of dust accumulation after the fourth long cutting trial. The dotted black lines indicate the expected plume directions during cutting, the dotted white arrow indicates the position of the connection to the rotary vane pump.

It is expected that by increasing the air velocity through the nozzle, either by increasing the flow rate of the rotary vane pump or changing the aperture geometry to have a smaller area, that the amount of dust deposited during cutting can be further reduced.

4.3 – Reynolds number and vortex shedding

The Reynold's number and air flow velocity were calculated for air travelling through a fixed geometry annular aperture and the air flow rate through the aperture used to control these variables. Establishing how turbulent the flow regimes are with respect to air flow rate through the aperture may highlight test points for investigation into how turbulence affects silica dust extraction. Analysis of the internal geometry of the extraction head with respect to vortex shedding could predict the locations of any stationary vortices that allow silica dust to accumulate and require periodic maintenance.

The air flow velocity at the aperture is calculated using the equation:

$$v = \frac{Q}{A} \tag{57}$$

where v is the air velocity, Q is the air flow rate and A is the aperture area. The flow rate is variable from 0-60 $\mathrm{Lmin^{-1}}$ using the Key Instruments flow meter . A nominal flow rate of 50 $\mathrm{Lmin^{-1}}$ and area of $2.1\mathrm{x}10^{-5}$ $\mathrm{m^2}$ corresponds to an average velocity of air through the aperture of 39.3 $\mathrm{ms^{-1}}$. The Reynold's number describes whether the flow is turbulent or not and is found using the equation (58).

$$R_e = \frac{QD_h}{V_k A} = \frac{vD_h}{V_k} \tag{58}$$

where D_h is the characteristic length of the aperture and V_k is the kinematic viscosity of the air. Characteristic length of the annular aperture is calculated as follows:

$$D_h = \frac{4\pi r_o^2}{2\pi r_o} - \frac{4\pi r_i^2}{2\pi r_i} = 2r_o - 2r_i \tag{59}$$

where r_o is the radius of the exterior of the annular aperture and r_i is the radius of the interior of the annular aperture. The fixed characteristic length of this annular aperture is therefore $3\mathrm{x}10^{-3}$ m; the kinematic viscosity is an empirically determined quantity which, for air at 300K and 1 atm, is $15.68\mathrm{x}10^{-6}$ $\mathrm{m^2s^{-1}}$.

Combining equations (58) and (59):

$$R_e = \frac{v(2r_o - 2r_i)}{V_k} \tag{60}$$

This shows that the Reynold's number for the system can only be varied by varying the flow rate through the aperture, as the rest of the variables are fixed by the system geometry and the physical characteristics of air. The relationship between the Reynold's number and air velocity with the flow rate of air are shown in Figure 123a and Figure 123b respectively.

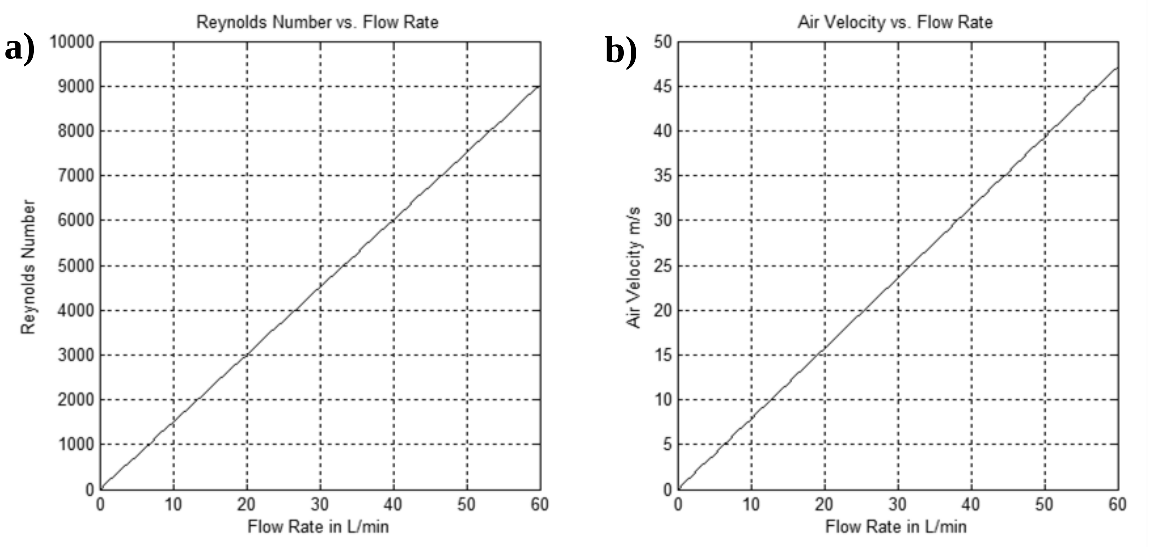

Figure 123: Graphs showing the variation of a) Reynold's number and flow rate and b) air velocity and flow rate for a fixed aperture geometry.

Turbulent flow is commonly classified as a flow within a system that has a Reynold’s number greater than 4000, while laminar flow is similarly classified as having a Reynold’s number of less than 2300, and the region of 2300-4000 has a mixture of turbulent and laminar flows. These values represent two test points for further investigation into how the Reynold’s number of the system affects its ability to remove silica dust during cutting: an R_e of 2300 is equivalent to a flow rate of 15.3 Lmin^{-1} and an R_e of 4000 is equivalent to a flow rate of 26.6 Lmin^{-1}. The equations show that at the nominal flow rate of 50 Lmin^{-1} used most often when testing the extraction system, the air flow through the aperture is turbulent, as it has a Reynold’s number of approximately 7500. This indicates that the turbulent flow results in variable air velocity across the aperture which could inhibit the growth of silica deposits from condensed silica vapour. It was expected that highly turbulent air flow would result in laser pointing instability due to rapid variation in the refractive index of the air near the ablation zone, but this does not appear to be correct.

Vortex shedding is a phenomenon that occurs when a flow of gas or liquid encounters an obstruction with a length shorter than that of the flow, for example a wire placed in a flow region. It is important in fields such as civil engineering, where the production of vortices can induce major structural instabilities if their shedding frequency is similar to the structure’s resonant frequency, and acoustics, where vortices can negatively affect sound production and radiation. In the annular aperture, the main vortex generation points are likely to be located at positions A and B on Figure 124 below, where the end of the air flow obstruction takes place. In the case of a wire within a uniform flow, the vortex generation point will alternate between either side of the wire, however for points A and B the vortices generated travel in one direction only and thus the vortex from A will travel towards the outside of the device and downwards while the vortex from B will travel inwards and upwards.

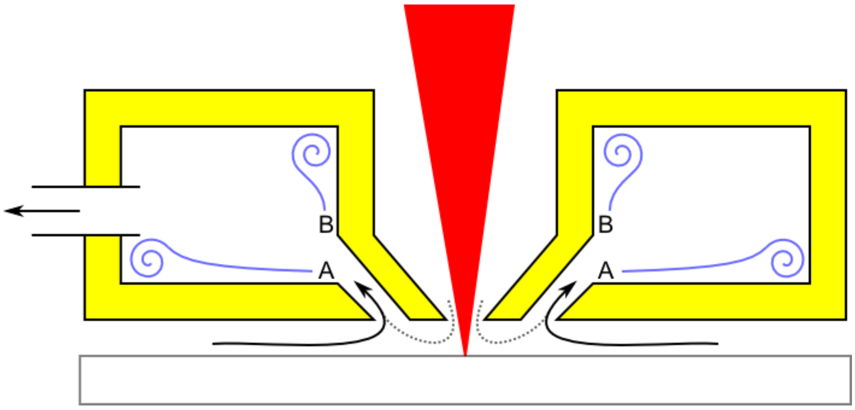

Figure 124: A schematic representation of the gas extraction head, showing the direction of air flows near the aperture. Points A and B show the trailing edges in the air flow where vortices (in blue) are created.

The vortex shedding frequency describes the *natural* frequency at which these vortices are formed and released at the interface point, and is governed by the following equation:

$$S_t = \frac{D_h f}{v} \tag{61}$$

where S_t is the Strouhal number, D_h is the characteristic length of the annular aperture, f is the vortex shedding frequency and v is the air flow velocity. The value of the Strouhal number describes how the viscosity of the medium affects the vortex generation and is typically in the range of 0.1-0.2, which would give a natural vortex shedding frequency of 1310-2620 Hz for a nominal flow rate of 50 Lmin^{-1}.

4.4 – Residual dust measurement

The measurement and comparison of the cut test structures with varying gas suction conditions is critical for optimizing the dust extraction process. Ideally the establishment of a method that produced a simple result would not only give easily interpretable results, but allow the system to be used in the future for quality control of optics fabricated using the standard production process. The approach chosen is similar to the measurement system used in [45], but it uses a diverging HeNe beam to illuminate the sample and a camera to capture the scattered light in order to facilitate a result that is easier to interpret.

This method relies on the fact that when incident linearly polarised light is scattered by silica dust nano-particles on the surface of the glass, the polarization is rotated by a random angle. This allows for the isolation of scattered light from any refracted or stray light produced within the system when used with a pair of crossed polarisers before and after the scattering surface. Initially the laser was placed on-axis (θ = 0°) with the camera and sample, assuming that the isolation provided by the crossed polarisers would be sufficient.

$$Degree\ of\ Polarisation = \frac{1 - cos^2(\theta)}{1 + cos^2(\theta)} \qquad (62)$$

where θ is the angle of incidence of light hitting a scattering object. However, plotting the above equation (Figure 125) shows that using on-axis illumination will give a poor or null result irrespective of isolation provided by the crossed polarisers:

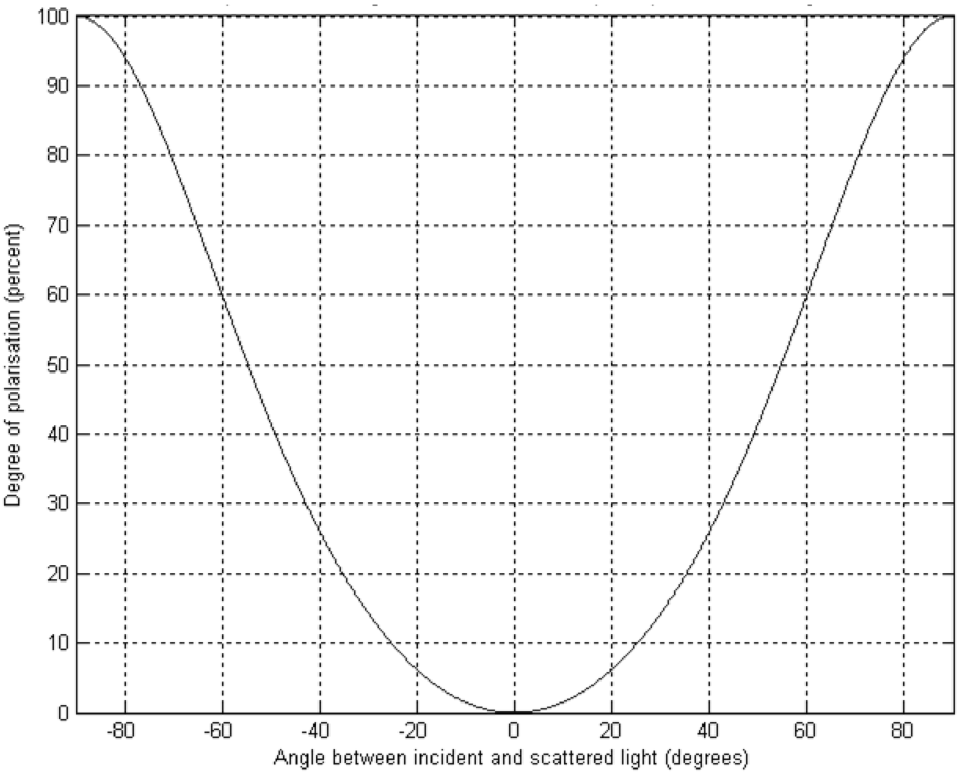

Figure 125: Dependence on angle of observation to polarisation change of the scattered light

The axial system setup was aiming to measure the light scattered via Mie scattering, on the basis that the particle sizes were similar to that of the wavelength of the illumination. Although the crossed polarisers did indeed provide very good reduction of the transmitted light, the image produced did not appear to show any light scattered by silica dust. This is due either to the reliance on angle between illumination and observation to affect polarization change of scattered light (as shown by the equation above) or the lack of Mie scattering due to particle sizes being significantly smaller than 632nm.

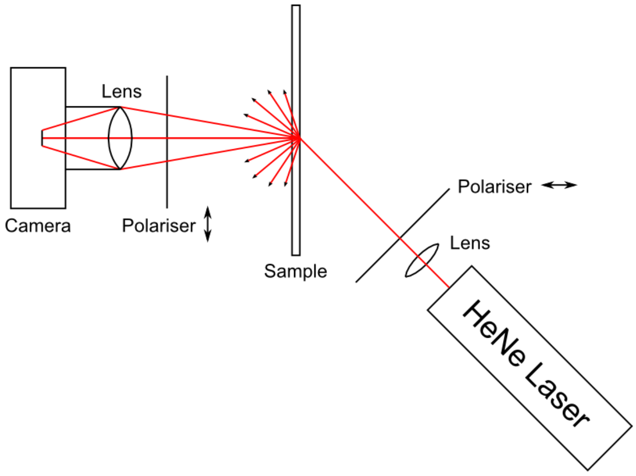

Figure 126: The setup used to illuminate and collect the scattered, randomly-polarised light from a sample

Equation 11 shows that an angle between incident light and observation axis of 45° will polarize ~33% of the light scattered from features on the sample in the Rayleigh scattering regime. Using an observation angle of 45° (shown in Figure 126), the test structure was illuminated with the expanded beam to produce the results seen in Figure 127, which clearly shows that the amount of scattered light increases with decreasing flow rate, and with no extract the amount of scattered light is significant.

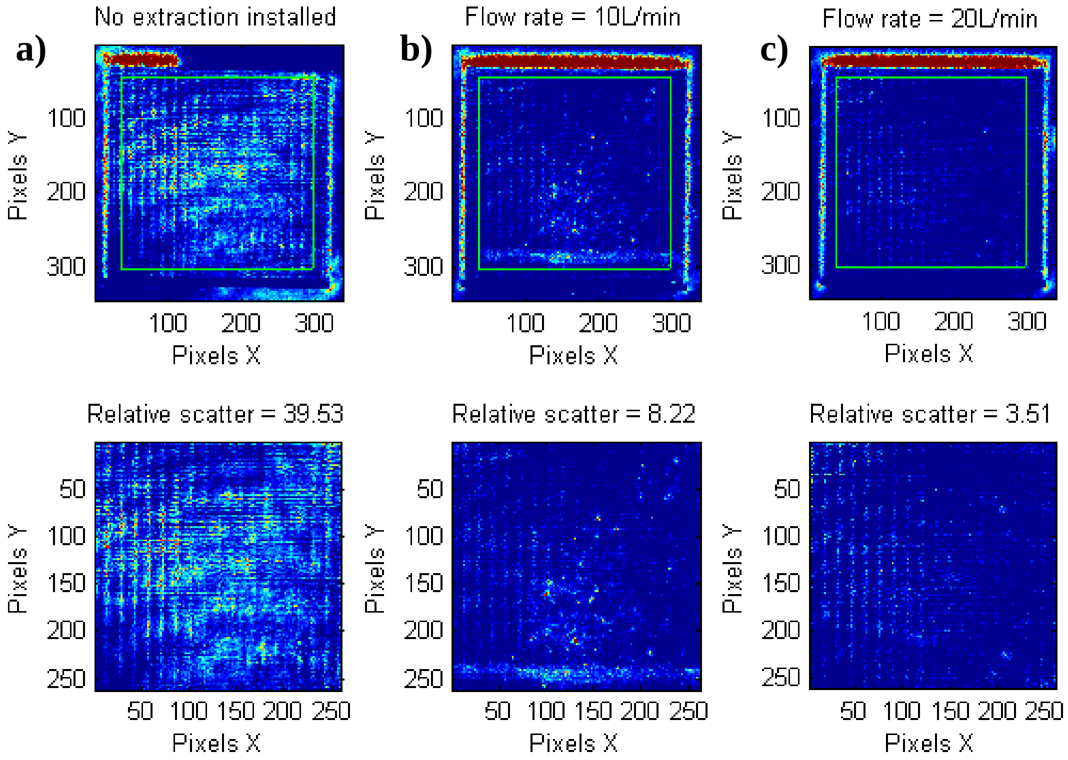

Figure 127: Images showing the scatter produced by test structures cut without the extraction head installed(a), and with the 5mm open nozzle extraction head installed and operating with flow rates of 10 L/min (b) and 20 L/min (c). The lower row show regions of interest indicated by the green box on the upper row.

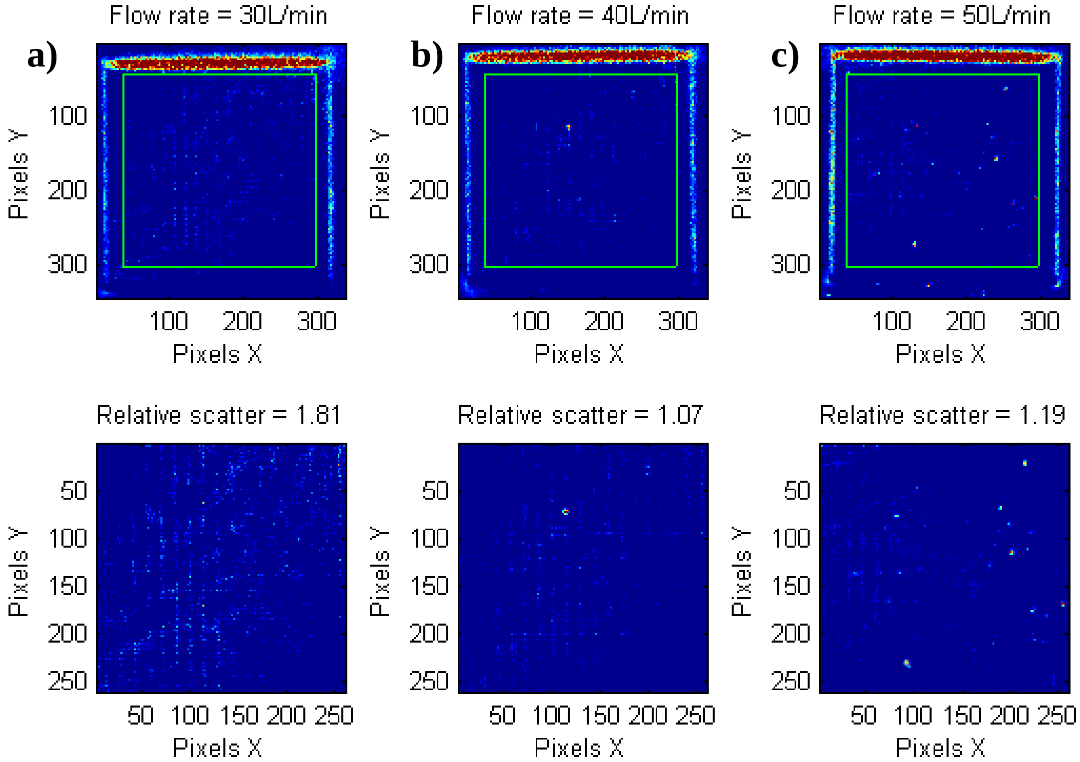

Figure 128: Images showing the scatter produced by test structures cut with the 5mm open nozzle extraction head installed and operating with flow rates of 30 L/min(a), 40 L/min (b) and 50 L/min (c). The lower row show regions of interest indicated by the green box on the upper row.

The circular fringes seen particularly in Figure 127a are due to the use of the spatially coherent HeNe laser with a number of parallel, flat optical components. The vertical bands seen on the images are a result of the cutting process itself, and the horizontal band of increased scattered light seen near the bottom of the 10 Lmin^{-1} flow rate image in Figure 127b is where the silica dust was able to condense and/or coalesce on the nozzle itself due to the low flow rate. This silica dust then fell back on to the surface of the test structure while cutting was taking place, creating a wide band of distortion on the surface.

In order to obtain objective values from the images that could be used for comparison of different extraction conditions, an equally sized region of interest was applied to each test structure in order to remove bias from edge effects (seen at the top of all images in Figure 127 and Figure 128). The pixel intensity values from the regions of interest were averaged, and this provided an indication of how much total scatter was occurring with the region of interest. Plotting these values (Figure 129) show that scatter due to silica dust decreases with increasing extraction flow rate.

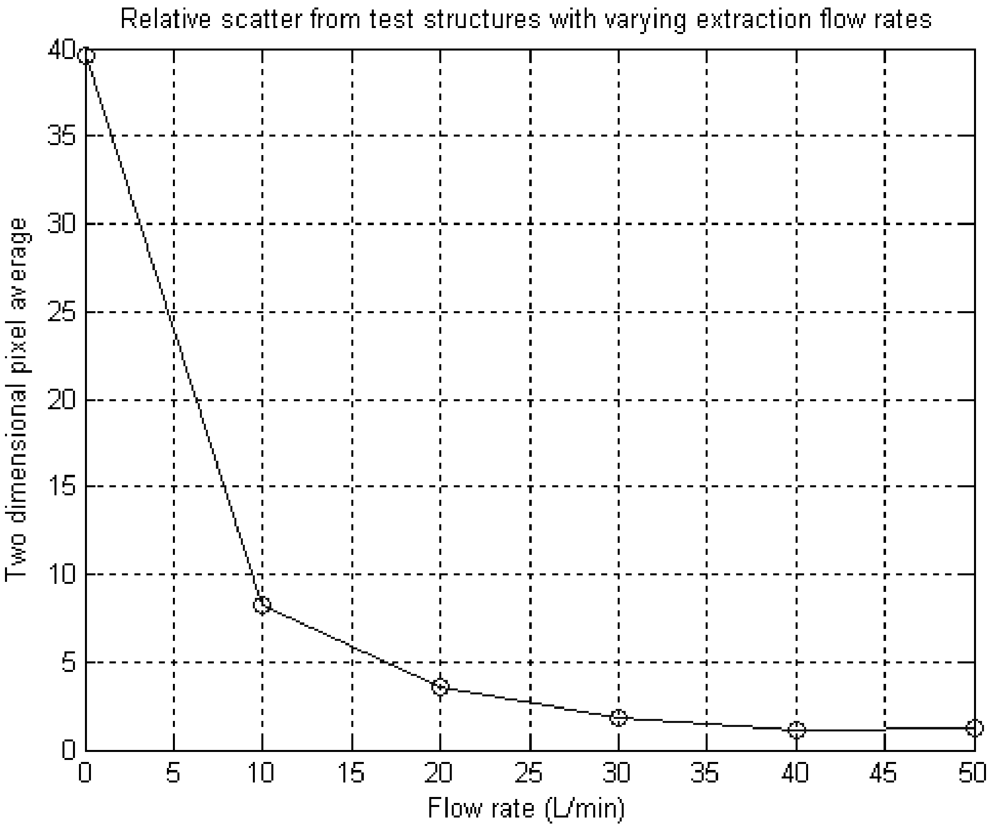

Figure 129: A graph of the two dimensional average of the pixel intensity values from the test structure's regions of interest as it corresponds to the extraction head flow rate used to cut the test structure.

These average values from the region of interest indicate that there is little improvement in silica dust extraction using flow rates greater than 30L/min and no improvement using flow rates greater than 40L/min. As no disadvantages have been noted by using high flow rates, it recommended that the flow rate is at least 40L/min when cutting with the extraction head in place.

The contrast of the signal from the scattered light can be further increased by using a shorter wavelength source to illuminate the sample, because in the Rayleigh scattering regime scattered light intensity is proportional to $\frac{1}{\lambda^4}$ as shown in the following equation taken from [46] that describes the intensity of light scattered from a small spherical particle:

$$I = I_o \frac{1 + cos^2\theta}{2R^2} \left(\frac{2\pi}{\lambda}\right)^4 \left(\frac{n^2 - 1}{n^2 + 2}\right)^2 \left(\frac{d}{2}\right)^6 \tag{63}$$

Where I_o is the initial intensity, θ is the scattering angle, R is the distance from source to the particle, λ is the source wavelength, n is the refractive index of the particle and d is the particle diameter.

$$I = I_o \frac{1 + cos^2\theta}{2R^2} \left(\frac{2\pi}{\lambda}\right)^4 \left(\frac{n^2 - 1}{n^2 + 2}\right)^2 \left(\frac{d}{2}\right)^6$$

Generating a graph of intensity *vs.* wavelength (Figure 130) where $I \propto \frac{1}{\lambda^4}$ allows for analysis on the benefit of altering source wavelength for greater contrast between regions of interest being measured.

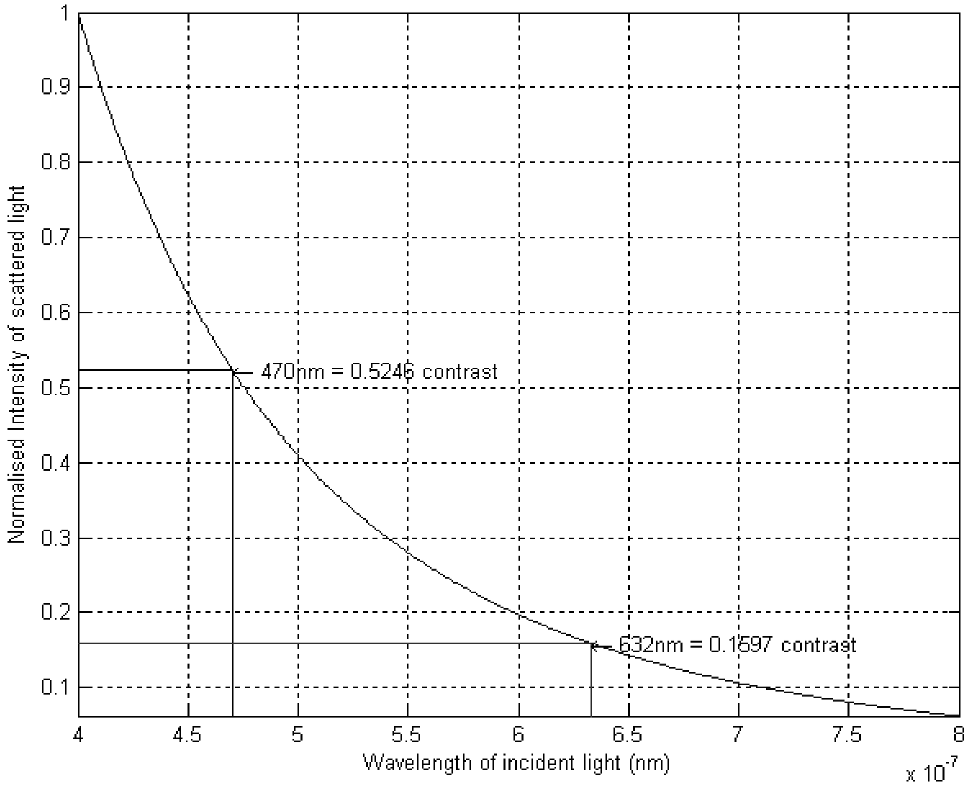

Figure 130: Intensity of the scattered light as a function of the incident wavelength, showing the HeNe source and a 470nm source.

This source should be chosen so that it has a wider emission bandwidth than the HeNe laser in order to eliminate fringing, a suitable example of such a source is the Thorlabs LED470L, which has an emission frequency of 470nm and a bandwidth of 22nm. This increase in contrast produced by a source of 470nm source compared to a 632nm HeNe source is shown on Figure 130).

This test setup has initially shown promise in selectively imaging the silica dust generated by the laser cutting process, enabling the optimization of suction device parameters during standard production processes. This will remove the washing step in single-pass optics as well as remove the inter-pass washing steps on multi-pass optics, the result of which will be decreased processing and handling time per optic.

4.5 – Recommendations for future work

Testing of the extraction systems described here has shown that silica dust can be removed during the cutting process, which results in lower dust deposition on as-cut optical surfaces. In order to further increase reproducibility and reliability and provide a stable manufacturing process, a number of changes to the extraction head geometry should be investigated:

1. In order to eliminate the asymmetry seen in the flow within the extraction head and allow use in all stage motion scenarios, two ports leading from the extraction head to the rotary vane pump should be placed at opposite sides of the extraction head. This will minimise the effect of dust deposition within the extraction head when the orientation of the plumes change due to motion stage direction.

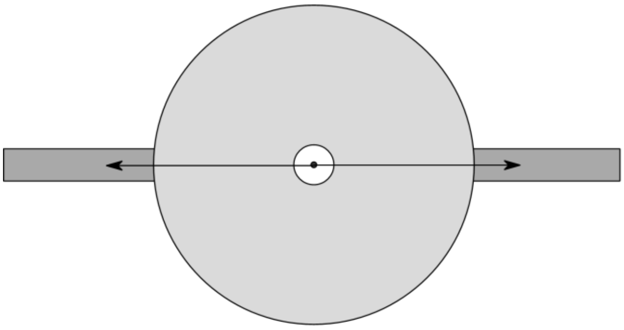

Figure 131: The extraction head shown with two opposing ports leading to the rotary vane pump in order to minimise plume related deposition

2. Offsetting the ports in angle relative to the surface normal at their point of intersection with the extraction head may induce a lateral flow on the particulate/gas mixture travelling from the annulus outwards. This will potentially create a more uniform air flow within the toroidal void and reduce silica dust deposition in localised regions of the extraction head interior as illustrated in Figure 132.

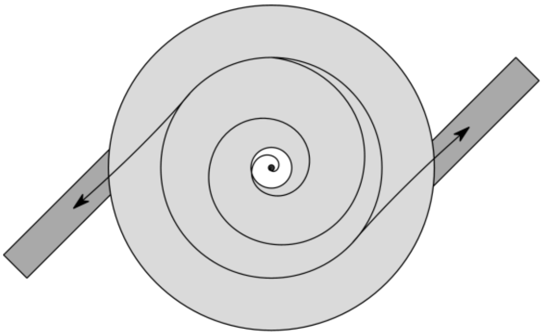

Figure 132: Off-axis ports in order to induce a lateral airflow, homogenising the flow direction and velocity within the toroidal void of the extraction head

3. Minimisation of the toroidal volume in order to remove unnecessary space and geometrical features such as corners should increase the efficiency of the extraction head. If possible, rounding all internal corners may also help increase airflow efficiency as shown in Figure 133.

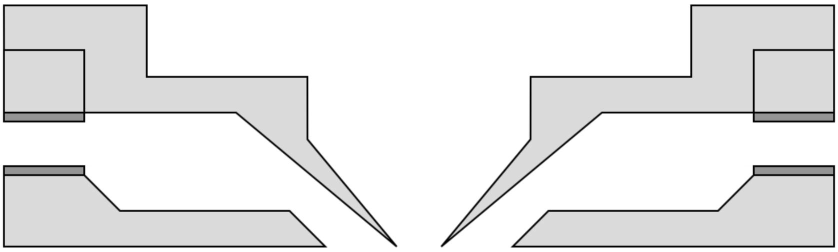

Figure 133: Cross section of the extraction head showing a more streamlined internal design

In addition to geometry changes in the extraction head itself, it may be beneficial to investigate alternative pump options that can achieve flow rates greater than used in this chapter. Based on the scattering measurements, the amount of silica dust present on the substrate after cutting reached a minimum steady state at a flow rate of 40 Lmin^{-1}, however it is anticipated that the flow required to reach this steady state when operating with a two port extraction head will be greater than with a single port alone.

4.6 – Summary and conclusions

This chapter presents a mostly empirical approach for minimisation of silica dust deposition during cutting. Modelling of the gas/particulate mixture thermal properties and flow is non-trivial and would likely require a skilled practitioner in computational fluid dynamics. Nevertheless, the results described show that reduction of silica dust deposition during cutting is possible. Further work needs to be undertaken in order to transform this experiment into a standard production process that can be maintained at reasonable intervals, for example with weekly maintenance checks, and operated by non-engineering personnel. Also presented in this chapter was a method to evaluate the qualitatively evaluate the level of silica dust present on a substrate surface which has the potential for use as a standard inspection tool for quality control purposes.

Chapter 5 – LightForge rapid fabrication service

5.1 – Introduction

One of PowerPhotonic's main long-term strategic goals is to sell large volumes of identical parts for integration into customer production components. Although the volumes of micro-optics purchased are large for products that are in production, the volumes of micro-optics required for research and development projects and feasibility studies are much smaller. In these kinds of projects, a premium is placed on short delivery times, relatively low upfront costs and the flexibility to try a number of designs to empirically determine the optimum design. As these small development projects are the precursors to production projects, PowerPhotonic has a vested interest in supplying micro-optics for both low- and high-volume projects.

The general PowerPhotonic fabrication process is inherently well-suited for low volume, fast turnaround supply in a number of design variants. Additionally the lack of requirement for any custom tooling (e.g. custom moulds or photolithographic masks) means that the upfront costs can be minimised or even eliminated. However applying the product development process described in Chapter 2 to each prototype design largely negates these advantages as it adds time to delivery, upfront cost to the customer in the form of Non-Returnable Engineering (NRE) to cover the internal cost of engineering time for iteration, and makes the supply of multiple variants more difficult as they often require individual product development. As customer development projects do not always transfer to production projects, there is also the risk that PowerPhotonic expend engineering time and effort for little future gain.

The different markets that purchase large numbers of micro-optics are very diverse, with the main 5 being industrial, telecommunications, medical, scientific and defence. The micro-optics each market requires are similarly diverse, ranging from simple cylindrical lens arrays for collimation of laser diode bars to custom phaseplates for correction of accumulated errors within a complex optical system. Examining a number of customer enquiries from each of the stated markets showed that approximately 50% of the requested micro-optical structures fall well within a process space that we have observed as reproducing a given design very well even without applying any product development resource. Specifically the characteristics are:

1. Total sag over the entire required surface is less than approximately 100µm

2. Maximum surface slope compared to the unprocessed surface is less than approximately 10°
3. The spatial sizes of the feature(s) are in the range of 0.25-15mm.
4. Optical centre thickness is 1mm
5. Maximum external dimension (W or H) are not greater than 15mm

Commonly, customers send an optical prescription consisting of a list of representative numbers (e.g. for a lens array: radius of curvature, clear aperture size, number of lenslets) describing the desired component as part of their enquiry. Importantly, most of these potential customers were optical engineers or had access to optical engineering expertise within their own companies, so there was potential for the customer to supply the actual optical surface design instead of the optical prescription. In this situation, where the customer can supply the fully specified surface of a design that does not necessarily require application of the product development process, PowerPhotonic may be able to fabricate a part very quickly with little or no NRE. This concept was particularly appropriate for potential university customers, as they often had significant design knowledge and available time, but strictly limited budgets and requirements of only a very few optics, or even a single optic. Because of this orders from university customers were very infrequently pursued by PowerPhotonic due to the normally high initial NRE costs with possibly no return on the investment.

In order for a system to be developed that could accept a customer surface design for fabrication without requiring product development resource, a new process needed to be developed that would address customer interface, fabrication limitations, fabrication tolerances, pricing and delivery time. A project was launched to investigate an appropriate solution and develop the concept into a branded service that could be used by anyone interested in obtaining a low-cost freeform silica optic within a short time frame. This branded service was to be called LightForge.

5.2 – Concept development

Due to the diverse experience gained in almost all aspects of the PowerPhotonic manufacturing process over the course of this EngD, the LightForge rapid fabrication service was developed and implemented with little requirement for external supervision or guidance. This was a multi-stage process and involved a broad range of technical, commercial and project management tasks that were handled almost entirely by me.

The main tasks were as follows:

1. Establishing standard parameters or processes:
    a. Creation of a file format that would allow for the transfer of customer surface information in a non-ambiguous way
    b. Determining a standardised substrate specification, including external dimensions, location of customer surface on the substrate and the location, type and size of test structures and alignment features
    c. Determining the production process parameters that would best reproduce any given input surface with no engineering input
    d. Creation of a full product specification used to describe the LightForge product to the customer
    e. Determining the best way to package the product so that it arrives safe and clean while also displaying the LightForge brand
    f. Determining what test data or conformance metrics are supplied to a LightForge customer after purchase and manufacture
2. Establishing pricing and delivery:
    a. Determining how to set the price (in multiple currencies) of the LightForge product in order to provide an attractive and affordable option while also providing a suitable return on investment for PowerPhotonic
    b. Setting appropriate price breaks for volumes in order to encourage higher revenue orders
    c. Determining the standard delivery time based on LightForge manufacturing time and average manufacturing queue length
3. Providing a usable interface for interacting with the service:
    a. Creation of a web browser based, online, single real-time session that allows for design submission, price quotation and payment
    b. Integrating a manufacturability rule check that ensures the surface uploaded by the customer is manufacturable using the LightForge process

    c. Real time generation of alternative surfaces that bring an uploaded unmanufacturable surface to a manufacturable state
    d. Setting up an online payment portal that allows for credit card payment through the website
4. Definition of options:
    a. Sourcing a suitable optional broadband anti-reflective (AR) coating that would cover the majority of potential LightForge customers
    b. Designing an optomechanical mount to allow the 1” square substrate to be mounted in standard 2” diameter catalogue optomechanics
5. Customer information transfer:
    a. Writing a custom macro in Zemax Programming Language (ZPL) to automatically extract a desired surface from Zemax non-sequential (NSQ) mode

5.2.1 – File format investigation

Initial consultation with customers who would constitute the market for LightForge indicated that the main tools used for designing optical surfaces were Zemax and Matlab. Internally, PowerPhotonic use a simple file format for describing a surface that is transferable to the laser micromachining rigs. This file format, known internally as gridXYZ, consists of a tab delimited text file from the ASCII character set and specifies surface height data values z at the points defined by a rectangular grid in x and y. This file format is straightforward to generate in Matlab. However, although Zemax has a number of output formats that it can produce, a simple tab delimited surface file is not one of them.

Zemax has two different modes of operation known as sequential (SQ) mode and non-sequential (NSQ) mode. SQ mode is commonly used for classical lens design, optimisation and analysis, whereas NSQ mode functions much more like a computer aided design (CAD) program. Evaluating the use cases of producing a surface design from Zemax showed that NSQ mode provided built-in support for generating optical structures, such as lens arrays, that might be desired by a customer as well as having significantly more flexibility in spatially locating features. Zemax NSQ mode allowed for the export of a number of industry standard file formats including Initial Graphics

Exchange Specification (IGES), STandard for the Exchange of Product model data (STEP) and STereoLithography (STL) formats.

Investigation of the IGES and STEP formats showed that, while they are industry standard formats that are very common particularly with CAD packages, they are also significantly more complex [47] than required to describe a LightForge surface. Implementation of a conversion process to translate from IGES/STEP to gridXYZ was therefore outside the scope of this project. The STL format is widely used in software for stereolithography which is in many ways similar to the PowerPhotonic fabrication process. Surfaces are represented as a collection of tessellated triangles described by the triangle normal vector and the x,y,z locations of the triangle vertices. The STL format describes a surface by placing a triangle vertex at a point of change (i.e. the surface normal at a given point is not parallel to the optical axis in Zemax) on the surface within a set maximum lateral resolution. In order to test the ability of Zemax to generate an STL file from a structure within NSQ mode, a simple system was constructed that consisted of a single plano-convex lens and a detector object located at the lens focus in order to visualise the focussed spot as shown in Figure 134.

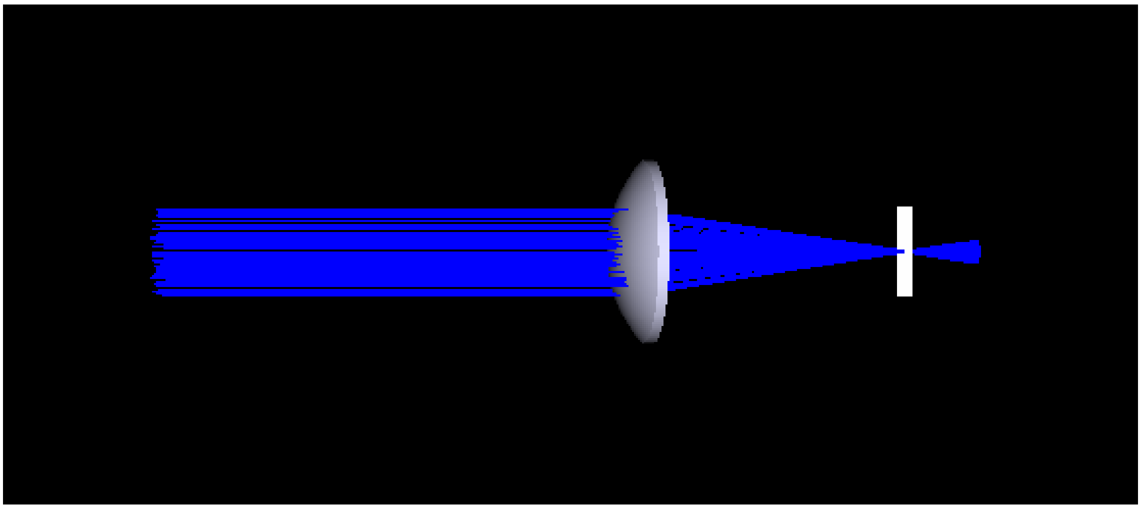

Figure 134: A simple optical system in Zemax NSQ mode: a plano-convex lens focusses a bundle of collimated rays (blue) on to a detector placed at the lens focal point.

The convex surface of the lens was exported from Zemax in the STL format. Although there are fields in the Zemax export control that allow for alteration of the lateral resolution of the STL file, these did not appear to change the output file resolution despite the convex surface slope being constantly changing from point to point. The 3-dimensional surface formed by these points is shown in Figure 135.

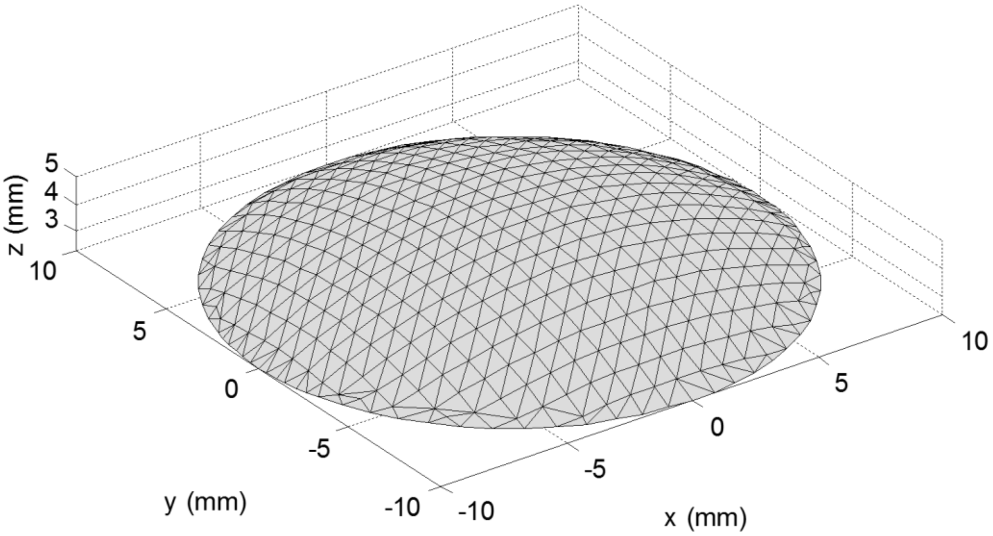

Figure 135: The STL file imported into Matlab, note the triangular array of nodes and the non-uniform point location near the edge.

The simplest way to transform this data, arranged as the vertices of triangles, to the rectilinear array of the gridXYZ format is to use the nodal points described by the triangle vertices rather than regenerating the surface using the triangular surfaces as shown in Figure 136. All of the triangles report their vertices in the .stl format, so almost all of the points have duplicate overlapping triangles associated with them, which were decimated to a single point.

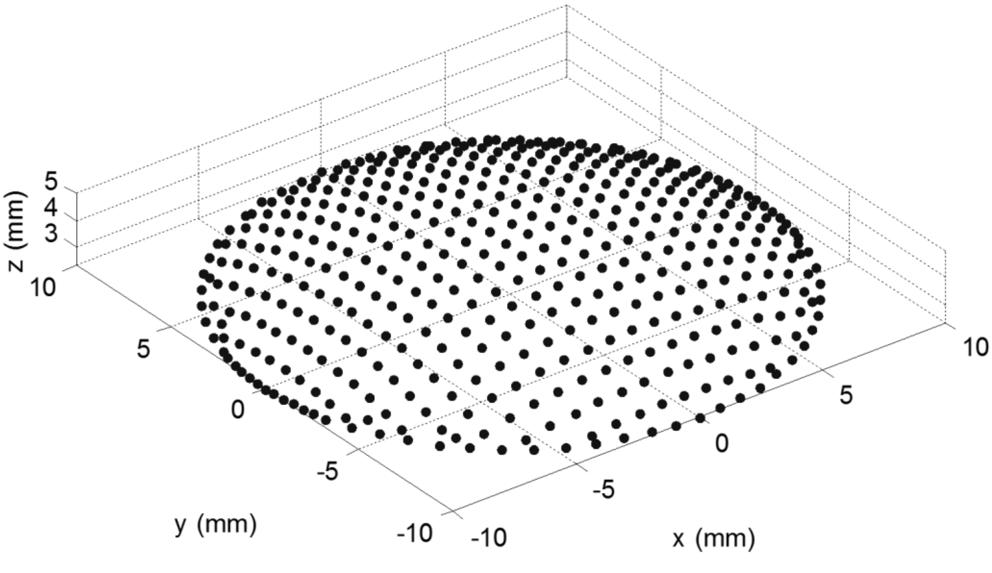

Figure 136: The surface described by the STL nodal points, after deleting all duplicate points

Interpolating the points to a square grid of 0.4x0.4mm resolution gives data that is compatible with the z matrix component of the gridXYZ format as shown in Figure 137.

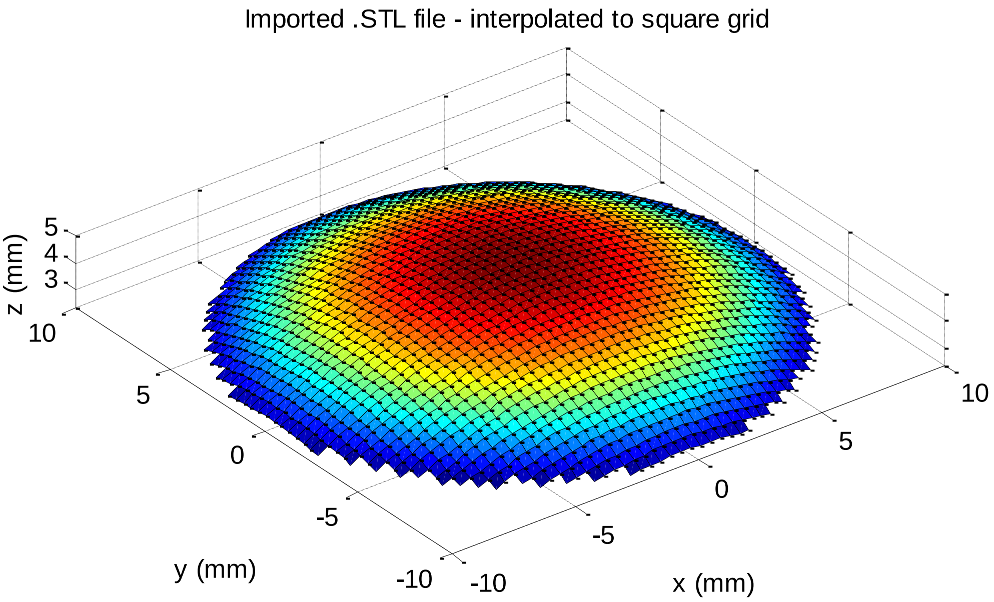

Figure 137: The STL surface after being interpolated to a 0.4x0.4mm grid

In order to determine the optical effect of approximating the lens design using the STL format, as well as the interpolation process that converts the triangle vertices to a square grid, the interpolated surface was exported from Matlab as a Zemax grid sag object. The grid sag format allows Zemax to load and analyse arbitrary surfaces that might be designed using Matlab, and is very similar to the gridXYZ format in content, but differs in layout. The grid sag lens was imported into the environment containing the original plano-convex design and focussing performance was compared.

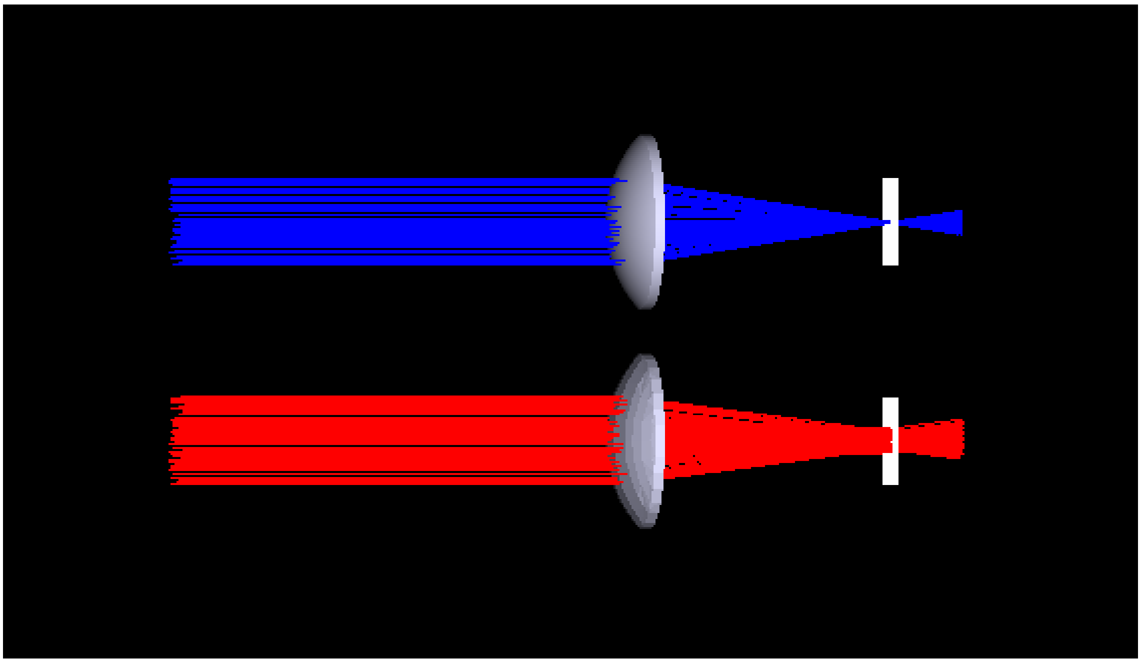

Figure 138: A comparison of simulated focussing performance between the original lens design (blue, top) and the imported, processed STL file (red, bottom). Note the clear facetisation of the imported lens surface.

As can be clearly seen in Figure 138, the focussing performance of the imported lens differs from the original lens design. Taking the difference of the lens profile through the centres of the design and imported lenses shows a maximum of more than 14µm of surface form error on the imported lens, the graph of this difference is shown in Figure 139.

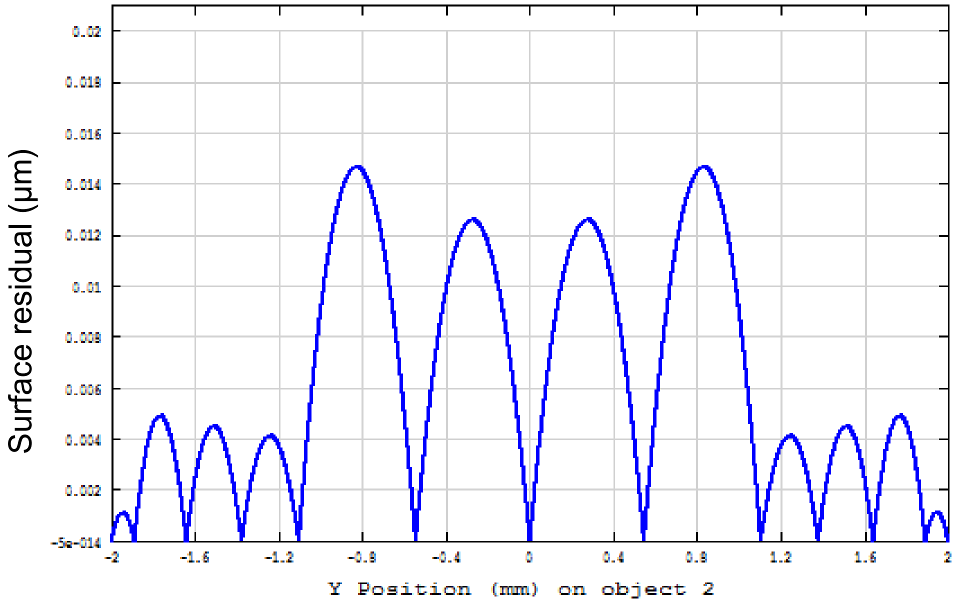

Figure 139: Difference of surface form between the central profiles of the design and imported, processed lens surfaces

Examination of the image at the focal plane using the detectors shows a marked difference as seen in Figure 140

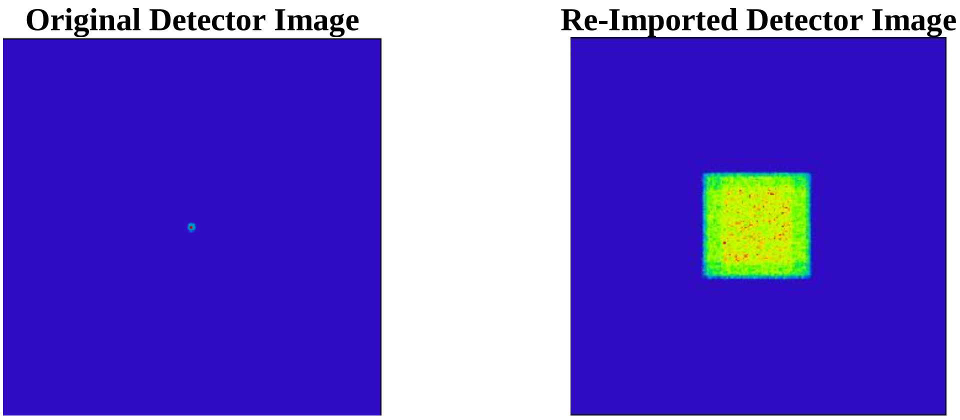

Figure 140: A comparison of focal plane detector image data between the original lens design (left) and the imported, processed design (right). The image size is 5mm x 5mm.

The facetisation of the surface has had a detrimental impact on the focussing performance of the lens, increasing the focussed spot diameter by around 30 times and altering its shape from a circle to a square. The shape alteration is due to the interpolation of the surface to a square grid, giving each facet a square aperture and thus giving a square image in the beam far-field. It is expected that increasing the lateral resolution of the STL file would increase the comparative performance of the imported lens, but this could not be investigated. This level of performance decrease using the STL format would be unacceptable for use with the LightForge process, so use of standard formats built in to Zemax was not an option for the LightForge surface design format.

The Zemax Knowledge Base provided [48] a potential solution for extracting the desired gridXYZ file directly from Zemax using the macro language included in Zemax. The method involves using a single ray which is parallel to the optical axis and is moved in a uniform xy grid over the desired surface. The spatial intercept point between the ray and the surface at the ray position is then calculated and recorded in an external file.

Significantly modifying this method to produce a file of the appropriate resolution in the gridXYZ format makes possible to extract a desired surface directly from Zemax. This modified method was encapsulated in a stand-alone macro file that can be shared and used in different Zemax systems. LightForge customers now regularly use this gridXYZ macro to generate files for uploading to the LightForge website, providing an easy and accurate method of generating LightForge-compatible design files.

5.2.2 – LightForge product definition

Defining the delivered product appropriately was critical in ensuring that the LightForge process effectively fulfilled its main functions of being attractive to potential customers as well as minimising engineering time. Analysis of customer requirements previously fulfilled by PowerPhotonic, showed that the majority of individual parts supplied had optical clear apertures of 10mm or less in the longest direction, with many customer parts having clear apertures of around 3 x 3mm. Often customers would request the same part dimensions with some variant of the optical parameter in order to empirically determine the optimal optical design for their application, for example 5 different lens arrays of the same mechanical dimensions but varying lenslet radius of curvature. The ability to offer this flexibility with relative ease compared to other micro-optics manufacturers is a significant advantage, and needed to be part of the fundamental LightForge concept. For this reason, the clear aperture available through the LightForge process needed to be a few times the size of the most common clear aperture size and accordingly it was determined that a 15 x 15mm clear aperture would be most suitable. This size would accommodate larger single optics and also allow for multiple design variations to be placed within a single substrate.

Internally at PowerPhotonic, the most common substrate used has dimensions of 25.4 x 25.4 x 1mm (width x height x thickness), as this easily accommodated the 15 x 15mm clear aperture it was decided that this would be the standard substrate used for all LightForge parts. The clear aperture is centred on the substrate and, to avoid manufacturing errors near the aperture's edge, a 250µm wide border is added around the entirety of the aperture. This border is parabolic in shape, with endpoints located at the clear aperture edge and the uncut substrate surface, ensuring that there are no sharp transitions between the machined and unmachined surfaces.

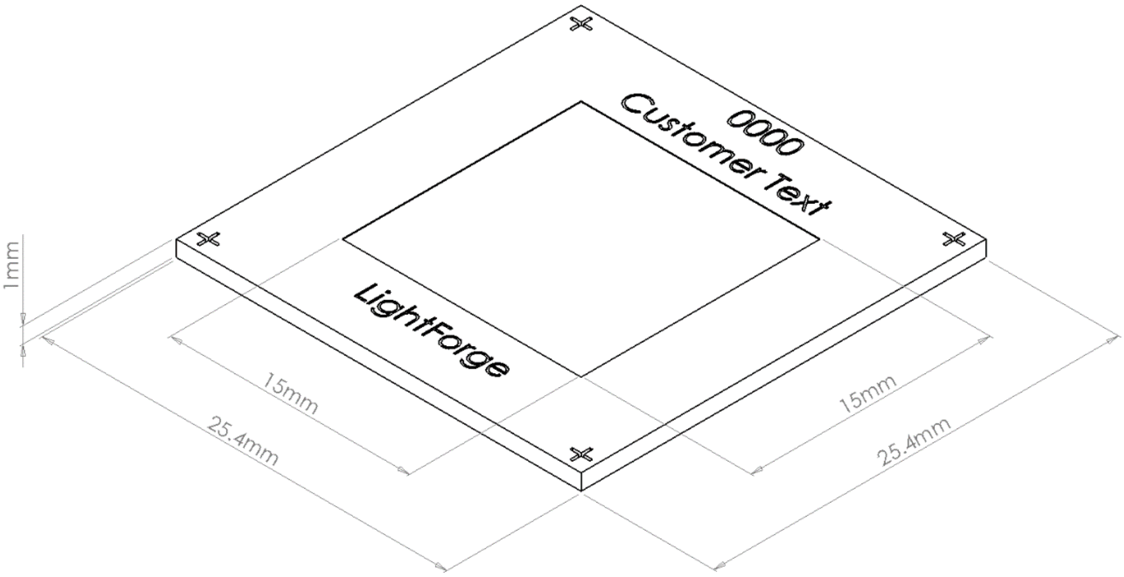

Figure 141: An isometric drawing of the standard LightForge layout showing standard features and mechanical dimensions of the substrate and clear aperture.

In order to identify the parts internally, a 4 digit identifier is cut in to the substrate as standard. For more intuitive identification by the customer the LightForge process offers the option to add up to 30 characters of text that are also cut in to the substrate along with a LightForge logo. For alignment purposes, 4 fiducials are added in the corners of the substrate that are precisely located with respect to the clear aperture. These features can be seen in Figure 141.

5.2.3 – Process parameters and product specification

Like the choice of substrate, the set of process parameters used needed to be well understood and commonly calibrated. This would ensure that the LightForge process remained stable without requiring extra production or engineering time.

Two cut passes were required in order to maximise symmetry for any given surface input, which limits the maximum depth of the material that can be removed. The most commonly used two pass cutting strategy can produce a maximum depth of 67µm, though it had been observed that the accuracy of the machined profile decreased slightly when cutting approaches the maximum depth of a given cut strategy. This is likely due to a deviation from a linear fit for the energy-depth relationship at high energy values. Therefore a maximum depth of 55µm was established which, in conjunction with a 5µm minimum depth, gives a maximum allowable sag for the LightForge process of 50µm.

Through discussion with customers, it was found that the specified values of surface depth scaling and form error (see Chapter 2) would need to be low enough to provide good performance in their system, but did not need to be as low as fully optimised and iterated parts. The surface scaling value is closely related to the variability of the laser micromachining process during fabrication of the optic, which was well understood to be <±3% change in slope of the energy-depth curve. Therefore the specification for surface depth scaling was set to be ±3%. The form error value needed to be low enough to remain attractive to potential customers but also high enough to account for any surface that could be made using LightForge. Analysis of a variety of previously fabricated parts that had sags of 50µm showed that surfaces with slopes of ≤8^o had RMS form error values of 200-300nm. Therefore the specification for form error was decided to be 500nm RMS for surface slopes ≤8^o in order to allow for unforeseen surfaces to remain within the form error specification. Surfaces with slopes above the 8^o limited are supplied without a form error specification on a best effort basis.

In order to ensure the clear aperture of the manufactured LightForge is consistent with the specification, and because the contents of the LightForge clear area were not necessarily known to PowerPhotonic, the full clear aperture must be measured and compared to design as a single dataset. Each surface was scanned after fabrication using a STIL CHR-350 non-contact chromatic confocal probe with a resolution of 10x50µm. This scan data is then compared to the design surface, scaling error is calculated and the scaled surface is subtracted from the design surface to obtain a surface form residual map. From this residual map the RMS form error is then obtained. If the values obtained for scaling and form error are lower than ±3% and 500nm RMS for slopes ≤8^o respectively, the part is judged to have met the specification criteria and is acceptable for delivery to the customer.

5.2.4 – Optomechanical mount

Although it is practical to use a square substrate for LightForge from the point of view of manufacturing, a square substrate is less practical for use in laboratory optical setups. A number of optomechanics vendors offer a wide range of mounts, translation stages and other optomechanical devices for round optics but a much more limited selection for square or rectangular optics. In order for a customer to quickly integrate a LightForge part in to an existing optical system using standard optomechanics, an interface mount was designed that would allow the square part to be mounted in standard 2” diameter optomechanics. The mechanical drawing of the mount is shown in Figure 142.

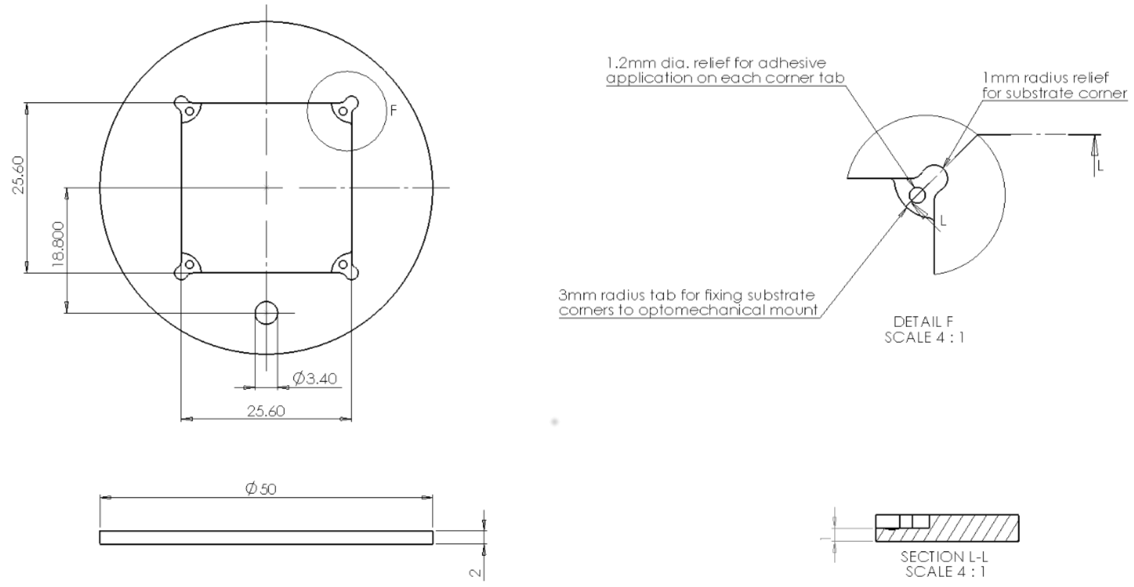

Figure 142: A mechanical drawing of the LightForge optomechanical mount detailing the main features.

The optomechanical mount is offered as an additional option.

5.3 – LightForge process

The initial objectives of LightForge were as follows:

1. To expand the PowerPhotonic customer base by capturing segments of new markets that could benefit from custom micro-optics.
2. To offer a product with superior characteristics (performance, price, lead time, etc.) over current custom micro-optic suppliers.
3. To reduce PowerPhotonic engineering time to a minimum when creating a product.
4. To increase the visibility of PowerPhotonic services by offering a product which has low barriers to entry, and enables quick and inexpensive qualification of PowerPhotonic fabrication technology.
5. To create an easy to use process to order custom micro-optics.

Integral to most of these objectives, is the requirement for an intuitive graphical user interface that provides clear feedback to the customer the component which is being ordered, as well as the ability for the software to automatically check the input file to ensure that it corresponds to a manufacturable surface. Therefore a website was designed with both functionality and ergonomics in mind, with the web page construction and data processing interface being provided by a subcontracted company called Objective Associates.

5.3.1 – Graphical User Interface (GUI)

The GUI (seen in Figure 143) was designed to be a single webpage that would allow for design upload, provide an image of the part that would be made, display pricing, give feedback from the rule check program, input customer information and accept payment.

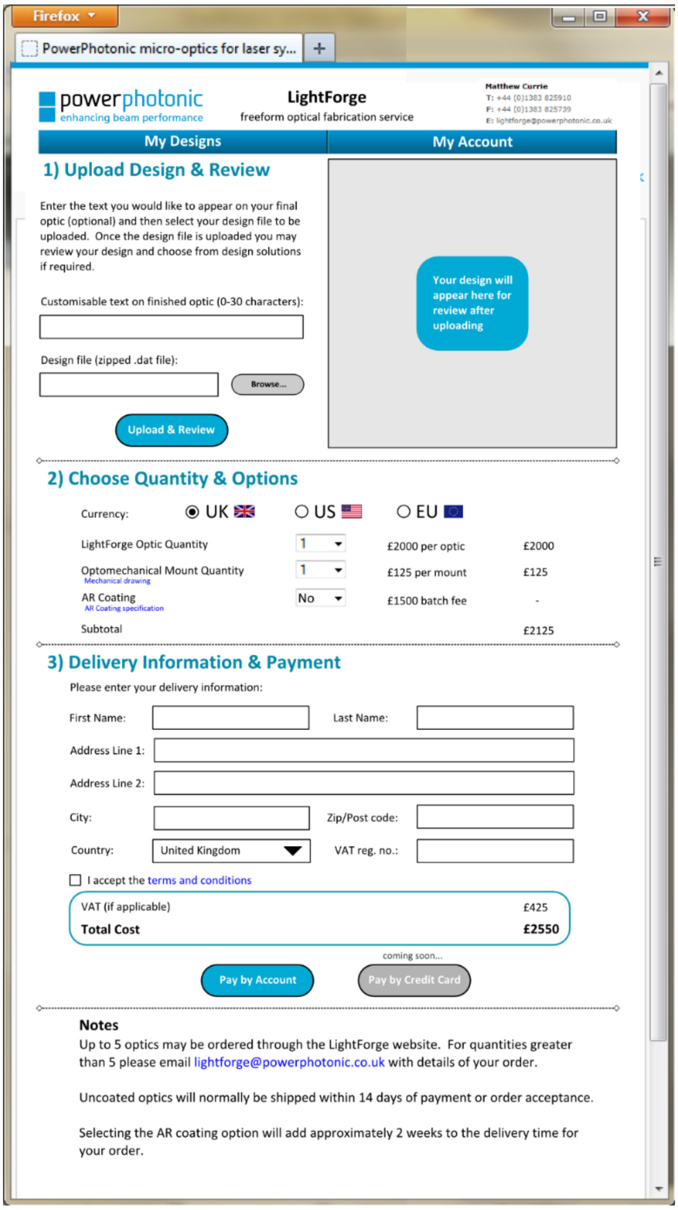

LightForge
freeform optical fabrication service

Matthew Currie
T: +44 (0)1383 825910
F: +44 (0)1383 825739
E: lightforge@powerphotonic.co.uk

1) Upload Design & Review

Enter the text you would like to appear on your final optic (optional) and then select your design file to be uploaded. Once the design file is uploaded you may review your design and choose from design solutions if required.

Customisable text on finished optic (0-30 characters):

Design file (zipped .dat file):

2) Choose Quantity & Options

Currency: ● UK ○ US ○ EU

LightForge Optic Quantity	1	£2000 per optic	£2000
Optomechanical Mount Quantity Mechanical drawing	1	£125 per mount	£125
AR Coating AR Coating specification	No	£1500 batch fee	-
Subtotal			£2125

3) Delivery Information & Payment

Please enter your delivery information:

First Name: Last Name:
Address Line 1:
Address Line 2:
City: Zip/Post code:
Country: United Kingdom VAT reg. no.:

☐ I accept the terms and conditions

VAT (if applicable)	£425
Total Cost	**£2550**

Notes

Up to 5 optics may be ordered through the LightForge website. For quantities greater than 5 please email lightforge@powerphotonic.co.uk with details of your order.

Uncoated optics will normally be shipped within 14 days of payment or order acceptance.

Selecting the AR coating option will add approximately 2 weeks to the delivery time for your order.

Figure 143: The main page of the LightForge process that allows for design upload, feedback and payment.

The LightForge process is designed to be a What You See Is What You Get (WYSIWYG) process, showing representations of the final complete part that will be delivered. To illustrate, consider a concave hexagonal lens array uploaded through LightForge as shown in Figure 144.

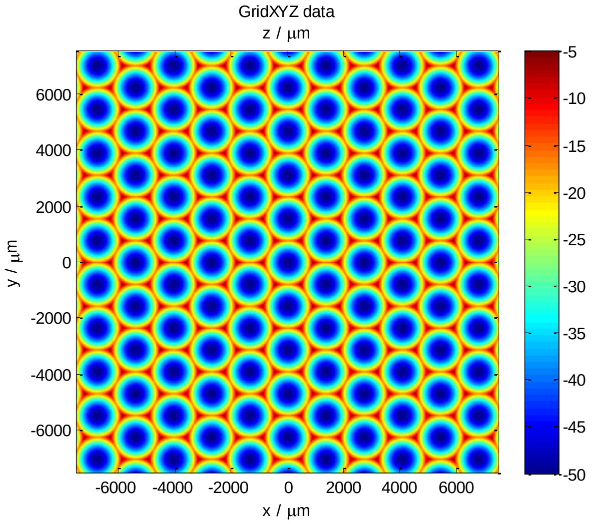

Figure 144: An example of a concave hexagonal lens array surface design in LightForge format, before uploading to the LightForge server.

The design surface is displayed after upload as it will be placed on the actual part, along with all accompanying features such as optional customised text, fiducials, LightForge logo, substrate identifier and also with added parabolic border as seen in Figure 145.

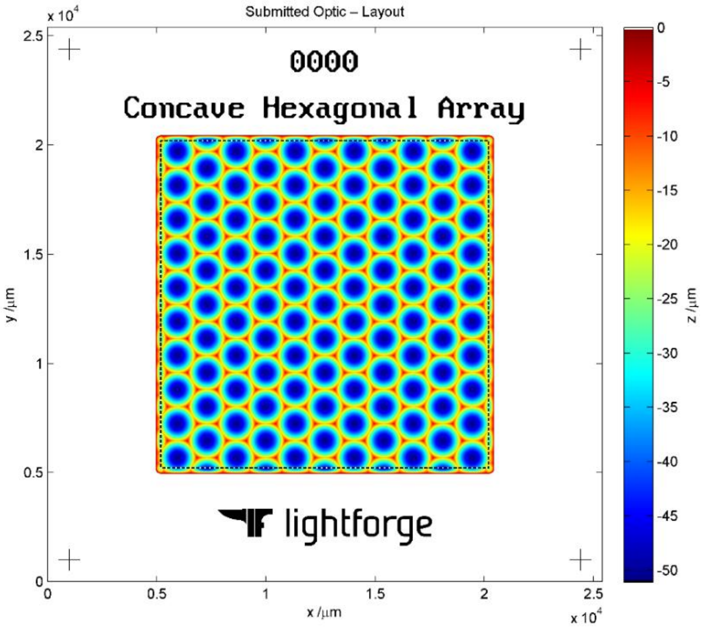

Figure 145: The concave hexagonal array after uploading to the LightForge server, showing the layout of the actual part to be manufactured. The area within the dotted black lines in the clear aperture denotes the originally uploaded surface.

5.3.2 – Rule check and potential solutions

The rule check function within LightForge is used to analyse whether a given surface fits the guidelines described to potential customers. One of the rules, the sag limitation, can also suggest solutions to the design and apply them on-line without requiring the user to regenerate the design off-line. The full list of rules that are analysed when a surface has been uploaded are:

1. Critical: The file must be in gridXYZ format
2. Critical: The grid must be on a 10x10µm spacing
3. Critical: The units must be in micrometres
4. Critical: The size of the surface in x or y must be ≤15000µm
5. Solvable: The maximum sag of the surface must be ≤50µm

The critical errors are not solvable online and the surfaces must be regenerated off-line to correct for the error, using feedback provided by the LightForge system to address the nature of the error. The sag limitation is solvable online, by processing the data to truncate the optical surface. Three different methods of truncation are offered to the user (shown in Figure 146), allowing for choice of the most appropriate method based on the user's application and ultimate use of the part.

1. Truncate from bottom – This function sets any point values in the surface that are less than -50µm to have values of -50µm. This is useful for preserving the functionality of surfaces like convex lens arrays.
2. Truncate from top – This function applies an offset to all points in the surface so that the minimum height point is located at -50µm, then sets all point values with a height greater than 0µm to be 0µm. This is useful for preserving the functionality of surfaces like concave lens arrays.
3. Truncate around midpoint – This function sets the point of the surface that's midway between the minimum and maximum values to be -25µm, that then sets all point values with height greater than 0µm to be 0µm and sets all point values that are less than -50µm to have values of -50µm. This is useful for preserving the most of the functionality of surfaces like cubic phase plates.

These options are presented only in the event of a sag limit rule failure.

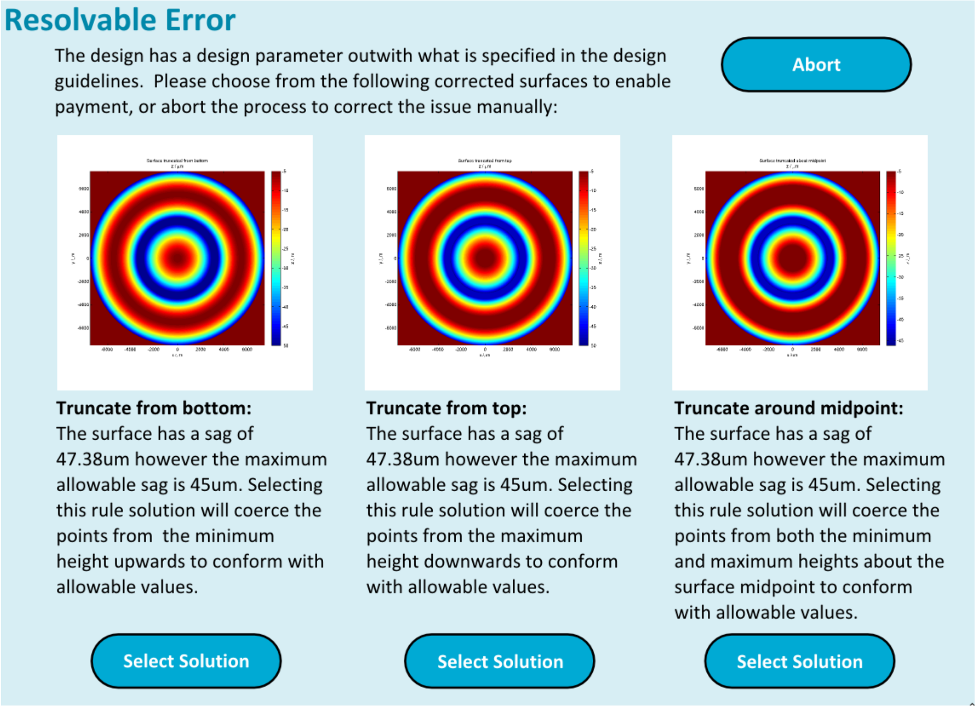

Resolvable Error

The design has a design parameter outwith what is specified in the design guidelines. Please choose from the following corrected surfaces to enable payment, or abort the process to correct the issue manually:

Truncate from bottom:
The surface has a sag of 47.38um however the maximum allowable sag is 45um. Selecting this rule solution will coerce the points from the minimum height upwards to conform with allowable values.

Truncate from top:
The surface has a sag of 47.38um however the maximum allowable sag is 45um. Selecting this rule solution will coerce the points from the maximum height downwards to conform with allowable values.

Truncate around midpoint:
The surface has a sag of 47.38um however the maximum allowable sag is 45um. Selecting this rule solution will coerce the points from both the minimum and maximum heights about the surface midpoint to conform with allowable values.

Figure 146: The interface presented when a sag limit rule failure has occurred, presenting the three options along with descriptive text and images of the corrected surfaces. In this case the truncate from bottom rule is the most appropriate as it preserves the functionality of the convex lenses in the surface.

5.3.3 – User experience flow chart

The different stages of the user experience can be most effectively illustrated using a flow chart (Figure 147), showing the actions and decisions available to a LightForge user:

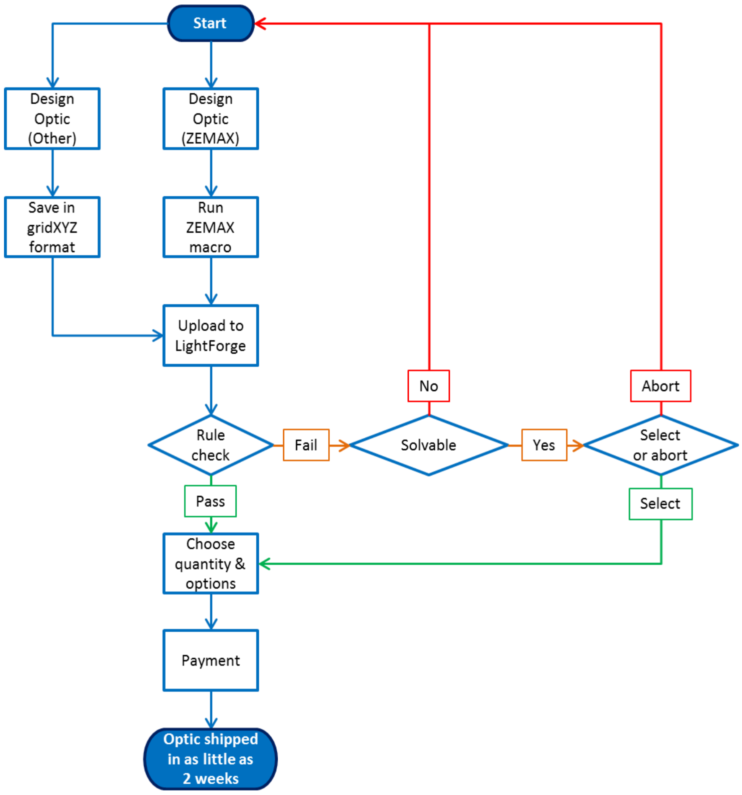

Figure 147: The LightForge user experience flow chart

5.3.4 – Backend implementation

Due to the requirement for custom data processing, image generation and interfacing with a web server, the data processing was written in Matlab and compiled as command line accessible executable functions. These functions reside on a remotely accessible web server and are called by the web server when an action is required. A strict folder structure was defined for the webserver that would allow the Matlab functions to be executed by the web server at the appropriate time. Communication between the Matlab functions and the web server was handled using appropriately named text files that flagged the outcome of an action. An OpenOffice spreadsheet contains most of the variables and feedback text used by these functions, which is loaded by the functions upon their execution. This allows many parameters, for example the sag limit or the width of the parabolic border, to be changed without requiring recompilation of the Matlab functions.

There are three separate functions used, with two of them used on every LightForge submission and the remaining function only used if a sag limit rule failure is encountered. These functions, their actions and outputs are as follows:

LayoutRuleCheck

The LayoutRuleCheck function loads the user supplied gridXYZ surface, user supplied text (if any) and LightForge logo. It then applies a piston term to the surface so that the maximum height point in the surface is located at the maximum height specified in the control spreadsheet. A rule check is run to check for critical errors, if one is found this function terminates the process and creates Abort_Text.txt file that contains information on the critical error. The function then generates and saves a gridXYZ fiducial element as specified in the control spreadsheet as well as a gridXYZ map of the user supplied text (if any). The x,y coordinates of the user supplied surface are then changed so that it is located centred on the 25.4 x 25.4mm LightForge substrate. A parabolic border is added around the entirety of the user supplied surface with width as specified in the control spreadsheet. The function then generates and saves an image of the substrate layout for the submitted design (this occurs and is displayed even if a solvable error is detected). It then generates an empty text file Image_Ready.txt to signal to the webserver that the substrate layout image is ready for display to the user.

The function then checks for solvable errors, if no errors are found it saves the modified optic surface and generates an empty text file Cut_Ready.txt to signal the webserver that initial processing is complete and payment actions can be unlocked. If an error is found, the function generates and saves images corresponding to the solved surfaces using the different solution methods available. It also generates Rule_Text.txt files for each solution method that describes the solution and its potential impact on the surface as well as generating an empty text file Rule_Ready.txt to signal the webserver that a solvable error has been detected.

SelectSolution – only executed if Rule_Ready.txt exists

If the Rule_Ready.txt file exists, indicating that the customer supplied surface has a solvable error, the SelectSolution function loads the user supplied gridXYZ surface, previously generated gridXYZ of fiducial and user supplied text (if any) and LightForge logo. It then applies the solution method chosen by the user. The method choice is communicated using a tag in the command line when the webserver executes this function. As in LayoutRuleCheck, SelectSolution adds a parabolic border around the entirety of the user supplied surface with width as specified in the control spreadsheet. It then generates and saves an image of the substrate layout for the corrected design, as well as an empty text file called Corrected_Image_Ready.txt to signal to the webserver that the corrected substrate layout image is ready for display to the user. The function then saves the corrected optic surface and generates empty text file called Cut_Ready.txt to signal the webserver that initial processing is complete and payment actions can be unlocked.

PrepareFiles – only executed after a payment method is chosen by the user

The last function, PrepareFiles, creates a descriptor file used by the PowerPhotonic laser micromachining software for each of the structures to be fabricated. It then creates a folder structure compatible with internal PowerPhotonic structure and moves all files in to the appropriate locations, along with the Layout_Image and a text file generated by the webserver containing information relevant for production such as job number and number of optics ordered.

These three functions, in conjunction with the webserver, create three use cases for the backend of the LightForge process: abort after critical error, success after solvable error and success with no error. These use cases can be effectively illustrated using Rummler-Brache (swimlane) diagrams which show the processes undertaken by customer, webserver and functions as well as the action of the interface files. These swimlane diagrams are shown in Figure 148, Figure 149 and Figure 150.

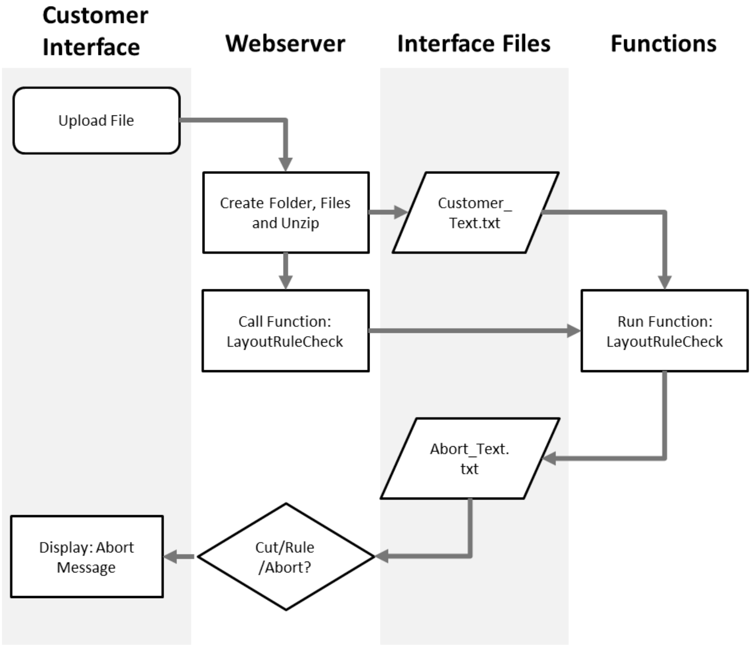

Figure 148: The processes and files involved in an "abort after critical error" event.

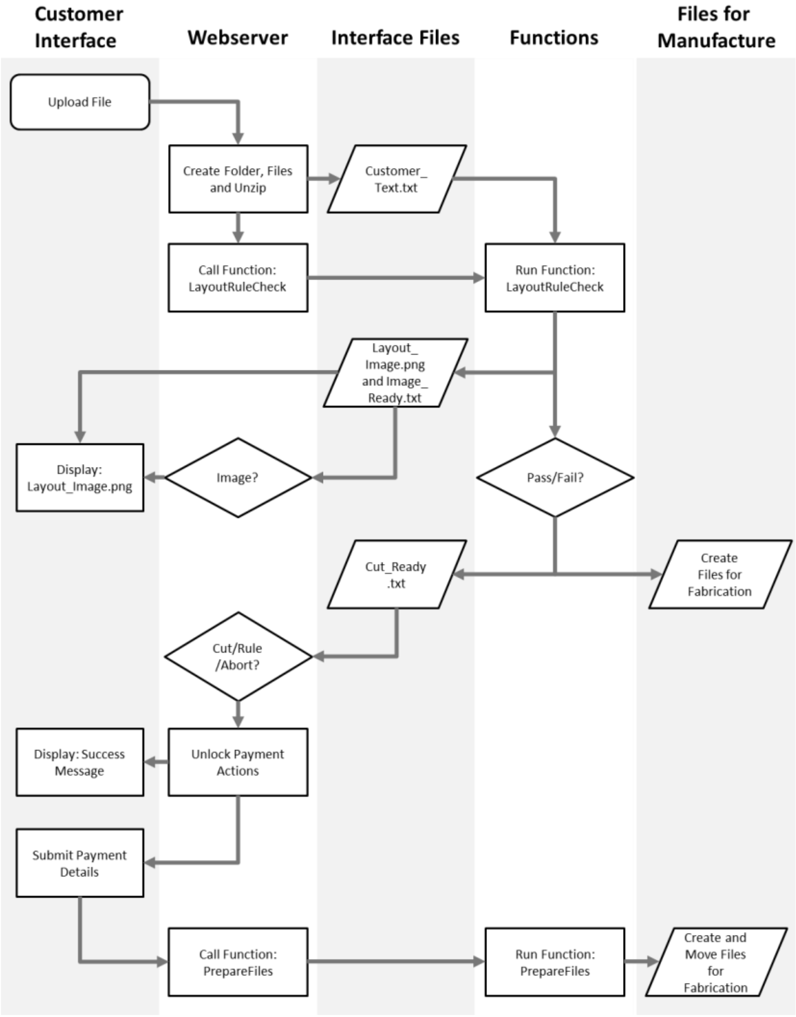

Figure 149: The processes and files involved in a "success with no error" event.

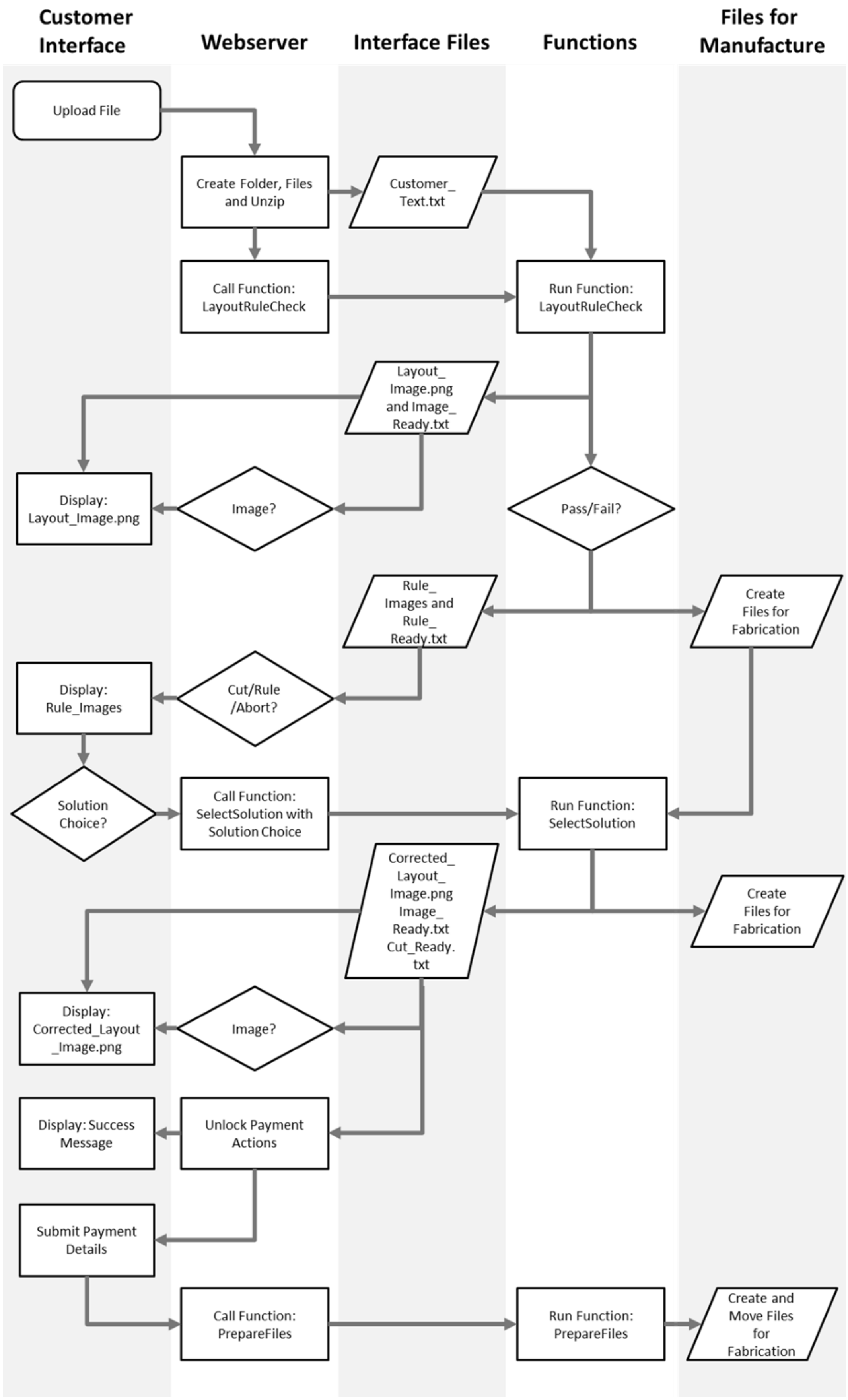

Figure 150: The processes and files involved in a "success after solvable error" event.

The result of this processing and file manipulation is such that when a LightForge design is ordered there is no upfront engineering resource required to analyse or modify the files to check their manufacturability or make them manufacturable. The LightForge files are organised to match the internal PowerPhotonic file management structure and thus a non-engineer can download the checked and formatted files directly for use on the laser micromachining system.

5.5 – Example of LightForge impact

The very first LightForge part fabricated was a cubic phase plate (shown in Figure 151) ordered by a team consisting of researchers from the University of Tartu and the Max Planck Institute for Science and Light, and was the subject of a paper [49] which compared the performance of the LightForge cubic phase plate with a spatial light modulator (SLM) in generating a laser beam that has a nondispersing Airy intensity distribution. Laser beams with Airy intensity distributions have shown promise in various fields, particularly in micromachining of diamond and silicon [50], and the ability to create a nondispersing beam with a single optical element allows for greater flexibility in integrating this functionality in to future micromachining applications.

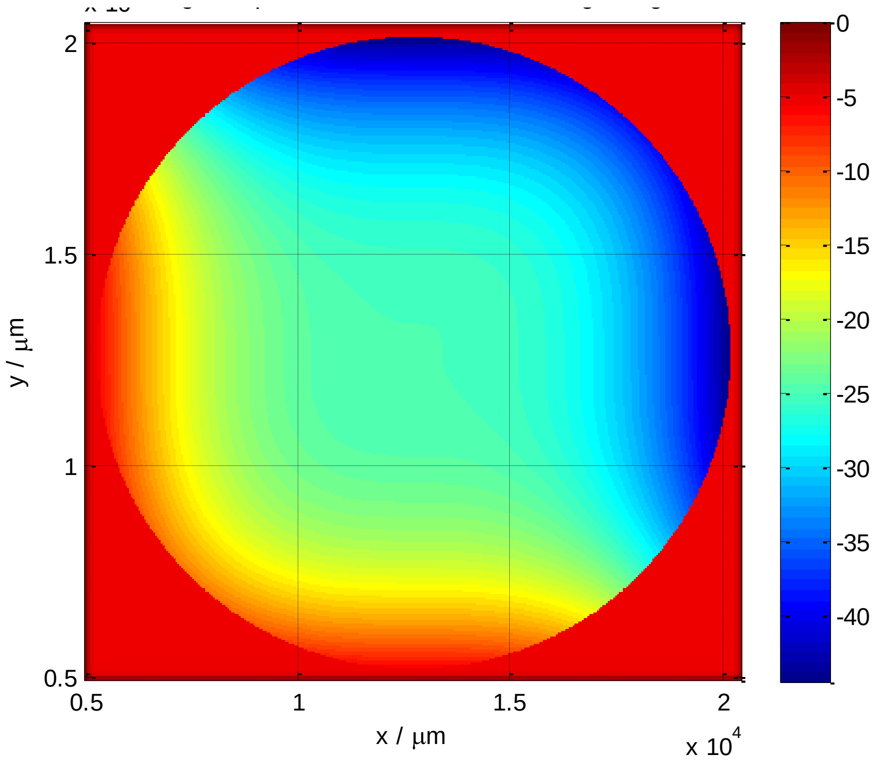

Figure 151: The cubic phase plate surface design that was manufactured by LightForge.

As described in [49], a laser beam with a cubic phase profile is used to create an Airy intensity distribution when Fourier transformed by a suitable lens. This phase profile has previously been generated using an SLM [51], but due to phase discontinuities in an SLM the Airy distribution showed strong dispersion (represented by noise in the images shown in Figure 152).

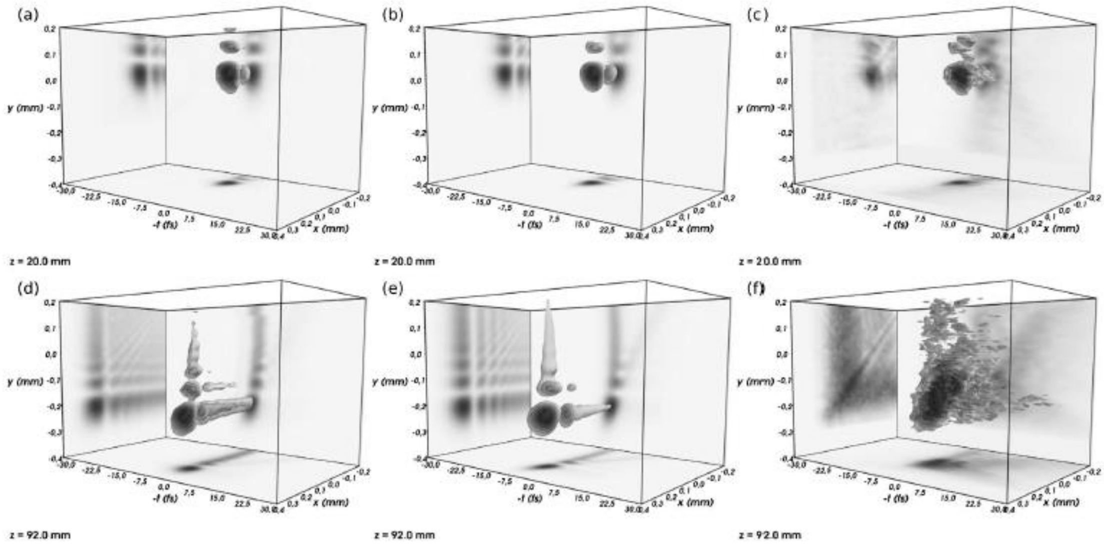

Figure 152: The spatiotemporal impulse responses at different propagation distances using the LightForge cubic phase plate (a and d), simulation (b and e) and an SLM (c and f). Taken from [49].

As the PowerPhotonic process cannot create discontinuities but instead creates smooth and continuous surfaces, it seems an ideal candidate to manufacture a phase plate that imposes a continuous cubic phase profile on a transmitted laser beam. The design was manufactured using the standard LightForge process and compared directly with an SLM using a white-light spectral interferometer to characterise the spatiotemporal impulse response of the two systems. The work showed that the cubic phase plate manufactured using LightForge was significantly better at producing a laser beam with a nondispersing Airy distribution than the SLM, and was close to theoretical simulation.

5.6 – Recommendations for future work

A number of improvements have been envisioned and suggested by customers since the launch of LightForge. Some of these improvements can be implemented without significant change to the architecture, some would require expansion or redefinition of the interface between the functions and webserver, and some involve fundamental changes to the functions and/or webserver themselves. Many of these improvements are desirable, but they fell outside the scope and timeframe given to this project and would likely involve on-going work to implement. Some of these are described below.

1. **Parameterised models:** Currently the LightForge process only accepts a fully specified surface design, however it could be expanded to generate a full specified surface design based on customer supplied parameters. For example if a user required a cylindrical lens array of 1.2mm pitch and 10mm focal length, software could generate this surface to fill the LightForge clear aperture instead of being uploaded by the user.

2. **Enhance the scope of rule checking:** Although the sag of an optic is very important to its manufacturability, other important parameters include its maximum absolute surface slope and the size of individual features in the surface. These rule checks would be beneficial, although due to their nature it would be difficult to offer solutions if they fail and they would likely remain as advisory warnings that the surface is not within specification.

3. **Zemax integration:** Discussion with Radiant Zemax has shown that it is possible to integrate the functionality of the gridXYZ macro, as described in Subsection 5.2.1, into Zemax itself. The current macro is relatively slow and takes about 30 minutes to create a LightForge compatible surface. Radiant Zemax are confident that an extension can be created for Zemax which generates the same gridXYZ file in a fraction of the time taken by the macro. Integration into Zemax, the main optical design package used in the laser and micro-optics industry, also acts as an effective marketing tool by increasing visibility of the LightForge service with an audience ideally suited to use it.

4. **Supply of Grid Sag file describing fabricated surface:** Zemax supports a file type called Grid Sag, that is somewhat similar to the gridXYZ format, but consists of 3 vectors describing x,y and z instead of a z matrix. This surface allows Zemax to import freeform surfaces that aren't easily described using the built-in objects, and their effect on a system can be simulated. As each fabricated part is fully measured using a non-contact profilometer, it is possible for the measurement file to be converted to Grid Sag format and supplied to the customer in order to simulate the performance of the real optic.

5. **Application of process filter function to design for visualisation:** The measured process filter function could be applied to the design in 2 dimensions for visualisation purposes, increasing the accuracy of the feedback given before

purchase. This could be used to highlight areas where change is above a specified threshold, such as vertical edges in the design or very small features.

6. **Function/webserver interface change:** The mechanics of the interface between the compiled functions and the website can be changed so that the functions have more flexibility in controlling content produced for display, for example by removing the empty text files acting as flags and pushing images and information to the website using cURL.
7. **Recompile individual functions as a single DLL:** The Matlab compiler also has the capability to compile functions as DLL (Dynamic Link Library) files which can contain multiple different functions that are called when required. Compiling all functions into a single DLL makes for easier version control and heightened ability to add and improve functionality in the future. This may also reduce the processing time required to complete the rule checking process (particularly if a solvable rule failure is detected) as data can be kept in memory in between function calls.

5.7 – Summary and conclusions

A patent describing the LightForge process has been applied for in the UK [52] and the US [53]. Since the LightForge service was launched in March 2013, there have been a total of 19 LightForge parts ordered from 12 different customers and providing a combined revenue of £28,940. The customer base has been a varied mix of commercial enterprises, military contractors and research establishments, with sales to commercial enterprises being the most numerous as seen in Figure 153.

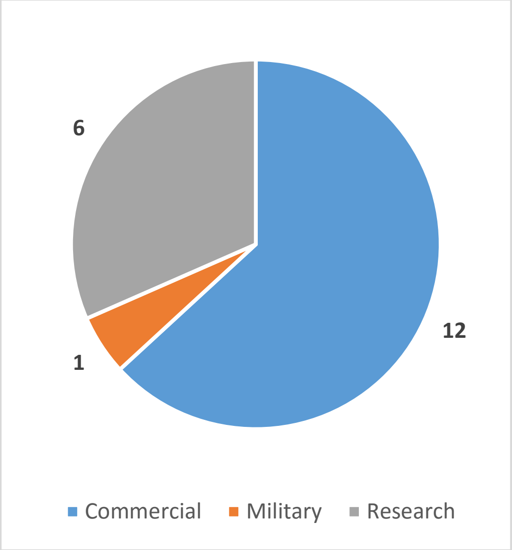

Figure 153: A breakdown of the types of customers that have purchased LightForge parts.

Since the first successful trial described in Section 5.5, the team of researchers have expanded to include researchers at the University of St. Andrews and have purchased a further 4 LightForge parts. This result has been of particular note as it shows LightForge has fulfilled the objective of successfully providing optics to university customers that previously were difficult to address while recouping all engineering costs. This also acts as a marketing tool because as the students potentially move on from their university career to an industrial setting they will carry the concept of LightForge with them, seeding commercial institutions with knowledge of the service.

Examination of the markets inhabited by each customer (see Figure 154) shows that the 19 LightForge parts ordered were destined for 9 distinct and diverse markets, with the actual clear apertures ranging from simple lens arrays to highly complex beamshapers.

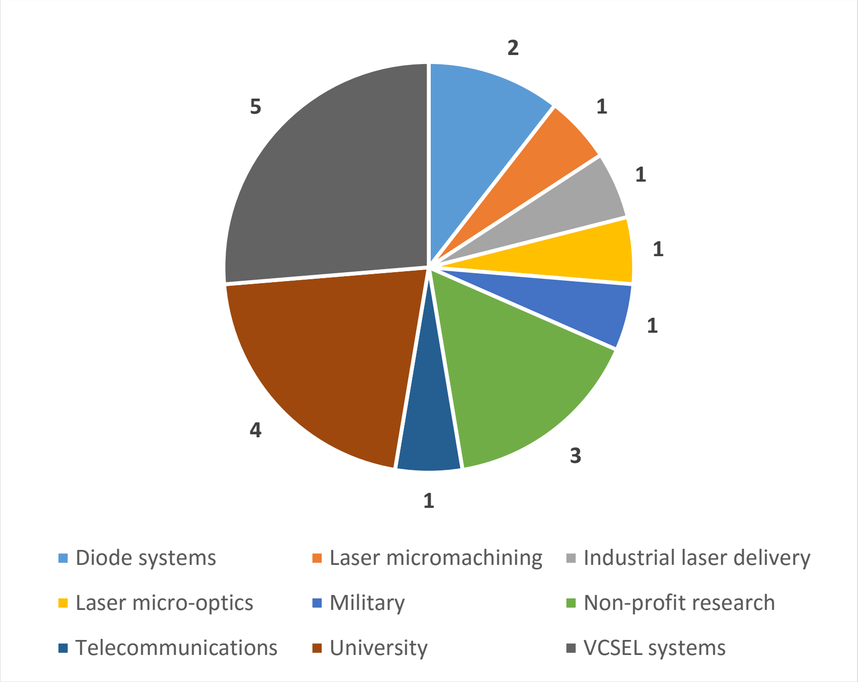

Figure 154: A breakdown of the markets supplied with LightForge parts.

A key objective of LightForge is to act as an initial low-risk trial of new optical surface designs, which may expand into repeatable volume business once trials are shown to be successful. What we found, was that LightForge also acted as an ideal low-risk trial of the PowerPhotonic fabrication technology for customers totally unfamiliar with the concept of freeform laser micromachining. This ability to evaluate not only new optical surface designs, but PowerPhotonic as a company, has proven to be a valuable sales and marketing tool, enticing new significant customers that have previously been difficult to capture. Indeed, some of the customers in the above Figure include the world's leading laser supplier and world's leading fibre laser delivery head supplier. Both of these

LightForge orders were the first sales to the companies and both have progressed to significant volume opportunities.

All LightForge parts sent out to customers were analysed to ensure conformity to the stated specification, and all parts shipped did conform. In many cases, particularly in the case of the low slope and low sag surface designs, the calculated scaling and form errors were well below the stated specification, in some cases achieving <100nm RMS form error. This shows that not only were the specified parameters well chosen, but the laser micromachining strategy was also well chosen.

Chapter 6 – Conclusions and Future Work

The work presented in this thesis represents significant advances in the manufacturing processes used by PowerPhotonic to fabricate micro-optics, enabling the noteworthy expansion of the product catalogue as well as defining methods to monitor, improve and scale existing processes. Presented in this final chapter are brief summaries of the outcomes of this EngD from each chapter, along with its impact on PowerPhotonic and the wider world as well as a short recommendation of future work.

6.1 – Chapter 2

A test methodology was developed for monitoring and calibrating the smoothing process using the chirped sinusoidal test structures, in order to maximise process stability and ensure operation is uniform across multiple laser systems. As soon as this method was proven to be a valuable way of characterising the smoothing process, it was implemented as a standard production procedure. It is now carried out twice a week as a monitor to ensure process stability, and is currently being used to construct a completely new laser micromachining system in order to confirm that the smoothing process is operating as expecting.

Future work involves using the test structures with varying laser parameters to determine whether a smoothing regime can be found where the sensitivity to process changes is reduced.

6.2 – Chapter 3

A test methodology was also developed for determining the effect of raster cutting directions on surface reproduction. This resulted in the unexpected outcome of the BISCAN cut strategy not giving the most symmetric result, which gave rise to investigation of the angular tolerances between the cutting beam and the substrate normal. The wedge test structure defined in this chapter is now also cut regularly to ensure that optimum form reproduction is being achieved when using the BISCAN cut strategy.

Further investigation should be undertaken into why the spatial offset between reference lines was higher than the expected value of <1μm. Suggested future work is for this analysis to be undertaken when cutting the test structure in the orthogonal direction, in order to examine the effect on form reproduction of the UNISTEP cut strategy compared to the BISTEP cut strategy.

A multi-pass cutting process was implemented that allowed for optics to be manufactured with cut depths many times deeper than previously possible using single-pass cutting strategies. This particular advance, along with the development of the FACA and the LightForge process, has likely had the biggest impact on the internal process at PowerPhotonic. The ability to cut deeper than 60µm while still maintaining a very high level of form accuracy has allowed the number of products in PowerPhotonic's product catalogue to grow by a number of multiples. Multi-pass cutting has also shown some evidence, since the writing of this thesis, that form reproduction is indeed superior in the step direction when using BISTEP multi-pass cutting techniques. This has meant that even optics that have maximum depths <60µm are regularly manufactured with multi-pass cut strategies in order to maximise form accuracy.

However, multi-pass cutting has not been fully characterised. Suggested future work is the detailed measurement of the higher frequency components of the as-cut surfaces after multi-pass cutting, and its comparison to single-pass cutting. Also, an investigation in to the influence of number of passes should be undertaken as this may have an impact not only on surface form accuracy but also production time required.

A method of compensating for defocus of the laser system when cutting optics with sags much greater than the system depth of focus was implemented and tested. This not only gave superior overall form reproduction of a test optic, but further insight into the depth of focus available to the laser system. Further work is required to more completely evaluate the system depth of focus and how form reproduction changes as the cutting region moves away from the system focal plane.

A novel fast-axis collimator array (FACA) was designed, a production process was developed and test parts were manufactured using the multi-pass cutting process and defocus compensation. As part of this initial work, parts were also manufactured to a customer specification and sold. This led to follow-on orders from that customer which resulted in them becoming the biggest single customer of PowerPhotonic's in revenue terms. This initial work led to the development of bi-convex versions of the FACA which are included in the HAPLS laser diode array that is going to be installed at the Extreme Light Infrastructure (ELI). This is a European Research Initiative that aims to produce femtosecond pulses with peak powers of up to 10 petawatts. Additionally, a patent covering the FACA optic is directly attributed to this work.

Suggested future work is the investigation of more suitable metrological systems that can accurately measure the very high slope surfaces required in a fused silica FACA. This should help enable higher performance FACA's to expand their market accessibility as, although they are currently generating significant revenue and are used in large and expensive systems, their ability to collimate the fast-axis of a laser diode still does not approach existing suppliers.

6.3 – Chapter 4

In this chapter a localised dust extraction system was designed, tested and refined such that it was able to reduce silica dust accumulation on the surface of the optics during the manufacturing process without affecting the process itself. This project had particularly difficult constraints to manage, as testing involved the modification of the laser micromachining system that was used for revenue generation at PowerPhotonic. Thus, not only aw available testing time limited but tests took longer as the extraction head required full assembly at the start of the test and full disassembly at the end. The reduction in silica dust accumulation is ultimately expected to increase the accuracy of form reproduction for optical surfaces where volume removal is high and a large amount of dust is generated.

The mechanical design undertaken and the investigations in to turbulence airflow and increased lubricity plating remain very valuable for future work. More work is required to analyse back-to-back comparisons of high volume optical surfaces manufactured with and without dust extraction, as well as evaluation of the mechanical design changes proposed in Section 4.5.

6.4 – Chapter 5

The design, development and implementation of the LightForge service is the culmination of many smaller tests, experiments and projects. Without a firm understanding in a wide range of the processes established at PowerPhotonic, execution of the LightForge service would not have been possible. Since its inception almost all of the customers have been completely new to PowerPhotonic and some have re-ordered through LightForge again. What is not shown in Section 5.7, is the follow-on impact to PowerPhotonic as customers now use LightForge as an initial trial to evaluate the manufacturing technology and progress to non-LightForge fully custom parts once satisfied.

Of particular note is a recent highly successful trial of a LightForge-manufactured, customer-designed beamshaper of novel design. This beamshaper is used to drastically alter the intensity distribution of a high-power industrial fibre laser so that it can be used in two distinct modes. However its surface topology is highly complex and the LightForge process allowed the customer to quickly and cheaply test a real-world prototype to determine the validity of the design. This prototype performed as intended, and a follow on order for full size parts to be integrated in to fibre laser process heads has been delivered. It is projected that this application could be worth several hundred thousand euros per year to PowerPhotonic, which stemmed directly from a low-risk LightForge trial of a speculative optical design. Additionally, the customer has applied for a patent on the surface design.

As can be seen from Section 5.6, there is significant room for development of the LightForge process. This deals not only with expanding the functionality of the LightForge service in order to expand the accessibility in the market, but also with customer feedback mechanisms and interface. Since the release of the LightForge service, its visibility to customers and the subsequent number of orders received has been constantly increasing. This can only benefit PowerPhotonic as a LightForge part not only requires very little engineering effort and is thus relatively straightforward to manufacture, but pays for itself while acting as a low-risk test mechanism to evaluate the PowerPhotonic fabrication technology.

References

[1] G. A. Markillie, H. J. Baker, F. J. Villareal and D. R. Hall, “Effect of vaporization and melt ejection on laser machining of silica glass micro-optical components,” *Applied Optics,* vol. 41, no. 27, 2002.

[2] K. M. Nowak, H. J. Baker and D. R. Hall, “Pulsed-laser machining and polishing of silica micro-optical components using a CO2 laser and an acousto-optic modulator,” *Proceedings of SPIE,* vol. 4941, 2003.

[3] P. A. Temple, W. H. Lowdermilk and D. Milam, “Carbon dioxide laser polishing of fused silica surfaces for increased laser-damage resistance at 1064 nm,” *Applied Optics,* vol. 21, pp. 3249-3255, 1982.

[4] K. M. Nowak, H. J. Baker and D. R. Hall, “Efficient laser polishing of silica micro-optic components,” *Applied Optics,* vol. 45, pp. 162-171, 2006.

[5] K. M. Nowak, H. J. Baker, R. M. McBride and J. J. Wendland, “Laser Pulse Generation Method and Apparatus”. Great Britain Patent GB2485985, 06 2012.

[6] K. M. Nowak, H. J. Baker, R. M. McBride and J. J. Wendland, “Laser Pulse Generation Method and Apparatus”. United States of America Patent US2012298650, 11 2012.

[7] K. M. Nowak, H. J. Baker, R. M. McBride and J. J. Wendland, “Method of and apparatus for generating a laser pulse by controlling a modulator”. European Union Patent EP2457685, 05 2012.

[8] J. F. Monjardin, K. M. Nowak, H. J. Baker and D. R. Hall, “Correction of beam errors in high power laser diode bars and stacks,” *Optics Express,* vol. 14, pp. 8178-8183, 2006.

[9] N. Trela, H. J. Baker, J. J. Wendland and D. R. Hall, “Dual-axis beam correction for an array of single mode diode laser emitters using a laser-written customer phase-plate,” *Optics Express,* vol. 17, pp. 23576-23581, 2009.

[10] H. J. Baker, C. Ott, R. M. McBride, J. J. Wendland and D. R. Hall, “Beam shapers for high power lasers, fabricated by laser micro-machining,” in *Conference on Laser and Electro-Optics (CLEO)*, Baltimore, US, 2009.

[11] F. M. Dickey, T. E. Lizotte, S. C. Holswade and D. L. Shealy, Laser Beam Shaping Applications, CRC Press, 2005.

[12] U. Brauch, P. Loosen and H. Opower, High-Power Diode Lasers for Direct Applications, Berlin: Springer-Verlag, 2000.

[13] H. J. Baker, J. F. Monjardin-Lopez, F. J. Villareal-Saucedo and R. M. McBride, “Optical Characteristic Mapping Instrument”. United States of America Patent US2010012818 , 01 2010.

[14] H. J. Baker, J. F. Monjardin-Lopez, F. J. Villareal-Saucedo and R. M. McBride, “Optical Characteristic Mapping Instrument”. WIPO Patent WO2008025958, 03 2008.

[15] H. J. Baker, J. F. Monjardin-Lopez, F. J. Villareal-Saucedo and R. M. McBride, “Optical Characteristic Mapping Instrument”. European Union Patent EP2074395, 07 2009.

[16] M. Peach, “PowerPhotonic develops optics for ELI high-power laser,” Optics.org, 06 2015. [Online]. Available: http://optics.org/news/6/6/11.

[17] T. R. Steyer, K. L. Day and D. R. Huffman, “Infrared absorption by small amorphous quartz spheres,” *Applied Optics,* vol. 13, pp. 1586-1590, 1974.

[18] H. R. Philipp, Handbook of Optical Constants of Solids, London: Academic, 1985.

[19] H. M. Presby, A. F. Benner and C. A. Edwards, “Laser micromachining of efficient fiber microlenses,” *Applied Optics,* vol. 29, pp. 2692-2695, 1990.

[20] E. Mendez, K. M. Nowak, H. J. Baker, F. J. Villareal and D. R. Hall, “Localized CO2 laser damage repair of fused silica optics,” *Applied Optics,* vol. 45, no. 21, pp. 5358-5367, 2006.

[21] K. L. Wlodarczyk, Surface deformation mechanisms in laser smoothing and micromachining of optical glasses, Edinburgh: Heriot-Watt University PhD thesis, 2011.

[22] E. Mendez Fernandez de Cordoba, Laser micro-polishing of silica optics, Edinburgh: Heriot-Watt University PhD thesis, 2007.

[23] K. M. Nowak, Rapid prototyping of micro-optics for brightness restoration of diode lasers, Edinburgh: Heriot-Watt University PhD thesis, 2003.

[24] Y. M. Xiao and M. Bass, "Thermal stress limitations to laser fire polishing of glasses," *Applied Optics*, vol. 22, pp. 2933-2936, 1983.

[25] K. L. Wlodarczyk, E. Mendez, H. J. Baker, R. M. McBride and D. R. Hall, "Laser smoothing of binary gratings and multilevel etched structures in fused silica," *Applied Optics,* vol. 49, no. 11, pp. 1997-2005, 2010.

[26] F. Laguarta, N. Lupon and J. Armengol, "Optical glass polishing by controlled laser surface-heat treatment," *Applied Optics,* vol. 33, pp. 6508-6512, 1994.

[27] F. Vega, N. Lupon, J. A. Cebrian and F. Laguarta, "Laser application for optical glass polishing," *Optics Engineering,* vol. 37, pp. 272-279, 1998.

[28] British Standards Institution, "BS ISO 10110 Optics and photonics - Preparation of drawings for optical elements and systems," British Standards Institution, 1997.

[29] V. N. Mahajan, "Strehl ratio for primary aberrations in terms of their aberration variance," *Optical Society of America,* vol. 73, no. 6, pp. 860-861, 1983.

[30] P. Ott, "Optic design of head-up displays with freeform surfaces specified by NURBS," *Proceedings of the SPIE, Optical Design and Engineering,* vol. 7100, 2008.

[31] H. Kogelnik and T. Li, "Laser Beams and Resonators," *Proceedings of the IEEE,* vol. 54, no. 10, pp. 1550-1567, 1966.

[32] Ingeneric GmbH, "Fas-Axis Collimation Optics," June 2010. [Online]. Available: http://www.ingeneric.com/pdf/FAC_INGENERIC.pdf.

[33] R. McBride, M. O. Currie and J. J. Wendland, “Fast-Axis Collimator Array”. United States of America Patent US8570657, 2014.

[34] R. McBride, M. O. Currie and J. J. Wendland, “Fast-Axis Collimator Array”. United Kingdom Patent GB2485464, 2014.

[35] R. McBride, M. O. Currie and J. J. Wendland, “Fast-Axis Collimator Array”. European Union Patent EP2450737, 2014.

[36] R. McBride, N. Trela and H. J. Baker, “Monolithic biconvex fast axis collimator array”. United Kingdom Patent GB2510401, 2014.

[37] UK Health and Safety Executive, “Control of Exposure to Silica Dust,” 2014.

[38] Corning Incorporated, “HPFS Fused Silica Standard Grade,” 2003.

[39] Army Engineer Waterways Experiment Station, “Characterisation and Reactivity of Silica Fume,” *DTIC report,* 1981.

[40] C. J. Johnston, K. E. Driscoll, J. N. Finkelstein, R. Baggs, M. A. O'Reilly, J. Carter, R. Gelein and G. Oberdorster, “Pulmonary Chemokine and Mutagenic Responses in Rats after Subchronic Inhalation of Amorphous and Crystalline Silica,” *Toxicological Sciences,* pp. 405-413, 2000.

[41] R. Merget, T. Bauer, H. U. Kupper, S. Philippou, H. D. Bauer, R. Breitstadt and T. Bruening, “Health Hazards due to the Inhalation of Amorphous Silica,” *Archives of Toxicology,* vol. 75, pp. 625-634, 2002.

[42] B. G. Gribov, K. V. Zinov'ev, O. N. Kalashnik, N. N. Gerasimenko, D. I. Smirnov and V. N. Sukhanov, “Structure and Phase Composition of Silicon Monoxide,” *Semiconductors,* vol. 46, no. 13, pp. 1576-1579, 2012.

[43] R. M. Hagenmayer, B. Friede and M. Janser, “Structural studies on amorphous Si2O3 and H2Si2O4 by means of dffraction using high energy photons,” *Journal of Non-Crystalline Solids,* vol. 226, pp. 225-231, 1998.

[44] K. L. Day and B. Donn, “Condensation of Nonequilibrium Phases of Refractory Silicates from the Vapor,” *Science,* vol. 202, pp. 307-308, 1978.

[45] M. R. Zachariah and H. G. Semerjian, “Silica Particle Synthesis in a Counterflow Diffusion Flame Reactor,” *Combustion and Flame,* vol. 78, pp. 287-298, 1989.

[46] C. F. Bohren and D. R. Huffman, Absorption and scattering of light by small particles, New York: John Wiley & Sons, 1983.

[47] British Standards Insitution, “BS ISO 10303 Industrial automation systems and integration - Product data representation and exchange,” British Standards Institution, 1994.

[48] S. Gangadhara, “How to Measure the Sag of an NSC Object,” Radiant Zemax, 23 November 2007. [Online].

[49] A. Valdmann, P. Piksarv, H. Valtna-Lukner and P. Saari, “Realization of laterally nondispersing ultrabroadband Airy pulses,” *Optics Letters,* vol. 39, no. 7, 2014.

[50] A. Mathis, F. Courvoisier, L. Froehly, L. Furfaro, M. Jacquot, P. A. Lacourt and J. M. Dudley, “Micromachining along a curve: Femtosecond laser micromachining of curved profiles in diamond and silicon using accelerating beams,” *Applied Physics Letters,* vol. 101, 2012.

[51] G. A. Siviloglou, J. Broky, A. Dogariu and D. N. Christodoulides, “Observation of Accelerating Airy Beams,” *Physical Review Letters,* vol. 99, no. 21-23, 2007.

[52] M. O. Currie, C. Y. Younger and R. M. McBride, “Design and Manufacture of Custom Optical Elements”. Patent GB2510420 (A), 08 2014.

[53] M. O. Currie, C. Y. Younger and R. M. McBride, “Process for the Manufacture of Custom Optical Elements”. Patent US2014222182 (A1), 08 2014.

[54] T. H. Maiman, “Stimulated Optical Radiation in Ruby,” *Nature,* vol. 187, p. 493, 1960.